

Visualization of
intermediates of
translation
in vitro and *ex vivo*
by cryo-EM.

Inaugural-Dissertation
to obtain the academic degree
Doctor rerum naturalium (Dr. rer. nat.)
submitted to the Department of Biology, Chemistry and Pharmacy
of Freie Universität Berlin

by
Julia Flis
2019

This thesis is the result of my work at the institute of medical physics and biophysics at Charite University, Berlin, under the direction of Professor Dr. Christian M.T. Spahn, from April 2015 to December 2018.

Diese Arbeit wurde von April 2015 bis Dezember 2018 am
Institut für Medizinische Physik und Biophysik, Charite
Universitätsmedizin Berlin, unter der Leitung von Professor Dr.
Christian M.T. Spahn angefertigt.

1. Gutachter: Christian M. T. Spahn

2. Gutachter: Markus Wahl

Disputation am 26.04.2019

Table of contents

1. Summary/Zusammenfassung	8
Summary	8
Zusammenfassung	9
2. Introduction	12
2.1 Common principles of protein biosynthesis	12
General features of the ribosome	12
2.2 Anatomy of the (mammalian) ribosome	15
rRNA is the catalytically active component of the ribosome	15
The three-dimensional shape of the ribosome is optimized for its function	16
2.3 The main interaction partners of the ribosome	18
Messenger RNA (mRNA) contains the protein sequence	18
Transfer RNAs (tRNAs) allow for exact selection and incorporation of amino acids	19
Translational GTPases tune the energy landscape of translation	20
2.4 Ribosome dynamics reshapes interaction sites and defines functional states	23
2.5 The key steps of mammalian translation are initiation, elongation, termination and recycling	25
Initiation places the start codon in the P site by ribosome scanning	27
Elongation is at the heart of translation	29
Translocation prepares the ribosome for a new elongation cycle	31
Termination releases the peptide chain and is followed by recycling	34
mRNA quality control prevents production of degenerated proteins	35

2.6 Translation is subject to multiple layers of regulation	36
Actively translating ribosomes are organized into polysomes	37
Phosphorylation of ribosomal protein eS6: a possible switch for translation regulation?	39
2.7 Single particle cryo-EM as a tool in structural biology	43
Construction of the transmission electron microscope	43
Cryogenic transmission electron microscopy allows imaging of biological specimens	45
Interaction of the electrons with the sample	45
Cryo-EM of biological specimens is dominated by phase contrast	47
Direct electron detectors contributed a great deal to the 'resolution revolution'	49
Image processing leads from 2D projections to 3D volumes	51
The final maps and resolution limits of cryo-EM	54
3. Aims	57
Aim 1: To visualize and mechanistically understand mammalian translocation.	57
Aim 2: To investigate the 80S•tRNA ₂ •mRNA•eEF2•GDP complex that is observed upon addition of eEF2•GTP to a programmed PRE complex.	58
Aim 3: To revisit the mammalian polysome landscape to find out if serum deprivation influences the distribution of states.	58
Aim 4: To look at the phosphorylation site of ribosomal protein eS6 and its possible impact on its surrounding structures to find out the role of eS6 phosphorylation.	58
4. Methods	60
4.1 List of materials	60
Table 1: Chemicals	60
Table 3: Web lab tools and devices.	63
Table 4: Microscopy tools and devices	63
Table 5: Software and online databases/tools	64
Table 6: Online tools and databases	65

4.2 Preparation of the cryo-EM sample of <i>ex vivo</i> derived polysomes	65
Cell culture conditions	65
Preparation of a cytoplasmic extract from HEK-cells	66
4.3 Biochemical analysis of <i>ex vivo</i> derived polysomes	68
Photometric estimation of protein/RNA concentration	68
Sucrose gradient centrifugation	69
Subunit preparation	69
Gel electrophoresis	70
Western blot	70
4.4 Preparation of the cryo-EM sample of 80S•tRNA₂•eEF2 complexes from rabbit.	71
Reconstitution of translocation intermediates stalled with eEF2•GMPPNP	71
Reconstitution of an 80S•tRNA ₂ •eEF2•GDP complex	72
4.5 Making of the grids and sample application	72
Making of negative stain grids	72
Making of cryo-EM grids	73
4.6 Data acquisition	73
Low and intermediate resolution imaging	73
High resolution imaging	74
4.7 Data processing	74
Screening of the micrographs, CTF estimation, motion correction and frame weighting	74
Particle identification and making of particle stacks	75
Refinement and sorting	75
Post-processing steps on final particle selection	76
4.8 Modeling	78
4.9 Validation of map and model, preparation of final maps and map-to-model correlation	80

5. Results	82
5.1 In-vitro reconstitution of intermediates of translocation reveal three late translocation intermediates.	83
The captured intermediates are distinguished by 40S body/platform rotation/rolling and 40S head swivel.	86
The tRNAs are translocated to their classical positions via a chimeric hybrid state	88
The G-domain is in an active conformation	91
Domain 4 of eEF2 protrudes into the A site.	92
Changing of the P-gate and subunit back-rolling.	94
The tRNAs move stepwise into a compacted state.	97
5.2 In vitro translocation with eEF2•GTP leads to a eEF2-binding subpopulation.	99
5.3 Intermediates of actively translating polysomes.	103
Sample preparation and analysis of polysomes	103
Multiple energy barriers control the mammalian elongation cycle.	106
Focused refinement of the e6 region.	111
Native initiation factor and ternary complex loaded 40S subunits found on polysomes.	119
6. Discussion	125
6.1 A model for mammalian translocation	126
Late translocation is governed by ribosome rearrangements	126
Conformational changes in the ribosome during translocation in mammalia compared to yeast	128
Table 7: Comparison of conformations of eEF2-bound ribosomes	130
GTP hydrolysis limits late steps of translocation in the mammalian ribosome	131
Translocation by mammalian ribosomes compared to bacterial translocation reveals a key role of the E-site tRNA	135
The role of the diphthamide modification of eEF2	143
Possible advantages of an ordered A-site codon	144
6.2 The other eEF2-complexes	144

<i>In vitro</i> reconstituted 80S•tRNA ₂ •mRNA•eEF2•GDP complexes	144
<i>Ex vivo</i> found monosomes binding eEF2	145
6.3 The expansion of the polysomal energy landscape	146
What is the role of serum deprivation and serum restimulation and eS6 phosphorylation in the energy landscape of translation?	146
Previously uncharacterized <i>ex vivo</i> states of translation	149
7. Conclusions	153
8. Supplemental material	154
9. References	160
10. Appendix	178
Publications	178
Acknowledgements	178

1. Summary/ Zusammenfassung

Summary

Ribosomal protein biosynthesis (translation) is a crucial process in all domains of life. This work aims to investigate the process of translation in the mammalian system by means of single particle cryogenic electron microscopy (cryo-EM). The focus of this thesis lies on the following two aspects of mammalian translation:

1) *Translocation by the mammalian cytosolic 80S ribosome.* Translocation moves the tRNA₂•mRNA module directionally through the ribosome during the elongation phase of translation and is associated with large scale conformational changes within both the ribosome and the bound tRNAs. It is catalyzed by the GTPase eEF2 (EF-G in bacteria). Although knowledge on translocation, especially in the bacterial system, has accumulated in the past years, the detailed mechanisms are not fully understood. In particular, the role of GTP hydrolysis is controversial and structural knowledge on translocation in the mammalian system has been missing.

In this work, three high-resolution structures of *in vitro* reconstituted authentic intermediates of translocation by the mammalian 80S ribosome are presented. They are trapped by the non-hydrolysable GTP analog GMPPNP and contain, in contrast to similar experiments in the bacterial system, the translocase eEF2 and a complete tRNA₂•mRNA module. Single-molecule imaging, carried out in collaboration with Prof. Scott Blanchard and colleagues, revealed that GTP hydrolysis principally facilitates rate-limiting, late steps of translocation, consistent with the presented cryo-EM structures. Comparison with the bacterial system showed that distinctions between bacterial and mammalian translocation mechanisms originate from differential dissociation rates of deacylated tRNA from the E site.

Summary/Zusammenfassung

Further, a cryo-EM structure of a mammalian 80S ribosome containing a complete tRNA₂•mRNA module and eEF2•GDP is presented, which stems from a sample prepared by *in vitro* translocating a PRE complex using eEF2•GTP. In contrast to the GMPPNP-stalled translocation intermediates, this structure gives insight into the interaction of unstalled eEF2 with the 80S ribosome.

2) The influence of serum on the energy landscape of mammalian translation and on the structure of ribosomal protein eS6. Serum treatment of cells intervenes with many signaling pathways, but it is not known if the energy landscape of translation is altered upon its influence. Serum deprivation and restimulation can be used as a model system to diminish and enhance phosphorylation of ribosomal protein eS6, which is a eukaryote-specific protein on the small ribosomal subunit. The phosphorylation of the C-terminus of eS6 has been investigated since a long time, however, its mechanistic role has not been elucidated yet. In particular, hardly anything is known on possible structural impacts of eS6 phosphorylation.

The presented work reveals that serum deprivation and restimulation do not have an impact on the energy landscape of translation for the *ex vivo* derived cytosolic fraction of polysomes. However, the observation of different yields of cell lysate from serum deprived and restimulated cells led to the proposition of a new hypothesis that suggests cellular redistribution of ribosomes. The phosphorylation of ribosomal protein eS6, which strongly correlates with serum treatment, does not lead to observable structural changes in the small ribosomal subunit.

Finally, the structural analysis and *in silico* sorting of the obtained translation intermediates led to the identification of two previously not observed substates of the 80S rotated PRE ribosome and to the unprecedented visualization of two distinct, native initiation complexes.

Zusammenfassung

Die ribosomale Proteinbiosynthese (Translation) ist ein zentraler Prozess in allen Lebensdomänen. In der vorliegenden Arbeit wird der Mechanismus der mammalischen Translation mithilfe der kryogenen

Summary/Zusammenfassung

Elektronenmikroskopie (cryo-EM) untersucht. Der Fokus liegt hierbei auf den folgenden zwei Aspekten der mammalischen Translation:

1) *Die Translokation durch das mammatische, zytosolische 80S Ribosom.* Die Translokation ist die gerichtete Bewegung des tRNA₂•mRNA Moduls durch das Ribosom während der Elongationsphase der Proteinbiosynthese und ist mit umfangreichen Konformationsänderungen des Ribosoms und der gebundenen tRNAs assoziiert. Sie wird durch die GTPase eEF2 (EF-G in Bakterien) katalysiert. Obwohl während der vergangenen Jahre viel über die Translokation, vor allem im bakteriellen System, zusammengetragen wurde, bleibt der genaue Mechanismus unverstanden. Insbesondere die Rolle der GTP-Hydrolyse ist kontrovers und es fehlen strukturelle Daten über die Translokation im mammatischen System.

In dieser Arbeit werden drei hochauflöste Strukturen *in vitro* rekonstituierter, authentischer Translokationsintermediate des mammatischen 80S Ribosoms präsentiert. Sie konnten mithilfe des nicht-hydrolysierbaren GTP-Analogons GMPPNP eingefangen werden und enthalten im Gegensatz zu ähnlichen Experimenten im bakteriellen System die Translokase eEF2 und ein komplettes tRNA₂•mRNA Modul. Die in Kollaboration mit Herrn Prof. Scott Blanchard und seinen Kollegen durchgeführte Einzelmolekül-Bildgebung ergab, dass die GTP-Hydrolyse hauptsächlich späte, geschwindigkeitslimitierende Schritte der Translokation fördert, eine Beobachtung, die in Einklang mit den präsentierten cryo-EM Strukturen steht. Der Vergleich mit dem bakteriellen System schließlich zeigt, dass Unterschiede zwischen bakteriellen und mammatischen Translokationsmechanismen in verschiedenen Dissoziationsraten der deacylierten tRNA von der E Stelle begründet sind.

Des Weiteren wird die cryo-EM Struktur eines mammatischen 80S Ribosoms mit einem kompletten tRNA₂•mRNA Modul und eEF2•GDP präsentiert, welche aus einer Probe stammt, für deren Herstellung ribosomale Prä-Komplexe *in vitro* mit eEF2•GTP transloziert wurden. Anders als die mit eEF2•GMPPNP eingefangenen Translokationsintermediate gewährt diese Struktur Einblick in die Interaktion von unmanipuliertem eEF2 mit dem 80S Ribosom.

Summary/Zusammenfassung

2) *Der Einfluss von Serum auf die Energielandschaft der mammalischen Translation und auf die Struktur des ribosomalen Proteins eS6.* Die Behandlung von Zellen mit Serum greift in viele Signalwege ein, doch es ist nicht bekannt, ob auch die Energienlandschaft der Translation beeinflusst wird. Serum-Deprivation und -Stimulation kann als Modellsystem für die Verringerung und Steigerung der Phosphorylierung des ribosomalen Proteins eS6, einem Eukaryoten-spezifischen Protein der kleinen ribosomalen Untereinheit, angewendet werden. Die Phosphorylierung des C-Terminus von eS6 wird seit langer Zeit erforscht, jedoch ist ihre mechanistische Bedeutung bisher unbekannt. Vor allem weiß man kaum etwas über mögliche strukturelle Auswirkungen der eS6-Phosphorylierung.

Die vorliegende Arbeit zeigt, dass Serum-Deprivation und -Stimulation keinen Einfluss auf die Energienlandschaft der Translation in der zytosolischen Fraktion der *ex vivo* gewonnenen Polysomen hat. Die Beobachtung eines Unterschieds in den Zelllysatausbeuten zwischen Serum-deprivierten und -stimulierten Zellen führte jedoch zu einer neuen Hypothese, welche die zelluläre Umverteilung von Ribosomen nahelegt. Die Phosphorylierung des ribosomalen Proteins eS6, welche stark mit der Serumbehandlung korreliert, führte zu keinen sichtbaren strukturellen Veränderungen in der kleinen ribosomalen Untereinheit.

Zu guter Letzt führte die Strukturanalyse und *in silico* Sortierung der erhaltenen Translationsintermediate zu der Identifikation zweier bisher nicht beobachteten Unterzustände des 80S rotierten Prä-Ribosoms sowie zu der erstmaligen Visualisierung zweier verschiedener, nativer Initiationskomplexe.

2. Introduction

2.1 Common principles of protein biosynthesis

A current theory states that it was RNA that stood at the beginning of life on our planet (Gesteland, R.F., Cech, T.R., 1999). Yet, the later appearing proteins outperformed RNA in so many fields that those early, self-sufficient RNA constructs are now extinct. Whereas RNA is composed by a combination of basically four different types of nucleotides and is relatively limited in its ability to form tertiary structure, proteins are highly flexible chains built from twenty amino acids that can fold in a larger variety of three-dimensional shapes. The amount of building blocks (twenty compared to only four in RNA – leaving aside base modifications) equips them with a high degree of adaptability to different tasks and might be the reason for their superiority to RNA in many fields.

To build such a peptide chain, amino acids have to be linked in the correct order via peptide bond formation. Although there exist proteins which are able to catalyze peptide bonds, like the sortase (Mazmanian et al., 1999), in all kingdoms of life the responsibility for building these peptide chains lies in a ribonucleoprotein particle: a macromolecular machine called the ribosome.

General features of the ribosome

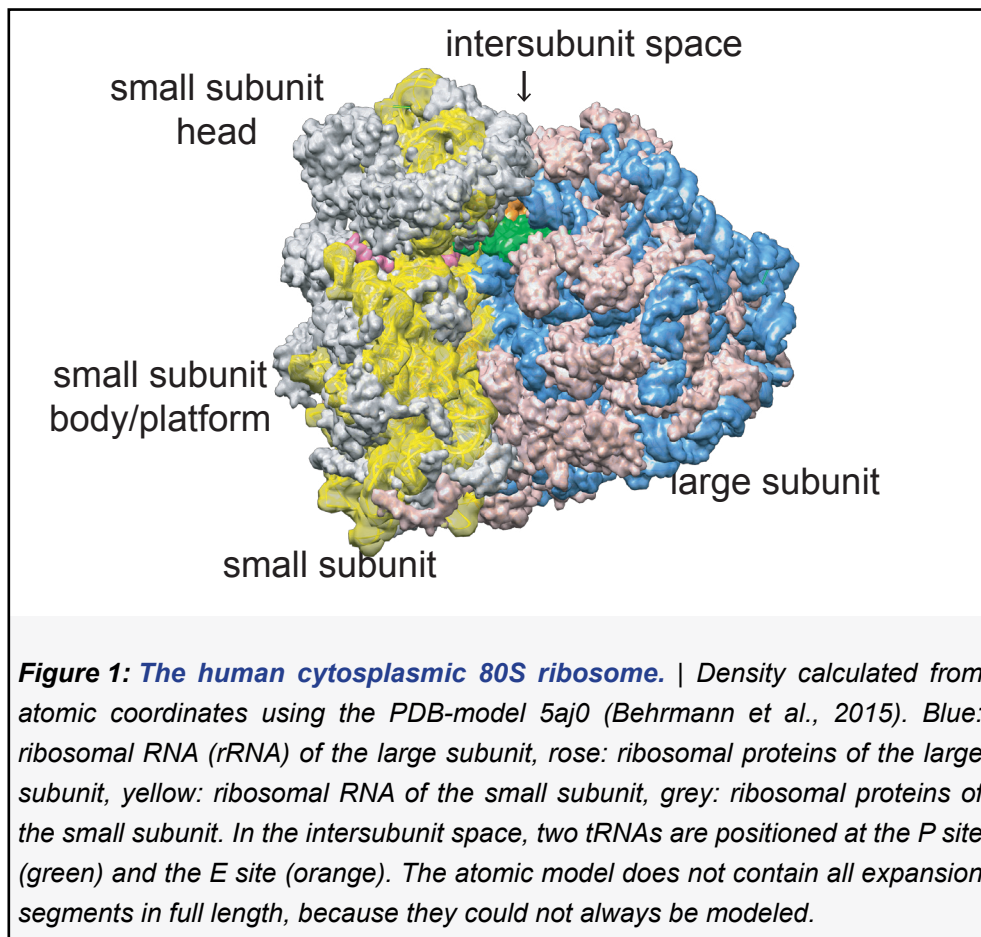
The ribosome consists of a large and a small subunit. Both are made up of ribosomal RNA (rRNA) and ribosomal proteins (**Figure 1**). The basic mechanism of protein synthesis is very similar in all domains of life: A messenger RNA (mRNA) contains the sequence of the protein and is bound and read by the small ribosomal subunit in collaboration with specific transfer RNAs (tRNAs). tRNAs carry the amino acids and contain characteristic anticodons, which establish

2. Introduction

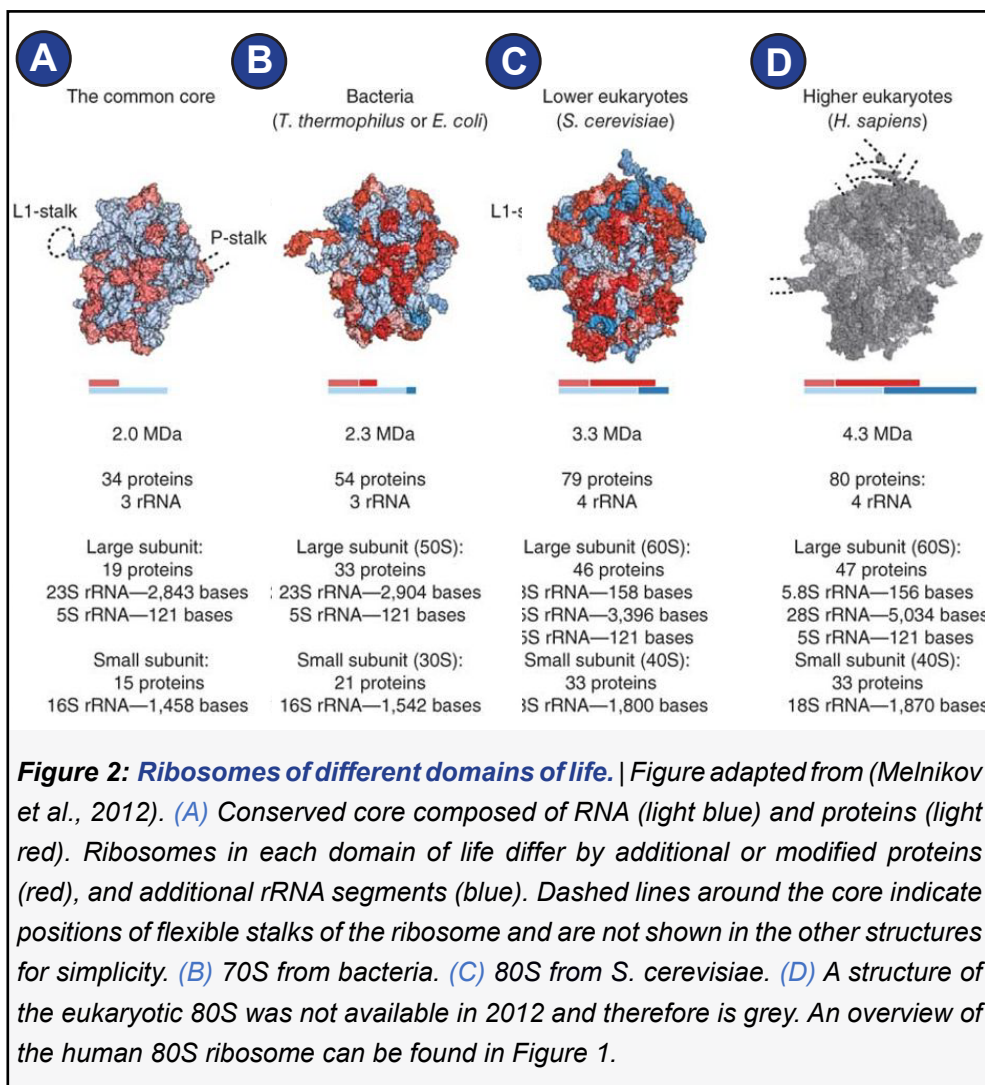
base pairing with the respective codons on the mRNA presented to them by the ribosome. Matching allows for addition of the amino acid to the growing peptide chain. After all amino acids have been added, the peptide chain is released from the ribosome and, if needed, further processed by other cell components to become the final, folded protein.

Although the three domains of life, bacteria, eukaryotes, and archaea, all possess ribosomes for protein synthesis, the composition of the ribosomes varies, leading to sometimes very different overall appearance of ribosomes from different kingdoms of life (Amunts et al., 2015; Behrmann et al., 2015; Dunkle et al., 2011; Melnikov et al., 2012; Ramrath et al., 2018) (**Figure 2**).

The eukaryotic cytoplasmic 80S ribosome is larger than the bacterial 70S ribosome, containing additional RNA segments and additional proteins. Comparison reveals that the eukaryotic ribosome possesses



2. Introduction



the same conserved structures as the bacterial ribosome in its core (**Figure 2A**) and an outer shell where eukaryote-specific elements are located (**Figure 1, Figure 2**) (Melnikov et al., 2012).

Not only the ribosomes themselves differ by certain features and are differently sensitive to antibiotics (Yusupova and Yusupov, 2017), but also the interacting factors that render translation possible are for some stages of translation remarkably different (Andersen et al., 2006) and might be an expression of the way the ribosome has been optimized for its bacterial, archaeal, or eukaryotic cell environment.

2. Introduction

2.2 Anatomy of the (mammalian) ribosome

The size of the assembled 80S mammalian ribosome is about 4.3 MDa (Wool, 1979). Both subunits are made of ribosomal RNA (rRNA) and ribosomal proteins (Wool, 1979). Upon joining of the large 60S (50S in bacteria) subunit and the small 40S (30S in bacteria) subunit to the 80S ribosome (70S in bacteria), a functionally important compartment is formed, the so-called intersubunit space (**Figure 1**), which is one of the main sites of action during protein synthesis. Across it span three tRNA-binding sites, named A (Aminoacyl)-, P (Peptidyl)-, and E (Exit)-sites. Additionally, the ribosome has specific factor binding sites for the interaction with protein factors, like the P-stalk (**Figure 3C-D**).

rRNA is the catalytically active component of the ribosome

The rRNA possesses the catalytic activity to perform peptide bond formation and is the main player in protein synthesis. The large (60S) subunit contains three rRNA molecules: the 28S rRNA, the 5S rRNA and the 5.8S rRNA (**Supplemental Figure 1, Supplemental Figure 2**). The small (40S) subunit contains only one rRNA molecule, the 18S rRNA (**Supplemental Figure 3**). The rRNA regions responsible for mRNA-recognition, tRNA-binding and peptidyl-transfer are highly conserved in all kingdoms of life (Gesteland, R.F., Cech, T.R., 1999). Among these conserved regions are the sarcin ricin loop (SRL) on the large subunit, interacting with GTP-hydrolyzing protein factors that catalyze certain steps of translation. In the peptidyltransferase center (PTC), also located on the large subunit, the RNA alone is responsible for catalyzing the formation of the peptide bond (Nissen et al., 2000; Spahn et al., 2000). The small subunit 18S rRNA contains the decoding center (DC), which monitors correct tRNA-anticodon matching to the mRNA codon.

Different from bacterial rRNA, eukaryotic 18S rRNA and 28S rRNA contain several expansion segments, long elements of additional

2. Introduction

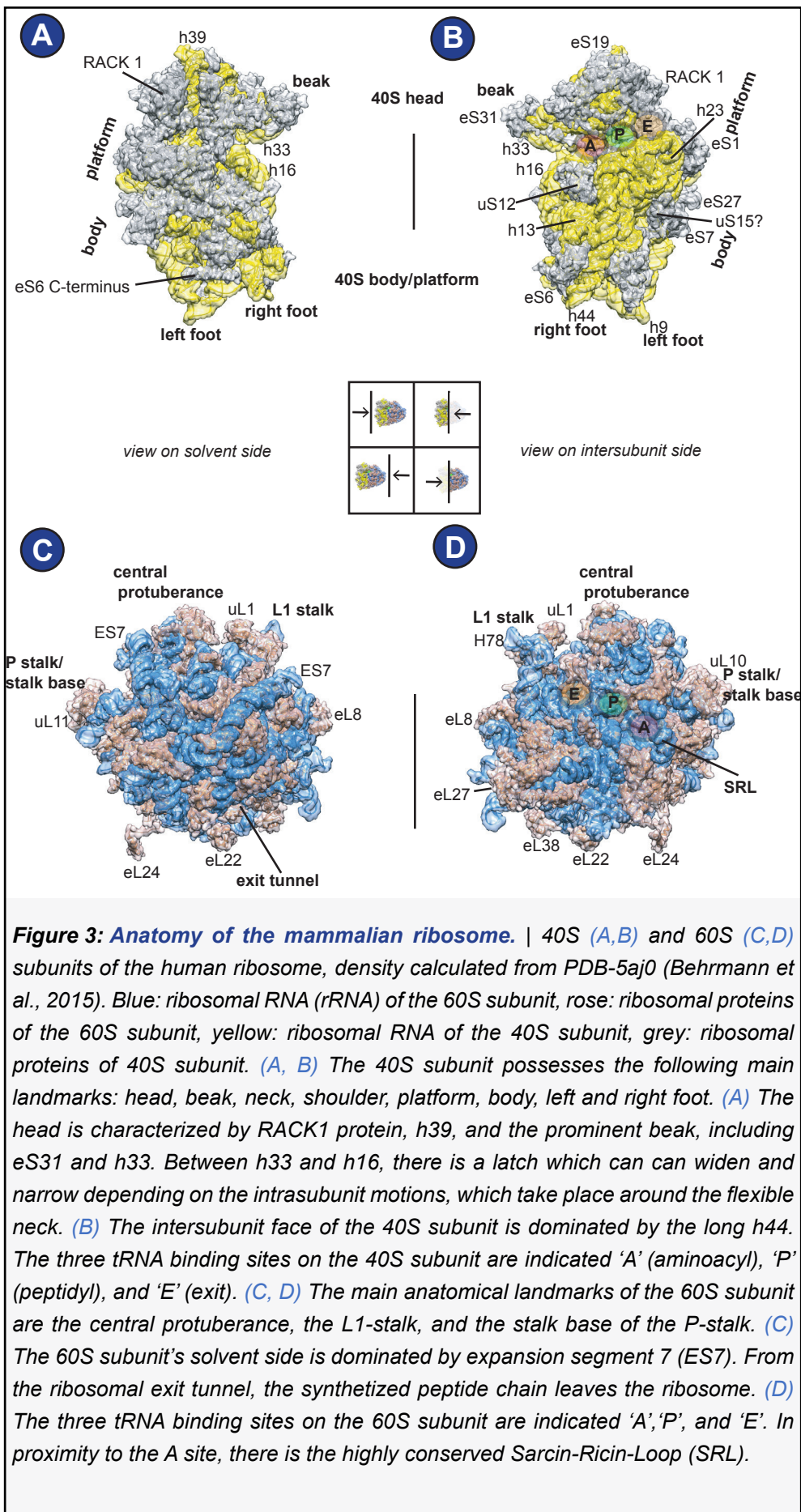
rRNA that are to a great deal responsible for the big difference in size between bacterial and mammalian ribosomes. The function of these expansion segments is not yet clear, and their structural investigation is hindered by their high flexibility and peripheral location, making it very difficult to obtain high-resolution structural information (Ramesh and Woolford, 2016; Yusupova and Yusupov, 2017). There is some evidence, however, that expansion segments may play a role in ribosome biogenesis (Ramesh and Woolford, 2016).

Despite the rRNA's prominent role in translation, the ribosome would not function without ribosomal proteins. They are important for rRNA folding and assembly and stabilize the tertiary structure of rRNA and the ribosome's functional centers. There are 33 ribosomal proteins on the 40S and 47 ribosomal proteins on the 60S subunit of the mammalian ribosome. Following a recent convention (Ban et al., 2014) universally conserved proteins are prefixed 'u', unique bacterial ones 'b', unique eukaryotic ones 'e', and unique archaeal ones 'a' (**Supplemental Figure 4, Supplemental Figure 5**).

The three-dimensional shape of the ribosome is optimized for its function

The 40S subunit can be morphologically divided into several regions, named after the 40S subunit's resemblance in shape to a bird: Looking at it from the solvent site, on top is the 40S 'head' with its prominent 'beak', below follows the 'neck', and the 'body' is supplemented by the 'platform', 'shoulder' and 'foot' domains (**Figure 3A**). In this work, a rough division into two parts will be used: the 40S head (including beak) and the 40S body/platform, comprising the remaining domains. Importantly, the link between the 40S head and 40S body/platform is flexible and allows for intrasubunit motions. Visible from the intersubunit space, there are the three 40S tRNA binding sites that are distributed among the 40S head and 40S body/platform: A, P, and E (**Figure 3B**). The rRNA residues that constitute the tRNA binding sites are well-conserved (**Supplemental Figure 1, Supplemental Figure 2, Supplemental Figure 3**).

2. Introduction



2. Introduction

The large (60S) subunit is characterized by several landmarks; The central protuberance, the P-stalk/stalk base and the L1 stalk (**Figure 3C-D**). From the solvent side, one can see the ribosomal exit tunnel, from which the newly synthesized protein emerges. The solvent side is to a large degree covered by expansion segment ES7, the largest expansion segment of the 28S rRNA (**Figure 3C**). Looking on the 60S from the intersubunit space reveals the A-, P-, and E-tRNA binding sites and the sarcin-ricin loop (SRL) (**Figure 3D**).

2.3 The main interaction partners of the ribosome

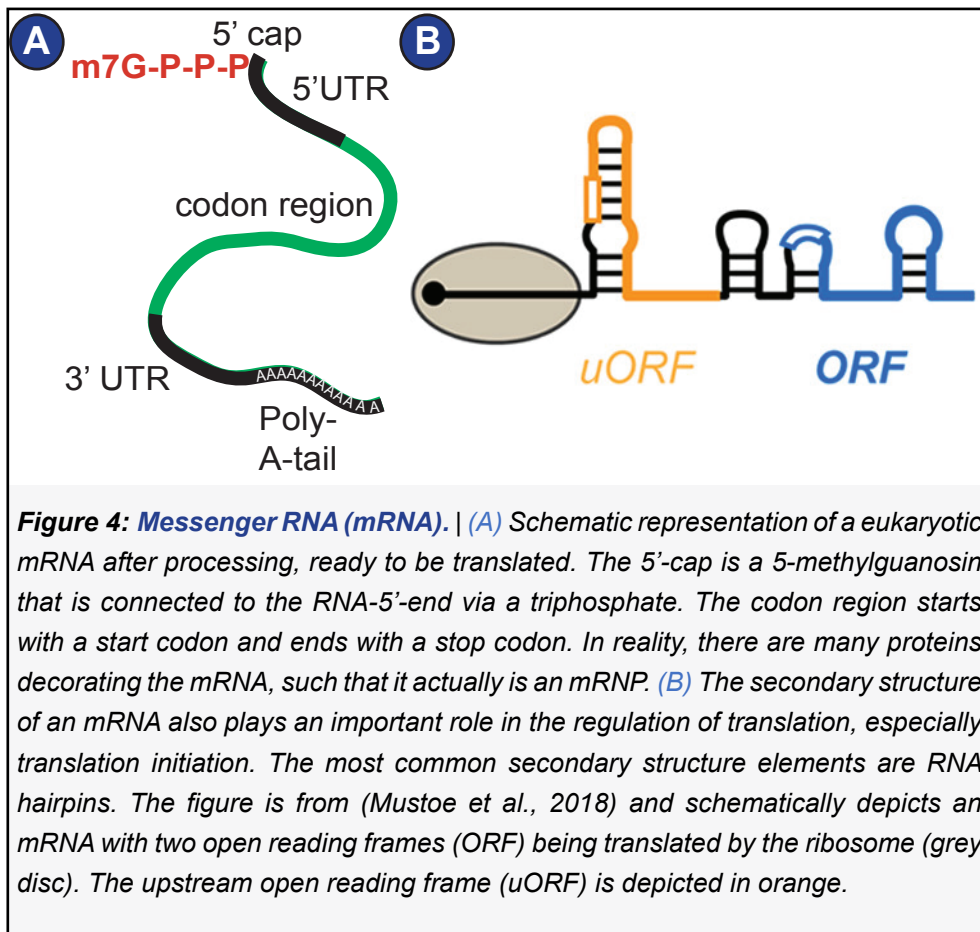
To carry out translation of an RNA template into a protein, the ribosome is dependent on a large set of molecules – mRNAs, tRNAs, protein factors and energy carriers.

Messenger RNA (mRNA) contains the protein sequence

The information on the sequence of amino acids is encoded in the DNA of a cell and has to be transferred to RNA first (paradigm of molecular biology (Crick, 1970)). Such RNA, which serves as template for protein synthesis, is called messenger RNA (mRNA). Its production involves transcription by polymerase II and processing steps such as splicing, polyadenylation and capping (Meister, 2011). The mRNA pool accessible to the ribosome is strictly controlled by a balance between production and decay, variation of polyadenylation, storage in P-bodies, and many other mechanisms that are not well understood yet (Meister, 2011). In eukaryotes, mature mRNA is characterized by a 5' cap, a 5' UTR (untranslated region), the coding region, a 3' UTR, and a poly-A-tail (**Figure 4**). Notably, the mRNA is intensely decorated with proteins that regulate its transport, stability, decay and translation, for example poly-A-binding proteins (PABPs). Thus, mRNA really is a messenger ribonucleoprotein (mRNP) (Mitchell and Parker, 2014). Moreover, mRNA forms secondary structure that influences its interaction with the ribosome (**Figure**

2. Introduction

4B). The entirety of the cellular mRNAs produced for translation at a given time-point is called transcriptome, and the actually translated mRNAs in a cell at a given timepoint constitute the translatome.



Transfer RNAs (tRNAs) allow for exact selection and incorporation of amino acids

tRNAs are specialized RNA molecules that usually consist of around 76 nucleotides. Their role in translation is to deliver the amino acids to the ribosome. Structurally, a tRNA consists of two parts, top and bottom, which organize into an L-shaped tertiary structure (Gesteland, R.F., Cech, T.R., 1999).

The top half comprises the TΨC-arm and the acceptor arm with the CCA-end, which is loaded with the amino acid by specialized enzymes, aminoacyl-transferases. There are elongator tRNAs and initiator tRNAs. Initiator tRNAs ($tRNA_i$) are always loaded with a

2. Introduction

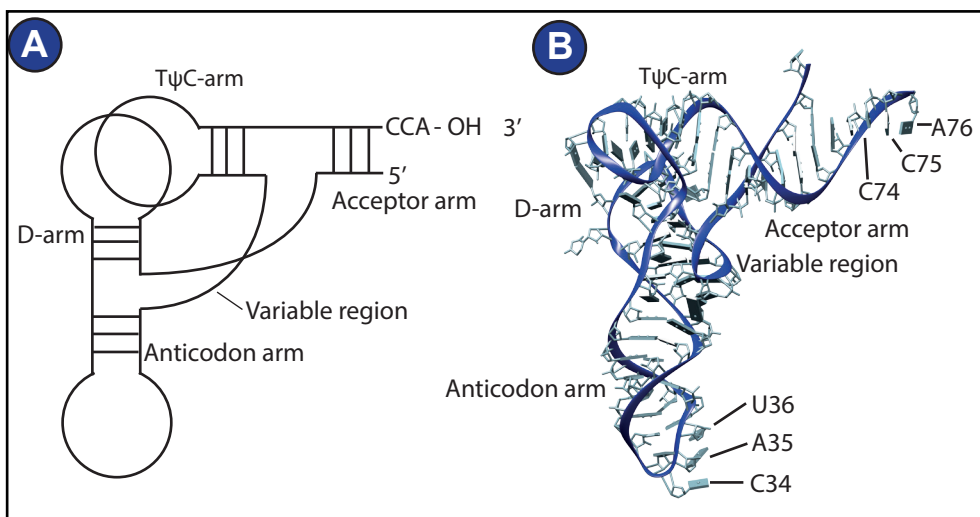


Figure 5: Transfer RNA. | (A) Schematic depiction of a tRNA showing the main features; anticodon arm, acceptor arm, D-arm and T ψ C-arm. This way of representing the tRNA is adapted from (Gesteland, R.F., Cech, T.R., 1999). (B) 3D structure of *E. coli* initiator tRNA (PDB 3CW5) (Barraud et al., 2008).

methionine. The bottom half of a tRNA consists of the D-arm and the anticodon loop, which can decode the mRNA (**Figure 5**). The tRNA nucleotides are often and extensively modified and these modifications are thought to be important for its structure and function (Meister, 2011). The life of tRNA outside of the ribosome is object of intensive research and much less is known about it than about its role on the ribosome. The modification of a tRNA, for example, is complex and includes big protein complexes (Dauden et al., 2017). Further, like the mRNA, the tRNA does not exist in the cytosol as free and naked RNA molecule. The eukaryotic cell operates an elaborate system that channels the tRNAs to and from the ribosome, involving aminoacyl-transferases and probably more factors (Andersen et al., 2006; Mirande, 2010; Stapulionis and Deutscher, 1995).

Translational GTPases tune the energy landscape of translation

Many protein factors are involved in translation by direct interaction with the ribosome, the mRNA or the tRNA. A special subgroup of protein factors involved in translation are translational GTPases. They are GTP-hydrolyzing proteins that control key steps of translation;

2. Introduction

for example the decoding-specific eukaryotic elongation factor 1A (eEF1A), or eukaryotic elongation factor 2 (eEF2), which is necessary for efficient translocation, eukaryotic release factor 3 (eRF3), which is responsible for stop-codon recognition and termination, and eukaryotic initiation factor 5B (eIF5B), which mediates subunit joining (see section ‘translation cycle’).

Structurally, they all have in common the GTP-hydrolyzing domain (G-domain), which forms an alpha-beta-propeller and contains the nucleotide binding pocket (Wittinghofer and Vetter, 2011). Five characteristic G-motifs (G1-G5) and three loops (P-loop, switch I, switch II) organize around the bound nucleotide and characterize the G-domain (**Figure 6; Supplemental Figure 6** shows alignment of the G-domain of EF-G/eEF2 from different species). The G1 motif is also known as Walker A motif and is located within the P-loop. It is responsible for phosphate binding. The Mg²⁺ that is required for nucleotide binding is positioned by the G2 motif and the G3 motif. The G2 motif is part of switch I, whereas the G3 motif (also known as Walker B motif), is located within switch II (Bourne et al., 1991; Wittinghofer and Vetter, 2011) (**Figure 6**). GTP-hydrolysis is achieved by a nucleophilic attack of an activated water molecule and is assisted by the SRL of the ribosome, which serves as GTPase-

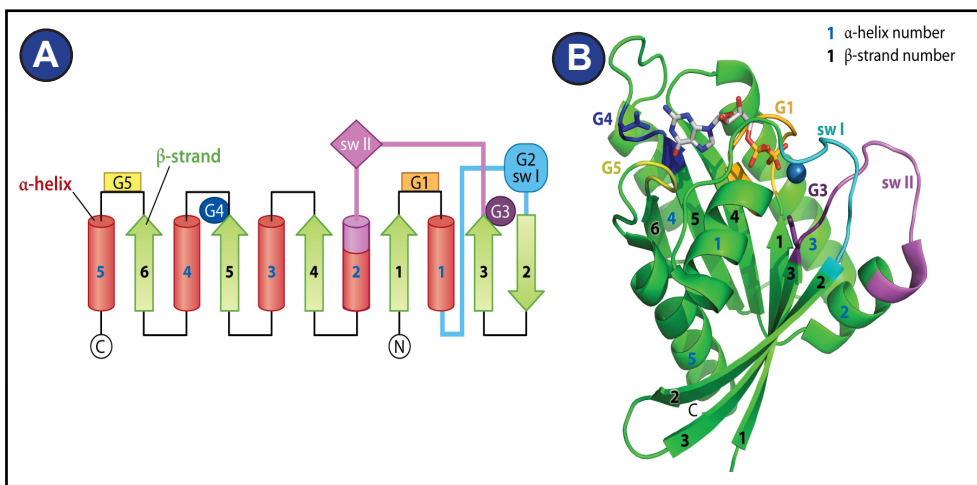
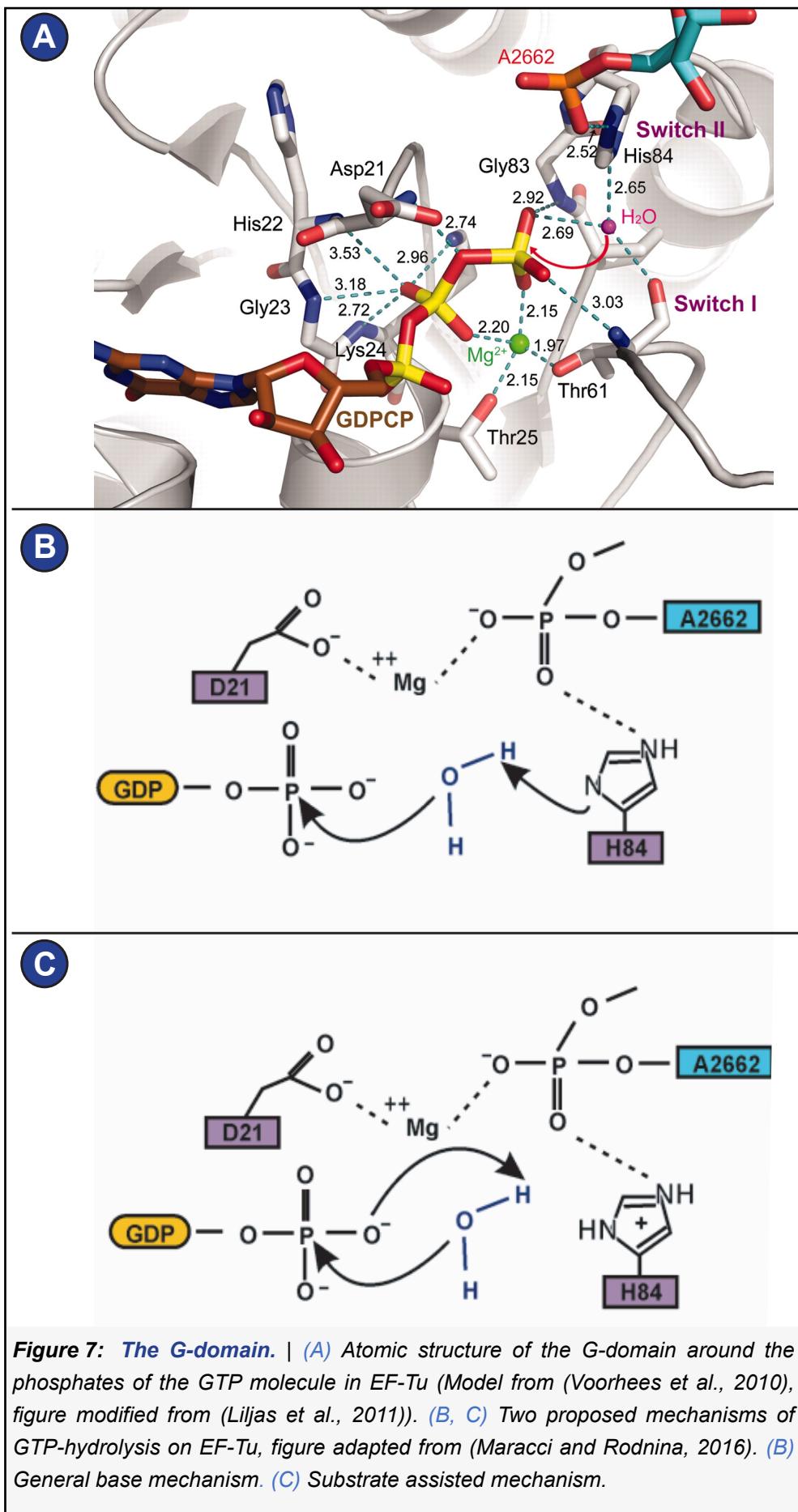


Figure 6: Features of the G-domain | (A, B) Figures adapted from (Wittinghofer and Vetter, 2011). (A) General organization of a G-domain on the level of secondary structure, alpha-helices are red, beta strands green. The localization of the G1-G5 motifs is indicated. (B) Three-dimensional structure of the G-domain of ras-GMPPNP•Mg²⁺ shows that the tertiary structure is an alpha-beta propeller.

2. Introduction



2. Introduction

activating factor for the translational GTPases. Depending on how one interprets the role of a histidine of switch II (His 84 in eF-Tu, His 108 in eEF2) (**Figure 7A**), two mechanism are being proposed that lead there: 1) A general base mechanism, in which the histidine abstracts a proton from the water molecule (**Figure 7B**), and 2) a substrate-assisted mechanism, in which GTP itself abstracts a proton from the water molecule while the histidine serves as allosteric enhancer of this process (**Figure 7C**) (Liljas et al., 2011; Maracci and Rodnina, 2016; Schweins et al., 1995; Voorhees et al., 2010).

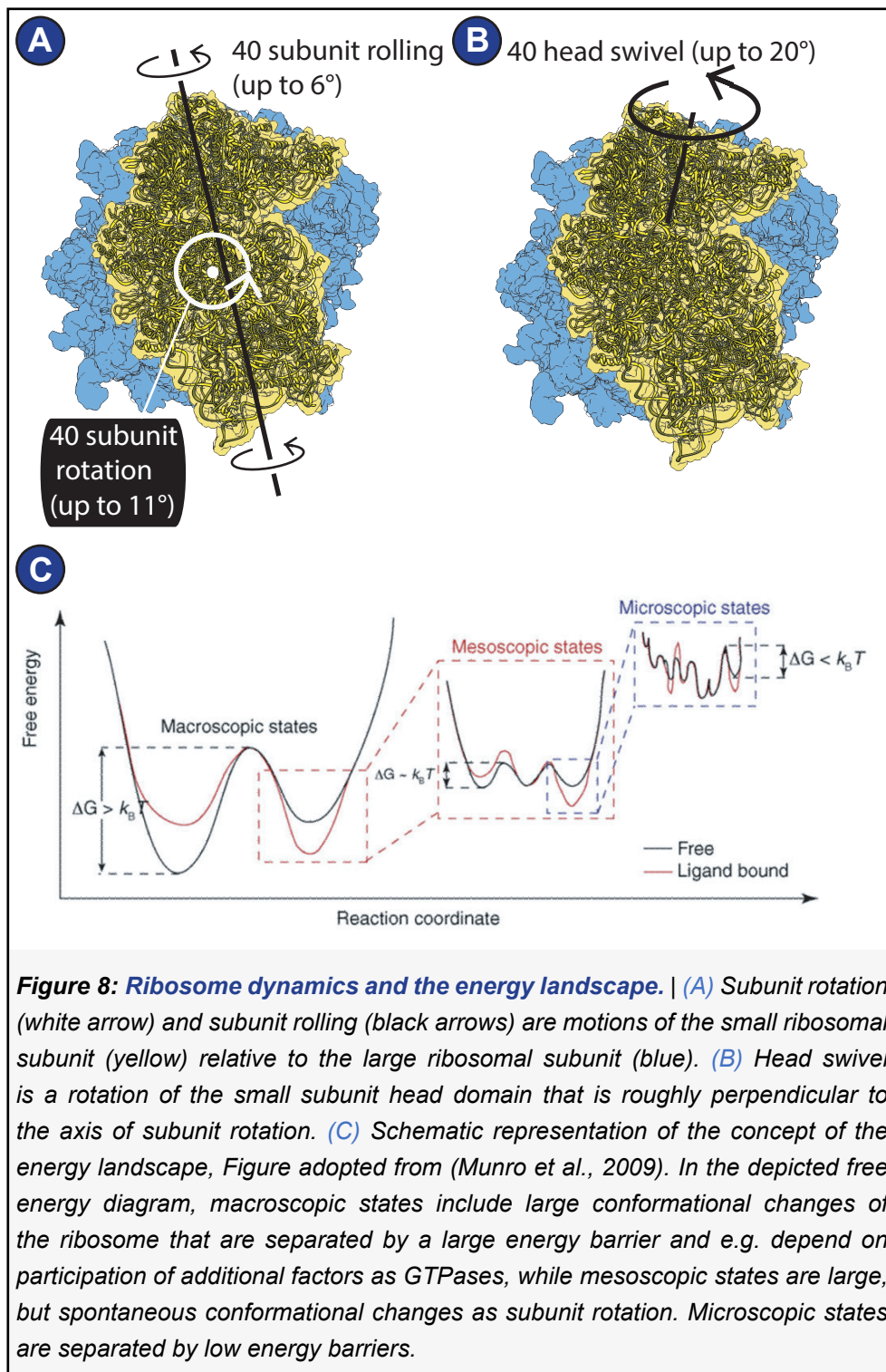
2.4 Ribosome dynamics reshapes interaction sites and defines functional states

Two main large scale motions can be observed in the assembled ribosomes of all domains of life: rotation of the small subunit relative to the large one and swivel of the small subunit head domain relative to the small subunit body/platform domain (**Figure 8A-B**). The combination of subunit rotation and head swivel, observed in early ribosomal structures (Frank and Agrawal, 2000; Horan and Noller, 2007; Valle et al., 2003), was termed 'ratcheting'. Subunit rotation and head swivel result in a reshaping of the intersubunit space, leading to changes in the positions of bound tRNAs and factors: Subunit rotation is known to be associated with the movement of the tRNAs on the large subunit (Moazed and Noller, 1989; Munro et al., 2007), leading to hybrid tRNAs, meaning that the tRNA is bound to one tRNA binding site on the small ribosomal subunit and to another on the large ribosomal subunit (A/P, P/E tRNAs). Head swivel and rotation combined ('ratcheting') are characteristic for the so-called chimeric hybrid state, an intermediate of translocation (Ramrath et al., 2013; Ratje et al., 2010; Zhou et al., 2013, 2014), where hybrid tRNAs bind to different tRNA binding sites on the small ribosomal subunit, one on the body/platform and another on the head domain

2. Introduction

(ap/P, pe/E tRNAs). Moreover, a somewhat ratcheted conformation is also observed in inactive mammalian ribosomes bound to eukaryotic elongation factor 2 (eEF2) (Katter et al., 2015; Voorhees et al., 2014).

A motion so far only observed in the eukaryotic 80S ribosome is rolling of the small subunit, a rotation around the small subunit's long axis (**Figure 8A**) (Behrmann et al., 2015; Budkevich et al., 2014).



2. Introduction

Subunit rolling takes place after decoding and is the main “net” conformational change characterizing the transition from the pre-translocational to the post-translocational state (See section 2.5).

Besides these main motions, there are some flexible parts of the ribosome that have also been observed to adopt distinct conformations: One of them is the L1 stalk (helices H76, H77, H78, and protein uL1) on the 60S subunit (**Figure 3C-D, Supplemental Figure 1, Supplemental Figure 2**), which is known to adopt different positions depending on the functional state of the ribosome (Mohan and Noller, 2017; Spahn et al., 2004a). Another flexible part is the stalk base (Helices H42, H43, H44, and proteins uL10, uL11) on the 60S subunit (**Figure 3C-D, Supplemental Figure 1, Supplemental Figure 2**). It changes its conformation by moving towards the A site upon binding of different factors (Gao et al., 2007; Schuette et al., 2009; Spahn et al., 2004b).

In 2009, Munro at al. applied the principle of the hierarchical energy landscape (Frauenfelder et al., 1991) to the dynamics of translation (Munro et al., 2009) (**Figure 8C**). The ribosome’s conformational degrees of freedom are directly connected to the forward movement of tRNAs during translation (Munro et al., 2009). The interplay of thermodynamically spontaneous motions (like subunit rotation), stabilizing and destabilizing contributions of the tRNAs (e.g. before and after peptide bond formation (Valle et al., 2003)) and the binding of protein factors like translational GTPases results in an ordered, organized sequence of conformational changes of the ribosome, which are coupled to efficient transport of the tRNA_A•mRNA module through the ribosome.

2.5 The key steps of mammalian translation are initiation, elongation, termination and recycling

Translation can be divided into four parts: 1) Initiation, which is the binding of the very first tRNA, positioning of the mRNA on the small ribosomal subunit, and joining of the large subunit; 2) iterative

2. Introduction

elongation cycles, wherein the amino acids coded for in the mRNA are successively connected to form the peptide chain; 3) termination, resulting in the release of the peptide chain from the ribosome, and

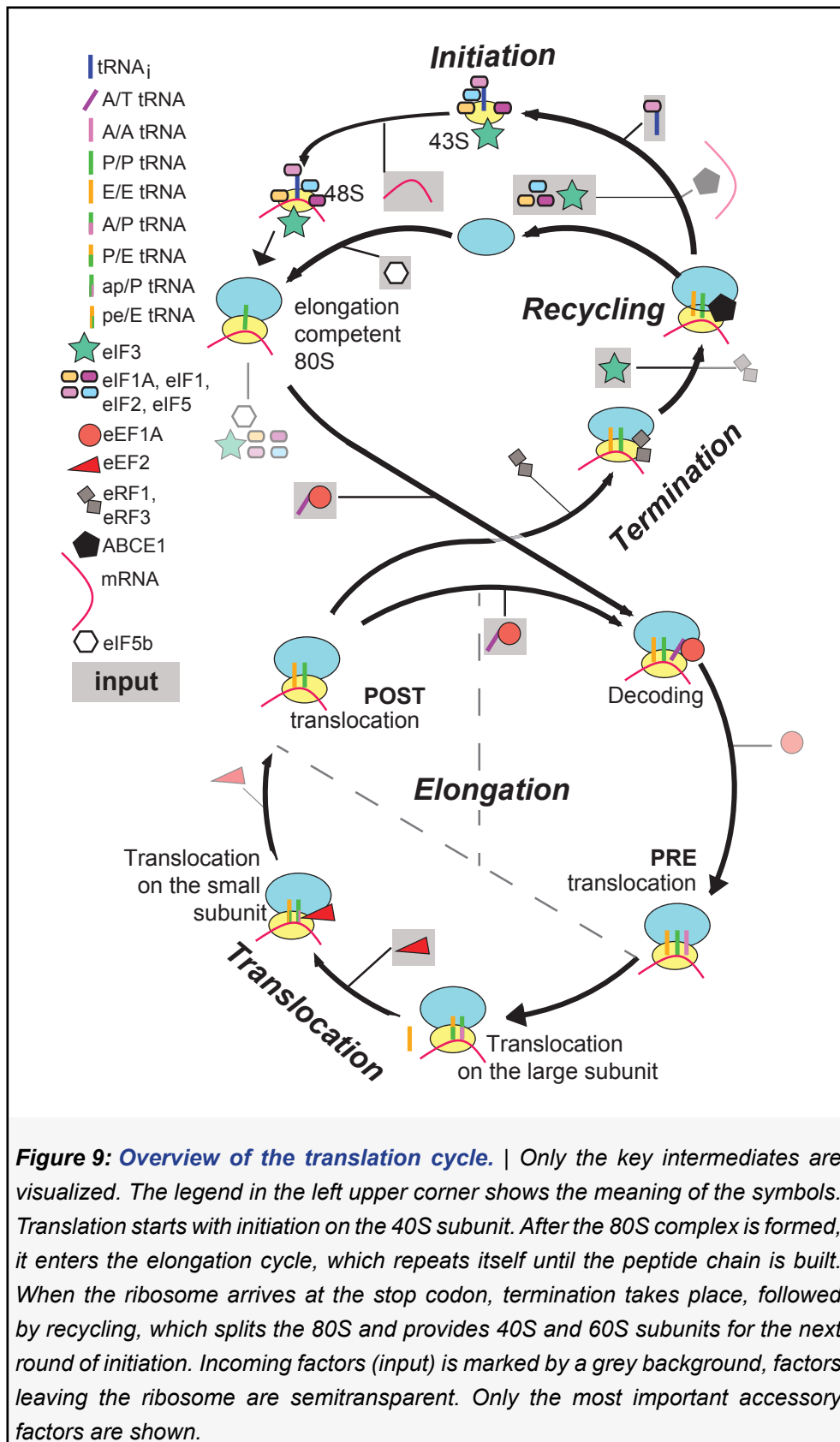


Figure 9: Overview of the translation cycle. | Only the key intermediates are visualized. The legend in the left upper corner shows the meaning of the symbols. Translation starts with initiation on the 40S subunit. After the 80S complex is formed, it enters the elongation cycle, which repeats itself until the peptide chain is built. When the ribosome arrives at the stop codon, termination takes place, followed by recycling, which splits the 80S and provides 40S and 60S subunits for the next round of initiation. Incoming factors (input) is marked by a grey background, factors leaving the ribosome are semitransparent. Only the most important accessory factors are shown.

2. Introduction

4) recycling, which is splitting of the associated subunits into small and large one such that they are ready to be fed in a new round of translation (**Figure 9**).

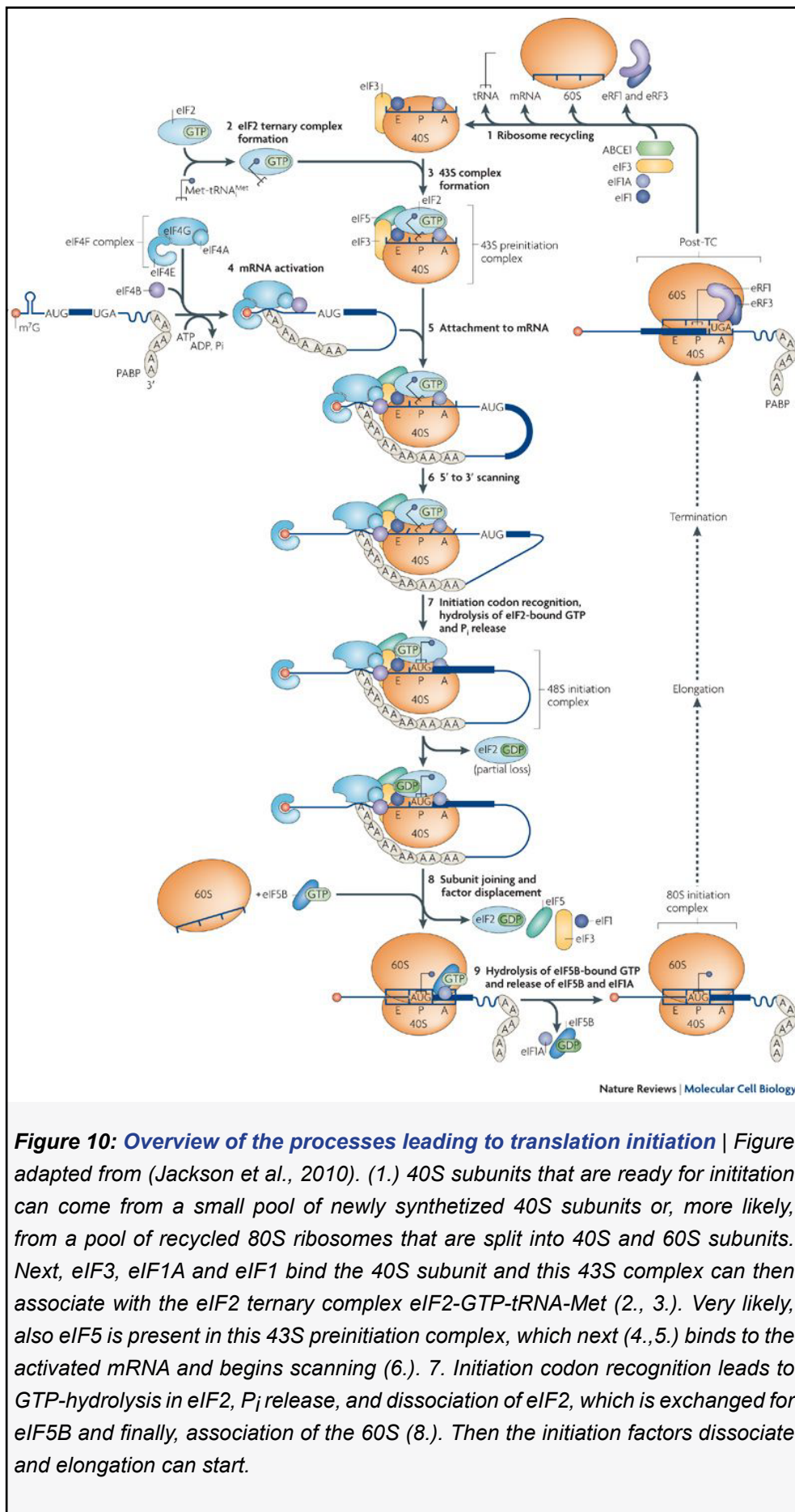
Initiation places the start codon in the P site by ribosome scanning

Initiation is the first step of translation. Here, the small subunit is prepared for joining with the large subunit (**Figure 9, Figure 10**). This preparation includes binding of an initiator tRNA_i^{Met} to the small subunit P site as well as binding of the mRNA and positioning of the mRNA start codon into the P site under assistance of initiation factors. In the next step, the large subunit joins this 40S•mRNA•tRNA_i^{Met} complex, the remaining initiation factors dissociate, and elongation can start with the incorporation of the tRNA carrying the amino acid that is coded for in the second codon.

Eukaryotic and bacterial systems profoundly differ at the stage of initiation. Bacterial 16S rRNA possesses a sequence, to which the characteristic Shine Dalgarno sequence of the mRNA aligns. This alignment facilitates positioning of the mRNA start codon in the P site of the 30S subunit (Shine and Dalgarno, 1974). Initiation factor 1 (IF1) binds at the 30S A site and induces a structural change in the 30S subunit (Allen et al., 2005; Carter et al., 2001; Milon et al., 2008). A ternary complex consisting of fMet-tRNA_i^{fMet} (the first amino acid in bacterial proteins is always formyl-methionine) and IF2•GTP binds to the P site, while initiation factor 3 (IF3) ensures that it is an initiator tRNA and not an elongator tRNA that binds (Milon et al., 2008). Positioning of the initiator tRNA in the P site is followed by joining of the large subunit, GTP-hydrolysis of IF2, and finally dissociation of the initiation factors (Simonetti et al., 2008).

In contrast, in eukaryotes, the positioning of the start codon into the 40S P site occurs after 'ribosome scanning' of the mRNA (Jackson et al., 2010; Kozak, 1999; Shine and Dalgarno, 1974). The protein machinery required for eukaryotic initiation is by far more complex

2. Introduction



2. Introduction

than in bacteria, where only three initiation factors are needed (Hashem and Frank, 2018; Jackson et al., 2010; Kozak, 1999; Shirokikh and Preiss, 2018).

Eukaryotic initiation starts with the formation of the 43S preinitiation complex, which consists of the 40S subunit, the ternary complex eIF2•GTP•Met-tRNA_i^{Met}, eIF3, eIF1 and eIF1A. This 43S complex is ready to bind to the mRNA, which can be circularized via the 5'-bound eIF4F that connects to the 3' end by binding to PABPs. eIF1 and eIF1A induce an open latch conformation of the 40S that facilitates mRNA binding, while eIF4G plays a key role in loading the mRNA on the 43S preinitiation complex via interactions with eIF3. The main role of the now assembled 48S complex is the scanning of the mRNA until finding a start codon in the correct environment (Jackson et al., 2010; Kozak, 1999). It is eIF1 that enables the 48S complex to discriminate the eligible start codon against other codons or start codons with poor nucleotide context. The establishment of codon-anticodon base pairing between the mRNA start codon and the tRNA leads to eIF1 dissociation, allowing GTP hydrolysis and dissociation of eIF2 under assistance of its GTPase activating protein eIF5. Finally, eIF5B mediates the joining of the 60S subunit and the assembly of the elongation competent 80S ribosome is completed when GTP hydrolysis of eIF5B leads to its dissociation from the 80S (**Figure 10**).

Additionally to this classical initiation pathway, in the eukaryotic system a group of RNA structures called IRESs (Internal ribosomal entry sites) are able to employ alternative initiation pathways partially or fully independent from the 5' cap and/or initiation factors (Pelletier and Sonenberg, 1988; Yamamoto et al., 2017).

Elongation is at the heart of translation

Elongation is an iterative process which is aimed at polymerization of the peptide chain until all amino acids encoded in the mRNA are incorporated into the peptide chain. It consists of the steps decoding/tRNA selection, peptidyl transfer and translocation. At

2. Introduction

each codon between start and stop, the ribosome must undergo one full elongation cycle with the result of one amino acid being added to the peptide chain.

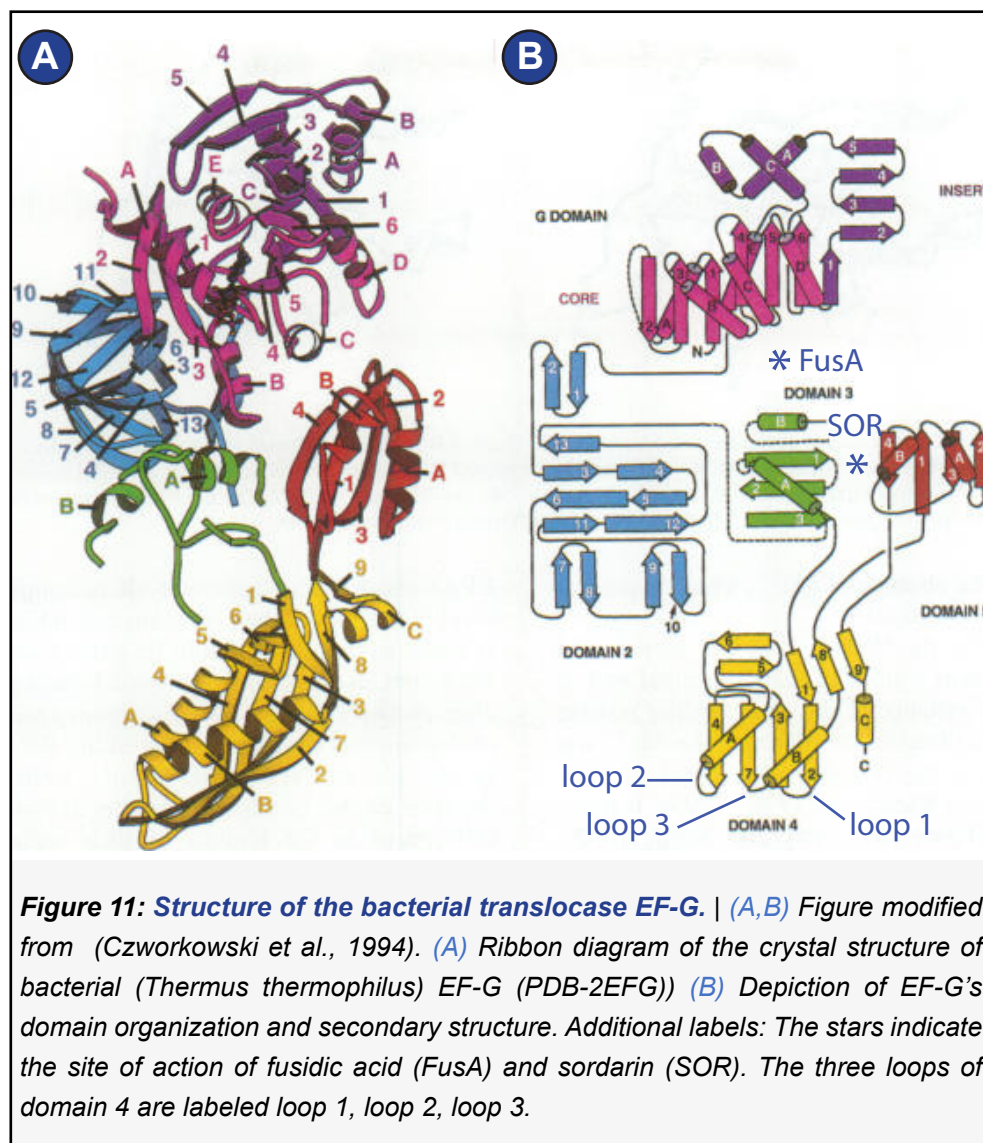
The very first elongation cycle takes place right after initiation and has as its starting point the assembled 80S ribosome with a Met-tRNA_i^{Met} in the P site. The A site is empty and must be occupied by a tRNA carrying the amino acid that is encoded next in the mRNA. The selection of the correct tRNA requires eEF1A (EF-Tu in bacteria), a translational GTPase which reaches the ribosome as ternary complex in association with a tRNA and GTP. The interaction of the ribosome with the ternary complex is referred to as 'decoding'. Here, the tRNA anticodon is brought to the small subunit A site ('decoding center') and interacts with the mRNA codon. Correct base pairing in case of complementary codons triggers conformational changes of the ribosome that in turn result in GTP-hydrolysis and eEF1A dissociation (Budkevich et al., 2014; Schmeing and Ramakrishnan, 2009; Schuette et al., 2009; Voorhees et al., 2010).

The dissociation of eEF1A allows the tRNA to be fully accommodated in the 60S A site. There, the CCA-end of the tRNA with the aminoacylated amino acid is positioned in proximity to the CCA-end of the P-site tRNA that carries the first amino acid, or in later rounds of elongation the entire peptide chain built so far. During peptide bond formation, this amino acid/peptide chain from the P-site tRNA is transferred to the A-site tRNA. As consequence, the ribosome contains a peptidyl tRNA in the A site, a deacylated tRNA in the P site, and in case of later elongation rounds, also a deacylated E-site tRNA (Behrmann et al., 2015). The ribosomal conformation at this point is characterized by an unrotated (canonical) 40S subunit that is rolled relative to the 60S subunit (Budkevich et al., 2011, 2014). It is referred to as the classical PRE state, where PRE means pre-translocation.

2. Introduction

Translocation prepares the ribosome for a new elongation cycle

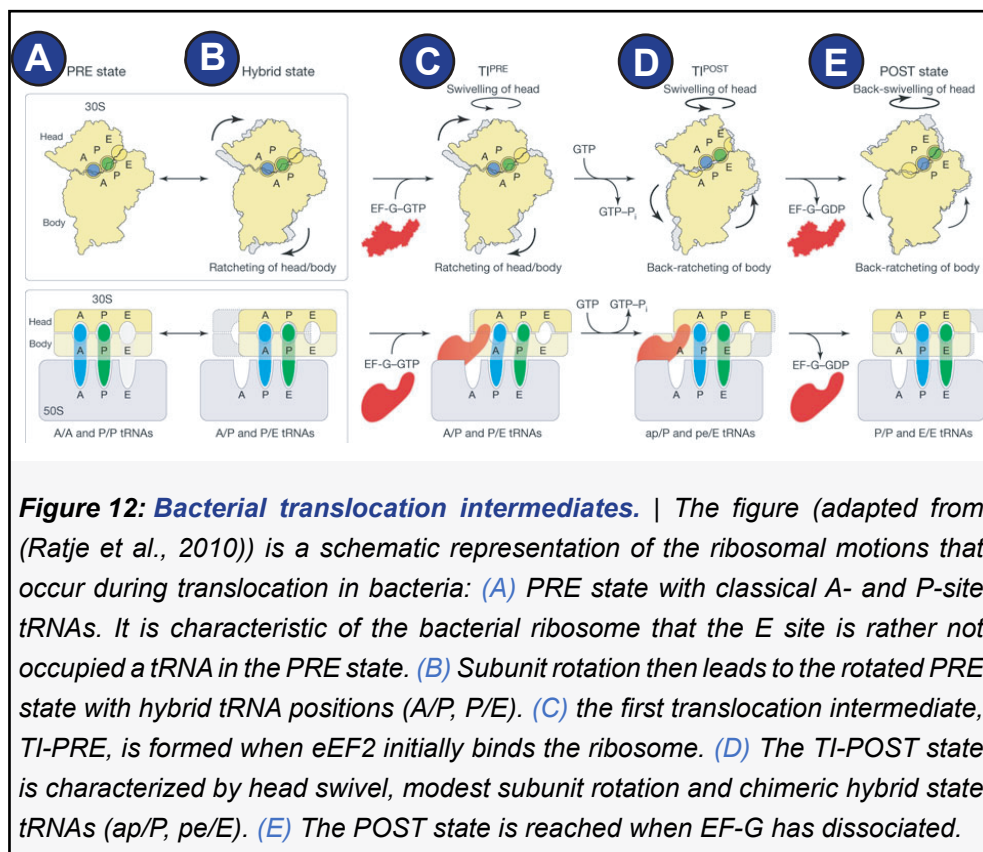
While the main task of the first half of the elongation cycle is the polymerization of the peptide chain, the second half serves as the preparation for the next elongation cycle. Translocation is the movement of both tRNAs as well as the mRNA, forming the tRNA₂-mRNA module, from the A- and P- to the P- and E sites, respectively. It is catalyzed by eEF2 (EF-G in bacteria) and leads from the pre-translocational (PRE) to the post-translocational (POST)-state ribosome. The POST-state ribosome can then accept a new tRNA in



2. Introduction

its A site. Alternatively, in case of the very last elongation cycle, the ribosome does not bind a new tRNA, but enters termination (see below).

eEF2/EF-G belongs to the group of translational GTPases and is a five-domain protein (**Figure 11**). Mammalian eEF2 is very similar to its homologs from other domains of life (**Supplemental Figure 6**) The G-domain (or domain I) is responsible for GTP hydrolysis and possesses the earlier described characteristic switch loops and G-motifs. Domains 2 and 3 are part of a bridge between the G-domain and the small ribosomal subunit when the factor is bound to the ribosome. Domain 4 is a mimicry of a tRNA anticodon arm and protrudes into the A-site of the ribosome. Domain 4 carries three functionally important loops: loop 1, facing the tRNA (Ramrath et al., 2013), loop 2, facing the small subunit body/platform (Ramrath et al., 2013), and loop 3 in the middle (**Figure 11B**). A unique feature



2. Introduction

of domain 4 of the eukaryotic and archaeal elongation factors eEF2 is a diphthamide modification on histidine 715 in mammalia (H699 in yeast) in loop 3 of domain 4 (Oppenheimer and Bodley, 1981).

EF-G/eEF2 function can be specifically targeted by antibiotic agents. Fusidic acid binds between the G-domain and domain 3 of EF-G. It occupies the place of the P_i after its release following GTP-hydrolysis (**Figure 11**) and prevents EF-G's dissociation from the ribosome. The concrete impact of fusidic acid on eukaryotic eEF2 is not fully understood yet. Sordarin binds between domain 2 and 3 of eEF2 and prevents dissociation of eEF2 in yeast (**Figure 11**) (Spahn et al., 2004a).

The diphthamide modification on loop 3 of domain 4 of eEF2 is known for being the target of toxins like diphtheria toxin and exotoxin A. When it is ribosylated, eEF2 cannot function in translation (Davydova and Ovchinnikov, 1990; Oppenheimer and Bodley, 1981).

There exists a current model on translocation based on bacterial and eukaryotic structures, however, a detailed understanding of the mechanism has not been (fully) achieved yet. Studies of bacterial translocation intermediates reveal the following sequence of events:

First, tRNA movement on the large 50S subunit occurs spontaneously after peptide bond formation which alters tRNA affinities and drives subunit rotation (Cornish et al., 2008; Valle et al., 2003). This subunit rotation is reversible and coupled to fluctuations between classical A/A, P/P states and hybrid A/P, P/E states of the tRNAs and has as well been visualized in eukaryotic ribosomes (Agirrezabala et al., 2008; Behrmann et al., 2015; Blanchard et al., 2004; Budkevich et al., 2011; Moazed and Noller, 1989; Munro et al., 2007).

Only after the tRNAs have reached their hybrid positions, EF-G/eEF2 comes into play. It contributes to the irreversibility and directionality of the translocation reaction. eEF2/EF-G probably binds to the rotated ribosome (Brilot, 2013). According to Rodnina et al., 1997, already at this early stage and before tRNA movement has started, GTP-hydrolysis takes place. The next state visualized is the TI (translocation intermediate)-POST state, where the tRNAs are

2. Introduction

already translocated on the 30S body/platform and adopt chimeric hybrid (ap/P, pe/E) positions. The ribosome at this state adopts a partly rotated conformation and exhibits a high-degree head swivel (Ramrath et al., 2013; Ratje et al., 2010; Zhou et al., 2014) (**Figure 12**). After completion of translocation, EF-G dissociates. The ribosome can now accept the next tRNA.

It is not clear how exactly EF-G/eEF2 and GTP-hydrolysis contribute to translocation. Two opposing models were suggested, 1) the ‘Brownian ratchet’ model, according to which binding of EF-G/eEF2 to the ribosome suffices to deflect the ribosome’s natural, thermodynamically driven propensity to backrotate, resulting in translocation (reviewed in (Spirin, 2009)). 2) The power stroke model, in which the energy of GTP-hydrolysis is used by eEF2/EF-G to actively push the tRNAs in the direction of translocation (Rodnina et al., 1997; Chen et al., 2016).

Termination releases the peptide chain and is followed by recycling

Usually, the last codon of the mRNA is followed by a stop codon (UAA, UAG or UGA). When this stop codon is positioned into the A site, no canonical tRNA will match it. The stop codon is recognized by class-1 release factor eRF1 (RF1 and RF2 in bacteria) which facilitates release of the peptide chain from the P-site tRNA. The activity of eRF1 is supported by class-2 release factor eRF3 (RF3 in bacteria), which belongs to the group of translational GTPases.

After termination, the ribosomal subunits dissociate and are then reused for the next round of translation. This process is called ribosome recycling. In bacteria, ribosomal recycling factor (RRF), EF-G and IF3 act together to disassemble the 80S ribosome (Hirashima and Kaji, 1970). In eukaryotes, ABCE1 splits the 80S ribosome (Jackson et al., 2012; Pisarev et al., 2010). Ligatin (also known as eIF2D) and DENR (density regulated protein) have been found to promote dissociation of tRNA and mRNA from the small subunit in eukaryotes (Skabkin et al., 2013).

2. Introduction

Some evidence points towards an alternative event after termination. It is referred to as 'reinitiation': Here, recycling and dissociation of the 60S subunit takes place as well, but the 40S subunit does not leave the mRNA. Instead, it continues with scanning and thus can translate a next open reading frame (ORF; see **Figure 4B**) (Jackson et al., 2012; Skabkin et al., 2013).

mRNA quality control prevents production of degenerated proteins

Corrupt mRNA will lead to defective protein products. To avoid mistakes in protein translation, the cell has developed multi-level control mechanisms to check for integrity and correctness of the mRNA. Already mRNA transcription and maturation are susceptible to errors, and control points at this level are there to detect and eliminate defective mRNA products. In the nucleus, aberrant mRNAs are degraded in the 5' to 3' direction by exoribonuclease Xrn2 and in the 3' to 5' direction by the nuclear exosome before reaching the cytoplasm (Fasken and Corbett, 2009). In the cytoplasm, the ribosome and protein factors are involved in controlling the translated mRNA in three main ways:

Nonsense-mediated mRNA decay takes place when there is a premature stop codon. Downstream of the premature stop codon, the exon junction complex contains the upstream frameshift proteins (UPF) 2 and 3. Upon recognition of the stop codon, UPF1 is recruited. The interaction of UPF1 with UPF2 activates the mRNA degradation process (Isken and Maquat, 2007).

Non-stop mRNA decay is induced by the absence of a stop codon. The ribosome is stalled at the 3' end of the mRNA because termination factors are not recruited (Isken and Maquat, 2007). Such stalled ribosomes are recognized by a mechanism that is not yet clearly understood, but apparently involving Dom34•Hbs1 (Hilal et al., 2016; Tsuboi et al., 2012). The exosome is recruited to the ribosome and degrades the mRNA.

2. Introduction

In some cases, the ribosome cannot continue translation due to stable secondary structure. The mechanism that rescues a ribosome in this situation is referred to as *no-go mRNA decay*. In yeast, a Dom34•Hbs1•GTP complex is able to mediate dissociation of such stalled ribosomes (Becker et al., 2011; Shoemaker et al., 2010).

2.6 Translation is subject to multiple layers of regulation

Translation offers many levers for regulation. The pool of ribosomes that can enter translation is determined by the production, processing and modification of rRNA and ribosomal proteins and their assembly in the nucleus. The actual synthesis of a translation-competent ribosome, followed by nuclear export and maturation in the cytoplasm, are long and complex processes and sensitive to many influences (Karbstein, 2011; Nierhaus, 1991; Wilson and Nierhaus, 2007). Their regulation controls the cell's basic disposition to perform translation. Similarly crucial to the synthesis of ribosomes is the synthesis of factors that are involved in translation.

The actual accessibility of both ribosomes and factors is the next layer of control. For example, 80S monosomes were found to bind eEF2, but not to be translationally active (Khatter et al., 2015; Voorhees et al., 2014); the 40S subunit in these complexes is thus not accessible for translation initiation. Stability of an 80S•eEF2 complex has also been observed *in vitro* (Budkevich et al., 2014; Davydova et al., 1993). An example for the control of protein factors is the eukaryotic initiation factor eIF4E, which can be bound and thus inactivated by eIF4E-binding protein (4E-BP), whose affinity is regulated by post-translational phosphorylation; initiation is reduced then by the decreased availability of eIF4E (Bah et al., 2015; Marcotrigiano et al., 1999). Also eEF2 is known to be inactivated by phosphorylation (Ling and Ermolenko, 2016).

Besides such quite simple mechanisms that are based on the accessibility of substrates, there might exist a more complex

2. Introduction

machinery that is aimed to enhance the production of specific proteins and down-regulate others. Whereas in long-term, the proteome of a cell is controlled by transcription, dynamic, rapid adaption mechanisms could base on differential translation. How this works exactly is not clear; discussed is among others the existence of 'specialized ribosomes' (Xue and Barna, 2012). An indicator for a possible regulation mechanism is that ribosomal proteins can be modified post-translationally. The ribosomal protein with the longest history of investigations of its posttranslational modification is ribosomal protein eS6, which is phosphorylated and whose putative impact on translation is one of the questions raised in this thesis (see below). Also, the topology of translation in the cell and the composition and architecture of polyribosomes (see below) might be a dynamic mechanism to alter the translatome.

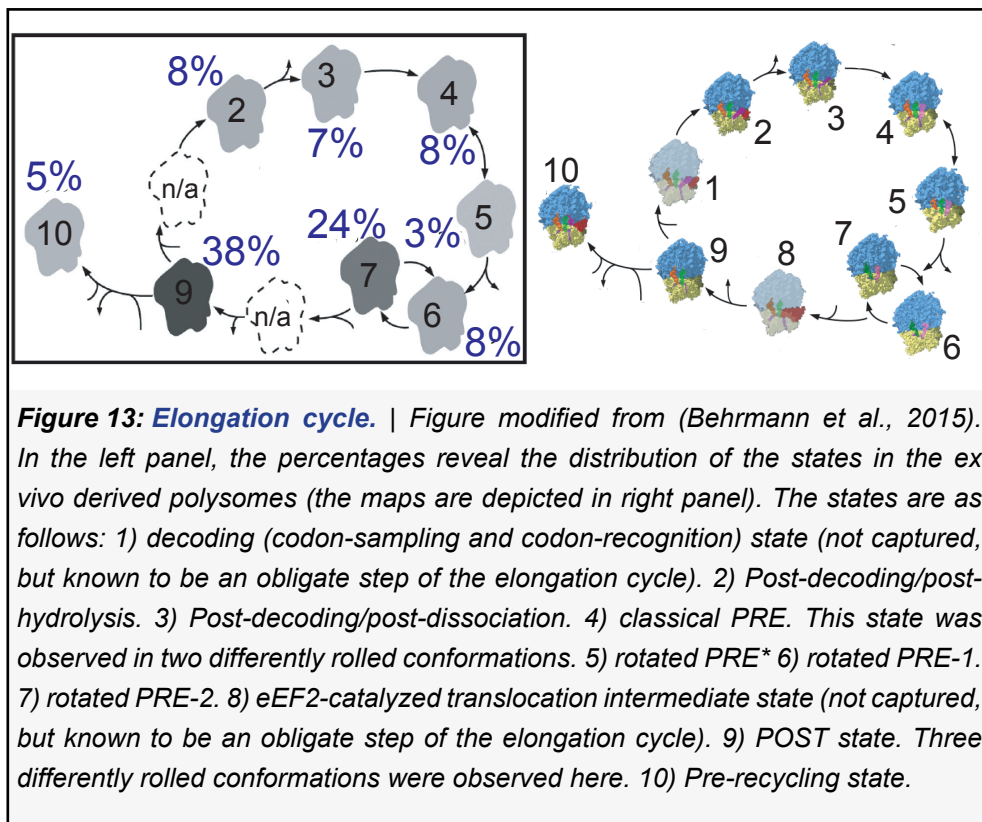
Actively translating ribosomes are organized into polysomes

It is the normal case that on one mRNA, multiple ribosomes are translating the message at the same time and that depending on the length of the mRNA, multiple initiation events happen before the first ribosome reaches the stop codon.

Such assemblies of multiple ribosomes on the same mRNA are called polyribosomes or polysomes. Each ribosome that is part of a polysome group is at some stage of translation (**Figure 13**). Elongation intermediates are the by far most often sampled states, because the elongation cycle must take place for each codon between start and stop in contrast to initiation, which takes place only at the start codon, and termination, which takes place only at the stop codon.

By isolating polysomes *ex vivo*, Behrmann et al. were able to reconstruct ten different states of mammalian elongation (Behrmann et al., 2015). The differential population of the states reflects the distribution of functional states in polysomes. Although the time between purification of the polysomes used for analysis and the

2. Introduction



freezing of the sample might allow for changes, that work shows the *in vivo* energy landscape of translation as close to the native state as possible. Of special interest for studying the regulation of translation is the distribution of functional states (**Figure 13**). The captured states by far don't represent the complete spectrum of possible conformational and functional states of the mammalian ribosome during elongation, but only local minima. Referring to the nomenclature of the 'dynamics' section, the states represent fluctuations in the macro- to mesoscopic range (Munro et al., 2009).

The shapes of polysomal assemblies have been extensively studied (Afonina et al., 2013, 2014; Brandt et al., 2010; Myasnikov et al., 2014; Viero et al., 2015). The relative orientations of the ribosomes in a polysomal assembly raise the question of how ribosomal proteins or RNA on the solvent side might promote these orientations via specific inter-ribosomal contacts. Moreover, it was observed that the abundance of rectangular shapes is associated with a low translation activity (Myasnikov et al., 2014; Viero et al., 2015) and that it can be increased by treatment of cells with rapamycin or by serum-withdrawal (Viero et al., 2015). Change in the ratio of ribosomes to

2. Introduction

mRNA can also modify the pattern of proteins synthesized (Lodish, 1974). Polysome patterns after post mitochondrial supernatant (Duncan and McConkey, 1982) as well as investigations of the shapes of polysomes (Myasnikov et al., 2014; Viero et al., 2015), suggest that polysomes react to different conditions, like serum withdrawal, by changing their shape and/or composition.

In eukaryotic cells, polysomes can be additionally differentiated by the cellular compartment they are attached to. Essentially, there are cytosolic polysomes and endoplasmatic reticulum (ER)-bound polysomes. So far, it is agreed upon that every ribosome has the potential to join either class and that it is the signaling peptide encoded in the mRNA that is responsible for recruiting the ribosome to the ER membrane (Meister, 2011).

Phosphorylation of ribosomal protein eS6: a possible switch for translation regulation?

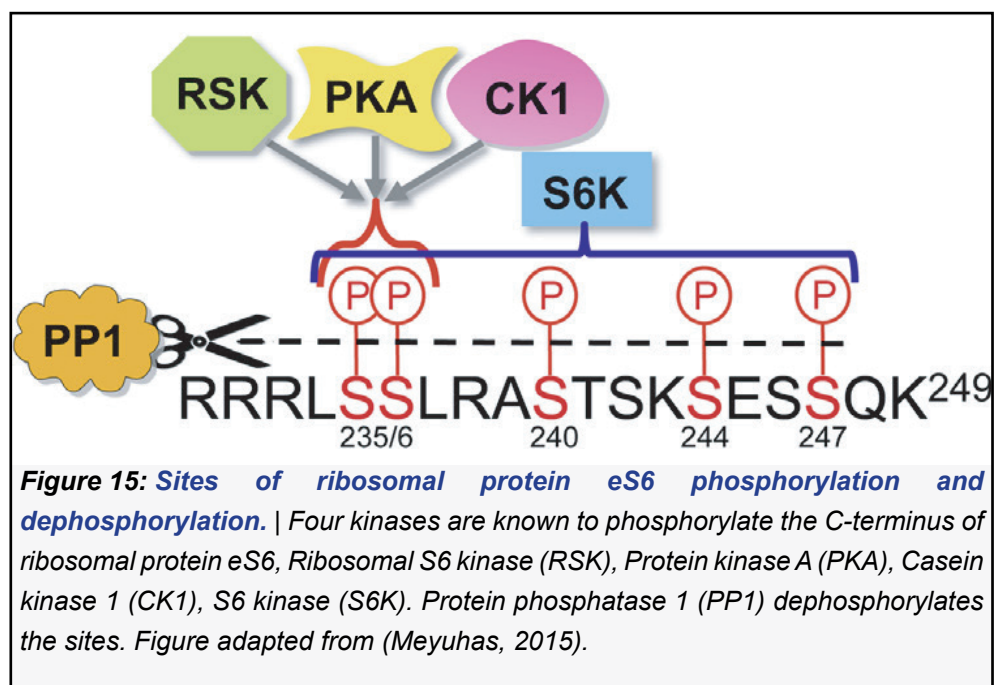
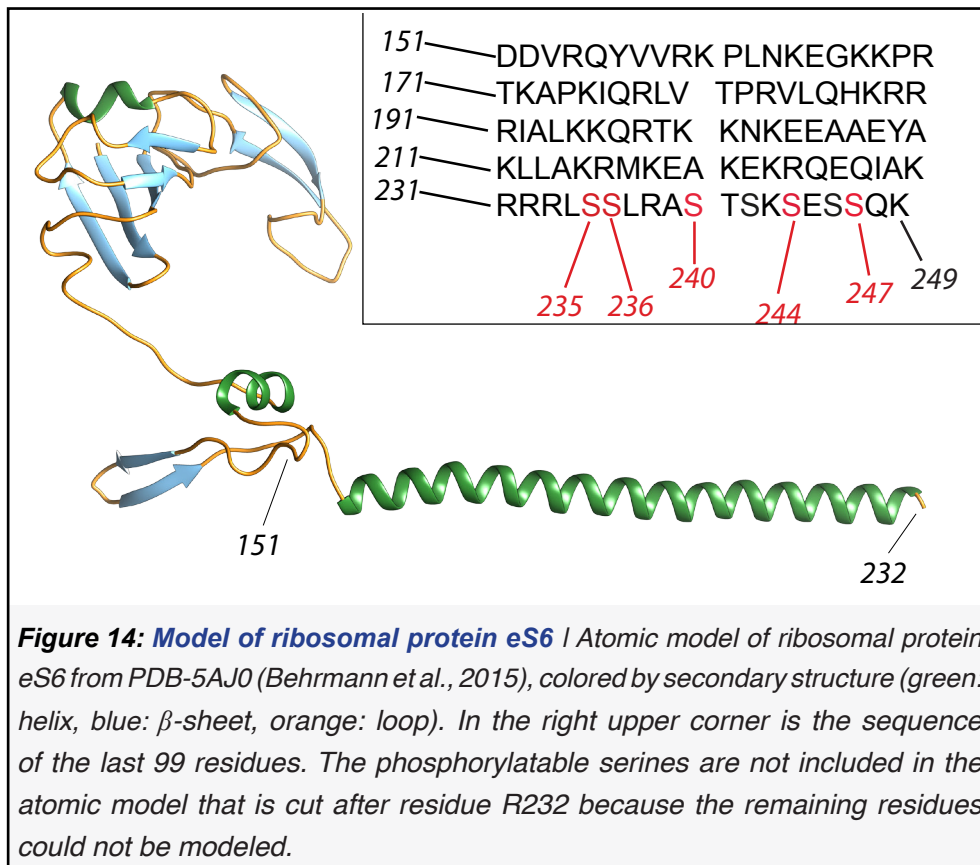
Among the many discussed possibilities of how translation might be regulated, there are post-translational modifications of ribosomal proteins (Xue and Barna, 2012). Some ribosomal proteins undergo phosphorylation, e.g. ribosomal protein eS6 (eS6), a eukaryote-specific protein of the 40S subunit located at the foot of the 40S body/platform (**Figure 3A**). eS6 is 249 residues long in humans and consists of a globular part and an alpha helical part with a flexible C-terminus (**Figure 14**).

eS6 is a necessary protein for ribosome biogenesis. Its conditional deletion has been shown to lead to a p53-dependent inhibition of cell cycle progression (Panić et al., 2006; Sulić et al., 2005; Volarevic, 2000) in multiple tissues.

The alpha helical, C-terminal part of eS6 reaches into the vicinity of expansion segment 6 of the 18S rRNA and displays five serine residues (S235, S236, S240, S244, S247) at its C-terminus, which are the substrates of four independent kinases (RSK, Protein kinase A, S6K and CK1) with partially overlapping specificities (Bandi et al., 1993; Krieg et al., 1988; Wettenhall and Morgan, 1984) (**Figure 15**).

2. Introduction

Phosphorylation happens in an ordered fashion, such that first, the residues serine 235 and serine 236 are phosphorylated, then serine 240 and serine 244 and last serine 247 (Martin-Pérez and Thomas, 1983; Wettenhall et al., 1992). Phosphorylation of serine 247 requires prior phosphorylation of serines 240/244, and phosphorylation of



2. Introduction

serine 247 in turn promotes/stabilizes phosphorylation of serines 240/244 (Hutchinson et al., 2011). The modification is counteracted by the action of phosphatase (PP) 1 which is responsible for dephosphorylation at all five sites (Barth-Baus et al., 2002; Belandia et al., 1994; Hutchinson et al., 2011; Li et al., 2012).

The phosphorylation of the five serine residues at the C-terminus is massively increased in regenerating liver cells by partial hepatectomy, which was the first model for studying eS6-phosphorylation (Gressner and Wool, 1974). In the context of growth, two pathways lead to eS6 phosphorylation: The PI3K/Akt/TCS/Rheb/mTORC1/S6K pathway and the Ras/Raf/MEK/ERK/RSK pathway (**Figure 16**) (reviewed in (Meyuhas, 2008, 2015)). A large number of stimuli have been shown to induce eS6 phosphorylation via these pathways, including stimulation of serum-starved cells with serum (Meyuhas, 2008, 2015; Roux et al., 2007).

As to the consequences of this modification, many observations have been made that are thought to be associated with eS6 phosphorylation, but none of them can be explained mechanistically. In 2005, Ruvinsky and colleagues found that global protein synthesis is higher in knockin mouse embryonic stem cells (MEFs) (P^{-/-}) compared to wild type MEFs, but these observations could not be reproduced by using S6K-deficient mice (S6K1^{-/-}, S6K2^{-/-}) (Chauvin et al., 2014; Mieulet et al., 2007; Ruvinsky et al., 2005). Many cell-types derived from eS6P^{-/-} mice are significantly smaller than in the wild type, among them pancreatic beta cells, IL7-dependent cells from fetal livers, MEFs, and muscle myotubes (Granot et al., 2009; Ruvinsky et al., 2005, 2009). However, some cells have normal size, for example acinar cells from pancreas (Pende et al., 2004; Ruvinsky et al., 2005). eS6P^{-/-} mice have impaired renal hypertrophy after unilateral nephrectomy (Xu, 2015). Interestingly, there seems to be a link to initiation, as phosphorylation of serine 247 promotes association with mRNA Cap-binding complex in vitro (Hutchinson et al., 2011), and phosphorylation of serines 240/244 is required for Cap binding (Roux et al., 2007). Further, by covariance analysis of

2. Introduction

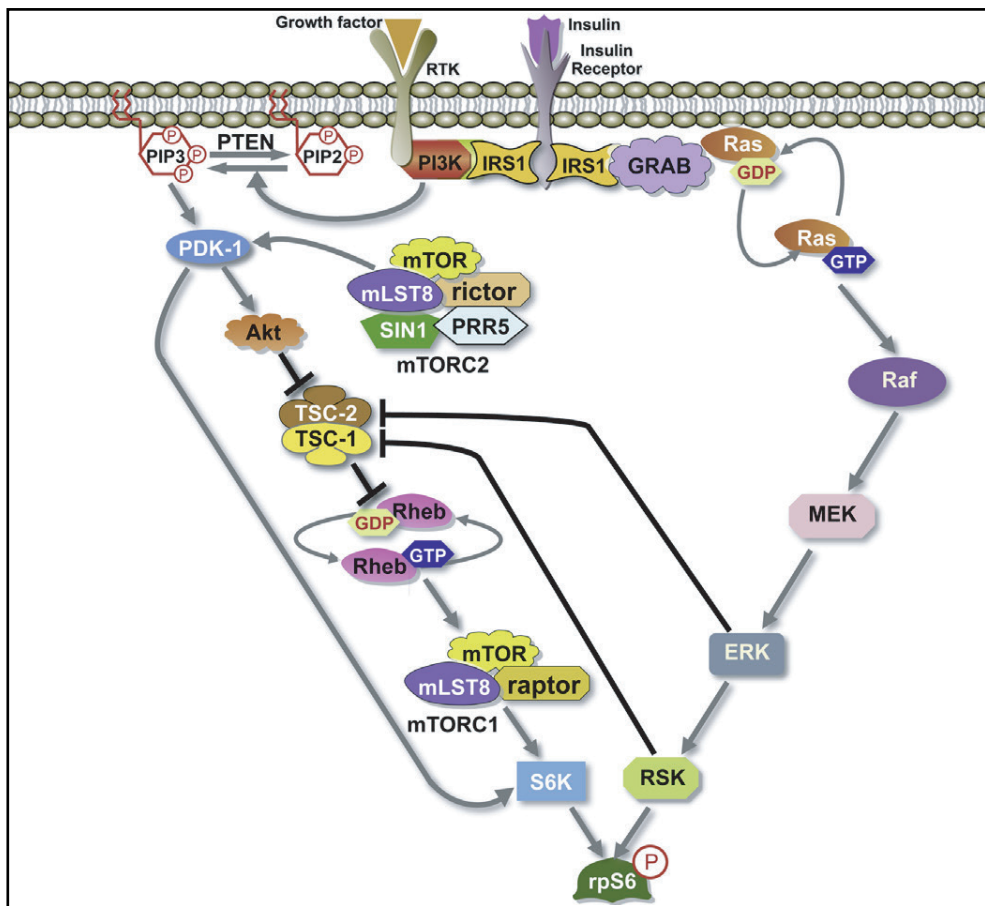


Figure 16: Pathways that lead to eS6 phosphorylation. | Two main pathways transduce signals that lead to phosphorylation of ribosomal protein eS6 via S6 kinase (S6K) or Ribosomal S6 kinase (RSK). **PI3K/Akt/TSC/Rheb/mTORC1/S6K pathway:** Activation of the receptor tyrosine kinase leads to activation of phosphatidylinositol 3-kinase (PI3K), which converts the lipid phosphatidylinositol-4,5-P2 (PIP2) into phosphatidylinositol-3,4,5-P3 (PIP3), (reversible by PIP3 phosphatase PTEN (phosphatase and tensin homolog deleted from chromosome 10)). PDK1 activates Akt, which blocks tuberous sclerosis complex 2 (TSC2), that normally would act as GTPase-activating protein (GAP) for Rheb (Ras-homolog enriched in brain). Rheb-GTP accumulates and activates the rapamycin-sensitive mammalian TOR complex 1 (mTORC1), consisting of target of rapamycin (TOR), RAPTOR (regulatory associated protein of TOR) LST8, and PRAS40 (proline-rich Akt substrate 40 kDa). Active mTORC1 phosphorylates S6K and eukaryotic initiation factor 4E (eIF-4E)-binding protein (4E-BP1, 2, and 3). Activated S6K phosphorylates rpS6, as well as many other substrates (Meyuhas, 2015). **Ras/Raf/MEK/ERK/RSK pathway:** Binding of growth factors induces activation of Ras (Rat sarcoma)-GTPase and recruits Raf (rapidly accelerated fibrosarcoma) to the membrane which is activated. Raf activates mitogen-activated protein (MAP) kinase, kinases 1 and 2 (MEK1/2), which activates the extracellular-signal-regulated kinases (ERK1 and ERK2). Activated ERKs activate many substrates, also the the RSK family. ERK and RSK can inhibit TSC-2 and TSC-1. Figure adapted from (Meyuhas, 2015).

2. Introduction

a cryo-EM map of a 43S initiation complex, density variance in the eS6 region was shown to be related to density variance of initiation factors (Liao et al., 2015) (the sample analyzed was (Hashem et al., 2013)). Nevertheless, if there is a clear structural role of eS6 phosphorylation is not known.

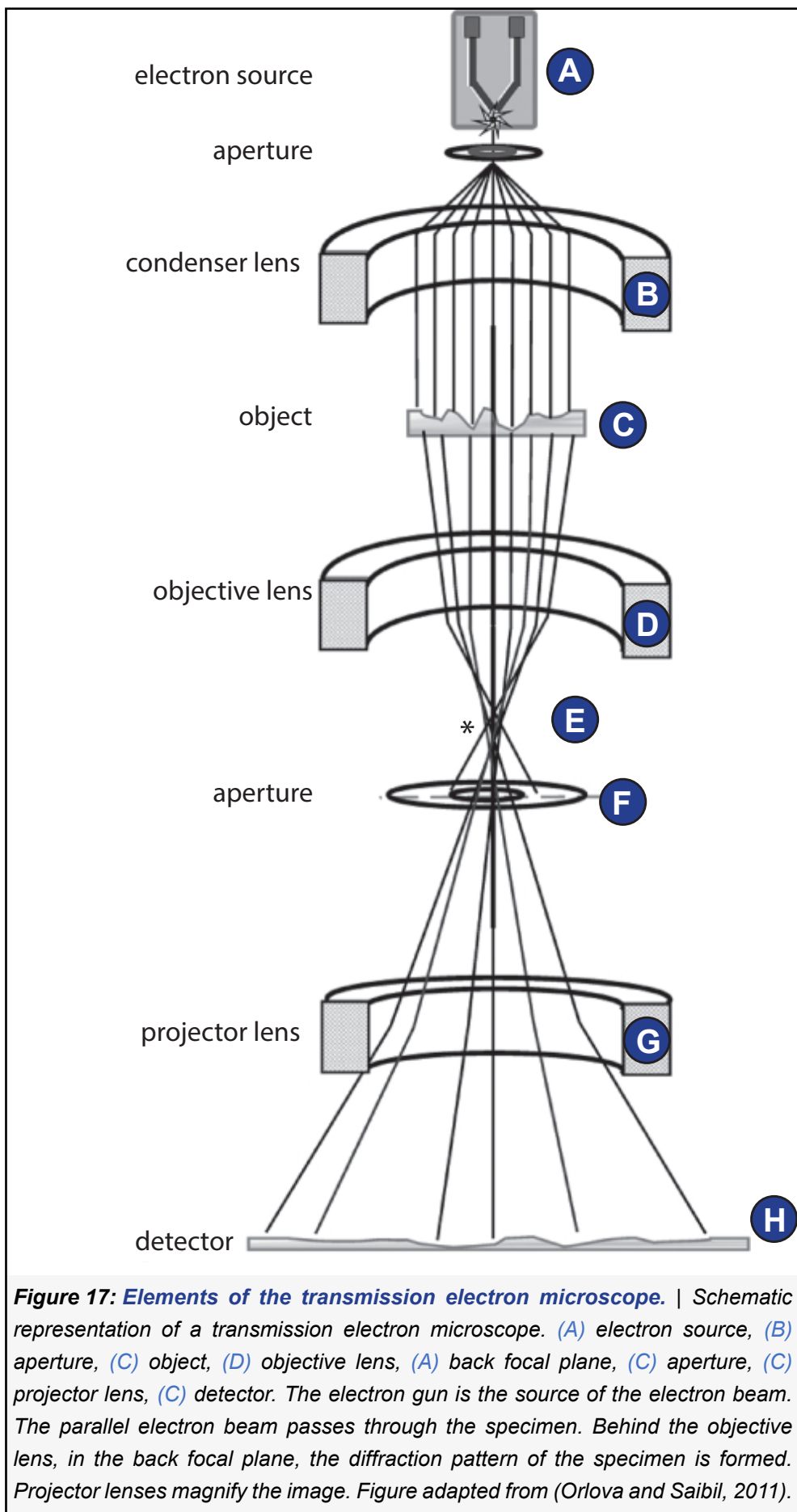
2.7 Single particle cryo-EM as a tool in structural biology

In cryogenic transmission electron microscopy (cryo-EM), a two-dimensional (2D) projection is generated from a thin vitrified specimen through which an electron beam is sent. In order to reconstruct the three-dimensional (3D) volume, multiple viewing angles of the same object must be covered. To this end, the specimen can either be imaged from different angles by tilting it, as done in cryo-EM tomography, or a specimen that is imaged at a fixed angle of 0° must contain multiple copies of the object in different orientations. The latter approach is used in single particle cryo-EM, which will be discussed in the following paragraphs.

Construction of the transmission electron microscope

The interior of a transmission electron microscope (TEM) is evacuated. Electrons are emitted from the cathode, or electron gun (**Figure 17A**). Because electrons interact with an electromagnetic field, they can be focused using magnetic lenses. The condenser lens (**Figure 17B**) transforms the emitted electrons to a parallel beam. The following acceleration of the electrons in the column is directly coupled to a theoretical point resolution limit, as will be explained below. Nowadays, usually 120-300 kV microscopes are used for single particle cryo-EM. The object (**Figure 17C**) is inserted into the column via a vacuum lock. The incident wave is modified by the object such that it carries the information about the object's structure. The objective lens system (**Figure 17D**) focuses

2. Introduction



2. Introduction

the scattered wave to form the real image. The focused beam forms the Fourier transform/diffraction pattern of the wave in the back focal plane (**Figure 17E**). A phase plate can be inserted here to shift the phases (Orlova and Saibil, 2011). As high frequency information is scattered at high angles, at this point the size of the objective aperture plays an important role (**Figure 17F**). The projector lens system contains several magnification lenses (**Figure 17G**). To exclude electrons of certain energies (e.g. those that lost energy and changed wavelength due to interactions with the sample), which would otherwise reduce image quality, an energy filter can be used. Finally, the electron wave reaches the detector (**Figure 17H**).

Cryogenic transmission electron microscopy allows imaging of biological specimens

The distinctive feature of cryo-EM versus other structural methods is that it allows imaging of biological samples at near-native conditions. The specimen is plunge frozen in liquid ethane, a process that happens so fast that the hydration state of the molecule and its native conformation are unaffected (Dubochet et al., 1988). The molecules are now embedded in a thin layer of amorphous ice and can be imaged in the microscope. Additionally to the basic elements of a TEM described above, the cryo-TEM must ensure that the specimen is steadily kept at a temperature of below -180° C. Therefore, the specimen is inserted into the column via a special cryo-holder where it is kept in liquid nitrogen. The microscope is cooled with liquid nitrogen or sometimes helium.

Interaction of the electrons with the sample

Electrons can interact with the specimen or pass through it without interaction. If the electron passes without interaction, no information about the specimen is gained, and it contributes to background. The changes that occur to the electron by interacting with the sample make it carry information about the sample. In case of interaction, two types are distinguished: elastic and inelastic scattering.

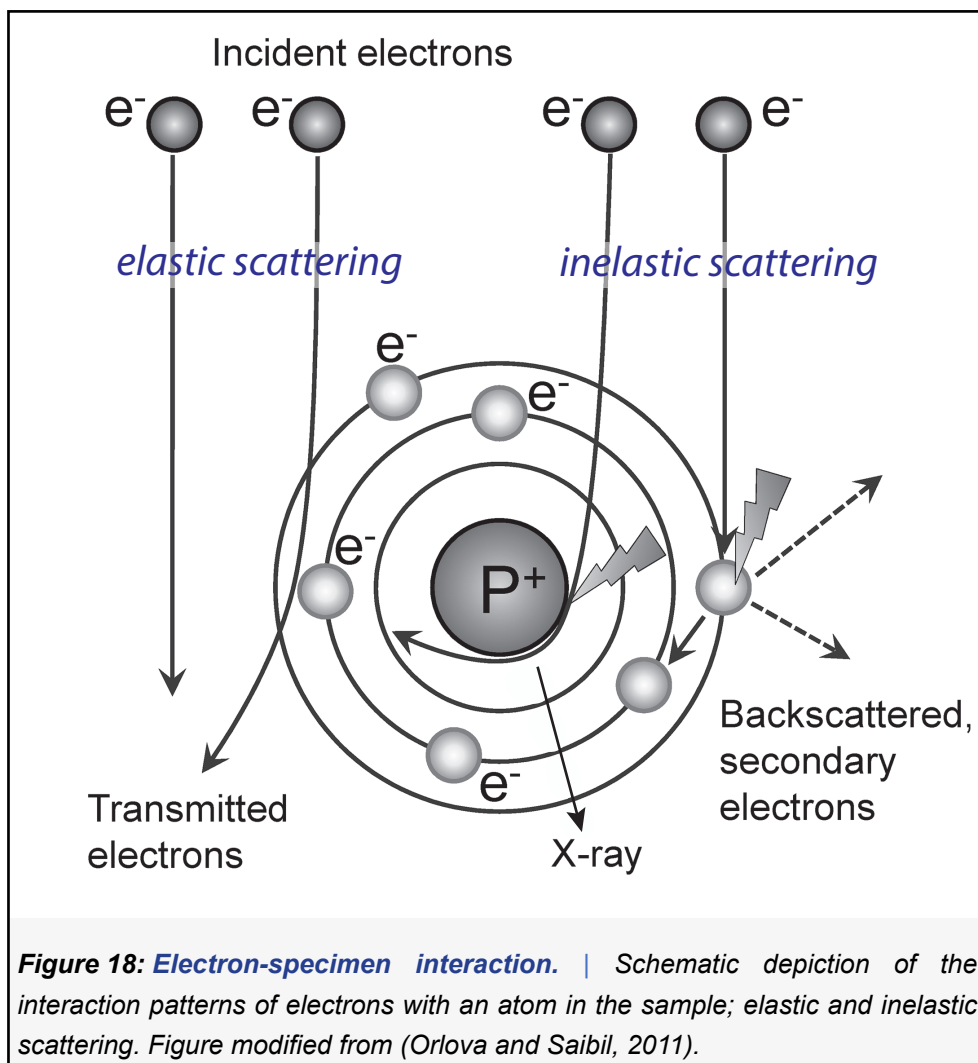


Figure 18: Electron-specimen interaction. | Schematic depiction of the interaction patterns of electrons with an atom in the sample; elastic and inelastic scattering. Figure modified from (Orlova and Saibil, 2011).

When scattered elastically, the electron is deflected by the Coulomb potential of the specimen atoms without loss of energy. The deflection is expressed in a change of phase of the electron wave (**Figure 18**). Elastic scattering is the main interaction of electrons with biological specimens, which consist of light atoms (H, C, N, O, P, S). Elastic scattering contributes to phase contrast. In inelastic scattering, the passing electron transfers energy to the specimen and both energy and phase of the electron change (**Figure 18**).

The lower the kinetic energy of the electron (e.g., at low voltage), the higher is the probability of inelastic and elastic scattering events. The general probability of electron-sample interaction and thus signal-to-noise ratio can be enhanced by increasing the electron dose. However, transfer of energy from the electron to the sample is associated with sample damage (Egerton et al., 2004). Low

2. Introduction

dose conditions with mean exposure of 20-30 electrons per Å² are therefore usually applied for cryo EM of biological samples to limit the damage. To obtain a meaningful signal nevertheless, cryo-EM single particle analysis uses many low dose measurements of copies of the sample, which are then summed up (Cheng et al., 2015; Frank et al., 1992).

Cryo-EM of biological specimens is dominated by phase contrast

Image detectors record the electrons that hit a pixel. Because of the negligible amplitude loss in biological material and under the necessary low dose conditions, there will be almost no contrast visible for an image taken by an ideal cryo-TEM in focus.

There are two ways to solve this problem:

1) To use heavy atoms to increase amplitude contrast. For example, in negative staining, uranylacetate is used to stain the outside of the particles, such that one obtains a ‘negative’ (as example, see **Figure 45**). This is often done for screening of a sample and is justified for determining the overall shape of a particle, but will not yield high resolution.

2) To optimize the (phase) contrast transfer function (CTF), which describes the relation between the original image and the one that is detected and contains microscope-specific information. It is the convolution of the sinus of the aberration function $\chi(f)$ (**1**) and an envelope function $E(f)$ that represents the dampening of the signal (de Jong and Van Dyck, 1993) (**2**). The aberration function $\chi(f)$ depends on the spatial frequency f , the wavelength λ , the spherical aberration C_s , which is microscope-specific, and the defocus δ ,

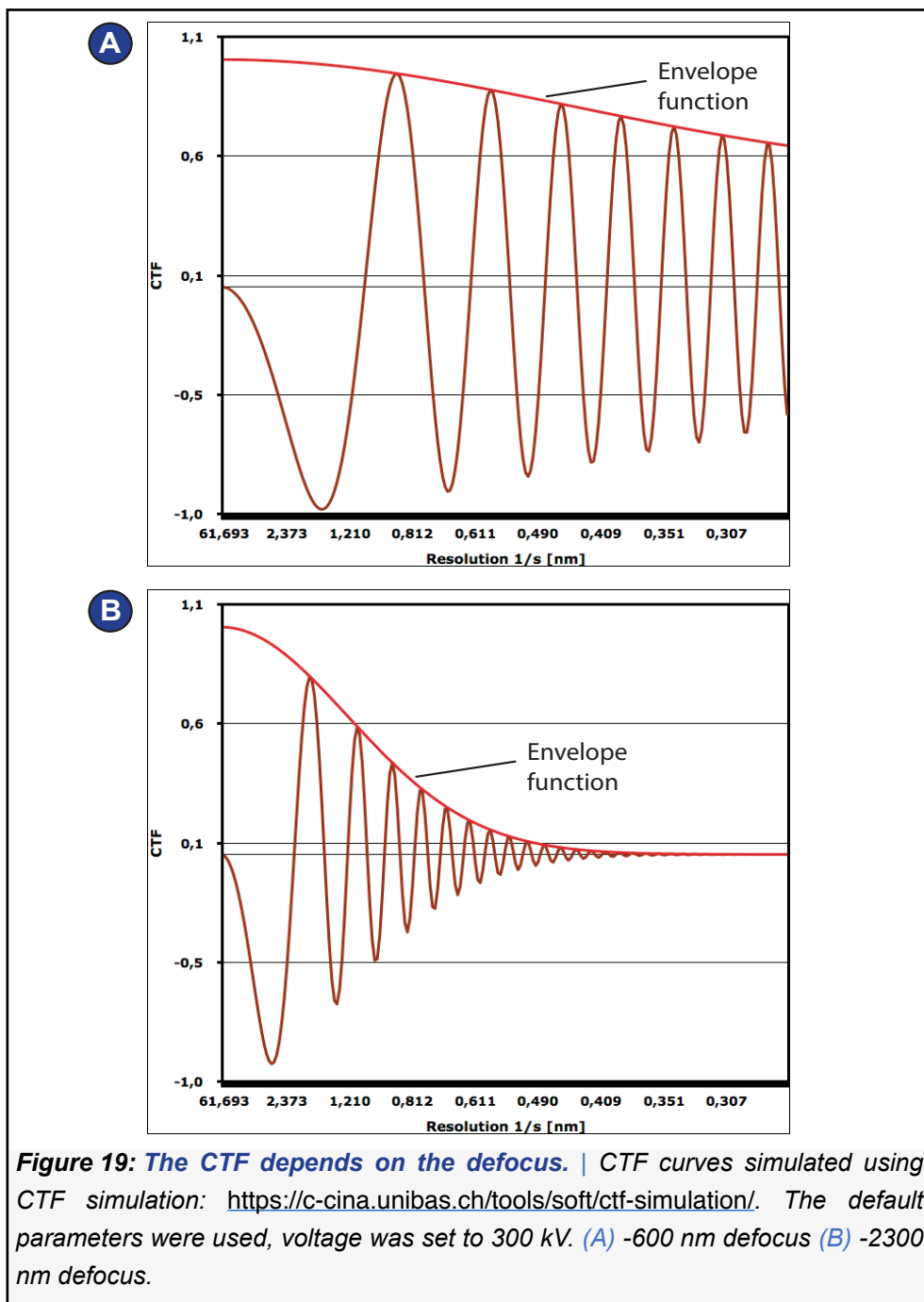
$$\chi(f) = \frac{\pi}{2} (C_s \lambda^3 f^4 + 2\delta \lambda f^2) \quad (1)$$

$$CTF = \sin(\chi(f)) * E(f) \quad (2)$$

2. Introduction

which can be adjusted via the objective lens current (de Jong and Van Dyck, 1993) (1). The envelope function depends amongst others on the defocus and on the electron source.

Images are usually not taken in focus. Instead, a defocus (δ) is employed, which increases the phase shift of the scattered vs. the unscattered beam. The efficiency by which the CTF transfers information depends on the spatial frequency and is different for



2. Introduction

different defocus values (**Figure 19**). Some information is missing completely, namely at each zero crossing. To compensate for this selective loss of information, images are usually taken at different defocus values, e.g. in a range of -500 to -2500 nm. Later, the exact defocus is recalculated for each micrograph (sometimes, even for each particle) and used for correction of the images during processing.

Spherical aberration (C_s) means that the electron beam is not focused exactly by the objective lens; instead, different components meet the optic axis at different heights, contributing to phase contrast as well.

By adjusting the defocus, $\chi(f)$ can be optimized such that the transferred contrast is enhanced. The samples presented in this work were all imaged employing this approach of taking images in defocus for enhancing phase contrast.

Another way of enhancing phase contrast is borrowed from light microscopy and consists in the usage of a phase plate (the term 'Volta phase plate' is often used in cryo-EM, in light microscopy the term ' $\lambda/4$ -plate' is used). It delays part of the electron beam and thus enhances the phase shift such that it can be measured as intensity (Zernike, 1942). Phase plates are not essential for visualizing large molecular assemblies like the ribosome, but their optimization and introduction into the field of cryo-EM nowadays allows visualization of very small molecular complexes that can hardly be realized when employing defocus variation (Danev and Baumeister, 2017).

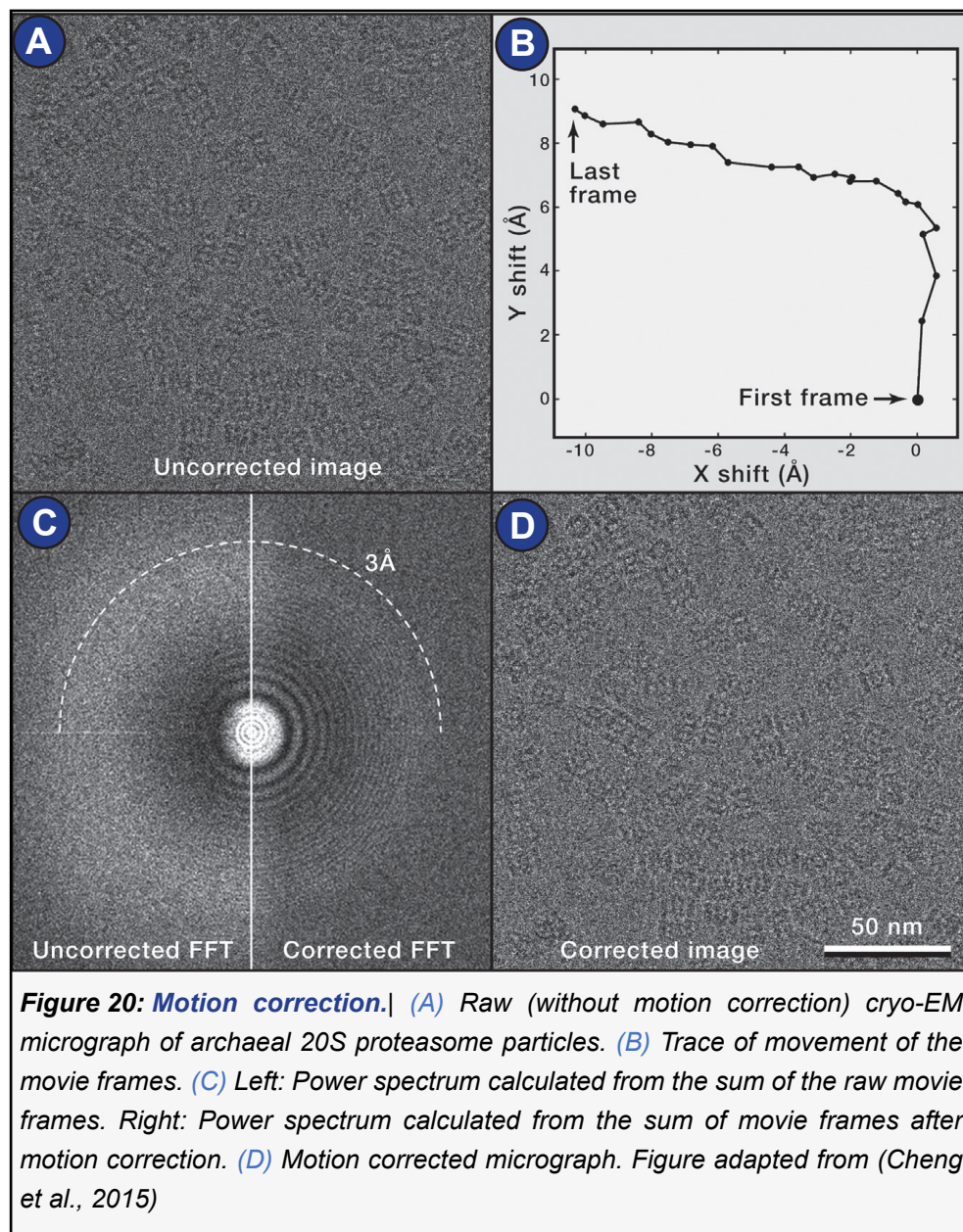
Direct electron detectors contributed a great deal to the 'resolution revolution'

The establishment of direct electron detectors contributed a great deal to the improvement of resolution in cryo-EM. Single electrons can be detected by these cameras, which possess a very thin active layer from which individual diodes can read single pixels (Faruqi McMullan, 2010). The key is that the incoming electrons are recorded as change in the potential of the diodes and not first converted to

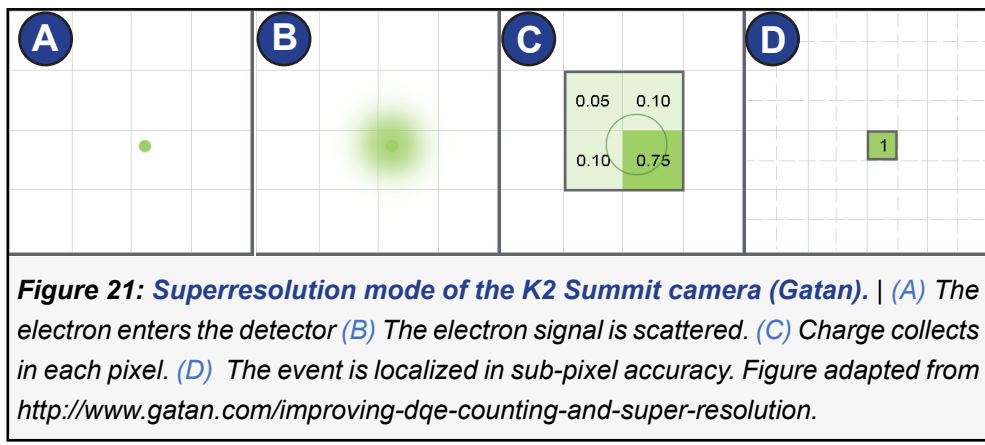
2. Introduction

light by scintillators as in old CMOS detectors. The point spread function (PSF) is therefore much smaller and the position of the incoming signal is recorded with a higher accuracy and a higher signal-to-noise ratio.

The current state of the art is that images are collected as multiple frames (movie mode). Thus, beam-induced motion of the sample can be compensated by realigning the movie frames, a process that is called motion correction (Cheng et al., 2015; Zheng et al., 2017) (**Figure 20**).



2. Introduction



Speed is also an important factor: The K2 Summit camera (Gatan), for example, has a sampling rate of ~400 images per second, enabling the detection of single events (incoming electrons). Such event is recorded over the whole detector area, of which each pixel detects a different intensity. Additionally to an intensity maximum in a certain pixel, the surrounding (weaker) intensities are measured by the neighboring pixels and thus the position relative to the maximum inside the pixel itself (quadrant-wise) can be recovered. Superresolution mode takes advantage of this and leads to a theoretically halved pixel size (**Figure 21**).

Image processing leads from 2D projections to 3D volumes

The particle images that are recorded present 2D projections formed by sending a set of parallel beams through the specimen. The intensity recorded by each pixel can be interpreted as the sum or integral of the object's intensities along the beam.

The information that a 2D projection image contains can be described by the sum of different wave functions. Low frequency information contributes to the overall shape of structures in the image, like the rough outline of a ribosomal particle, whereas high frequency information contributes to fine details, like the position of single residues.

The Radon transform (Radon, 1917 -originally published in 1917) describes the function that calculates the integrals of a 2D image at

2. Introduction

given angles and thus disassembles the 2D image in its projections. Importantly, if all angles are completely covered, an object can be completely reconstituted from its projections using the inverse Radon transform. The inverse Radon transform is the approach that in principle is used to obtain 3D reconstructions of the molecules imaged by cryo-TEM, only that the set of projections from a cryo-EM experiment is not 100% complete. Moreover, the data contains noise that might interfere with high-frequency information.

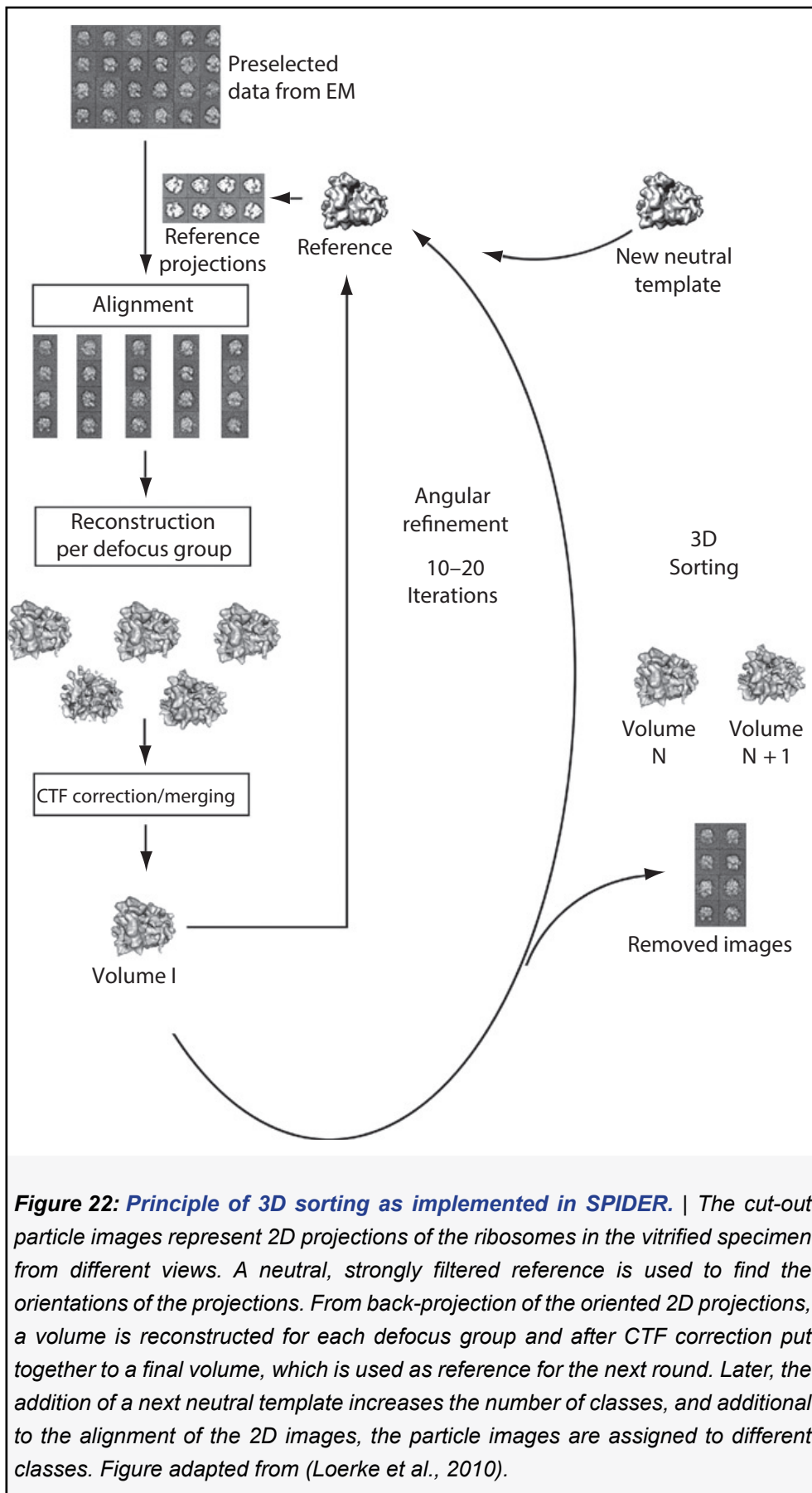
To carry out inverse Radon transform from experimental data, several methods can be used: 1) Filtered backprojection, where the 2D image is smeared along the projection axis in real space, 2) Fourier interpolation, where the Fourier transforms of the projection are interpolated in Fourier space, forming the Fourier transform of the reconstructed image, which is then inverse Fourier transformed. A high-pass filter (e.g., ramp filter) can be applied to the Fourier transforms to unblur the resulting image. 3) Algebraic reconstruction technique (ART), where the reconstruction problem is formulated as a large set of equations that are then iteratively solved (Kaczmarz, 1937).

However, for these methods, of which nowadays Fourier interpolation is most commonly used for cryo-EM reconstructions, the angles from which the projections were generated must be known. Therefore, a key procedure in single particle cryo-EM is the finding and optimization of the orientation parameters (see below).

Notably, a single projection image has a very low signal to noise ratio. Therefore, similar projections can be grouped to one image stack. Subsequent class averaging improves the signal-to-noise ratio. 2D classification of particle images is a good start when handling data of which the 3D structure is unknown. From these 2D classes or a selection, an *ab initio* reconstruction can be calculated by back-projecting the 2D images to guess a 3D volume, which over several rounds of comparison with the backprojections is improved.

In case that one has already an idea of the structure, this step can be skipped and one can proceed with refinement and sorting.

2. Introduction



2. Introduction

Refinement is the optimization of the orientation parameters. In the approach of projection matching, cross-correlation or maximum likelihood methods are used to compare the original projection images with computed projection images of the reconstructed volume/the reference.

Sorting means that one splits the dataset into subpopulations in case of heterogeneity of the sample. The ribosome is a good example for an object that gives quite heterogeneous datasets because of its intrinsic dynamic described above (subunit rotation, head swivel, etc.). Large differences can be sorted by adding a neutral reference, for example an empty, strongly filtered volume (**Figure 22**). Smaller, more local differences can be unveiled by masking the region of interest and comparing reference projections obtained through this mask (focused reassignment) (Penczek et al., 2006).

Pitfalls to avoid when calculating a structure are reference bias and overrefinement. Reference bias means that noise can align to features of any given reference volume and reproduce it (example: Mao et al., 2013). Therefore, the reference must be chosen with care, optimally it is a volume coming from the dataset itself by *ab initio* reconstruction, and it must be low pass filtered. Filtering is also important for avoiding overrefinement, that means that noise in the images aligns to fine structure of the reference projections and thus distorts the overall result.

The final maps and resolution limits of cryo-EM

Both the hardware (the microscopes and the image detectors) and the software that is used to reconstruct the 3D volume from 2D projections have been optimized in the past years and the slogan ‘resolution revolution’ has become very popular to describe the improving quality of single particle cryo-EM structures (Kuhlbrandt, 2014).

In analogy to light microscopy, the theoretical resolution limit of a transmission electron microscope is directly coupled to the wave length. In a 300 kV microscope, the electron gains a kinetic energy

2. Introduction

$$\lambda = \frac{h}{p} = \frac{hc}{\sqrt{2EE_0 + E^2}} \quad (3)$$

$$d = \frac{\lambda}{2N_A} \quad (4)$$

of 300 keV, and its wavelength is 1.969 pm according to formula (3) (Relativistic formula for the calculation of velocity, where λ is the wavelength, h is the Planck constant, E is the energy, m_0 is the rest mass of the electron, E_0 is the rest energy of the electron (Reimer and Kohl, 2008)). One possible way of estimating the resolution limit of a (light) microscope is to use Abbe's equation (4) (Lipson et al., 1995). For a microscope with a numerical aperture $N_A=0.01$ and light at the wavelength $\lambda=1.969$ pm, the theoretical point resolution limit would be ~ 0.99 Å: atomic resolution.

This example of Abbe's equation illustrates the potential of an EM compared to a light microscope due to the difference in wavelength. However, for estimating the resolution of a final map, the point resolution of the microscope does not play any role. Instead, statistical measures are used.

The final map's resolution is based on self-consistency of two raw (unfiltered) half maps: In Fourier space, the Fourier transforms of the half maps are compared pixel by pixel using cross correlation along the radius (representing the spatial frequency) of the Fourier shells. As result, correlation values (FSC) are found for each spatial frequency. The spatial frequency that falls below the threshold of 0.143 FSC is defined as the last spatial frequency with a sufficient correlation value, and thus all information that is in a higher frequency range is considered unreliable because it contains more noise than signal (Rosenthal and Henderson, 2003). The reciprocal spatial frequency corresponds to the resolution (Examples in the results section, **Figure 28**, **Figure 40**, **Figure 50**, **Figure 51**).

In practice, the resolution and, importantly, the quality of the final map that is obtained of a biological object depends on many factors. During the first half of 2018 (01/01/2018-01/07/2018), there was only

2. Introduction

one structure released in the EM-database (<http://emsearch.rutgers.edu>) from single particle cryo-EM of less than 2 Å resolution. It was the structure of beta-galactosidase at 1.9 Å (Bartesaghi et al., 2018). 423 structures had a resolution between 2-5 Å, and the number of structures greater than 5 Å was 221. The structure with the currently best resolution deposited in the EM-database is reported to have 1.6 Å resolution (*Danev R, Yanagisawa H, Kikkawa M Cryo-EM structure of mouse heavy-chain apoferritin at 1.62 Å*). Usually, biological objects reach a high resolution when they are very symmetric and exhibit a low degree of flexibility.

Finally, it is important to note that the estimation of the resolution of a cryo-EM structure is based on conventions which not the entire community agrees upon (van Heel and Schatz, 2005, 2017) and which are susceptible to distortion by improper refinement (e.g. 'overrefinement' or model bias). One number is not enough to entirely and reliably assess the quality of a cryo-EM reconstruction. Also the local resolution is important, especially local resolution of factors or any regions that are important for answering the biological question asked when imaging the given molecule.

The technical advances of the recent years resulting in an improved quality of cryo-EM maps makes it possible to model structures at near atomic resolution. *De novo* atomic modeling, so far only possible in X-ray crystallography, can now be done using cryo-EM. That means that at its current state, cryo-EM can be used to actually *solve* a structure.

3. Aims

The focus of this thesis lies on the mammalian 80S ribosome. Structural and functional knowledge about the mammalian ribosome promises elucidation of the basic mechanisms of translation in mammals compared to other domains of life. With regard to the human ribosome, its investigation promises to shed light on interactions and side effects of antibiotics, as well as opening therapeutic possibilities for pathological conditions.

Aim 1: To visualize and mechanistically understand mammalian translocation.

Translocation is one of the least understood processes in protein biosynthesis. Its correct completion is crucial for the continuation of the translation elongation cycle, and ultimately for protein synthesis. As upon translocation, the contacts between the ribosome and the tRNA₂•mRNA-module extensively rearrange, it is a process which requires utmost accuracy. Efficient translocation depends on the action of the specialized GTPase eEF2; however, detailed insights into the mechanism, by which eEF2 catalyzes translocation is lacking and opposing hypotheses are vividly discussed: The Brownian ratchet model, in which eEF2 is supporting intrinsic conformational changes that lead to translocation, and the power stroke model, according to which eEF2, being a motor protein, actively moves the tRNAs in the direction of translocation (Chen et al., 2016; Liu et al., 2014; Rodnina et al., 1997; Spirin, 2009).

Moreover, structural knowledge on tRNA translocation is dominated by studies carried out in the bacterial system, and structural data on mammalian tRNA translocation does not exist. Therefore, this work is dedicated to studying how translocation is performed in the mammalian system, using an *in vitro* reconstitution of a rabbit 80S•tRNA₂•mRNA•eEF2•GMPPNP

3. Aims

complex. The goal is to obtain structures of mammalian translocation intermediates to characterize mammalian translocation and compare it to translocation in the bacterial and yeast system.

Aim 2: To investigate the 80S•tRNA₂•mRNA•eEF2•GDP complex that is observed upon addition of eEF2•GTP to a programmed PRE complex.

To understand why eEF2 can stably bind to ribosomes and two tRNAs *in vitro* (Budkevich et al., 2014), and how this fits to the model of translocation, I look at an *in vitro* reconstituted rabbit 80S•tRNA₂•mRNA•eEF2•GDP complex.

Aim 3: To revisit the mammalian polysome landscape to find out if serum deprivation influences the distribution of states.

Cryo-EM of actively translating polysomes gives insight into the energy landscape of mammalian translation (Behrmann et al., 2015). Among other stimuli, serum deprivation and subsequent serum restimulation has been hypothesized to influence translation, e.g. via changing polysome patterns (Duncan and McConkey, 1982; Viero et al., 2015). I want to investigate if overnight serum starvation and 30 minutes of serum deprivation can change the energy landscape of translation.

Aim 4: To look at the phosphorylation site of ribosomal protein eS6 and its possible impact on its surrounding structures to find out the role of eS6 phosphorylation.

The investigation of structural changes induced by eS6 phosphorylation is the fourth aim of this thesis. eS6 is a eukaryote-specific protein of the 40S subunit. It undergoes phosphorylation in response to various stimuli, including serum deprivation/restimulation. Surprisingly, there are almost no works tackling the role of eS6 phosphorylation from a structural perspective. Since structural information on the eukaryotic ribosome from crystal structures and cryo-EM density maps have emerged in the last years, eS6 could be structurally characterized in yeast and recently also in mammalian ribosomes. However, the last residues of the C-terminus

3. Aims

of eS6, including all five phosphorylatable serines, are missing in the available structures, and similarly the neighbouring expansion segments are not well resolved, such that the phosphorylation and its structural consequences are not characterized yet (Behrmann et al., 2015; Ben-Shem et al., 2011). This thesis aims to investigate the C-terminal region of eS6 and its surrounding.

4. Methods

4.1 List of materials

Table 1: Chemicals	
Substance	Supplier
Acetic acid	Roth, Merck
Anti-eS6-P235/236 antibody (rabbit)	Thermofischer Cell signaling technology
Anti-eS6-P240/244 antibody (rabbit)	ThermofischerCell signaling technology
Anti-L22-antibody (rabbit)	Novusbiological
BSA	AmbionNew England Biolabs (NEB)
Digitonin	Sigma-Aldrich
DMEM (Dulbecco's modified eagle serum)	Gibco
DTT (1,4-Dithiothreitol)	Fluka
ECL Prime detection kit	GE Healthcare
EDTA	Merck
Ethanol	J.T. Baker
FBS (fetal bovine serum)	Gibco
Goat Anti-mouse IgG HRP (horseradish peroxidase) -conjugate secondary antibody	EMD Millipore
Goat Anti-rabbit IgG HRP-conjugate secondary antibody	Cell signaling technology
H ₂ O ₂	Merck
Heparin	Sigma-Aldrich
HEPES	Roth
KCl	ChemSoluteSigma Aldrich
KOH	EmsureSigma Aldrich
Magnesiumacetate	Merck
MES running buffer, 20x	Thermofischer
Methanol	Merck
MgCl ₂	Sigma
Milk powder	Roth
NaCl	Merck
Nupage 4-12% acrylamide, in Bis-tris gel, and NuPAGE Gel electrohporesis and western blot kit	Invitrogen

4. Methods

Phosphatase inhibitor	Roche
Phosphate-buffered saline (PBS)	Gibco
Potassiumacetate	Merck
Protease Inhibitor complete EDTA free	Roche
RNAse-free water	Invitrogen
RNAsin plus RNase inhibitor (40U μ l)	Promega
Sepharose 4B	GE Healthcare
Spermidine	Fluka Biochemica
Spermin	Sigma
Sucrose RNase-free	Sigma
TEMED	Invitrogen
Tris pH 7.5	Merck
Tween-20	Sigma-Aldrich
Uranylacetate	Fluka/Balzers Union AG

Table 2: Buffers and reagents

Name	Compound	amount
10x 48S buffer-HEPES (+DTT) (for Western blot)	HEPES (pH 7.5) Potassiumacetate DTT EDTA Magnesiumacetate Spermidine Spermine	200 mM 1000 mM 20 mM 1 mM 50 mM 2.5 mM 0.25 M
Column buffer	PEB Spermidine 0.5 mM Spermin DTT	1x 0.5 mM 0.04 mM 1mM
HEK-cell full medium	DMEM (Dulbecco's Modified Eagle's medium, Gibco) FBS Pen/Strep (Gibco) L-Glutamine	500 ml 50ml 5.5 ml 2.75 ml
High salt sucrose gradient 10-30%	HEPES KCl $MgCl_2$ Sucrose DTT	20 mM 500 mM 4 mM 10(30)% 1 M
HKM	HEPES KCl $MgCl_2$	20 mM 50 mM 4 mM
PEB 10x	Hepes pH 7.5 (KOH) KCl $MgCl_2$	200 mM 1M 15 mM

4. Methods

Permeabilization buffer	HEPES (pH 7.5) KCl $MgCl_2$ DTT Protease Inhibitor Digitonin 0.015% (2% in case of reextraction)	20 mM 100 mM 5mM 1 mM 1x 0.015% (2%)
Polyamine buffer	HEPES pH 7.5 $MgCl_2$ KCl, spermine spermidine 2-mercaptoethanol	20 mM 5 mM 100 mM 0.6 mM 0.8 mM 6 mM
RDL (Ribosome dilution buffer)	HEPES KCl $MgCl_2$ EDTA Sucrose 250 mM DTT	20 mM 10 mM 2 mM 0.1 mM 250 mM 2 mM
RRB (Ribosome resuspension buffer)	HEPES KCl $MgCl_2$ RNase Inhibitor DTT	20mM 50mM 4mM 200OU/ml 1 mM
Sucrose 1M in HKM	HEPES (KOH, pH 7.6) KCl $MgCl_2$ Sucrose Heparin DTT	20 mM 50 mM 4 mM 1 M 650 µg/ml 1 mM
Sucrose gradient 10-45%	sucrose in PEB 1x	10(45)%
TBS(T)	Tris pH 7.5 NaCl (Tween 20)	20 mM 137 mM (0.1%)
Uranylacetate staining solution	Uranylacetate Deionized water	2%
Western-blot-blocking milk	Milk TBST	5% 1x
western-blot-blocking BSA	BSA TBST	3% 1x
WB-Transfer buffer Nu-Page	20x NuPAGE transfer buffer NuPAGE antioxidant agent Methanol deionized water	25ml 1 ml 100ml 849 ml

4. Methods

Table 3: Web lab tools and devices.

Substance	Supplier
Amersham (chemiluminescence) Imager	GE HEalth care
Amicon filter	Millipore
Cell culture flasks	Sigma Aldrich
Cell culture hood	Heraeus instruments
Cell culture incubator	Heraeus instruments
Chromatography columns ('large': 50ml, 'middle': 25ml, 'small': 8ml)	BioRad (Econo-Column)
Fine balance	Sartorius, Aventurer
Glass bottles	Schott
Gradientmaster 107	BioComp
Laboratory supplies	Roth, Eppendorf
Magnetic stirrer	Heidolph, Kiker
Minishaker	IKA
Optima max centrifuge	Beckman
pH-Meter 510	Cyberscan
Photometer DU 800	Beckman
Photometer Nanodrop 1000	Peqlab
Pipet boy	Integra
Pipettes	Gilson
Piston Gradient Fractionater	BioComp
Pure water device	Milli-Q Millipore
PVDF membrane for western blot	Sigma-Aldrich
Rotors MLS-50, SW-55Ti, MLA 80	Beckman
Serological Pipets, different volumes	Falcon
Shaker Vortex-Genie	Bender&Hobein
Tabletop centrifuges 5415 D, R	Eppendorf
Thermomixer	Eppendorf
Ultracentrifuge cups	Beckman

Table 4: Microscopy tools and devices

Device	Producer
1K TemCam	Tietz
Carbon evaporator	Denton
CM100 Electron microscope	Philips
F416 4k camera	Tietz
Glow discharger	Harrick
Holey carbon grids	Quantifoil
K2 Summit DED Camera	Gatan
Light microscope for evaluating cells	Olympus

4. Methods

MegaView III camera	Soft imaging system GmbH
Morgagni 268 Electron Microscope	FEI company
Tecnai G2 Polara F30 Electron Microscope	FEI Company
Tecnai G2 Spirit Electron Microscope	FEI Company
Vitrobot II	FEI Company

Table 5: Software and online databases/tools		
Software	Reference	Link
Adobe CC	-	https://www.adobe.com/
Chimera, UCSF	Pettersen et al., 2004	https://www.cgl.ucsf.edu/chimera/
Coot	Emsley and Cowtan, 2004	http://www2.mrc-lmb.cam.ac.uk/Personal/pemsley/coot/
CryoSPARC	Punjani et al., 2017	https://cryosparc.com/
CTFFIND4	Rohou and Grigorieff, 2015	http://grigoriefflab.janelia.org/ctffind4
EMAN2	Tang et al., 2007	http://ncmi.bcm.tmc.edu/ncmi/software/
ERRASER	Chou et al., 2012	https://www.phenix-online.org/documentation/reference/eraser.html
Gautomatch	-	http://www.mrc-lmb.cam.ac.uk/kzhang/
GCTF	Zhang, 2016	https://www.mrc-lmb.cam.ac.uk/kzhang/
iTasser	Roy et al., 2010; Yang et al., 2015	https://zhanglab.ccmb.med.umich.edu/I-TASSER/
Leginon	Suloway et al., 2005	http://leginon.org
Linux CentOS	-	CentOS.org
MDfit	Ratje et al., 2010	http://sanbonmatsu.org/gmx-4.5.5-mdfit.tar.gz
MotionCorr1v.2	Li et al., 2013	http://msg.ucsf.edu/em/software/
PHENIX	Adams et al., 2010	https://www.phenix-online.org/
Relion	Scheres, 2012	https://github.com/3dem/relion
ResMap	Kucukelbir et al., 2014	http://resmap.sourceforge.net/
Rosetta	-	https://www.rosettacommons.org/
Serial EM	Mastronarde, 2005	http://bio3d.colorado.edu/SerialEM/
SIGNATURE	Chen and Grigorieff, 2007	http://grigoriefflab.janelia.org/signature
SPIDER	Frank et al., 1996	https://spider.wadsworth.org/
Word, Microsoft	-	https://products.office.com/en/word

4. Methods

Table 6: Online tools and databases

Online-tool	Reference	Link
Blast sequence alignment	-	https://www.uniprot.org/blast/
CTF simulator	-	https://c-cina.unibas.ch/tools/soft/ctf-simulation/
EM database	-	http://www.emdatabank.org/
Matcha Math editor	-	https://www.mathcha.io
Molprobity	Chen et al., 2010	http://molprobity.biochem.duke.edu/
Pubmed	-	https://www.ncbi.nlm.nih.gov/pubmed/
RCSB PDB database	Berman, 2000	https://www.rcsb.org/
RCSB PDB Validation-service	-	https://validate-rscb-1.wwpdb.org/
tRNA sequences	Juhling et al., 2009	http://trna.bioinf.uni-leipzig.de
Uniprot	UniProt Consortium, 2008	http://www.uniprot.org/

4.2 Preparation of the cryo-EM sample of *ex vivo* derived polysomes

Cell culture conditions

HEK (T293) cells were seeded in a density of 8×10^4 cells per cm^2 and grown in 720 ml cell culture flasks in 50 ml HEK-cell-medium with 10% serum (HEK-cell full medium). After 30 hours, the medium was exchanged for serum-free medium. The cells were serum-deprived for 14 hours and then divided into two equally sized groups. In one group, 20 ml of medium were removed without further treatment, (serum-deprived group, the sample from this group is called sample 'D'). In the other group, 25 ml of medium was pipetted off and 5 ml serum was added (serum-restimulated group, the sample from this group is called sample 'S'). Both groups were then incubated for 30 minutes at 37° C (**Figure 23A**).

4. Methods

Preparation of a cytoplasmic extract from HEK-cells

For cell harvesting and preparation of a cytoplasmic extract from HEK-cells, two methods were used. In the 'Amicon method' (described in detail in (Behrmann et al., 2015), after discarding the medium, the cells were immediately cooled on ice and washed with 20 ml of PBS. Following the washing, 3 ml of permeabilization buffer were added and the cells were detached from the flask's surface by repetitive pipetting. The permeabilization buffer gently permeabilizes the cell membrane and allows the cytoplasm to leave the cells (Jagannathan et al., 2011).

The cell lysate was cleared from intracellular organelles and other particles, e.g. the cell membrane, by centrifugation. The supernatant was then concentrated via several rounds of centrifugation in Amicon filter tubes, yielding a highly concentrated (ca. 90 OD/ml at A260) sample that could be used for gel filtration or other steps.

In the second method ('freezing method'), after the washing step the cells were collected in 4 ml PBS per flask, and low-speed centrifugation (4000g for 3 minutes) and subsequent discarding of the supernatant resulted in a cell-pellet that was immediately frozen in liquid nitrogen. This cell pellet was then resuspended on ice in the same permeabilization buffer as above, but in a volume as little as 1.5 ml per 5 flasks or 200 µl per 1 flask. After centrifugation, the supernatant was directly used for experiments.

For a part of the material, a reextraction experiment was performed. Here, material was further extracted from the pellet that remained after centrifugation by resuspension in permeabilization buffer containing 2% of digitonin and subsequent centrifugation as described above.

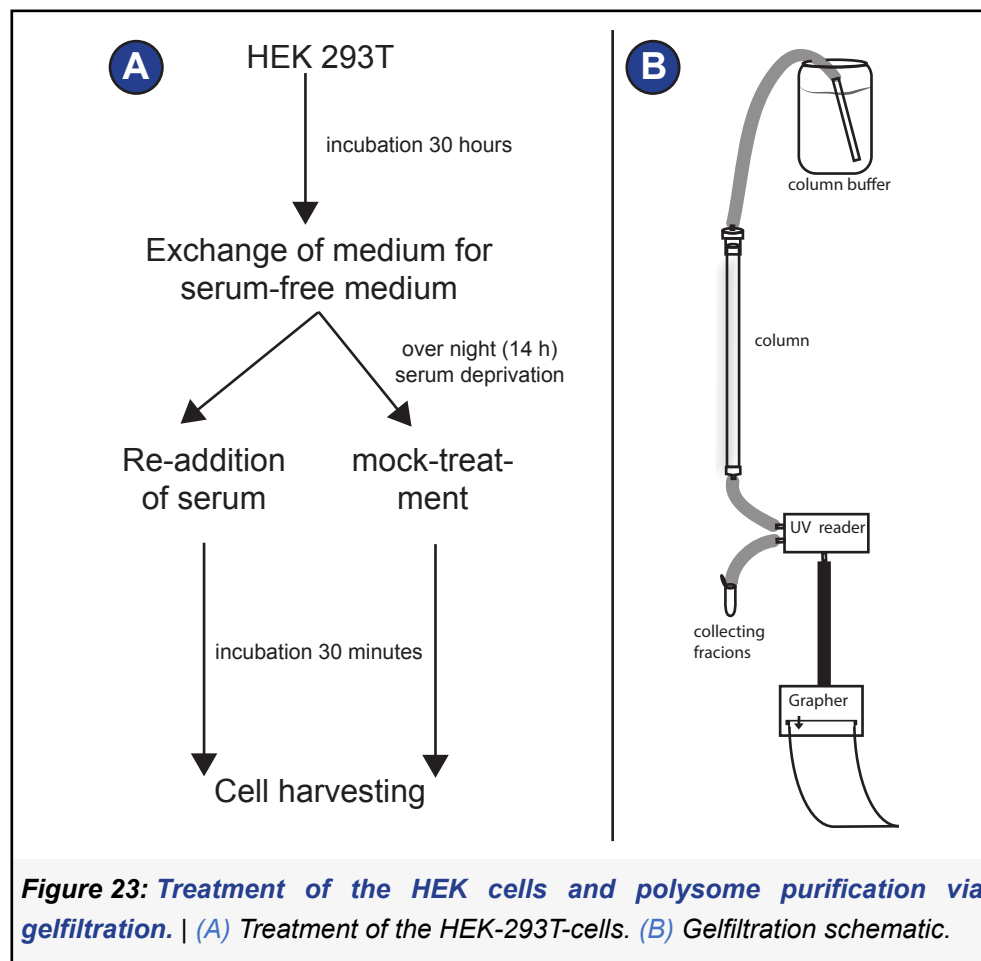
Size exclusion chromatography (Gelfiltration)

Gelfiltration is a method to isolate polysomes from monosomes and other components of the cell lysate via size exclusion (Behrmann et al., 2015). The sample is run through a column packed with sepharose 4B. The matrix of sepharose 4B causes the different components of

4. Methods

the cell lysate to run through the column at different speeds. The peak of the polysomes is recognized by continuous monitoring of the optical density (A₂₆₀) (**Figure 23B**). One can directly apply the fractions from this peak to a grid for negative stain or cryo-EM, or use them for other experiments. They contain actively translating polysomes.

For each run, a freshly packed column was used. Column packing was done by standard procedure using degassed resin and buffer solutions. The column was blocked and calibrated in the cold room (at 4°C) using Chinese hamster ovarian lysate or yeast lysate. This step is important both for blocking unspecific binding sites in the column to avoid loss of material when using the real sample (blocking) and for estimating the time that is necessary for the sample to run through and especially the time point around which the peak appears (calibration). The cell lysate was applied directly



4. Methods

onto the gel matrix, and the buffer supply was connected only after it got fully absorbed. After the sample has run through, the column was run with column buffer to wash out residues of the sample.

The volume that can be loaded on a gel filtration column is limited to maximally 4% of the total column volume; 500 µl were applied on a middle column, 1-2 ml on a large column, and 200 µl on a small column. The sample was applied directly on the gel matrix as described above for the blocking procedure. Fractions were manually collected from the first evidence that the OD (A260) was rising, and until it descended back to baseline. The concentration of the collected fractions was subsequently measured using the Nanodrop photometer. For grid preparation, the peak fraction was used. For procedures that demanded a high amount of material, like RNase digestion, the peak and neighbouring fractions were pooled.

4.3 Biochemical analysis of *ex vivo* derived polysomes

Photometric estimation of protein/RNA concentration

The concentration of RNA or proteins in the samples, e.g. for identification of the peaks after gel filtration, was carried out using a Photometer; for rough estimation the Nanodrop photometer, for a more precise estimation the Beckmann photometer was used. A Photometer reveals the concentration of RNA or protein or other components in a sample by its property to cause extinction of incoming light of a certain wave length following the law of Lambert Beer (**5**), where ϵ is the extinction coefficient, c is the concentration and d is the layer thickness. Concentration of proteins was estimated by reading out the absorption maximum at 280 nm (A280), whereas for estimating the concentration of RNA the maximum at 260 nm (A260) was used. The concentration of ribosomal particles as 80S, 60S and 40S was estimated based on the A260 and (**6**).

4. Methods

$$E_\lambda = \epsilon \times c \times d \quad (5)$$

$$c_{rp} = \frac{A_{260}}{ml} \times \frac{\alpha}{A_{260}} \times x \quad (6)$$

rp ribosomal particle; *x* dilution factor; α rp-specific coefficient;

$$\alpha_{80S} = 20 \text{ pmol}$$

$$\alpha_{60S} = 29 \text{ pmol}$$

$$\alpha_{40S} = 65 \text{ pmol}$$

Sucrose gradient centrifugation

A sucrose gradient can be used for separation of polysomes, monosomes and even lighter particles as 48S complexes. The friction/viscosity of the sucrose is used to separate particles of different sizes, shapes and molecular weights. Depending on the gradient composition, it allows resolution up to separation of different sizes of polysomes, monosomes and ribosomal subunits, and separation from lighter molecules.

For the characterization of the effects of serum deprivation and restimulation on the composition of the polysomes and the relative proportions of heavy polysomes, light polysomes and monosomes, the cell lysate or selected peak fractions after gel filtration were centrifuged over a 10%-45% sucrose gradient in PEB for 2.15 hours at 36,000 rpm (SW40 rotor). Then, the different fractions were collected.

Subunit preparation

The cell lysate can also be used to purify ribosomal subunits (Bommer et al., 1997). First, a ribosomal pellet is prepared by 4 hours centrifugation over a 1M sucrose cushion in HKM-buffer at 75,000 rpm (MLA 80 rotor). After resuspension in 1ml RRB, which is rendered by stirring for 30 minutes, a 10 minutes centrifugation at 21,000g is used to obtain a clear supernatant. Subunit dissociation is induced by addition of 1mM Puromycin and 20 minutes incubation on ice followed by 10 minutes incubation at 37°C. Next, all remedies of binding factors, tRNAs, ect., are washed off the subunits by addition

4. Methods

of 4M KCl until a final molarity of 0.5 M is reached in the sample. Centrifugation over a high salt sucrose gradient (10%-30%, 500 mM KCl) for 18 hours at 22,000 rpm (SW40 rotor) separates the ribosomal subunits into different layers along the gradient. After collection and identification of the respective fractions, a potassium concentration of 83 mM has to be established by stepwise dilution with RDL; finally, the diluted sample is concentrated via centrifugation in Amicon filter tubes. Ribosomal subunits were concentrated to reach between 50-100 OD at 260 nm per ml.

Gel electrophoresis

Gel electrophoresis serves as versatile tool for analyzing the protein composition of samples. The preheated samples are loaded on the gel and a voltage of 180 V is applied for ca. 1 hour. The proteins are separated according to their molecular weight. A marker is run to allow for assignment of the individual bands. The gel can further be used for several gel staining methods, western blot, or the band of interest can be cut out and for example used for mass spectrometry.

Western blot

In Western blot, the proteins were transferred from the gel to a PVDF membrane in transfer buffer at 180 V (Nupage system, Invitrogen). The membrane was then incubated in milk or BSA (depending on the afterwards used type of antibody) for 60 minutes to block unspecific binding sites. After several washing steps in TBS(T), the membrane was incubated with the antibody against the protein of interest. After further washing and a second incubation step with the secondary antibody, which serves the detection by its conjugated HRP enzyme, which produces chemiluminescence, the protein was visualized via a chemiluminescence reader (Amersham Imager 600) using the ECL Prime detection kit.

4. Methods

4.4 Preparation of the cryo-EM sample of 80S•tRNA₂•eEF2 complexes from rabbit.

The samples were prepared by Dr. Tatyana Budkevich.

Reconstitution of translocation intermediates stalled with eEF2•GMPPNP

For reconstitution of mammalian translocation intermediates *in vitro*, purified components have been used: ribosomal subunits from rabbit ribosomes, eEF2 from rabbit, N-acetyl-[¹⁴C]-Val-tRNA^{Val}, deacylated tRNA^{Phe}, *in vitro* transcribed mRNA with the coding sequence Met-Phe-Val-Lys (MFVK-mRNA) and GMPPNP. Ribosomal subunits were purified from rabbit reticulocyte lysate following (Bommer et al., 1997) as described for HEK-cells in Section 4.3. eEF2 purification from rabbit reticulocyte lysate is based on (Pestova and Hellen, 2003). The heteropolymeric MFVK-mRNA was prepared using run-off transcription with T7 RiboMax Express large scale RNA Production (Promega) as described in (Triana et al., 1994). tRNA^{Val} was purified from a total tRNA pool obtained by acid phenol extraction (Rogg et al., 1969).

The translocation intermediate complexes were assembled in polyamine buffer by stepwise addition of the purified components and immediately applied to the cryo grids. First, 80S ribosomes were re-associated from the subunits in the presence of the mRNA and deacyl tRNA^{Phe} was added in 2 times excess over 80S to occupy the P site (20 minutes incubation at 37° C). In the next step, 2 times excess addition of N-acetyl-[¹⁴C]-Val-tRNA^{Val} resulted in the occupation of the ribosomal A site (10 minutes incubation at 37°C). The acetyl group is known to enhance stability and mimic the state after peptidyl-transfer (Hansen et al., 2002). In the third step tRNA^{Phe} and N-acetyl-Val- tRNA^{Val} in the P- and A-sites, respectively, were translocated to the E and P sites by addition of eEF2 (2 times excess over 80S) and 200 μM GMPPNP (20 min, 37°C). The efficiency of the translocation reaction and the binding state of the tRNAs was

4. Methods

determined in a fourth step by means of puromycin reaction (at 37°C, 1 hour): puromycin reacts with P site-, but not A site-bound aminoacyl-tRNA. The occupancy of N-acylated Val-tRNA^{Val}, estimated via filter binding assay, was approximately 40% of 80S ribosomes and more than 90% of the bound tRNA was reactive to puromycin, indicating a nearly complete translocation and P-site location. The methods are described in detail in (Flis et al., 2018).

Reconstitution of an 80S•tRNA₂•eEF2•GDP complex

The 80S•tRNA₂•eEF2•GDP complex was prepared in the same way as the translocation intermediates stalled with eEF2•GMPPNP, only that GTP was used instead of GMPPNP.

The occupancy of N-acylated Val–tRNA^{Val}, estimated via filter binding assay, was approximately 66% of 80S ribosomes and more than 90% of the bound tRNA was reactive with puromycin, indicating a nearly complete translocation and P-site location. The methods are described in detail in (Budkevich et al., 2008, 2014).

4.5 Making of the grids and sample application

Making of negative stain grids

The grids for negative staining were coated with a thin carbon layer in-house. The carbon film was made by spraying carbon particles on a chip using a carbon evaporator (Denton). The purchased holey carbon grids (Quantifoil Microtools GmbH) were washed with chloroform and dried before finally being coated with the thin carbon film in a water bath. The carbon film should not be used right away but needs about one week to mature. The carbon film on the grid is usually hydrophobic; before sample application, it is made hydrophilic in a Plasma Cleaner (PDC002, Harrick) (pressure 0.3 mbar, 30 seconds). 3.5 µl of sample was applied on the grid, excess was removed with blotting paper after 45 seconds, then 2% uranylacetate solution was applied, excess removed after 20 seconds, and the grids were air-dried at room temperature.

4. Methods

Making of cryo-EM grids

The grids used for cryo-EM already had a thin layer of carbon. Again, before sample application, ionization of the grid in a Plasma Cleaner (Harrick) must occur to increase hydrophilicity (Pressure 0.3 mBar, 30 seconds). The sample was then applied (3.5 µl) on the grid inside the chamber of a Vitrobot (FEI) with 90% humidity at 4°. In the Vitrobot, excess of sample was blotted off (blotting time 2 or 4 seconds), and the sample was plunge-frozen in liquid ethane. The grids were stored in liquid nitrogen until imaging.

4.6 Data acquisition

Low and intermediate resolution imaging

Negative stain was used for evaluation of the sample quality and finding of the right concentration (screening). For this, the CM100 microscope (Philips) or Morgagni microscope (FEI) was used. A reconstruction can be made using negative stain data, however, that was not necessary in the described projects.

Cryo-EM on the Tecnai G2 Spirit microscope (FEI) produces images that are suited for reconstruction of intermediate resolution structures. The resolution-limiting factors of this microscope are the electron source (LaB₆ cathode), the overall optical and mechanical stability of the microscope, and the camera (TemCam F416 (Tietz), 4096x4096, pixel size 2.65 Å). The resolution that is usually obtained is about 20 Å.

For the 80S•tRNA₂•mRNA•eEF2•GMPPNP complex and the 80S•tRNA₂•mRNA•eEF2•GDP complex, a 3D reconstruction from Spirit data has been done to estimate the factor occupancy.

For the polysomes from serum deprived and serum restimulated HEK cells, a reconstruction from data from the Spirit microscope has been done for quality assessment of the sample and checking if there is a difference in the distribution of the states.

4. Methods

Leginon (Suloway et al., 2005) was used for automated data collection.

High resolution imaging

The data used for reconstruction of high-resolution translocation intermediates with eEF2-GMPPNP and eEF2-GDP was acquired with a Tecnai F30 G2 Polara Microscope (300kV) and a K2 Summit DED camera (Gatan, pixel size=0.6275, magnification 31,000x, super-resolution mode. Leginon (Suloway et al., 2005) was used for automated data collection.

Both datasets of polysomes from serum deprived and restimulated HEK cells were obtained from a Titan Krios microscope (FEI) using a K2 Summit DED camera (Gatan, pixel size=0.665, magnification 31,000x, super-resolution mode). SerialEM (Mastronarde, 2005) was used for automated data collection. The access to the Titan Krios microscope at EMBL (European Molecular biology Laborator) in Heidelberg was provided by iNEXT (Infrastructure for NMR, EM and X-rays for Translational Research).

4.7 Data processing

Screening of the micrographs, CTF estimation, motion correction and frame weighting

Following data collection, the micrographs were screened manually using e2boxer and e2display from the EMAN2 package (Tang et al., 2007) aiming to select only micrographs of high quality. Criteria for discarding micrographs were low particle density, contamination, and power spectra calculated with SPIDER (Frank et al., 1996) that indicated bad quality, e.g. a limited radius in which Thon rings were visible, astigmatism, and drift (see **Figure 24** for examples of selected and discarded micrographs). Ctffind4 (Rohou and Grigorieff, 2015) in the case of the translocation intermediates and GCTF (Zhang, 2016) in the case of the polysomes were used to calculate the defocus values for each micrograph. MotionCor2 (MotionCorr1.2 in case of

4. Methods

the eEF2•80S data) (Li et al., 2013; Zheng et al., 2017) was used to correct for beam-induced motions of the sample by aligning the dose fractionated movie stacks on each other, and for background correction using a reference image taken at the beginning of the data collection (gain correction).

Particle identification and making of particle stacks

Semiautomated particle picking in e2boxer from the EMAN2 package (Tang et al., 2007) (for the es6 dataset and low resolution (Spirit) screening data) or (in the case of data of translocation intermediates) Signature (Chen and Grigorieff, 2007) were used to identify ribosomal particles on the micrographs and to save the corresponding coordinates. SPIDER (Frank et al., 1996) or RELION (Scheres, 2012) were used to cut out the particle images and make particle image stacks for each micrograph. In the case of automated Picking with Signature, the stacks were further processed using an ‘autopicking’ procedure based on statistical features of the images (SPIDER) to discard false positive particle images. The selection of particle images was normalized using SPIDER for further refinement with SPIDER, and RELION for further refinement with CryoSPARC (Punjani et al., 2017) or RELION (Scheres, 2012). Decimation was carried out in SPIDER to obtain six-fold (DC6), three-fold (DC3) and two-fold (DC2) decimated particle images besides the undecimated (DC0) data, or RELION, where decimation can be implied in the cutout process (Scheres, 2012) (**Figure 24**).

Refinement and sorting

For the data on translocation intermediates, SPIDER (Frank et al., 1996) was used for both refinement and multiparticle sorting (Loerke et al., 2010). Focused reassignment (described in Budkevich, 2011) was used to separate classes of different conformation or composition. 3D variability analysis (described in Behrmann et al., 2015) was used to evaluate the presence/absence of elongation factor eEF2. PDB enhancement was included at the level of DC3 data to enhance high-frequency information. PDB enhancement is a method for map

4. Methods

sharpening. It applies the computationally simulated frequency spectrum of an atomic model to the experimentally obtained density map to enhance information that is expected to be present in the experimental data, but is damped by the envelope function of the CTF.

After obtaining the three final populations representing the translocation intermediates (see section 5 (results)), several post-processing steps were added and then small angle alignment of the post-processed final particle image stacks was performed. The particle images belonging to the three final populations were processed together until the end without separate refinement of isolated particle images. To screen for differences in the eS6 region, the largest population (TI-POST-3) was isolated and particle images at DC2 level were used to perform a focused reassignment using a spherical mask on the eS6 region.

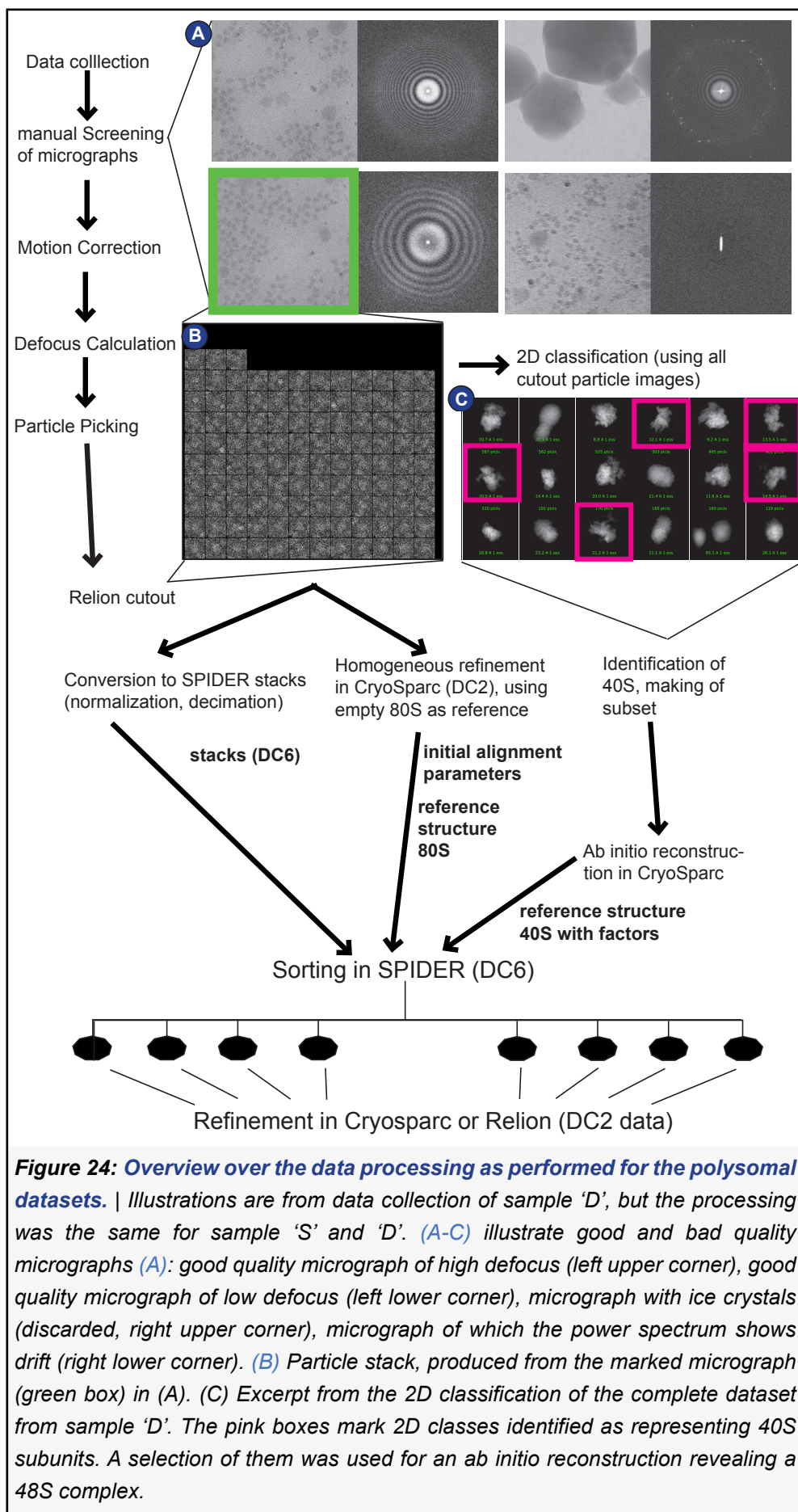
For the reconstruction of polysomal states, an initial homogeneous Refinement in cryoSPARC (Punjani et al., 2017) was carried out to align all particle images on an empty, strongly filtered reference volume of a eukaryotic ribosome. After this initial alignment, SPIDER was used for sorting the DC6 particle images, using mostly focused reassignment (described in Budkevich, 2011).

In order to inspect the eS6 region of all particle images belonging to the 80S class in the polysomal datasets, the particle images were aligned on density included in a 40S body-platform soft mask using RELION auto refine.

Post-processing steps on final particle selection

In the case of the translocation intermediates stalled with GMPPNP, several processing steps on the raw data were added after final selection and sorting of the particle images: Particles were realigned individually to correct for anisotropic motion (Rubinstein and Brubaker, 2015) and separate reconstructions were calculated for each frame. From comparison of these reconstruction with an external reference simulated from atomic coordinates, SSNR-based

4. Methods



4. Methods

weighting curves were calculated for each frame and all particles were combined using this frame weighting for the final refinement steps and reconstruction. In addition, cross-correlation-based recalculation of the CTF-values in SPIDER (Frank et al., 1996) was used to improve the resolution, as well as creation of a particle image stack that consisted of (the post-processed) undecimated (DC0) particle images interpolated to a pixel size of approximately 1Å.

4.8 Modeling

To interpret the maps of the three translocation intermediates, three atomic models were built. As starting point for modeling, already existing models were used. The sequences of the tRNA models from the mammalian POST-complex PDB-5aj0 (Behrmann et al., 2015) was mutated in Coot (Emsley and Cowtan, 2004) to the correct sequences (<http://trna.bioinf.uni-leipzig.de>). The model of domains 1-3 of the elongation factor eEF2 was obtained by a homology model with the online tool iTasser (Roy et al., 2010; Yang et al., 2015) using the yeast 80S•IRES•eEF2•GMPPCP translocation intermediate (PDB-5it7) as template (Murray et al., 2016). The mRNA was modeled *de novo*.

The models were first fit as rigid bodies with Chimera (Pettersen et al., 2004). If necessary, rRNA domains or helices were separated and docked separately, particularly the L1 stalk, the 40S head and the 40S body/platform. The 40S head was defined as the rRNA C1215-C1685 and the 40S body/platform as A1697-A1869 and U1-U1202, while the linking element of h28 was separately docked. For docking of the stalk-base RNA, MD-Fit was used (Ratje et al., 2010; Whitford et al., 2011). The separated parts were then re-ligated in Coot.

The RNA geometry was improved with ERRASER (Chou et al., 2012). Then, the fit of the model to the density was improved manually

4. Methods

with Coot and refined with Phenix real-space refinement (Adams et al., 2010). Manual correction in Coot and refinement in Phenix were repeated iteratively.

To avoid overfitting, the weighting for the Phenix refinement was estimated from comparing the crossresolution curves (Greber et al., 2015): The models were refined with a map comprising half of the particles from the original density map, using different weights. Then density maps were calculated from these refined models. Next, cross resolutions between those maps and both half maps, as well as the corresponding full density map were calculated. The weight was chosen based on evaluation of the cross-resolution curves, focusing on the best compromise between good correlation with respect to the full map and consistency of the curves from cross correlation between the half map used for refinement and the other half map (**Figure 25**).

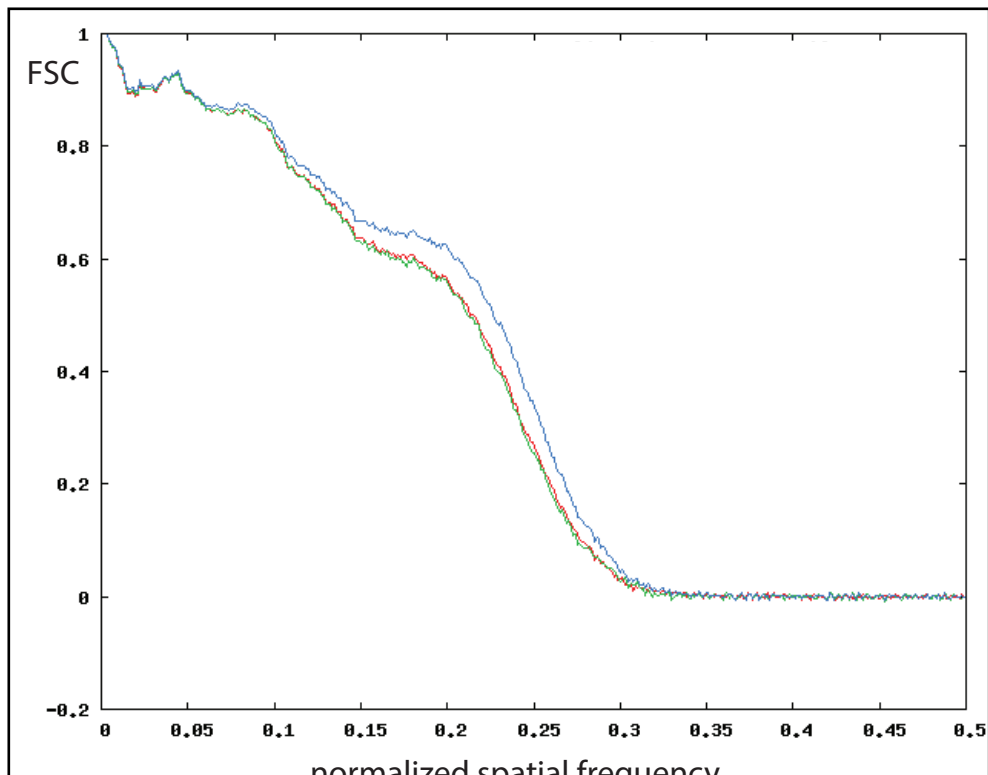


Figure 25: Finding of the correct weight for phenix refinement. | Global crosscorrelation between the simulated density from the model for TI-POST-2, refined in phenix using a weight of 2, and 1) both half maps (red and green curves), 2) the full map. y-axis: FSC, x-axis: normalized spatial frequency. A weight of '2' was chosen for the final refinement of the model for this population.

4. Methods

For modeling of the native 48S initiation complex, existing models of the human 48S complex (PDB-6fec, PDB-4kzz) (Eliseev et al., 2018; Lomakin and Steitz, 2013) were rigid body-fitted in Chimera (Pettersen et al., 2004). Specifically, the model for the 40S, eIF3, tRNA, eIF2, was taken from PDB-6fec (Eliseev et al., 2018), and only the model for eIF1A was adopted from PDB-4kzz (Lomakin and Steitz, 2013).

4.9 Validation of map and model, preparation of final maps and map-to-model correlation

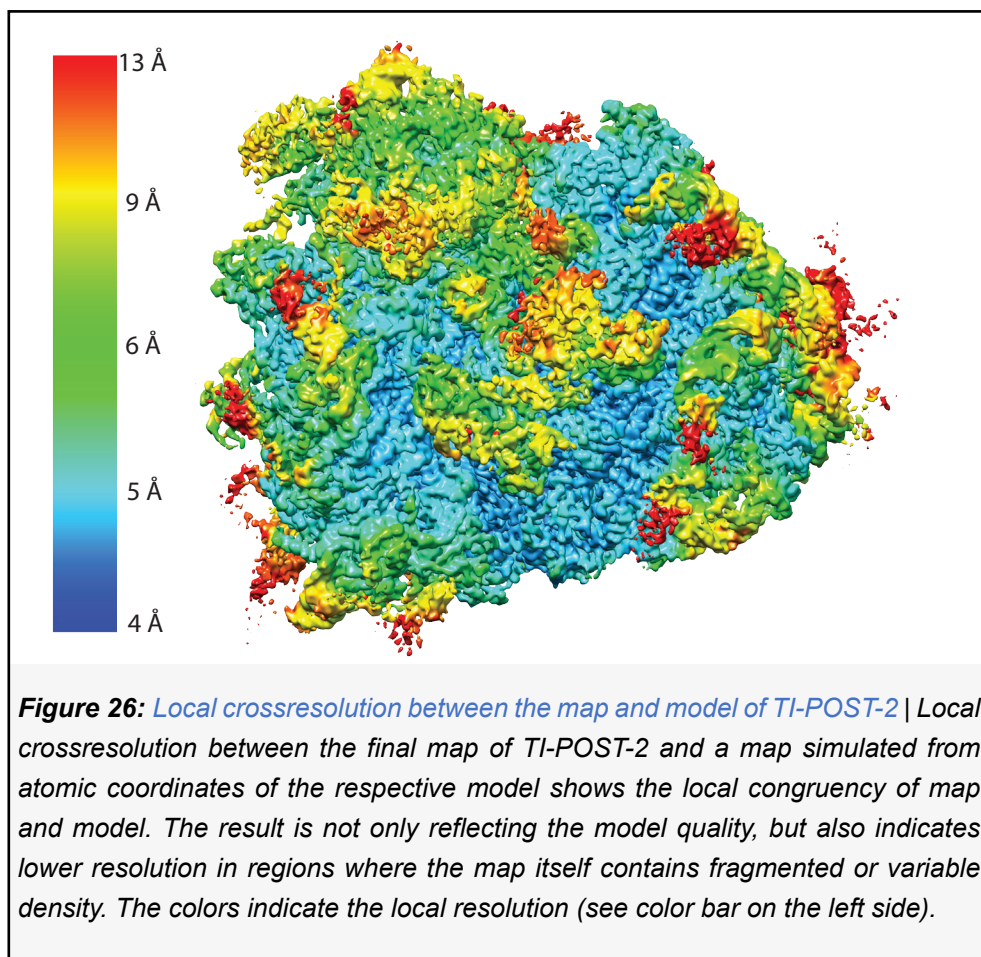
The resolution of the cryo-EM maps was assessed by the Fourier Shell Correlation FSC (Harauz, G. and van Heel, 1986) using a threshold value of 0.143 (FSC 0.143) (Rosenthal and Henderson, 2003). Before FSC-calculation, a soft mask was applied to the raw, unfiltered half maps. The local resolution was calculated with ResMap (Kucukelbir et al., 2013) for each map.

The unfiltered raw maps from the refinement were filtered in SPIDER to the resolution retrieved from the Fourier shell correlation (FSC) value (cutoff criterion 0.143) using a Butterworth filter function. The pixel size was re-estimated by comparison with a crystal structure of a yeast ribosome (using the 60S subunit from PDB-4v88 (Ben-Shem et al., 2010)) and applied to the maps. These were the maps, which were then used for modeling.

For *validation of the models*, the pdb-database (<https://validate-rcsb-1.wwpdb.org/>) and Molprobity (<http://molprobity.biochem.duke.edu/>) were used.

Local cross resolution is an important parameter for comparing volumes. Cross-resolution is calculated between both maps in a sliding-window manner using SPIDER procedures (**Figure 26**). Additionally, the global cross-correlation can give an idea about the congruency of two densities (**See Figure 41**).

4. Methods



5. Results

The results section contains three parts.

First, three cryo-EM structures of *in vitro* reconstituted, authentic 80S mammalian translocation intermediates stalled with GMPPNP will be presented in **section 5.1**. This presentation includes description of the conformational and functional states of the structures and interpretation of their role in the context of previously identified structures from the elongation cycle. Furthermore, some characteristic molecular interactions will be analyzed.

In **section 5.2**, a cryo-EM structure of an *in vitro* 80S•tRNA₂•mRNA•eEF2•GDP structure is presented and compared with the results from the previous section.

Section 5.3 comprises all results associated with the two *ex vivo* polysomal samples. After a short summary of the biochemical results, the functional states discovered via *in silico* sorting will be presented, including a comparison between sample 'S' (from serum-restimulated HEK-cells) and sample 'D' (from serum-deprived HEK-cells). Next follows an inspection of the region surrounding the eS6 C-terminus in the structures from polysomes as well as in one of the structures from section 5.1. The ribosomal structures from sample 'D' were refined to high resolution and are discussed in detail in the last parts of section 5.3.

5. Results

5.1 *In-vitro* reconstitution of intermediates of translocation reveal three late translocation intermediates.

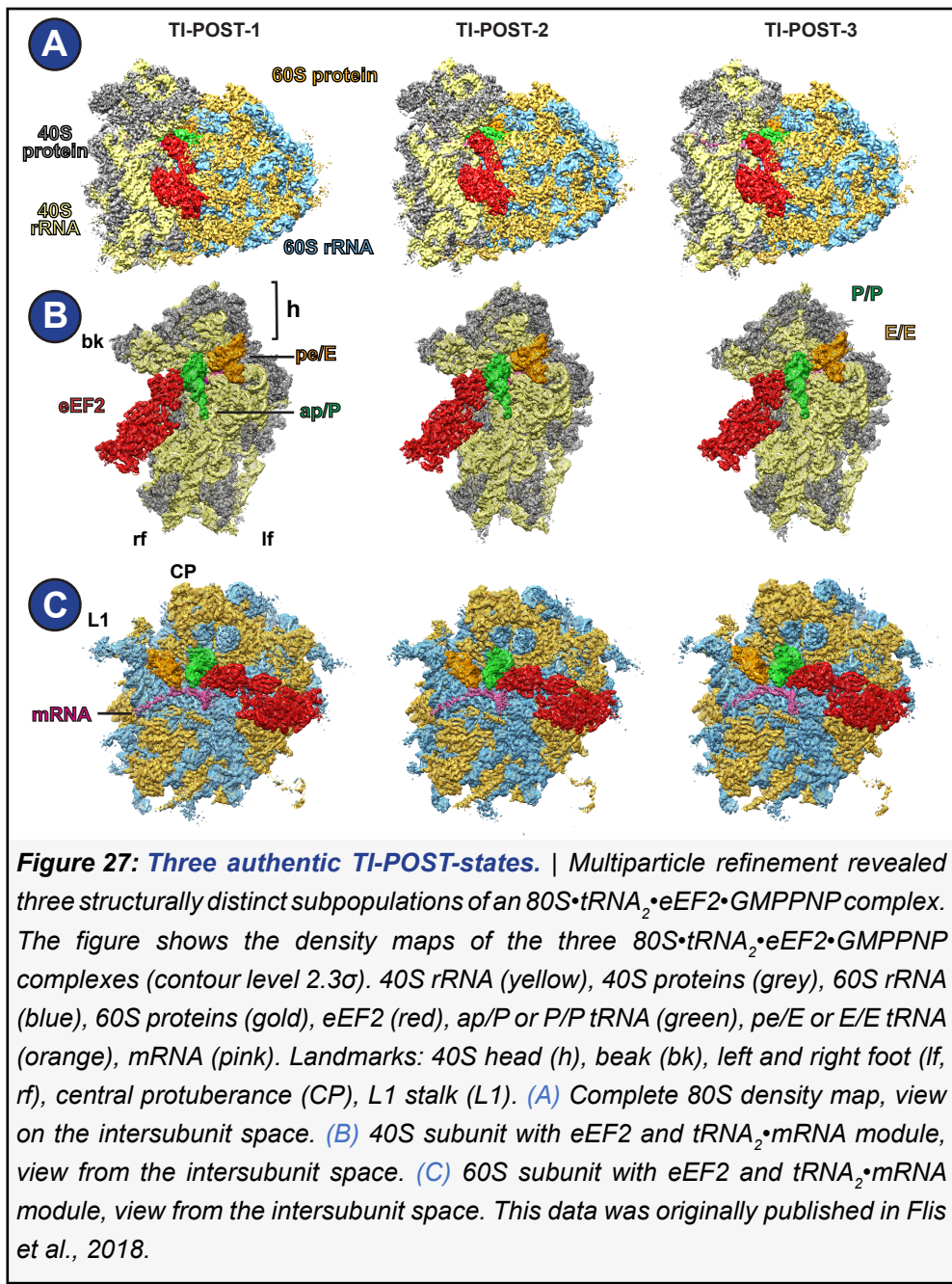
The 80S•tRNA₂•mRNA•eEF2•GMPPNP complex was reconstituted *in vitro* using purified components as described in the methods section (4.4). In total, four high-resolution datasets had been imaged from (multiple preparations of) this sample and processed. In the first three, insufficient sample and/or micrograph quality prevented the reconstruction of volumes with sufficient resolution. Combination of datasets did not improve the map quality (data not shown).

For the fourth dataset, after preparation of the grids, 417 micrographs imaged with a Spirit Tecnai microscope and F416 camera (Tietz) were used for screening at intermediate resolution. *In silico* sorting (Frank et al., 1996; Loerke et al., 2010) revealed that a majority of particle images yielded a population containing eEF2 and two tRNAs. This result confirmed that the sample qualified for high resolution imaging. In total 5,261 micrographs were collected using a Polara microscope equipped with a K2 Summit camera (Gatan) in superresolution mode. Out of those, 4097 micrographs were further used for manual screening and particle picking, resulting in 445,131 particle images. After autopicking, 274,077 particle images remained and were used for SPIDER multiparticle refinement and sorting (Frank et al., 1996; Loerke et al., 2010).

As expected, the dataset first split into a “junk” and a ribosomal population. The latter was isolated and after further rounds split according to the absence/presence of the peptidyl tRNA. Focused reassignment using a mask on eEF2 and/or the 40S head revealed three different 80S structures containing eEF2•GMPPNP and a complete mRNA•tRNA₂ module (**Figure 27**, **Figure 28A**).

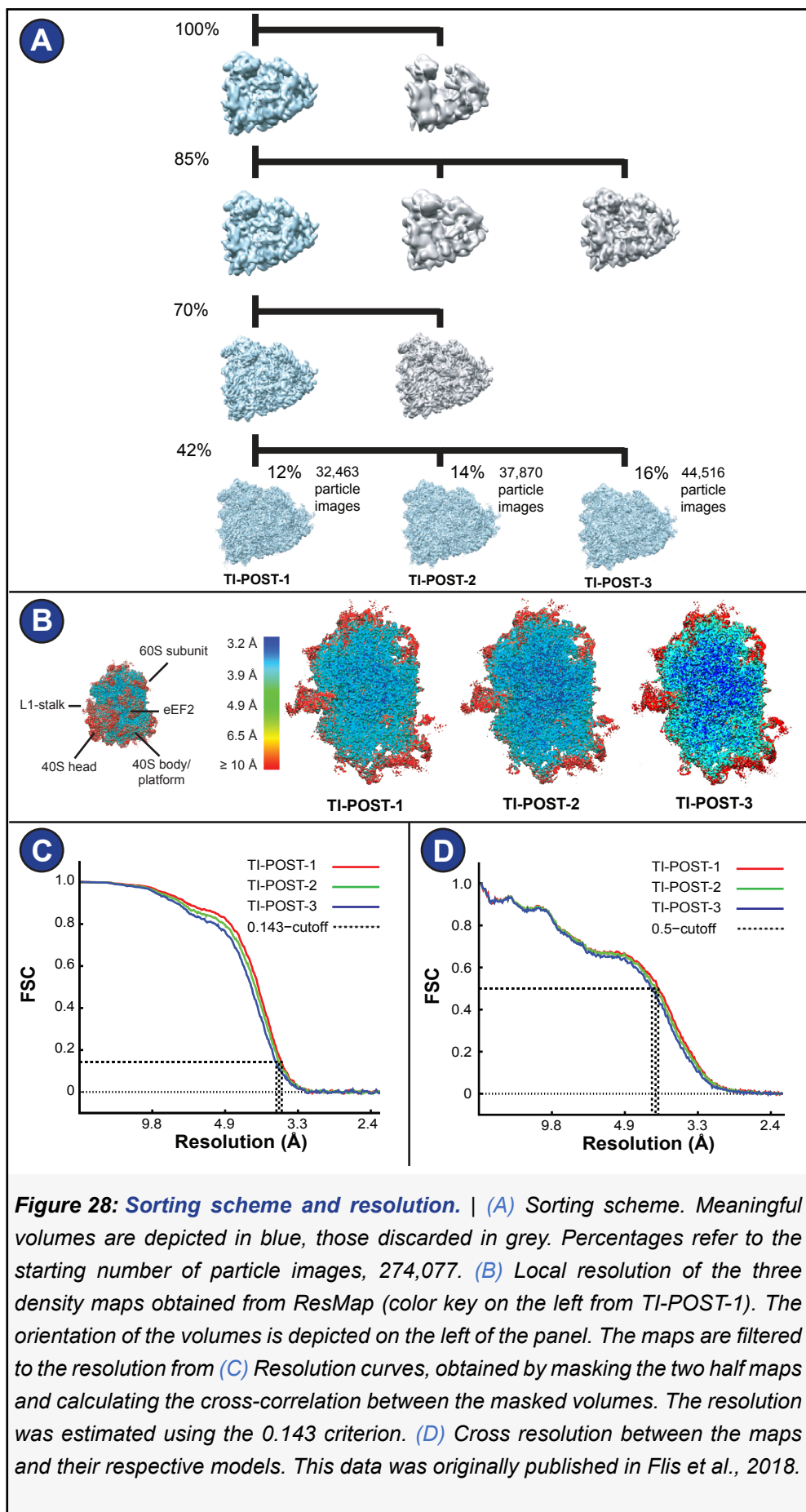
The three 80S structures differ in conformation and can be arranged in a sequence based on comparison of the respective structures with the final POST state (Behrmann et al., 2015). In all three structures, the tRNAs are already translocated with respect to the 60S subunit

5. Results



and the 40S body/platform. Therefore, they reveal the stepwise conformational changes of the ribosome during late steps of tRNA translocation and are termed translocation intermediate (TI)-POST-1, TI-POST-2 and TI-POST-3. Their global resolutions range between 3.5 to 3.6 Å, while the local resolutions reach 3.2 Å in the cores of the ribosomal subunits (**Figure 28B-C**). The resolution was sufficient for building an atomic model for each translocation intermediate with reasonable statistics and good map-to-model correlation (**Figure 28D**).

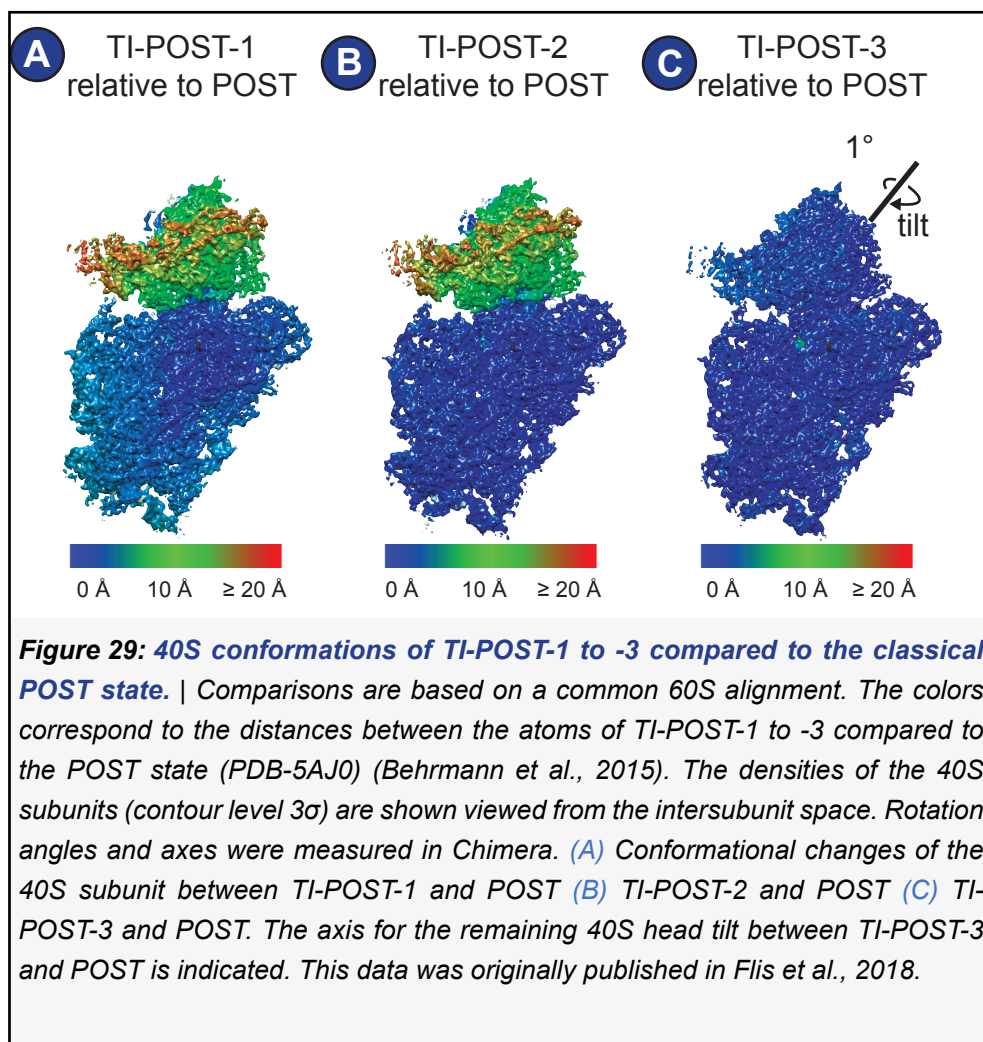
5. Results



5. Results

The captured intermediates are distinguished by 40S body/platform rotation/rolling and 40S head swivel.

In silico separation into the three final TI-POST states was based on large-scale differences in the ribosomal conformation which are of functional importance. The structure representing the earliest translocation intermediate TI-POST-1 is characterized by 4° rotation/rolling of the 40S body/platform (measured relative to the 60S subunit) and a pronounced head swivel of 18° (measured relative to the 40S body/platform) compared to the POST state (Behrmann et al., 2015) (**Figure 29A**). A head swivel had been observed in bacterial translocation intermediates before and the mammalian TI-POST-1 state presumably represents the mammalian equivalent of the bacterial chimeric hybrid state, termed TI-POST (Ramrath et al., 2013; Ratje et al., 2010).

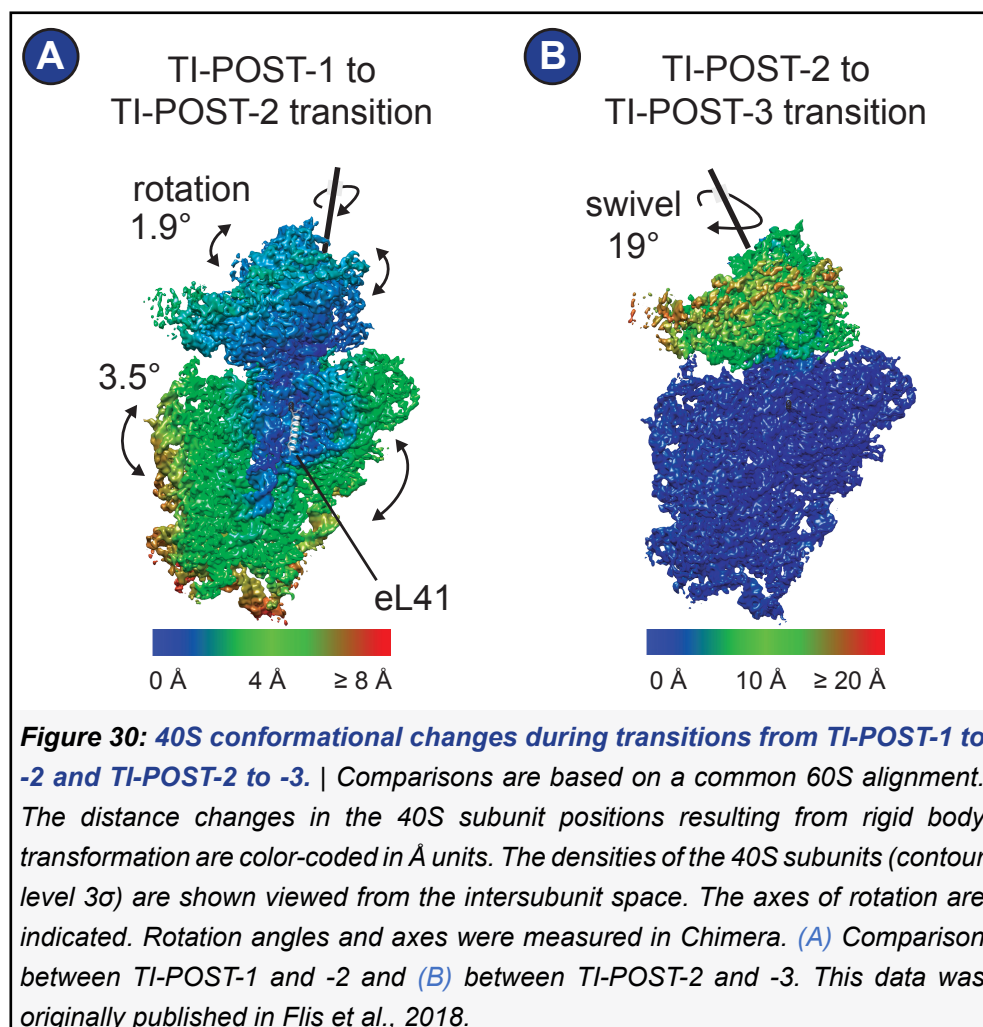


5. Results

The structure that represents the next step in the sequence, TI-POST-2, reveals a 40S body/platform that is almost completely in its canonical – that is classical-POST-like - position, and a 40S head that is swiveled by 19° (**Figure 29B**). Such an intermediate has not been observed in bacteria yet.

The TI-POST-3 state (**Figure 29C**) exhibits the same conformation as the classical POST state except a small residual head-tilt of 1°. Despite the conformational similarity to the classical POST state, the still-bound eEF2 defines TI-POST-3 as translocation intermediate.

In summary, the structures reveal that late translocation steps are dominated by movements of the 40S subunit relative to the 60S subunit, aimed to re-establishing the canonical conformation of the classical POST state: From TI-POST-1, which represents the mammalian equivalent of the bacterial TI-POST state (Ramrath et al.,



5. Results

2013; Ratje et al., 2010; Zhou et al., 2014), the 40S body/platform rotates back and reaches its classical, unrotated position. Notably, the 40S head domain only partially follows back-rotation of the 40S body/platform (1.9° instead of 3.5°) (**Figure 30A**), resulting in an increased 40S head swivel ($\sim 19^\circ$). In the second step, the transition from TI-POST-2 to TI-POST-3 is dominated by 40S head reverse swivel (**Figure 30B**). It takes place after the 40S body/platform is already in its canonical position and transforms the chimeric ap/P, pe/E tRNAs into P/P, E/E tRNAs (see below).

The tRNAs are translocated to their classical positions via a chimeric hybrid state

In TI-POST-1 and TI-POST-2, the tRNAs adopt the chimeric hybrid positions ap/P and pe/E. They are defined by characteristic interactions on the small subunit. For the ap/P tRNA it is the interaction with C1701 (body p-site, *E. coli* C1400) and C1331 (head a-site, *E. coli* C1054) (**Figure 31A-B**). The pe/E tRNA interacts with U1248 (head p-site, *E. coli* G966) and G961 (body e-site, *E. coli* G693) (**Figure 31C-D**).

On the 60S subunit, the acceptor stem CCA end of the ap/P-site tRNA interacts with the P-loop located at the tip of H80 of the 28S rRNA (G4158, G4159, *E. coli* G2251, G2252.) (**Figure 31E**). The CCA-end of the E-site tRNA points towards G4332 and G4333 of Helix 88 and is restrained by ribosomal protein eL42 (**Figure 31F**). Overall, the positions of the CCA ends of the ap/P and the pe/E-site tRNAs in the 60S subunit are very similar to those of the previously observed classical POST state (Behrmann et al., 2015).

In TI-POST-3, the tRNAs are bound in their classical POST-like positions P/P and E/E. On the small subunit, the P/P tRNA position is defined by molecular interaction of tRNA nucleotide A34 with U1248 (head p-site, *E. coli* G966) and C1701 (body p-site, *E. coli* C1400). The E/E tRNA position is defined by molecular interaction

5. Results

of tRNA nucleotide A34 with G961 and the anticodon's proximity to U1056 and U1057 (body E-site) (**Figure 32**). The contacts on the 60S subunit correspond to those observed in TI-POST-1 and TI-POST-2.

The L1-stalk is another element that changes its position in the course of the TI-POST-1 to TI-POST-3 transition. It adopts an “intermediate-1”-like conformation in both TI-POST-1 and TI-POST-2 and contacts

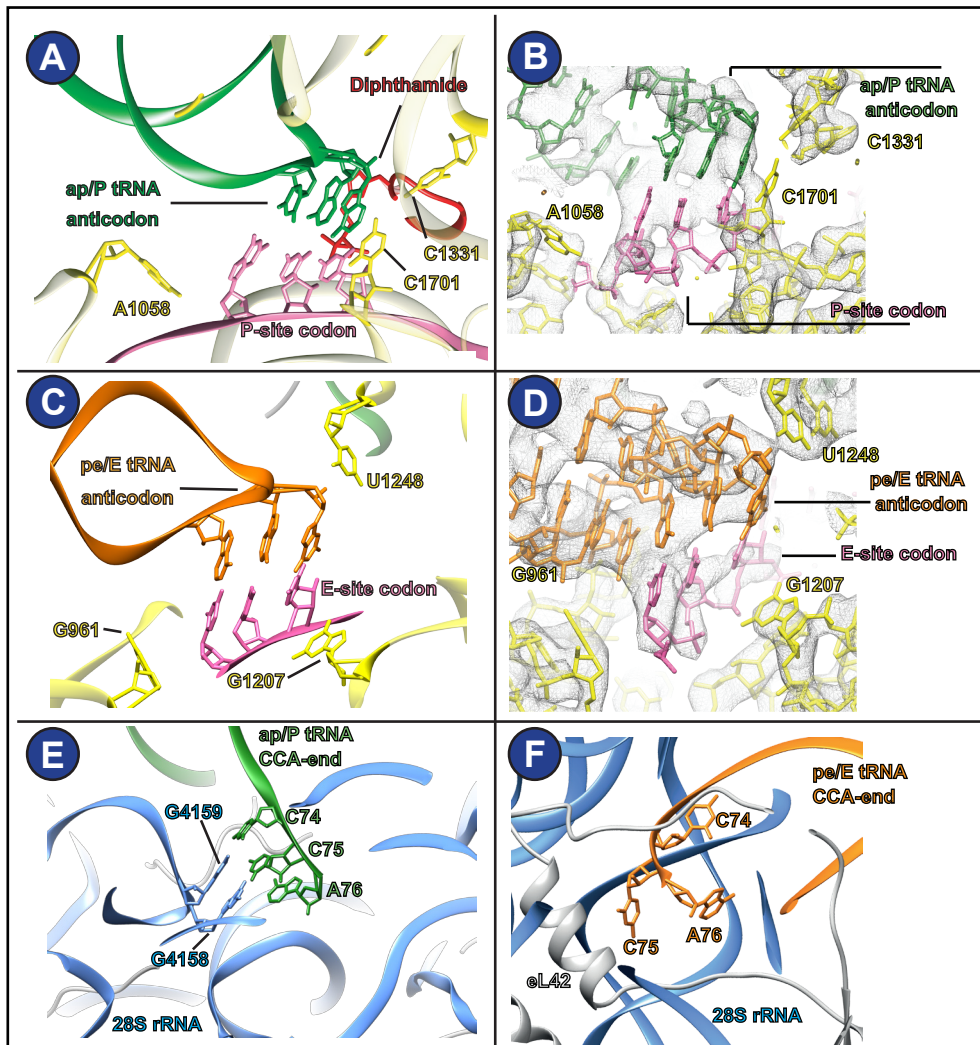
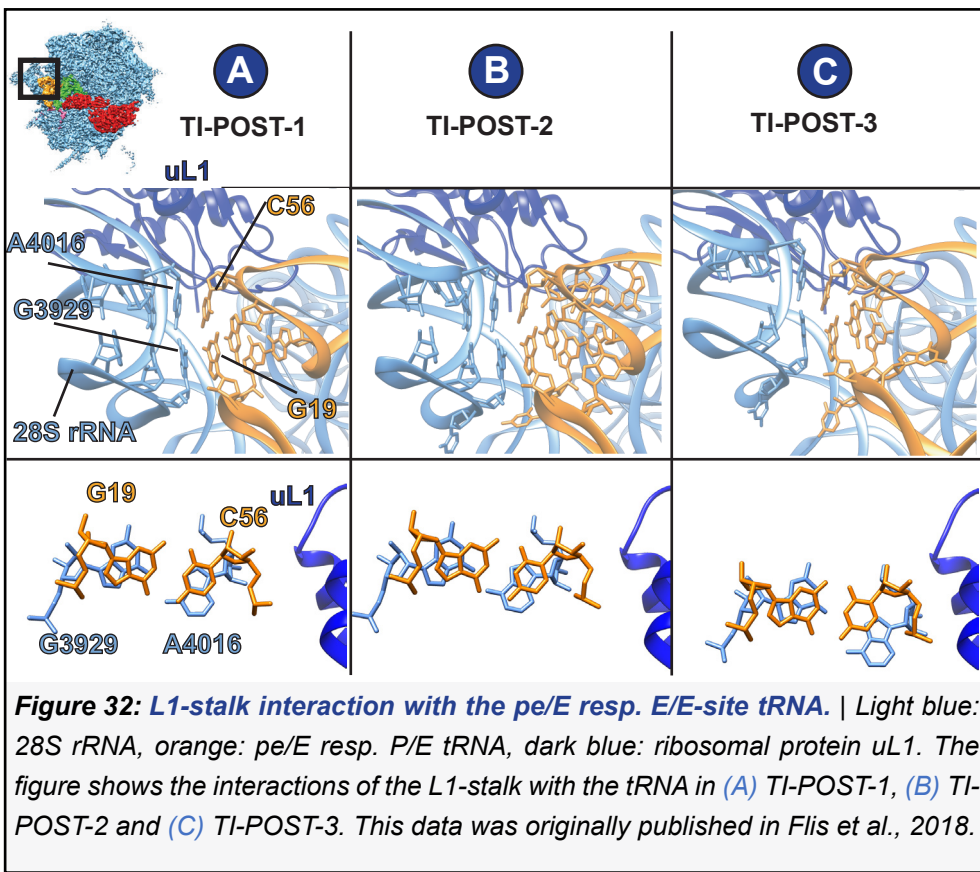
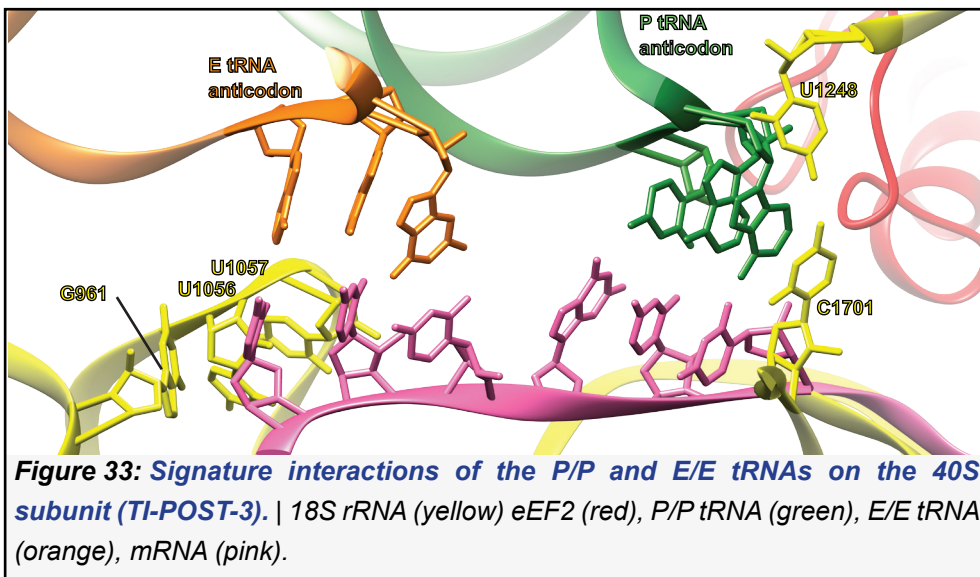


Figure 31: Signature interactions of the chimeric hybrid state tRNAs (TI-POST-1). | 18S rRNA (yellow), 28S rRNA (light blue), eEF2 (red), ap/P or P/E tRNA (green), pe/E or E/E tRNA (orange), mRNA (pink), protein eL41 (grey). (A) ap/P tRNA, codon-anticodon interactions, ribbon depiction. (B) ap/P tRNA, codon-anticodon interactions, atomic model depiction with density (contour level 3σ). (C) pe/E tRNA, codon-anticodon interactions, ribbon depiction. (D) pe/E tRNA, codon-anticodon interactions, atomic model depiction with density (contour level 3σ). (E) The CCA end of the P-site tRNA interacts with the 28S P-loop. (F) The CCA-end of the E-site tRNA is pointing towards H88. The data from A-D was originally published in Flis et al., 2018.

5. Results



the elbow of the pe/E-site tRNA through a stacking interaction between the bases G3929 (*E. coli* G2112) and A4016 (*E. coli* A2169) of the L1-stalk-rRNA with tRNA bases G19 and C56, consistent with what has been observed for bacteria (Mohan and Noller, 2017; Zhou et al., 2013). In TI-POST-3, the L1-stalk adopts an ‘intermediate 2’ position similar to bacterial POST structures (Behrmann et al., 2015; Mohan and Noller, 2017) (**Figure 33**) .



5. Results

The G-domain is in an active conformation

On the 60S subunit, the G-domain of eEF2 is bound to the stalk base (H42, H43, H44, uL11, uL10) and the sarcin ricin loop (SRL; H95 of 28S rRNA) (**Figure 34A**). As expected, the stalk base is stabilized by that interaction and moved towards the ribosomal A site, a conformation consistent with binding of a GTPase.

In all three structures captured, eEF2's G-domain is in the active conformation that renders GTP-hydrolysis possible. Histidine 108 of switch II is pointing towards the SRL and most of switch I is well-resolved, as expected for an active state. Also, complete density for GMPPNP is visible in all three maps, suggesting that it is indeed the non-hydrolysability of GMPPNP that keeps the G-domain in its activated state (**Figure 34B**). The conformation of eEF2's G-domain in the presented GMPPNP-stalled intermediates is consistent with previous structures of EF-G or eEF2 in the GTP-like-bound-state (Connell et al., 2007; Murray et al., 2016; Tourigny et al., 2013) (**Figure 34C**).

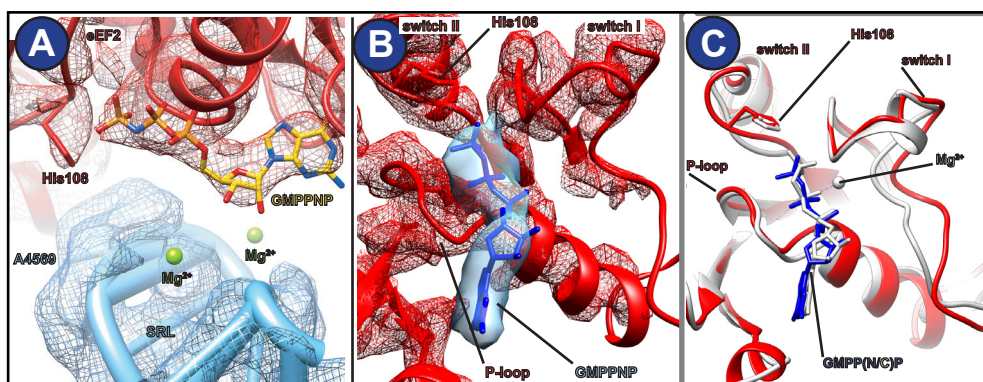


Figure 34: Features of the G-domain of eEF2 in TI-POST-1. | (A) Contacts of eEF2 (red) with the sarcin ricin loop on the 60S (SRL, blue). Histidine 108 (His 108) points to A4569 of the SRL. The red mesh (contour level 4σ) corresponds to the density for eEF2 and GMPPNP. The density for the SRL is shown as blue mesh at contour level 4σ . Density for the magnesium ions is only seen at contour level 2σ and is not depicted here. (B) The G-domain of eEF2 (red) adopts an active conformation. Transparent blue density belongs to the nucleotide, GMPPNP, red mesh depicts density for eEF2 (contour level 3σ). This data was originally published in Flis et al., 2018.

5. Results

Domain 4 of eEF2 protrudes into the A site.

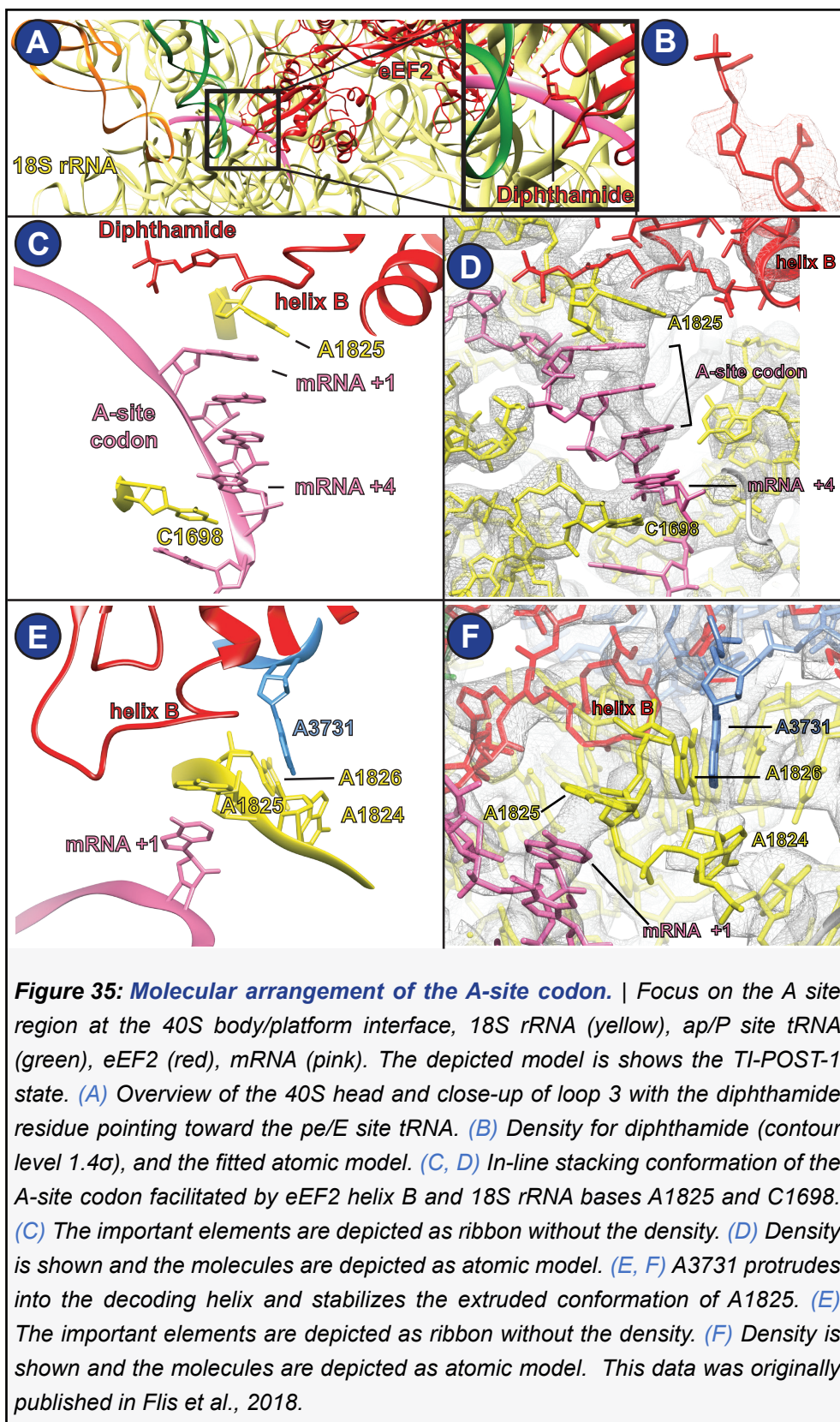
In TI-POST-1 to TI-POST-3, domain 4 of eEF2 reaches into the interface between 40S body/platform and 40S head (**Figure 35A**). As its bacterial counterpart, domain 4 of eEF2 contains 3 loops. In the eukaryotic elongation factor eEF2, loop 3 carries the diphthamide modification on histidine 715. In all three structures we observe that the imidazole ring of the diphthamide packs against the ribose of A36 of the peptidyl-tRNA (**Figure 35A**). The diphthamide residue is not fully visible, but density showing up at low contour level indicates its orientation, reaching to the backbone of the P site codon (**Figure 35B**).

Furthermore, loop 3 of eEF2 protrudes between the P- and A-site codons of the mRNA and from all loops is closest to the P-site tRNA and to 18S rRNA helix h44, which carries the two decoding nucleotides A1824 and A1825 (*E. coli* A1492 and 1493). In order to recognize the binding of an A-site tRNA, both bases flip out from helix 44 to form A-minor interactions with the codon-anticodon duplex at the A-site during decoding (Ogle et al., 2002; Selmer et al., 2006).

In our structures instead, only A1825 extrudes from helix 44 (**Figure 35C-F**). The extruded A1825 is sandwiched between a Glycine-triplet (G717-G719) at the beginning of helix B of eEF2 and the first base of the next mRNA codon that has just been translocated into the A-site. Thus, A1825 serves as the base for a stacking interaction with the downstream codon of the mRNA extending over four bases of the mRNA (mRNA +1 to mRNA +4) and C1698 of the 18S rRNA on the other side (Selmer et al., 2006; Zhou et al., 2013) (**Figure 35C-D**).

Together, those bases form an inline-stacking sextet that is confined by A1825 on one and C1698 on the other side (Selmer et al., 2006; Zhou et al., 2013) (**Figure 35C-D**). The extruded position of A1825 is probably additionally stabilized by A3731 (*E.coli* A1913) of 28S rRNA helix 69, which participates in the formation of bridge B2a and protrudes into the decoding loop, establishing interactions with both the A1824 base and the A1825 ribose (**Figure 35E-F**).

5. Results



5. Results

Changing of the P-gate and subunit back-rolling.

The classification of the obtained structures as late steps of translocation is also apparent when comparing the overall ribosome conformations of TI-POST-1, TI-POST-2 and TI-POST-3 to already known states preceding or following eEF2-catalyzed translocation. The states preceding it are the classical PRE and rotated PRE states (Behrmann et al., 2015) whereas the classical POST state stands at the end of translocation.

For comparison with those states, tRNA models from the classical PRE state (PDB-3J0O) and the rotated PRE state (PDB-3J0Q) (Budkevich et al., 2011) were rigid body fitted in the density maps of the classical PRE state (EMD-2909) and rotated-PRE-2 state (EMD-2905) (Behrmann et al., 2015). For the classical POST-state, a model (PDB-5aj0) was already available and used directly.

During the late events of translocation observed here from the perspective of the 60S subunit, active movement of tRNAs does not play a significant role. Instead, the 40S components move around the tRNA-mRNA module to stepwise re-establish canonical 40S-tRNA contacts. This can be demonstrated by following the movements of the residues A1641 on the 40S head (*E. coli* A1340) and A1058 on the 40S body/platform (*E. coli* A790). Between them, there is the so-called P-gate, a constriction that separates the small subunit P site from the small subunit E site (Schuwirth et al., 2005). Its width is directly associated with intrasubunit motions, and the 40S head swivel and 40S body/platform rotation observed in TI-POST-1 and TI-POST-2 result in its maximal opening of ~28 Å (**Figure 36**).

The process of translocation embodies not only the transportation of the tRNAs but also the transformation from one conformational state to the other. Subunit back-rotation and back-rolling are the main conformational differences that have to take place to convert the PRE- to the POST state. By direct comparison of the conformational changes involved in the transition from the rotated PRE state to the classical PRE state and from the rotated PRE state to the TI-POST-1 state, we could observe that going from the rotated PRE state to

5. Results

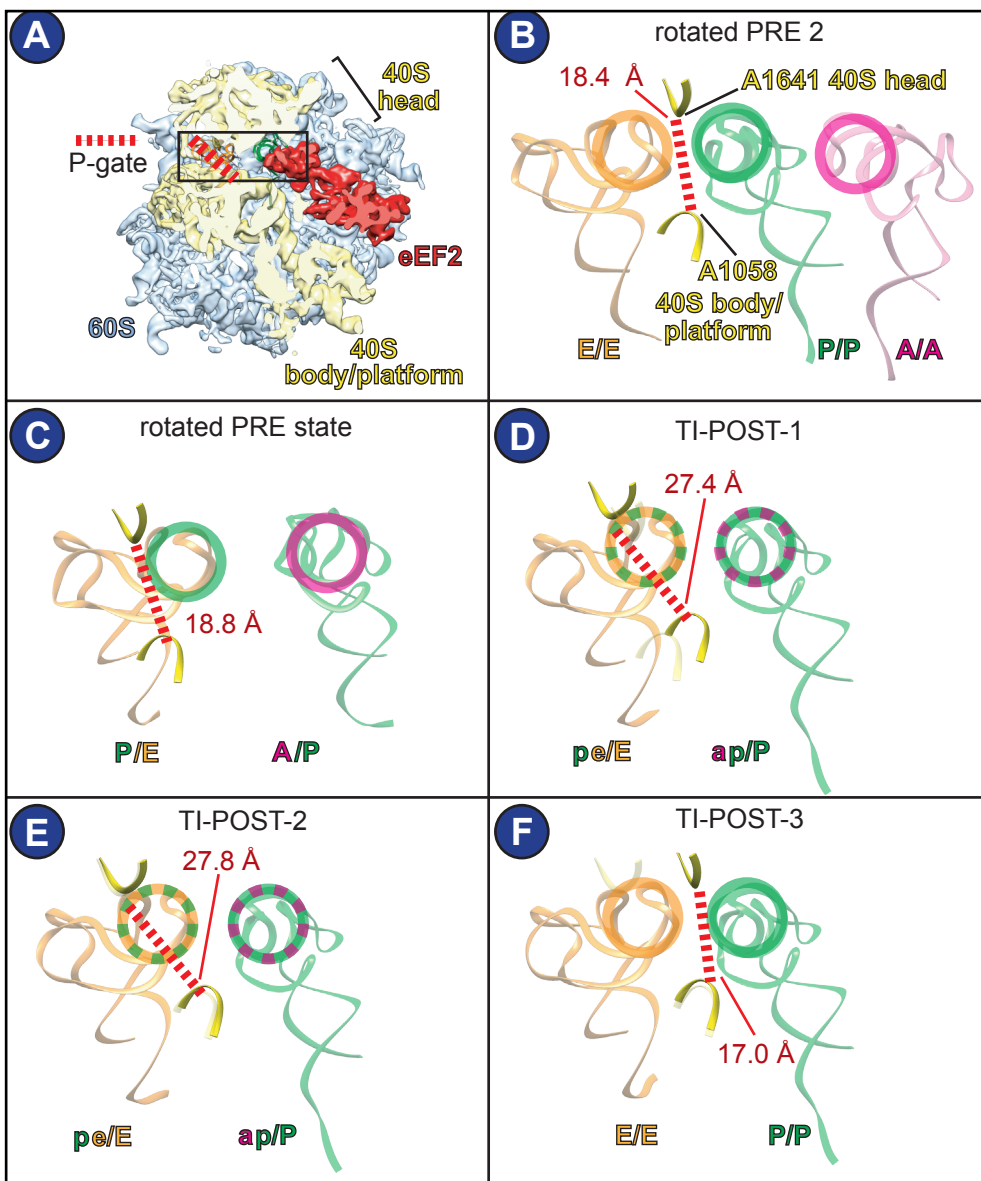
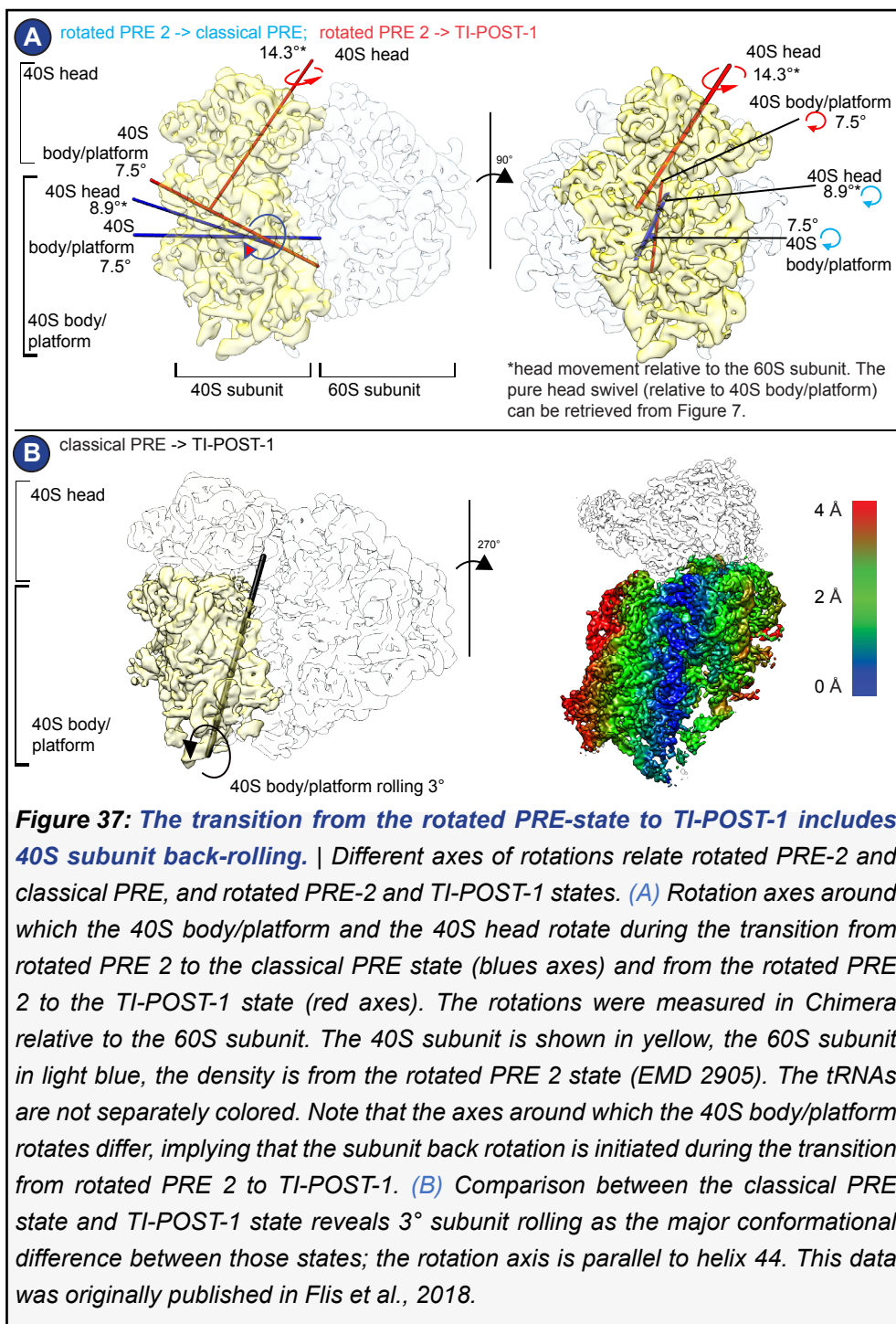


Figure 36: P-gate movement. | **(A)** View on the tRNAs in the 40S body/platform-head interface from the solvent side of the 40S body/platform. The boxed region is the area shown in B-F. Used for this overview was the TI-POST-1 state. The P-gate distance is measured between the phosphates of A1058 and A1641 of the 18S rRNA. **(B)** Classical PRE state (EMD-2909, PDB-3J0O) (Behrmann et al., 2015; Budkevich et al., 2011). The P-gate distance is 18.4 Å. **(C)** The transition to the rotated PRE-2 state (EMD-2905, PDB-3J0Q) (Behrmann et al., 2015; Budkevich et al., 2011) involves the largest tRNA movement from the 60S perspective. The P-gate distance in the rotated PRE state is 18.8 Å. **(D)** In TI-POST-1, the tRNAs are compacted. The P-gate distance is 27.4 Å. **(E)** TI-POST-2. Minimal P-gate and tRNA movements accompany 40S rearrangements. The P-gate distance is 27.8 Å. **(F)** TI-POST-3. Reverse 40S head swivel actively moves the P-gate, allowing the incoming E-site tRNA to complete translocation. The P-gate distance is 17.0 Å. This data was originally published in Flis et al., 2018.

5. Results

TI-POST-1 involves back-rolling of 3° (**Figure 37**). That means that the bound eEF2 impacts the back-rotation of the 40S subunit to take a path that includes back-rolling. The comparison between the classical PRE and classical POST states reveals a total difference of 6° in rolling of the 40S body/platform. Half of the rolling is reversed during early steps of translocation after initial binding of eEF2.



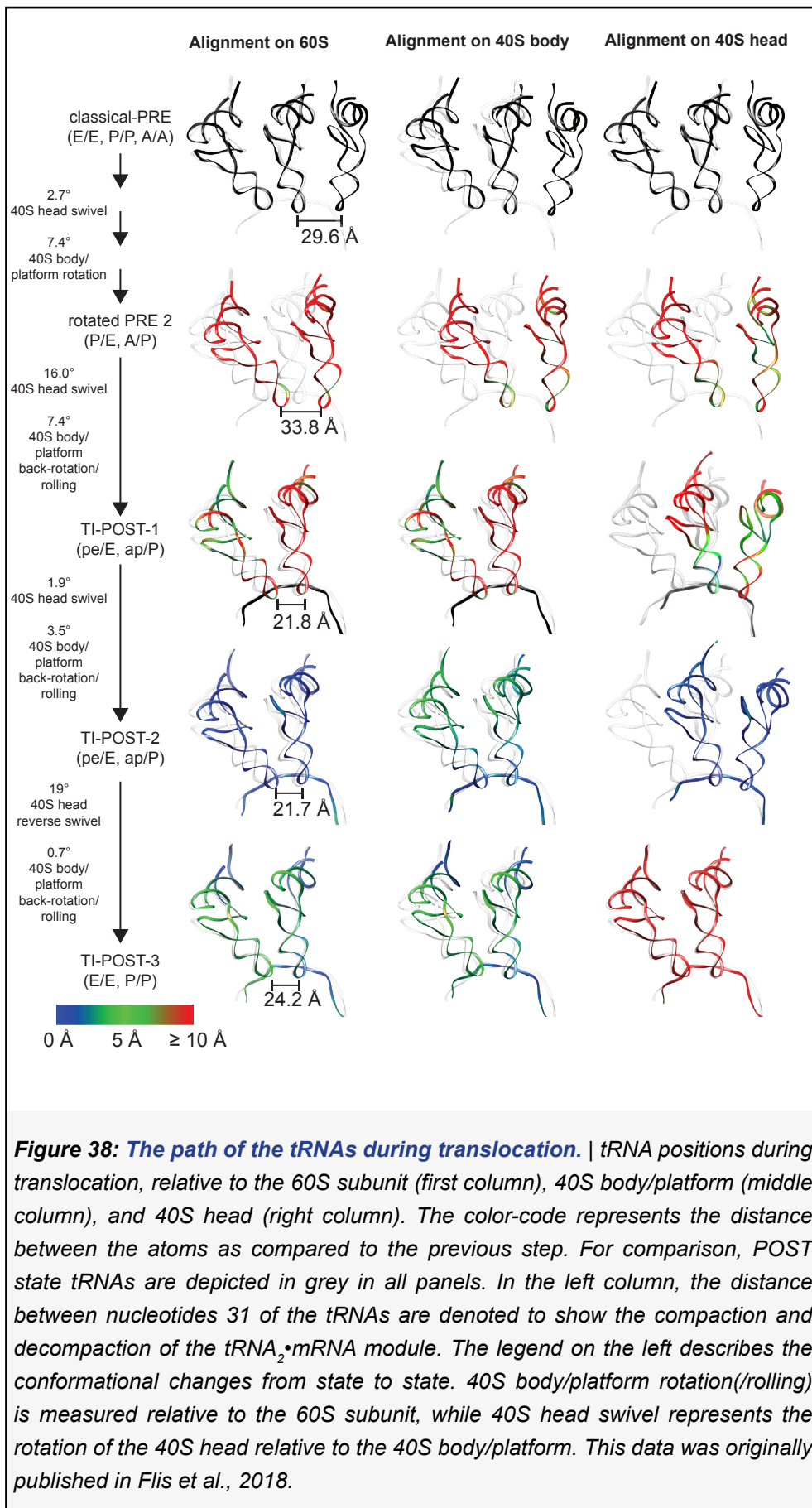
5. Results

The tRNAs move stepwise into a compacted state.

Whereas the movement of the tRNAs with respect to the 60S subunit appears almost negligible in our observed intermediates, the broader context shows that the main tRNA movement relative to the 60S subunit movement takes place during the transition from the classical PRE state via the rotated-PRE-2 to the TI-POST-1 state (**Figure 38**). Transition of the tRNAs from their hybrid to chimeric hybrid positions entail a compaction that reduces the tRNA-tRNA distance (measured at the tRNA nucleotides 31) by 12 Å. In TI-POST-1 and TI-POST-2, this compacted conformation is kept, and only when reaching TI-POST-3, there is a slight decompaction by 2.5 Å.

The usage of additional reference frames for visualization of tRNA movement helps to understand the stepwise character of translocation: from the perspective of the 40S body/platform, the tRNAs have still a large way to go until reaching their final positions coming from the rotated PRE-2 state. It is the 40S body/platform back-rotation/rolling that is the decisive conformational change in translocation on the 40S body/platform. From the perspective of the 40S head, the tRNAs only move in the very last step, the transition from TI-POST-2 to TI-POST-3 that is characterized by head reverse-swivel, to reach their final positions (**Figure 38**).

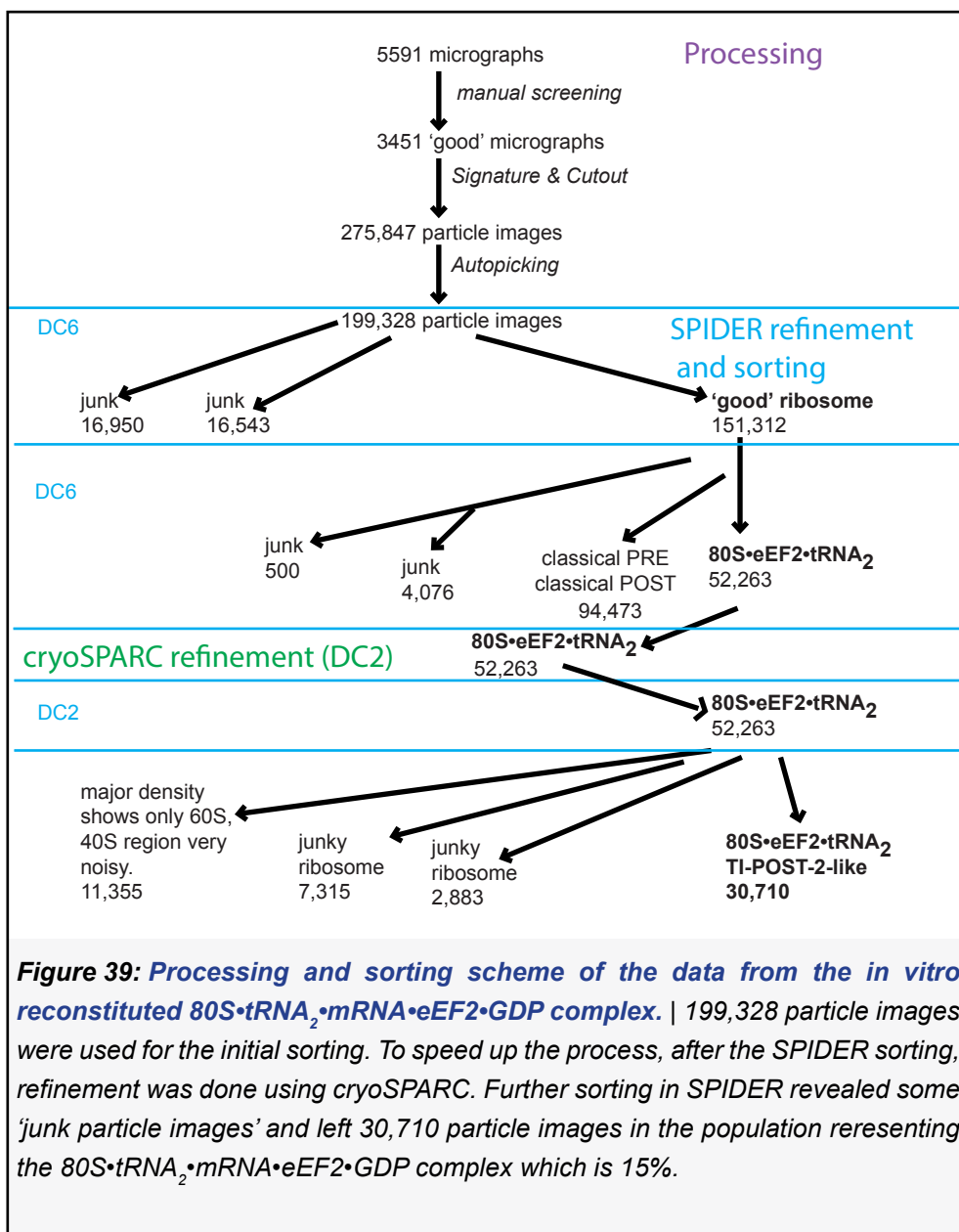
5. Results



5. Results

5.2 *In vitro* translocation with eEF2•GTP leads to a eEF2-binding subpopulation.

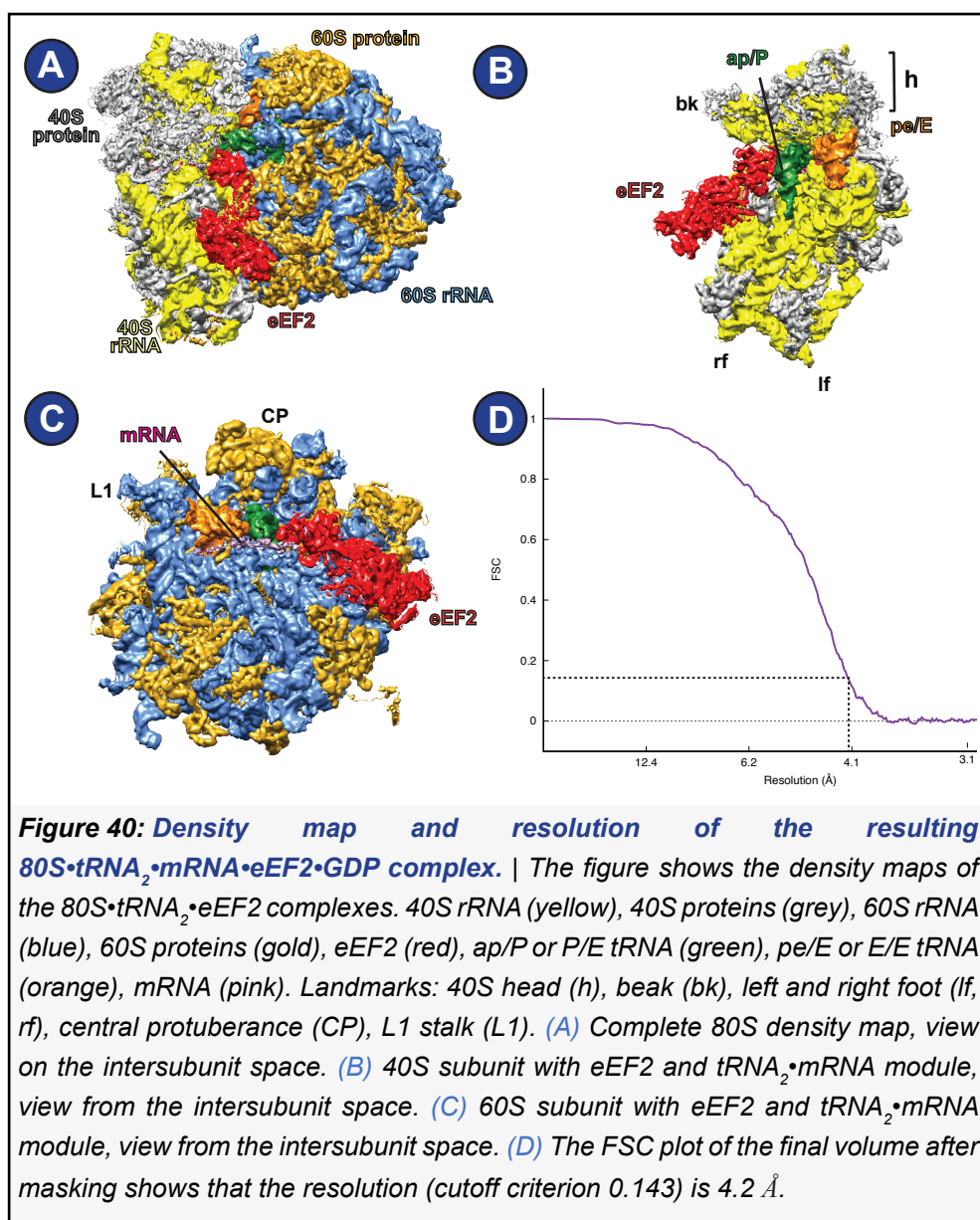
In a previous work, it was observed that when rabbit 80S ribosomal POST-complexes were *in vitro* reconstituted by translocating PRE complexes using eEF2•GTP, a subpopulation was found to bind eEF2 while containing a complete tRNA₂•mRNA module (Budkevich et al., 2014). To investigate this complex with the current improved hardware, the complex was reconstituted *in vitro* as in (Budkevich et al., 2014) and imaged. Low-resolution screening on a Tecnai



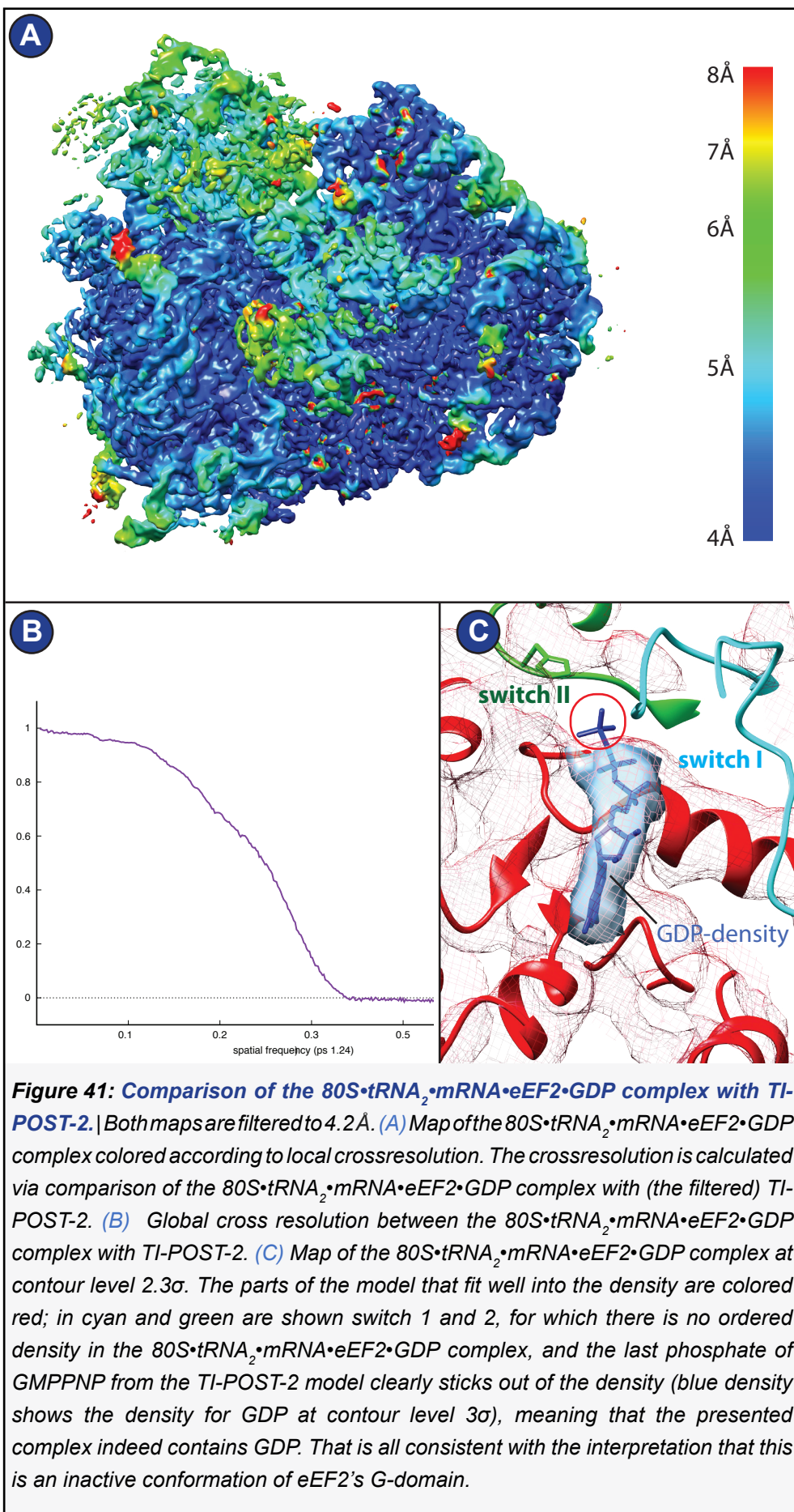
5. Results

Spirit microscope equipped with a Tietz F416 camera revealed the presence of an 80S•tRNA₂•mRNA•eEF2 complex, and high-resolution images were taken on a Polara microscope equipped with a K2 Gatan camera in superresolution mode and further processed as summarized in (**Figure 39**).

The final volume, a rabbit 80S ribosome containing eEF2 and two tRNAs reached a resolution of 4.2 Å (**Figure 40**). Comparison with the structures stalled with GMPPNP (TI-POST-1, 2, 3), shows that it adopts a very similar conformation to TI-POST-2 (**Figure 41A-B**), that is a classical, unrotated 40S body/platform and swiveled 40S head, and the two tRNAs occupying chimeric hybrid positions. The



5. Results



5. Results

40S head is quite poorly resolved compared to the remaining map and shows the least congruence with GMPPNP-stalled TI-POST-2, and most likely there is still variability in this region. However, further sorting, even using a 40S head mask, did not yield any new population, most probably because of the already small number of particle images in this final population (**Figure 39**).

Not only the conformation of the ribosome, but also the position and conformation of eEF2 is hardly different from GMPPNP-stalled TI-POST-2 (**Figure 41A**).

Although the resolution of the final structure is not very high, an important observation on the molecular level can be made to characterize it and reveal an important functional difference to TI-POST-2: The G-domain is not in an active conformation, as in the case of the complexes stalled with GMPPNP. Instead, eEF2 binds GDP and switch 1 and switch 2 are disordered (**Figure 41C**). This is consistent with an inactive conformation of the G-domain.

5. Results

5.3 Intermediates of actively translating polysomes.

Sample preparation and analysis of polysomes

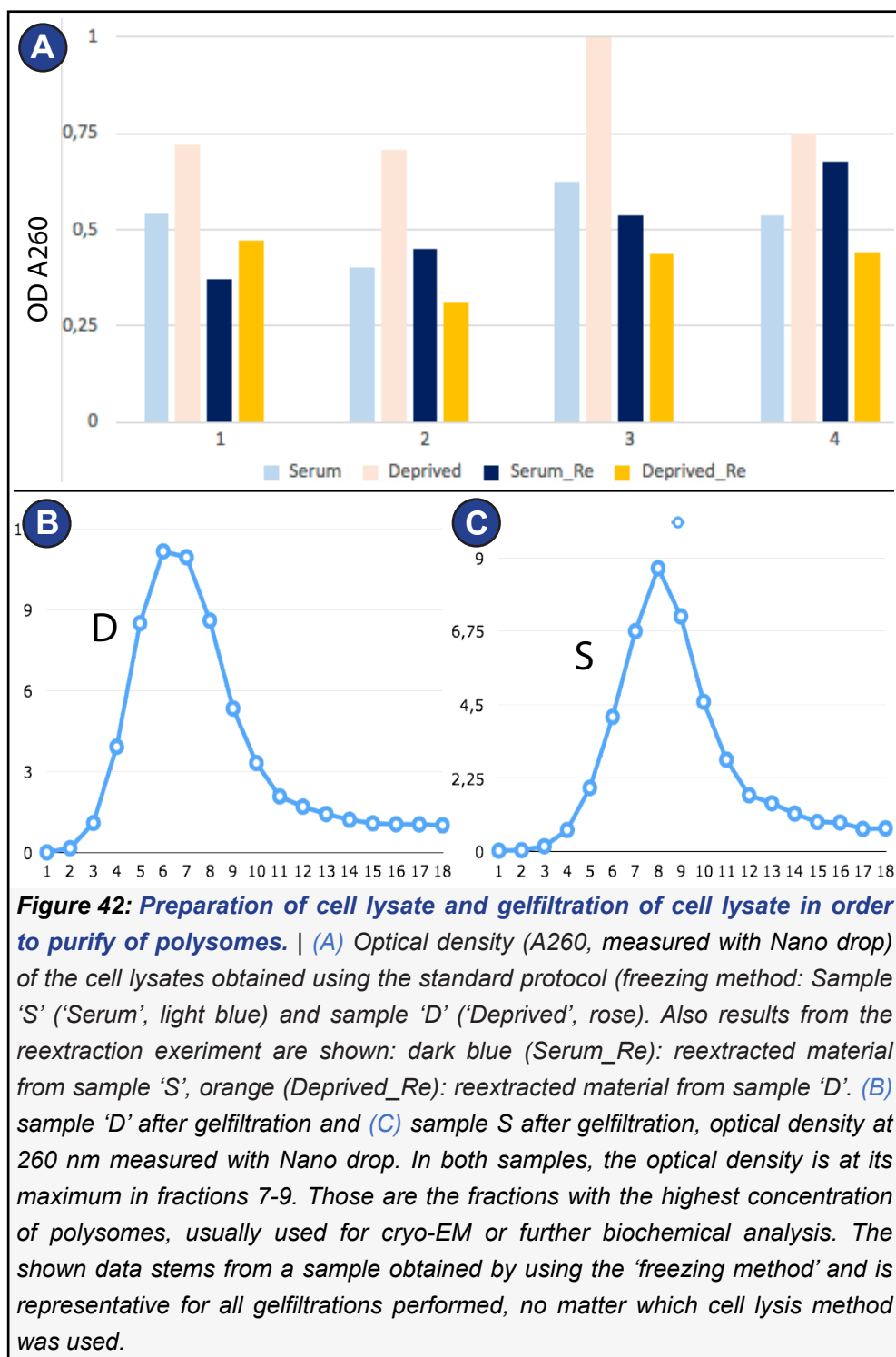
HEK 293T cells were treated in the way described in section 4 (methods). Restimulation of HEK cells with serum for 30 minutes has been shown to be optimal for reaching a maximal phosphorylation of eS6 (Hutchinson et al., 2011), thus, the duration of 30 minutes was chosen for this project because of its effect on eS6 phosphorylation and to see if there is a change detectable in the energy landscape, possibly associated with a changing degree of eS6 phosphorylation.

The procedure resulted in HEK-cell cohorts that were either solely serum-deprived ('D') or 30 minutes restimulated after serum-deprivation ('S'). Interestingly, the optical density at A260 from the sample from serum-deprived HEK-cells was consistently higher than of the sample from serum-restimulated HEK-cells (**Figure 42A**) shows typical yields from the freezing method approach, each of the four experiments shown contains cell lysate from five 720 ml flasks with initially 8×10^4 cells). A reextraction experiment using permeabilization buffer with 2% digitonin revealed an inverse behaviour of the reextracted material in three of four tested cases (**Figure 42A**).

Gel filtration of the cell lysate with continuous measurement of the optical density at 260 nm resulted in the expected peaks containing polysomes. Measurement of the optical density at 260 nm of fractions collected from the peak confirmed the fractions with the highest concentration (**Figure 42B-C**).

The fractions were also analyzed via western blot using antibodies specific against two phosphorylation sites of eS6, anti-P-235/P-236-antibody and anti-P-240/P-244-antibody. Western blot revealed a difference in the signal for eS6-phosphorylation (**Figure 43**), consistent with Hutchinson et al., 2011, where serum treatment had been shown to alter eS6 phosphorylation, while ribosomal protein eS6 being constant.

5. Results



A sucrose gradient of the starting material (after cell lysis) as well as of the peak fractions after the gel filtration showed a similar pattern for sample 'S' and sample 'D' (**Figure 44**). The peak fractions after gel filtration were applied on grids. Negative stain confirmed sample purity and sufficient concentration. Negative stain was also used to evaluate the quality of the alternative 'Freezing method' compared

5. Results

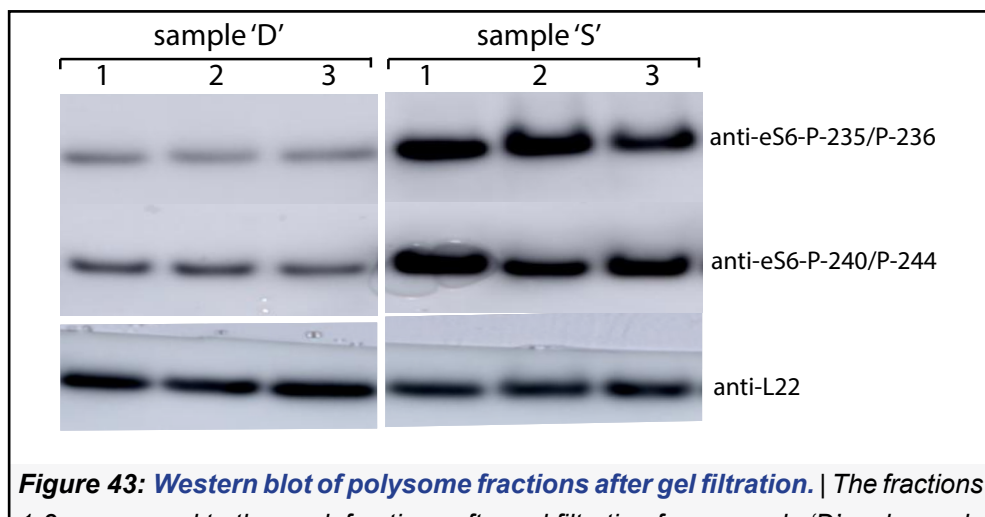


Figure 43: Western blot of polysome fractions after gel filtration. | The fractions 1-3 correspond to the peak fractions after gel filtration from sample 'D' and sample 'S', respectively. Antibodies against two phosphorylation sites (anti-eS6-P-235/236 and anti-eS6-P-240/244) and against L22 (anti-L22, as loading control) were used. The fractions '2' are the ones used for making of the grids and cryo-EM analysis. The Western blot shows that in sample 'D', the signal for eS6 phosphorylation is much less than sample 'S'.

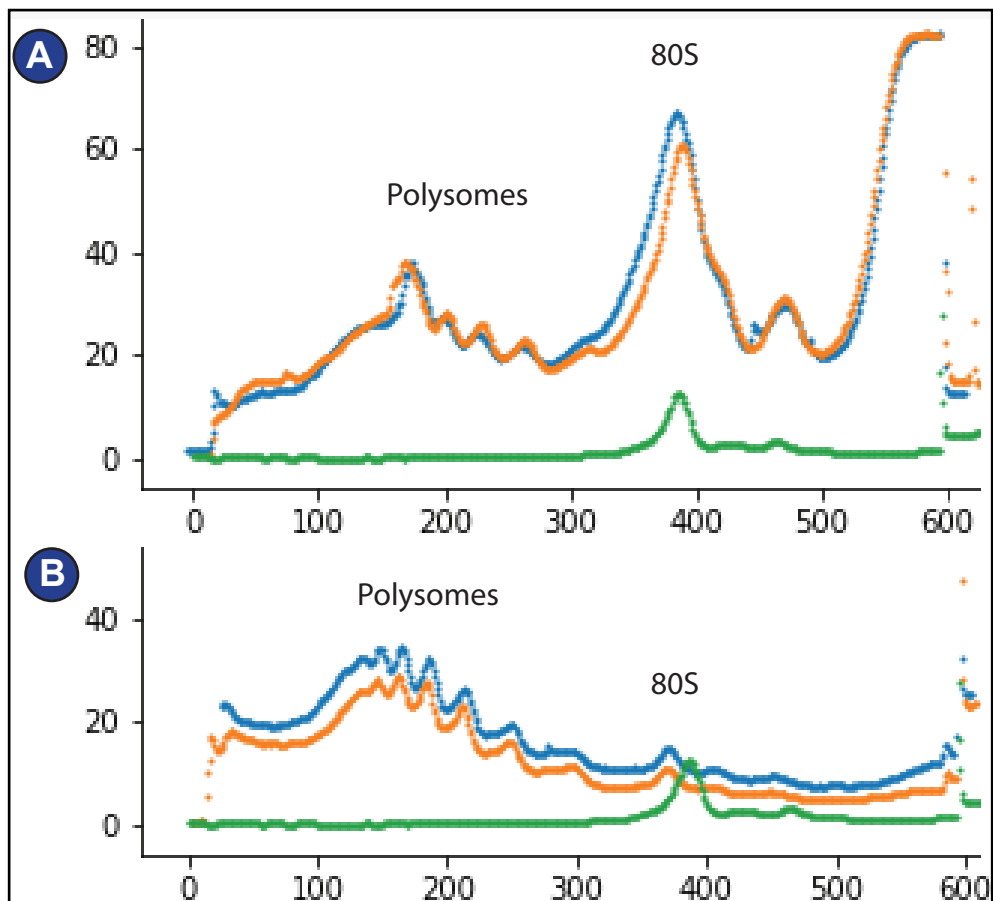


Figure 44: Polysome patterns in sucrose gradients. | Sample from serum-deprived HEK-cells (blue), from serum-deprived and serum-restimulated HEK-cells (orange), 80S monosomes (control, green) (A) Start material. (B) Fractions with the highest OD after gelfiltration.

5. Results

to the ‘Amicon filtration method’ (the sample analyzed via Cryo-EM was obtained using the latter method) (**Figure 45**). No significant difference in concentration or purity was observed, and the ‘Freezing method’ was used for most of the following biochemical procedures because of its speed.

Multiple energy barriers control the mammalian elongation cycle.

Intermediate-resolution imaging on a Tecnai Spirit microscope equipped with a Tietz F416 camera and subsequent refinement and sorting confirmed good quality of both sample ‘D’ and sample ‘S’.

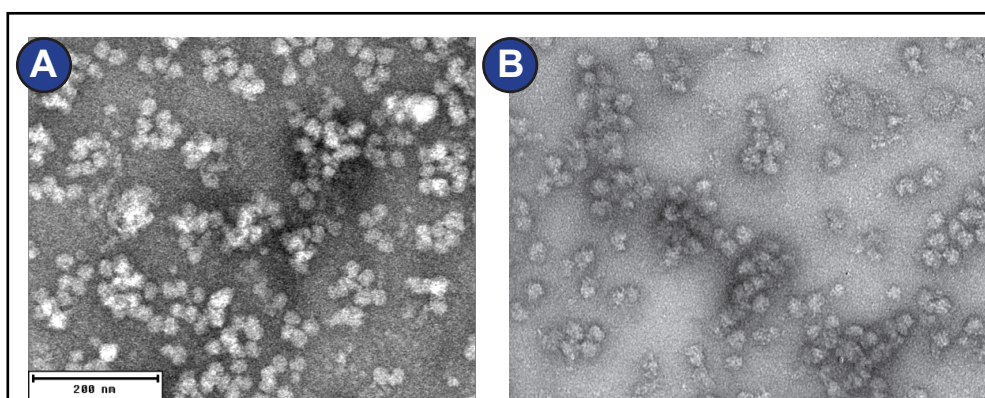
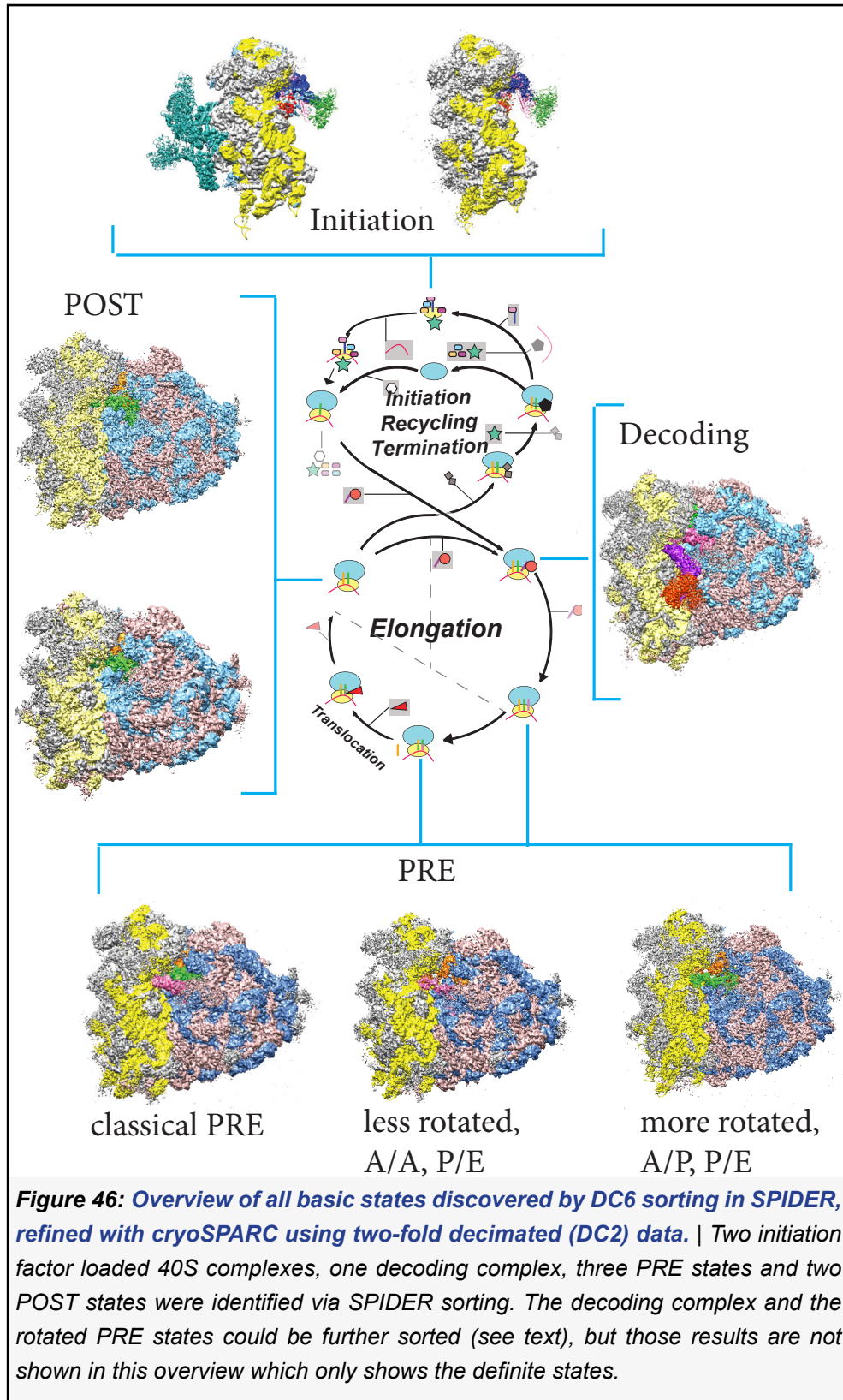


Figure 45: Negative stain images from polysomes. | Both images show negative stain with uranylacetate of a peak fraction after gel filtration from sample ‘D’. (A) Sample that was used for freezing grids and further processing (obtained with ‘amicon method’), imaged with CM100 microscope (Philips) (B) Sample equivalent to (A), but obtained by freezing method, imaged with Morgagni microscope.

Both samples were imaged using a Titan Krios microscope and a K2 Gatan Summit camera in superresolution mode at EMBL, Heidelberg. For the dataset representing sample ‘D’, 5,913 out of 6,008 collected micrographs were used, counting in total 390,359 particle images. Of 7,070 micrographs collected in case of sample ‘S’, 7,021 were processed and resulted in 295,127 particle images. Because particle picking with Gautomatch and Signature (Chen and Grigorieff, 2007) did not lead to the desired result, the particle images were picked manually in e2boxer (Tang et al., 2007).

5. Results

In total eight intermediates of translation were identified by sorting six-fold decimated (DC6) particle images in both datasets (**Figure 46**). 3D *in silico* sorting followed a hierarchical scheme in which first, the 80S particle images had to be separated from the particle images



5. Results

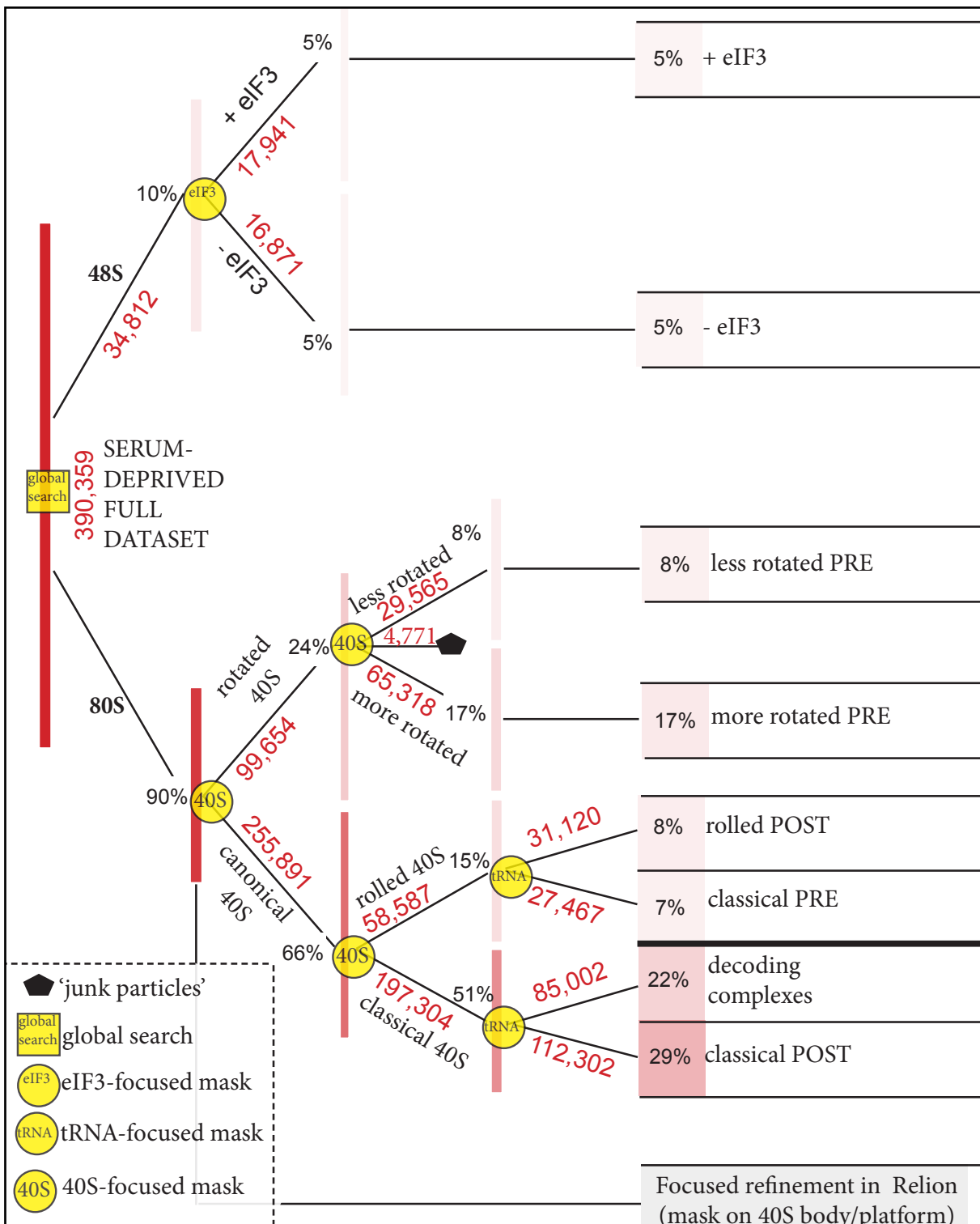
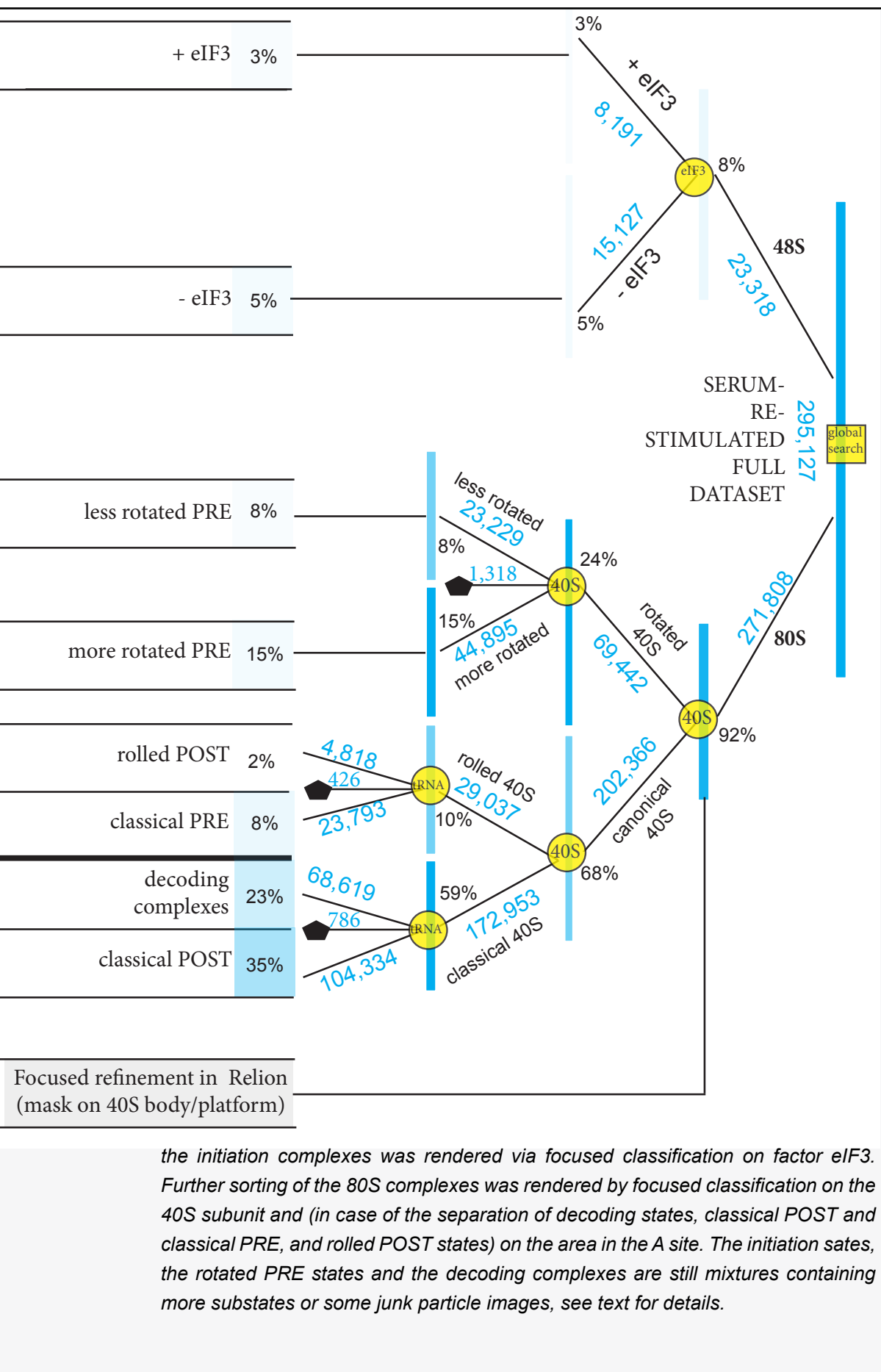
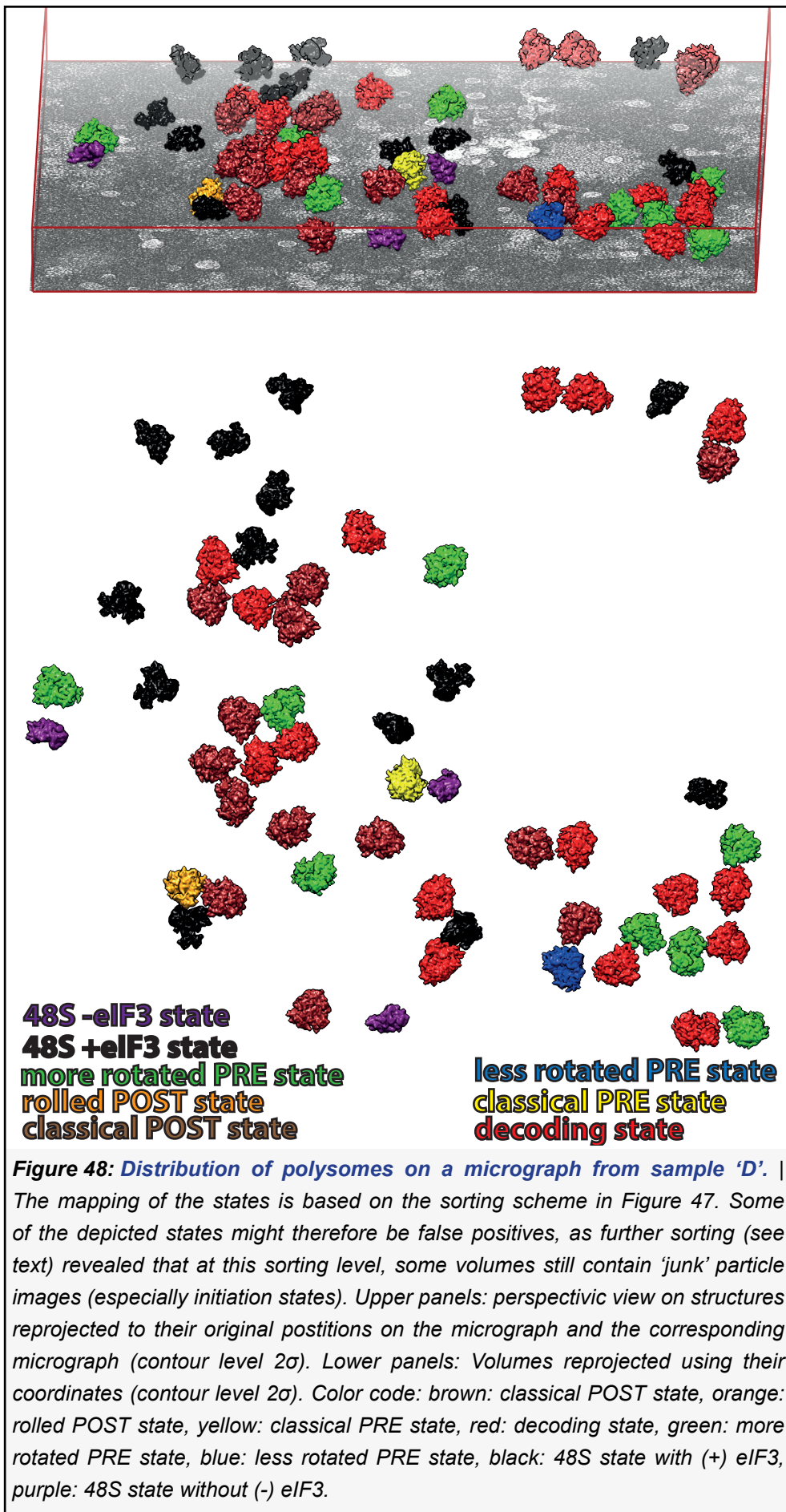


Figure 47: Sorting scheme for both datasets. | Sorting in SPIDER, sample 'D', left, and sample 'S', right. The first step was the separation of 48S and 80S via a global search, using the 40S subunit as orientation structure on which the resulting volumes were aligned after each round. All 80S particle images were additionally used for a focused refinement in Relion (bottom line). As initial references, the 80S structure from CryoSpac homogeneous refinement and the structure from the ab initio refinement (using selected 40S 2D classes) were applied. Further sorting of

5. Results



5. Results



5. Results

representing small subunits, found by 2D classification. Next, the 80S particle images could be further separated into several classes by repeated focused classification using a 40S subunit mask and isolation of the resulting classes (**Figure 47**).

The identified structures can be grouped into four functional classes: Initiation states, decoding state, PRE states, POST-states (**Figure 46**). Reprojection of the states to their original position on the micrograph reveals that the ribosomes are part of polysome groups, meaning they are on the same mRNA (**Figure 48**).

The group of *initiation states* (around 5% after initial classification, but further sorting at DC6 level suggests a smaller number of about 3%) contains two 48S structures, one with and one without initiation factor eIF3. Both states contain a tRNA bound in the P-site and eIF2 as well as eIF1A (see below).

The decoding process is represented by one structure in both datasets, but further substates were identified by focused classification of three-fold decimated (DC3) data from sample 'D' (see below). Two differently rotated representants of the *hybrid PRE state* were identified in both datasets; similarly to the decoding states, further sorting in sample 'D' revealed further substates in this group (see below). The *POST state* group contains two differently rolled substates.

The comparison between sample 'S' and sample 'D' revealed no difference in the energy landscape of translation. Thus, at least for the cytosolic fraction of polysomes, 30 minutes of serum re-stimulation and the associated increase of phosphorylation of eS6 is neither accompanied by a change in the energy landscape nor with a change of the the polysome pattern as observable via sucrose gradient fractionation.

Focused refinement of the e6 region.

To study possible local structural changes in the neighborhood of the phosphorylation site, the polysome sample preparation includes an overnight serum starvation step to lower eS6 phosphorylation

5. Results

and subsequent 30 minutes serum restimulation to enhance eS6 phosphorylation, a method that has been previously described (Meyuhas, 2008). The goal is to focus on the region surrounding the C-terminus of eS6 and compare the structural changes between highly phosphorylated (serum-starved) and low phosphorylated (serum-restimulated) eS6.

To look at the structure of the C-terminus and the elements surrounding it (expansion segments ES3 and ES6), first, the largest population from the above described translocation intermediates stalled with GMPPNP (TI-POST-3) was analyzed by focused classification in SPIDER using a mask on the C-terminus of eS6. It revealed two sub states of TI-POST-3 distinguished by differences

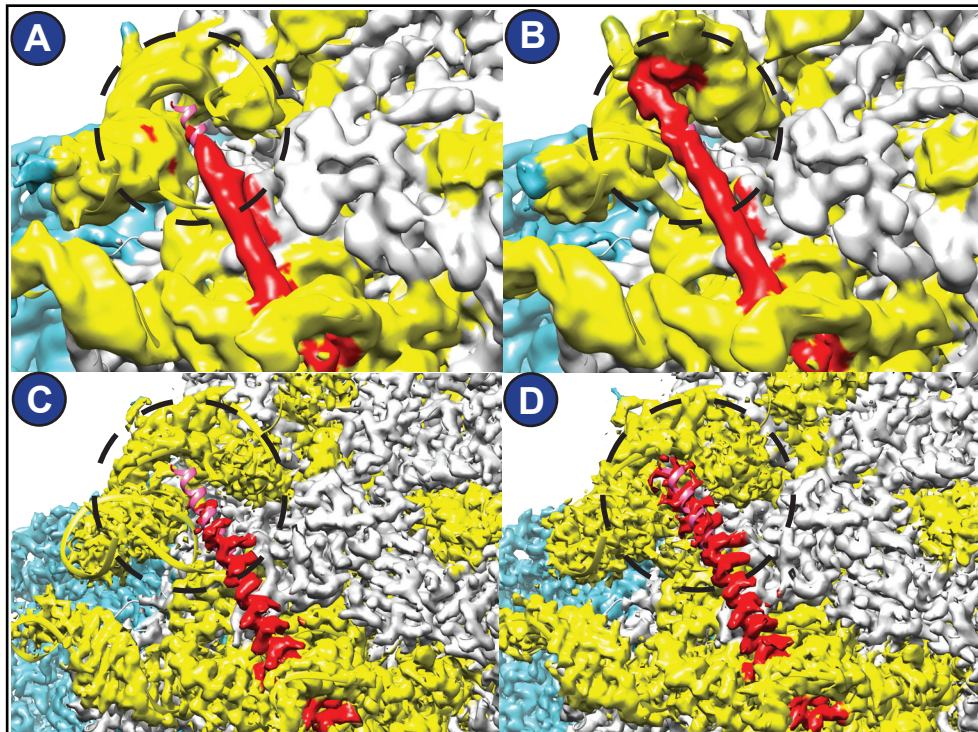


Figure 49: Focus on the eS6 region in three different samples. | Zoom on the region of the eS6 C-terminus on the 40S body/platform. Grey: 40S ribosomal proteins, yellow: 18S rRNA, blue: proteins and rRNA of the large subunit, red: ribosomal protein eS6 (in the figures only the terminal alpha-helix is visible), pink: fitted PDB model of eS6 (PDB-5aj0, Behrmann et al., 2015). The black circles help to see the difference. (A) First substate from TI-POST-3, contour level 2.5σ . (B) Second substate from TI-POST-3, contour level 2.5σ . (C) Volume for sample 'S' obtained by RELION focused refinement on the 40S body/platform, contour level 0.5σ . (D) Volume for sample 'D' obtained by RELION focused refinement on the 40S body/platform, contour level 0.5σ .

5. Results

in the region surrounding eS6; the C-terminus of eS6 differed in length, further, the definition of expansion segment ES6B is different (**Figure 49A-B**).

To inspect the structure of the C-terminus and the elements surrounding it in the polysome datasets, a refinement of all particle images belonging to the 80S class was run in Relion with a focus on the 40S body/platform. That means that all particles were realigned on the structure contained in a 40S body/platform mask. The comparison between the resulting structures of sample D and sample S revealed a similar difference in the length of the C-terminal alphahelix of eS6, but no difference in the eS6 C-terminus containing the phosphorylatable serines nor in the structure of the surrounding rRNA helices (**Figure 49C-D**). Neither structure revealed the structure of the part of the C-terminus of eS6 where the phosphorylatable serines are located, and neither map extends beyond the already modeled part of eS6 from the human 80S model (PDB-5aj0, Behrmann et al., 2015) (until residue 232, compare Figure 14).

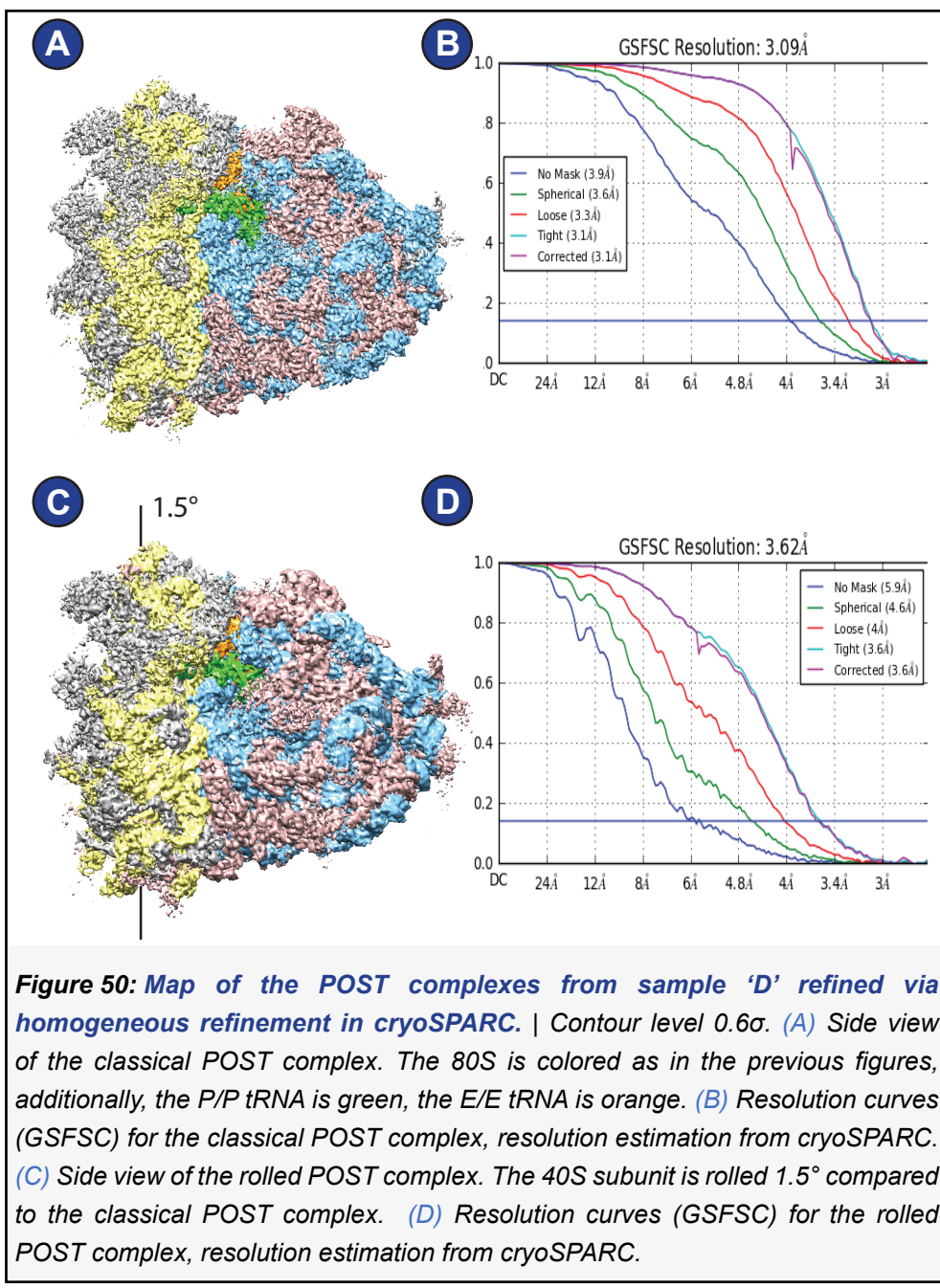
Thus, the difference in phosphorylation seen in the western blot does not translate in obvious structural changes that are visible in the refined structures. However, to study the eS6 region more in depth, one could perform a focused classification (as done for TI-POST-3) using the structures refined in RELION. Maybe this would reveal subpopulations that show a different conformation in the eS6 region.

High-resolution insights into the elongation cycle

For the polysome dataset from sample 'D', the structures resulting from sorting particle images at DC6 level were further processed to higher resolution using two-fold-decimated data (DC2) and analyzed.

The POST complex group (37%) contained a classical POST state and a state in which the 40S subunit was rolled by 1.5° (rolled POST state) (**Figure 50A, C**). The classical POST state is the structure with

5. Results



the best resolution: the FSC at 0.143 (gold standard FSC (GFSC) using half maps masked with a loose mask is estimated to 3.3 Å in sample 'D' (**Figure 50B**).

31-32% of the particle images in both datasets belong to PRE complexes (**Figure 51**). Further SPIDER sorting of sample 'D' particle imaged at DC6 level using a mask on the tRNA revealed in total five different substates of PRE states . Previously, the PRE-state was found to be either non-rotated (classical PRE) or rotated with A/A, P/E (rotated-PRE-1) or A/P, P/E tRNAs (rotated PRE-2) (Behrmann et

5. Results

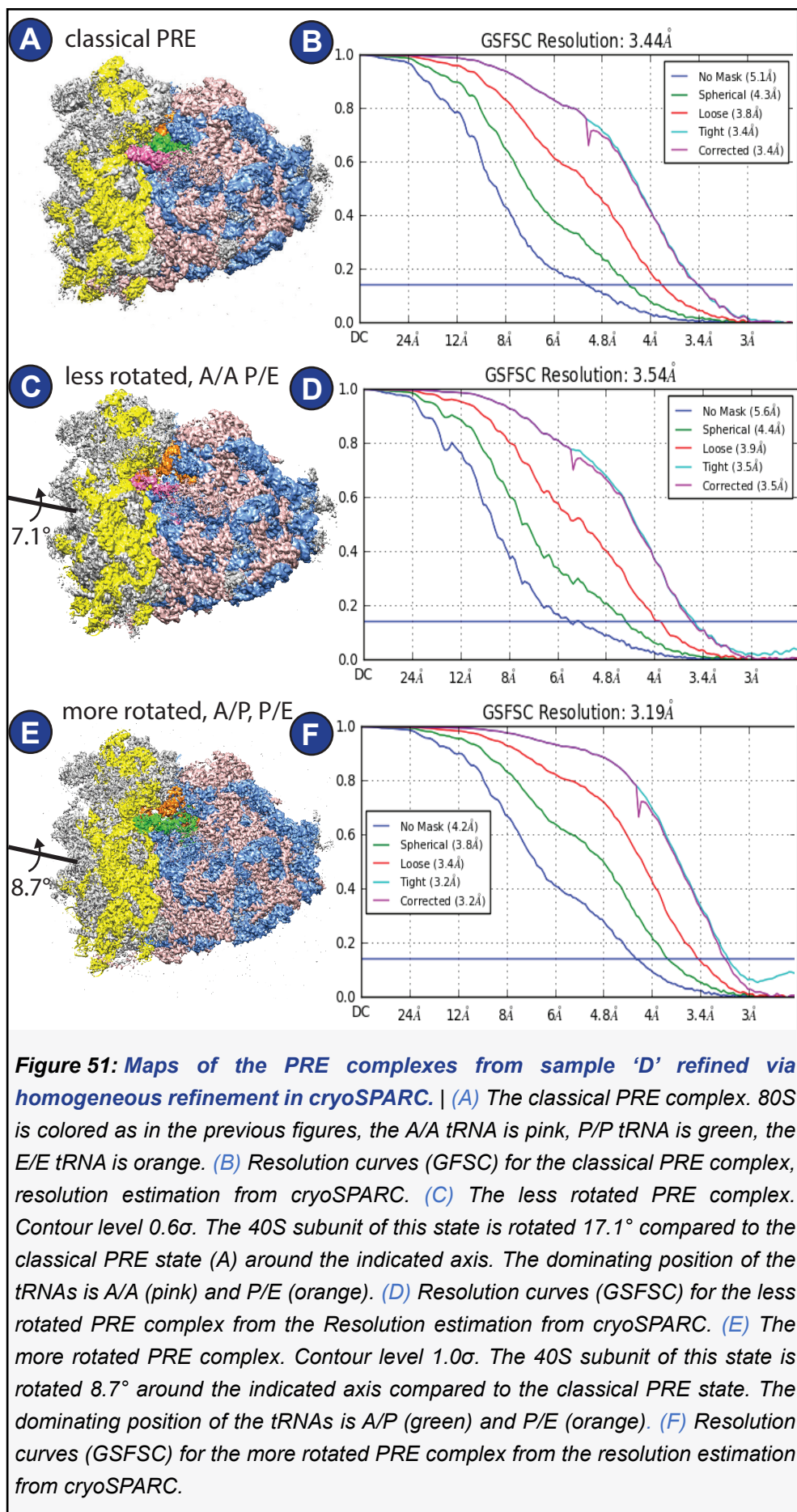
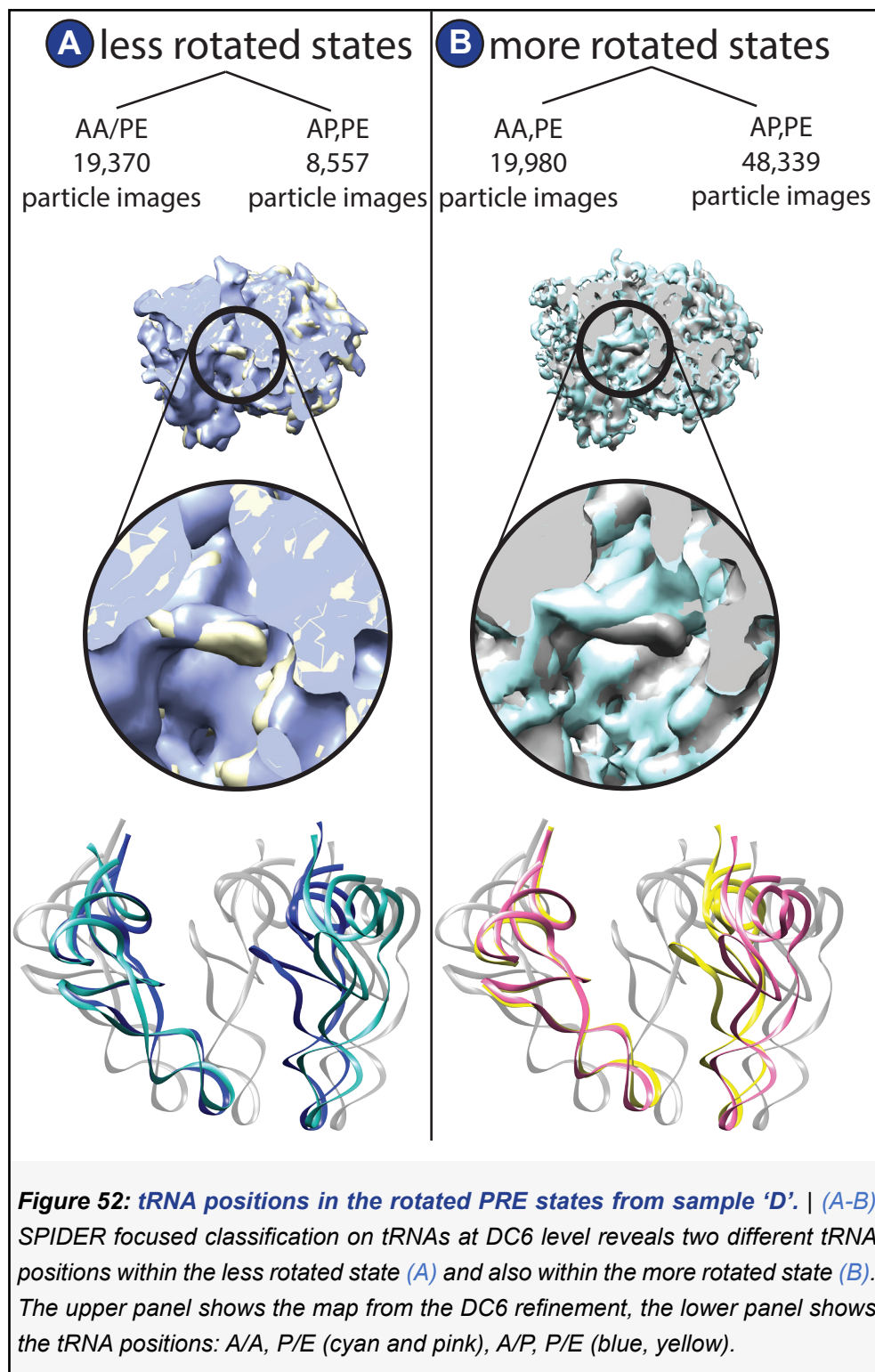


Figure 51: Maps of the PRE complexes from sample 'D' refined via homogeneous refinement in cryoSPARC. | (A) The classical PRE complex. 80S is colored as in the previous figures, the A/A tRNA is pink, P/P tRNA is green, the E/E tRNA is orange. (B) Resolution curves (GSFSC) for the classical PRE complex, resolution estimation from cryoSPARC. (C) The less rotated PRE complex. Contour level 0.6 σ . The 40S subunit of this state is rotated 17.1° compared to the classical PRE state (A) around the indicated axis. The dominating position of the tRNAs is A/A (pink) and P/E (orange). (D) Resolution curves (GSFSC) for the less rotated PRE complex from the Resolution estimation from cryoSPARC. (E) The more rotated PRE complex. Contour level 1.0 σ . The 40S subunit of this state is rotated 8.7° around the indicated axis compared to the classical PRE state. The dominating position of the tRNAs is A/P (green) and P/E (orange). (F) Resolution curves (GSFSC) for the more rotated PRE complex from the resolution estimation from cryoSPARC.

5. Results



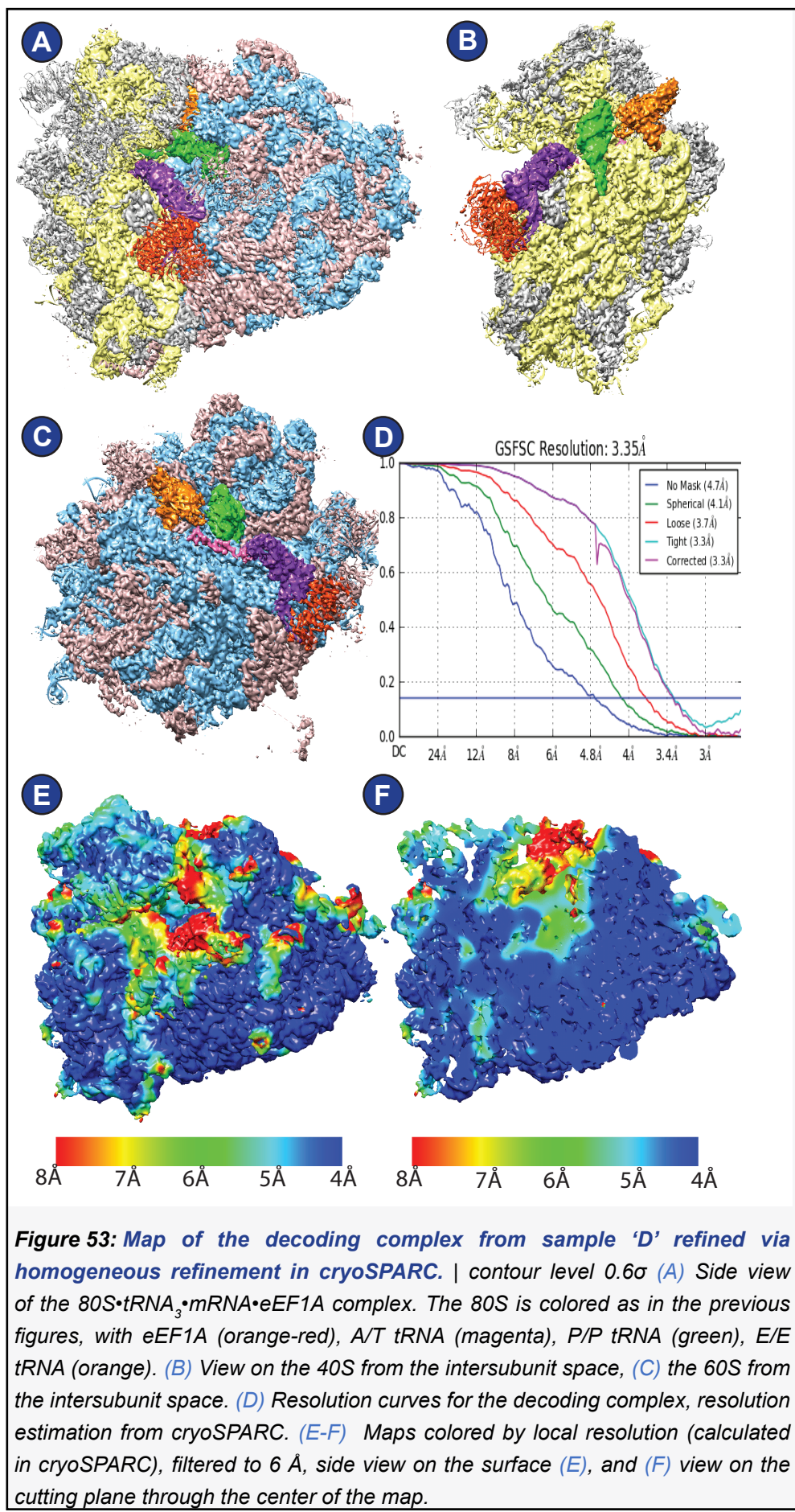
5. Results

al., 2015). In both polysome datasets presented here, however, the separation of the rotated PRE states was based on a difference in rotation of the 40S subunit and not the state of the tRNAs (**Figure 47**). In sample ‘D’, compared to the classical PRE state (**Figure 51A**), there is a less rotated state (7.1° 40S subunit rotation) (**Figure 51B**) and a more rotated state (8.7° 40S subunit rotation) (**Figure 51C**).

A next sorting step performed for the dataset from sample ‘D’ employed a mask on the tRNA and revealed that each of the rotated states could be split into two substates, respectively, distinguished by the positions of the tRNAs (**Figure 52**).

About 22% of the particle images classified as decoding complex, reaching a resolution of 3.7 \AA in sample ‘D’ (loose mask) (**Figure 53**). This decoding complex contains P/P and E/E site tRNAs as well as a pre-accommodation tRNA (A/T tRNA) that is bound on the ribosome as ternary complex with the elongation factor eIF1A (**Figure 53**). Pre-accommodation means that the anticodon stem loop is located in the 40S A site, while the acceptor stem is located bound to eEF1A at the stalk base. The resolution of the structure differs locally and is lowest in the density for eIF1A, the tRNAs and the L1 stalk, consistent with a high variability and/or flexibility in this region (**Figure 53E-F**). The captured state is most likely representing the decoding state after GTP-hydrolysis and the process of eIF1A dissociation, which would then be followed by accommodation of the A/T tRNA in the A site. Sorting of this state at the level of three-fold decimated data (DC3) suggests that this state could be separated into several substates differing by the conformation of eEF1A and the stalk base. A first attempt to do so suggests that the conformational rearrangements of eEF1A includes a movement of the G domain towards domains 2 and 3 of eEF1A (**Figure 54**). Associated with this movement, the stalk base moves inwards (towards the A site) (**Figure 54**).

5. Results



5. Results

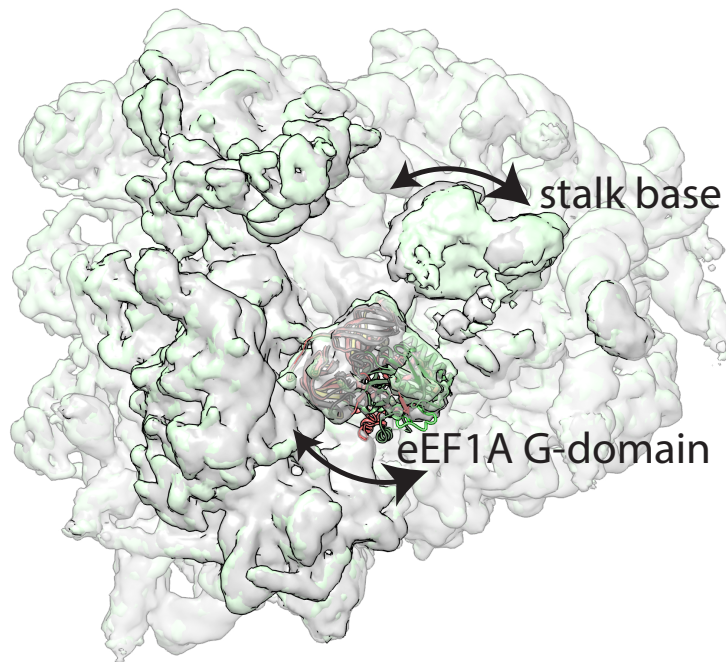


Figure 54: Decoding and eEF1A movements. | Overlayed maps of the two structures (green and grey) of decoding complexes that were separated at DC3 level using a mask on eEF1A and the stalkbase/P-stalk region. The results show very fragmented density for eEF1A, but a movement the G-domain of eEF1A relative to domains 2 and 3 can be seen, associated with movement of the stalk base. A model of eEF1A (provided by Tatyana Budkevich), is rigid body docked domain wise into the density, the green model corresponding to the green, the red model to the grey density. This conformational variability of eEF1A and the stalk base explains the low local resolution in this region.

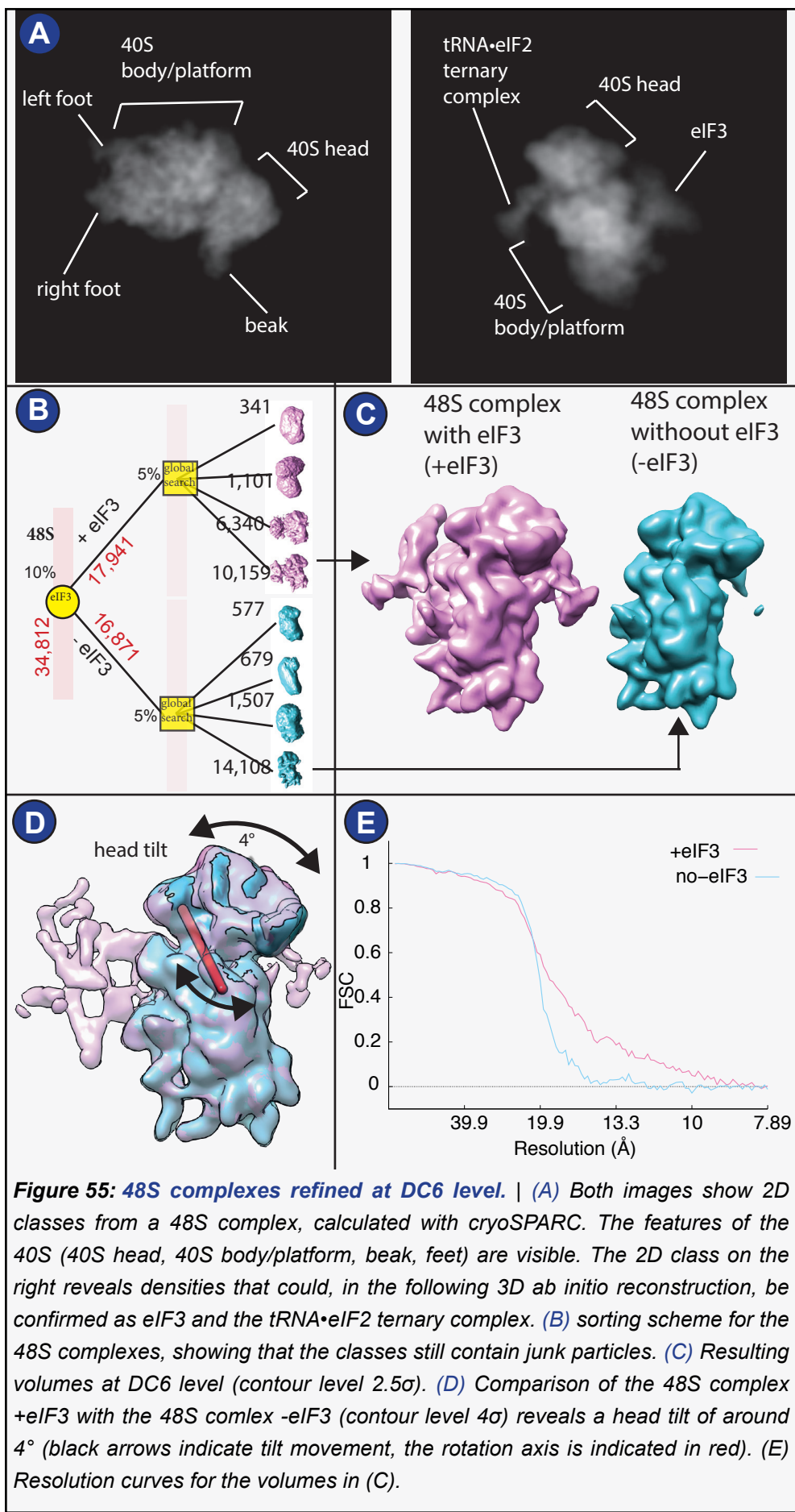
Native initiation factor and ternary complex loaded 40S subunits found on polysomes.

Additionally to the intermediate states of the elongation cycle, initiation-factor loaded 40S subunits were identified which have not been noticed in previous polysome datasets (Behrmann et al., 2015).

The presence of those complexes was revealed by 2D classification, which showed several classes which contained 40S subunits (**Figure 24, Figure 55A**). An *ab initio* 3D reconstruction in cryoSPARC revealed that those classes represent initiation-factor loaded 40S subunits.

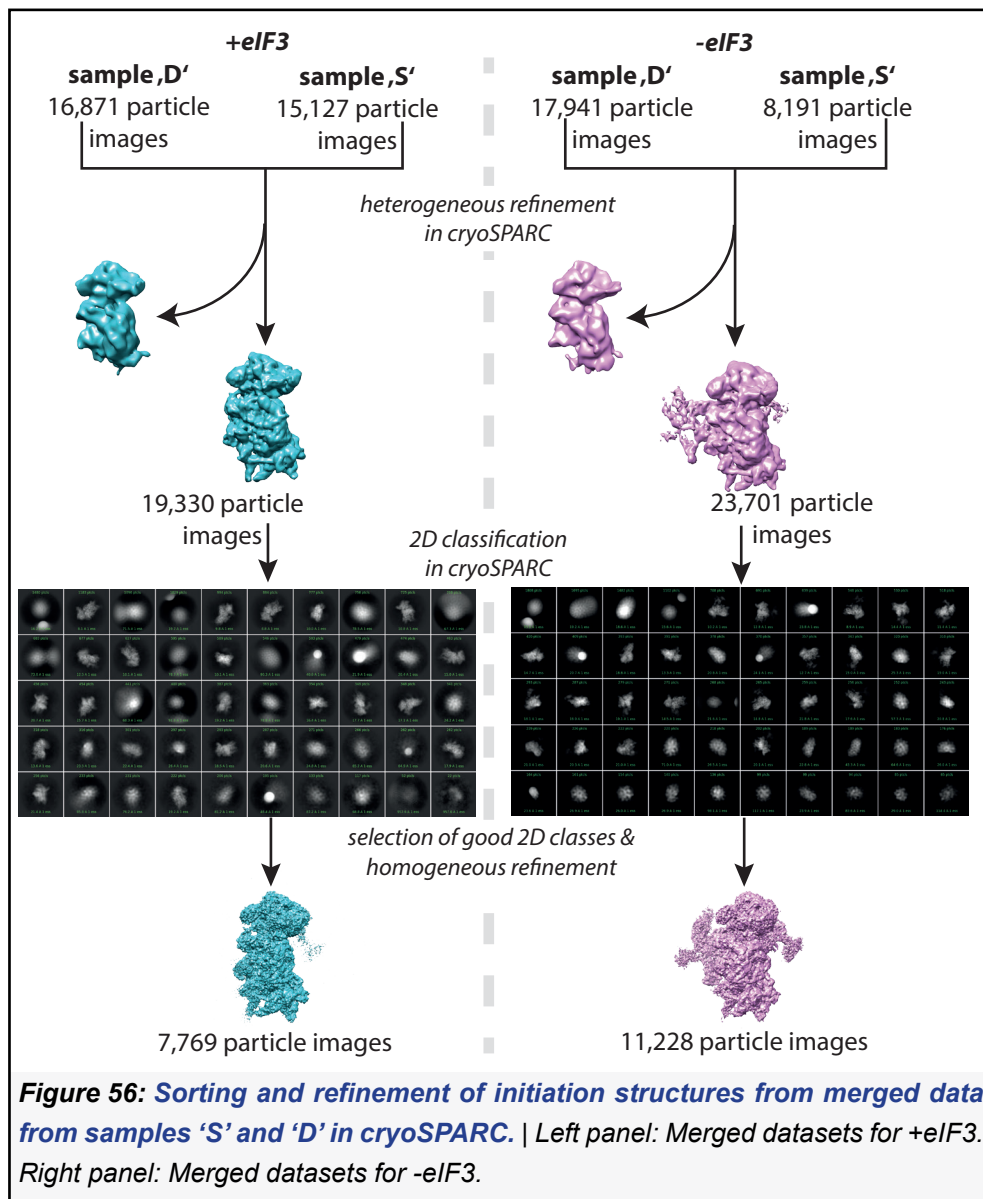
Further refinement in SPIDER yielded two 3D classes (**Figure 55B, C**). One contained eIF3, one not, but both were bound to ternary complex (initiator tRNA and eIF2) and eIF1A. The assignment of

5. Results



5. Results

those complexes as initiation complexes was confirmed by the comparison with published density maps and atomic models of *in vitro* reconstituted initiation complexes and crystal structures from initiation factors (Eliseev et al., 2018; Hashem and Frank, 2018; Lomakin and Steitz, 2013). Comparison of the 48S complexes with and without eIF3 revealed that they differ by head tilt which at the level of six-fold decimated data was measured to be 4° (**Figure 55D**). The resolution is quite low; around 15 Å for the 48S complex without and around 12 Å for the one with eIF3 (**Figure 55E**). This is way below the limits given by six-fold decimation, where the theoretical resolution limit would be 7.89 Å.



5. Results

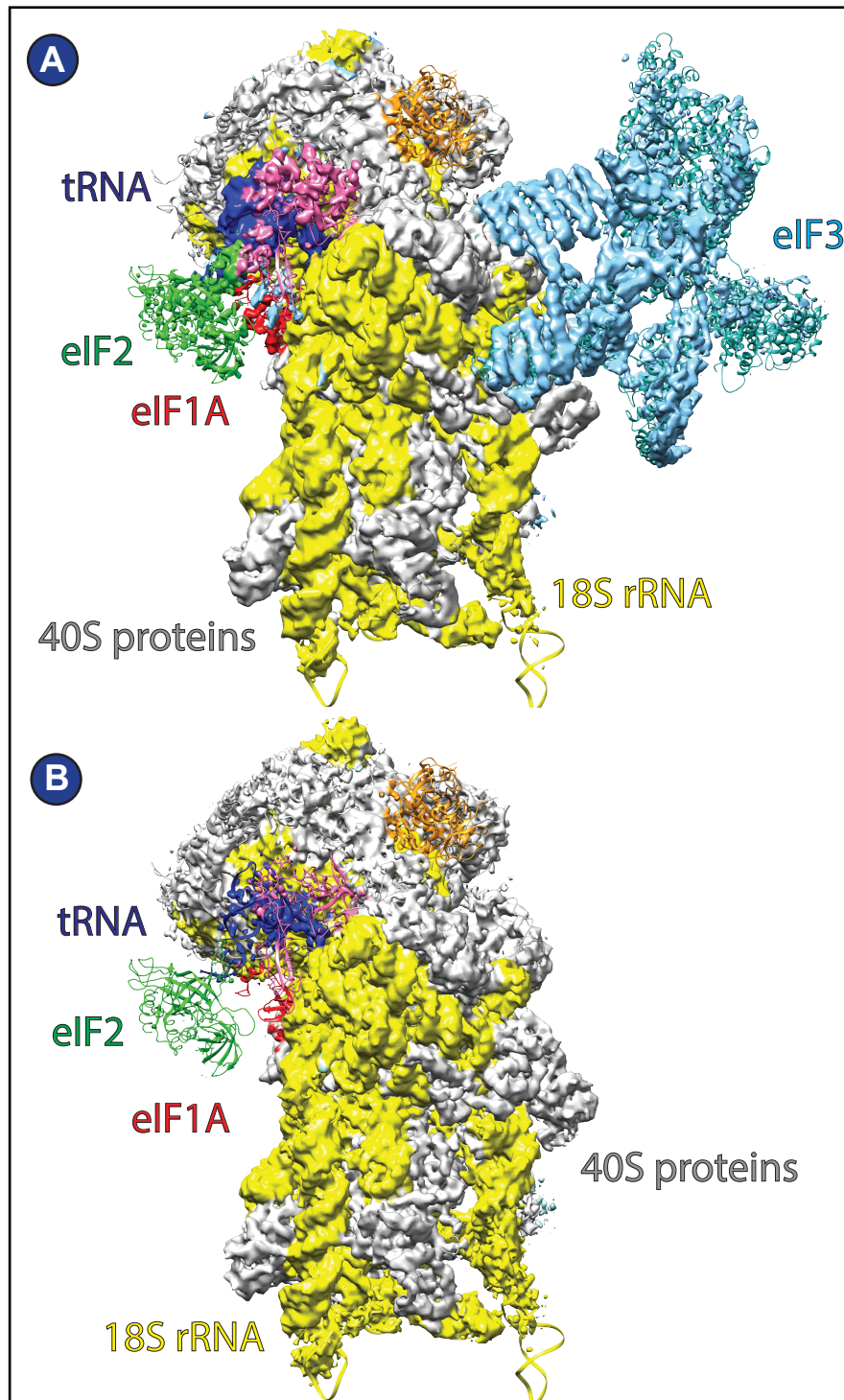
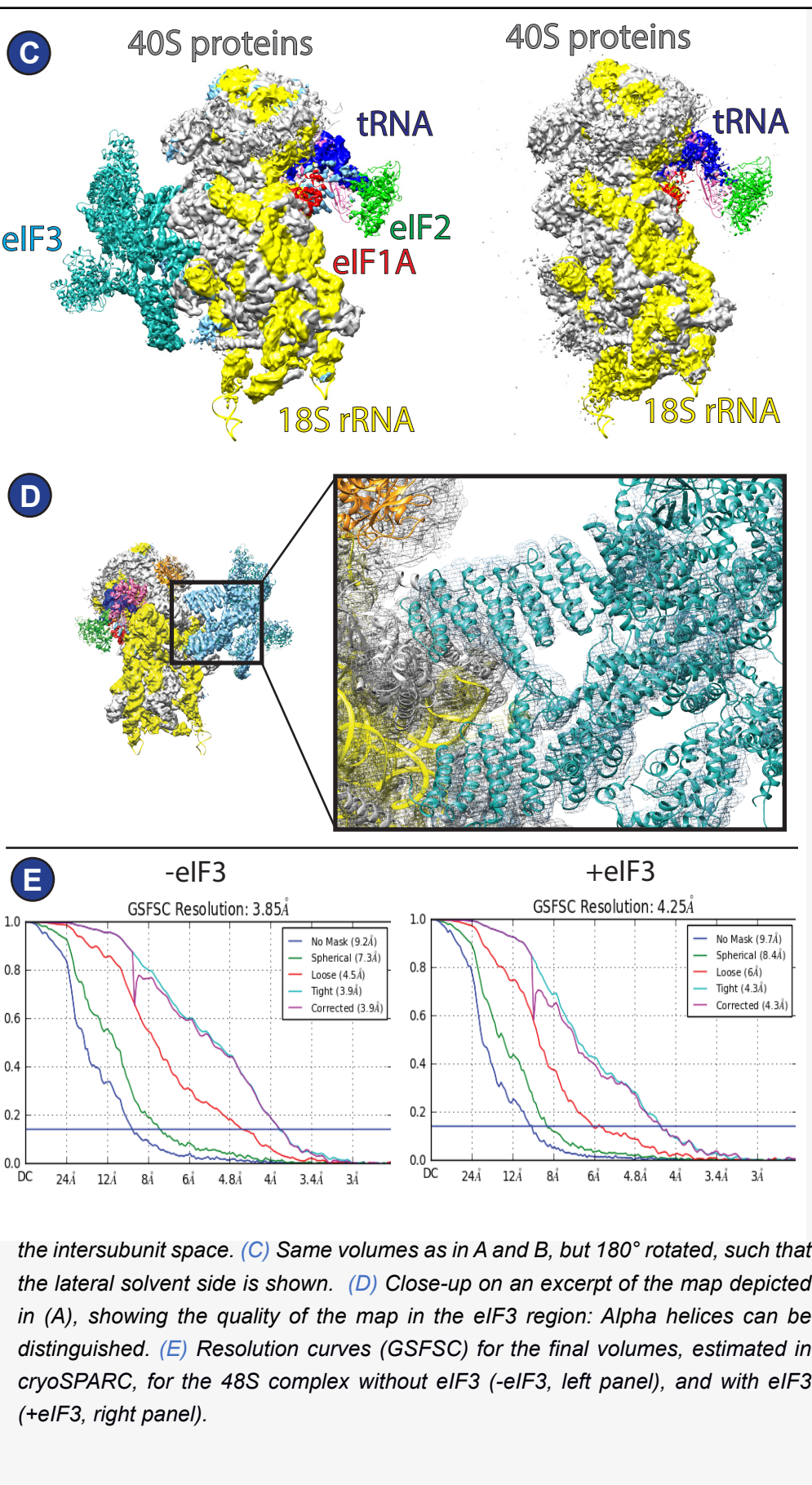


Figure 57: Initiation structures from merged data from sample 'S' and sample 'D'. | For the coloring of the map, PDB models (PDB-4KZZ used for eIF1A and PDB-6FEC used for remaining model parts) were rigid body fitted and the density was colored according to those models: 18S rRNA (yellow), ribosomal proteins (grey), eIF2 (green), tRNA (blue), eIF1A (red), ??? (orange)(A) 48S complex with eIF3 (+eIF3) (contour level 0.5 σ), view on the intersubunit space with the tRNA binding sites. (B) 48S complex without eIF3 (-eIF3) (contour level 0.5 σ), view on

5. Results



5. Results

The low resolution is a sign of poor self consistency as explained in the introduction, section 2.7). This can be an indication for the volumes being still heterogeneous, e.g. containing head tilt or different occupancy with factors and/or tRNA, or even still containing some junk. Therefore, to improve the datasets that made up the resulting initiation volumes, the particle images from sample 'D' and sample 'S' were merged at the level of separation shown in Figure 47 (**Figure 56**). To make sure that 'junk' particle images are sorted out, a heterogeneous refinement was preformed in cryoSPARC using a highly filtered 40S subunit; subsequently, obvious junk particle images were discarded via 2D classification in cryoSPARC (**Figure 56**). The final particle image number was low as well, but the idea behind merging the particle images is that the fraction of good particle images would be higher. Indeed, the resolution improved, probably also, because two-fold decimated data was used for refinement: Even without applying any mask, the resolutions are around 9-10 Å (**Figure 57**). A tight mask results in resolutions around 4 Å. However, the biologically interesting parts in the maps, i.e. the ternary complex containing eIF2 and the tRNA, or eIF3, are of low quality. The resolution estimation might be appropriate for the core 40S subunit, but not for the flexible parts. Interestingly, the 40S subunit is quite well-refined indeed, but the ternary complex and eIF3 quality decreased; this might be due to a tendency of cryoSPARC to align all particles on the better resolved 40S subunit, thereby averaging out information on more flexible parts.

6. Discussion

In **section 6.1.**, I will discuss a model of mammalian translocation as it can be drawn from the three discovered cryo-EM structures of *in vitro* reconstituted 80S•tRNA₂•mRNA•eEF2•GMPPNP complexes. In the first part, the sequence of conformational changes of the ribosomes and their association with the functional states is discussed. Next, I will discuss smFRET (single molecule fluorescence resonance energy transfer) results from our collaborators that complement the cryo-EM work and reveal important functional differences between the mammalian and bacterial systems. Last, some observations on the molecular interactions in the cryo-EM structures are discussed.

Section 6.2. illuminates the role of the *in vitro* reconstituted 80S•tRNA₂•mRNA•eEF2•GDP complex.

In **section 6.3.**, I first will discuss the role of serum deprivation and serum restimulation and the role of eS6-phosphorylation. Next, I will allocate the discovered polysomal states in an expanded energy landscape of translation and discuss the *ex vivo* decoding, rotated PRE, and initiation complexes.

6. Discussion

6.1 A model for mammalian translocation

Late translocation is governed by ribosome rearrangements

The three cryo-EM structures TI-POST-1, TI-POST-2 and TI-POST-3 represent late steps of translocation and show how large scale conformational changes drive the tRNA₂•mRNA module into its classical POST-position. In the chimeric hybrid state, the tRNAs in the translocating ribosome have already reached their P and E sites on the 60S subunit. The final rearrangements during the late steps of translocation are dominated by 40S body/platform back-rotation (TI-POST-1 to TI-POST-2) and 40S head reverse swivel (TI-POST-2 to TI-POST-3).

Although the observation of the TI-POST-1 state was expected from previous studies in bacteria (Ramrath et al., 2013; Ratje et al., 2010; Zhou et al., 2014), the structure of our TI-POST-1 state could add information on how the eukaryote-specific motion of subunit rolling is integrated into the conformational changes taking place during translocation.

It appears that up to 3° of subunit back-rolling is covered during the transition from the rotated PRE to the TI-POST-1 state. The remaining part of subunit back-rolling is accounted for during the transition of TI-POST-1 to TI-POST-2 (and negligible portion from TI-POST-2 to TI-POST-3). However, the observed intermediates are stalled with GMPPNP and dissociation of eEF2 is inhibited, the reason why we can observe those intermediates in the first place; additionally, the *in vitro* conditions imply excess of eEF2•GMPPNP and tRNAs. To what extent this second portion of subunit back-rolling is completed before dissociation of eEF2 under physiological, *in vivo* conditions, remains unclear.

From *ex vivo* derived polysomes, we know that additionally to the classical POST population that is made up of the majority of particle images, two partially rolled (~1° and ~3°) POST-states can be observed (Behrmann et al., 2015, and the results on polysomes

6. Discussion

in this work also reveal a rolled POST state.). Thus, it might be possible that under physiological conditions, the second portion of subunit rolling is completed after dissociation of eEF2. Alternatively, in the case that 40S back-rolling must be completed before eEF2•GDP dissociation, those rolled POST-states could be explained by spontaneous thermodynamically driven motions similar to reversible intersubunit rotation. A third possibility is that completion of subunit back-rolling is rather loosely coupled to the process of translocation and that multiple conformations allow for completion of translocation, including a range of rolled states.

There are two details in the conformation of the discovered TI-POST-states that might be of importance. First, the TI-POST-2 state with its 1° head swivel increase compared to TI-POST-1 fits well to a previously observed ‘exaggerated head swivel’ in bacteria (Wassermann et al.). Wasserman and colleagues conducted smFRET experiments in which they measured conformational changes during bacterial translocation using multiple labeled sites and identified several states of which INT2, INT3 and POST1 share features with our TI-POST-1, TI-POST-2 and TI-POST-3.

When labeling the ribosomal proteins uS13 and uL5, they could observe short-lived intermediates consistent with larger 30S head swivel emerging from INT3 (TI-POST-2). Although we measure 40S head swivel relative to the 40S body/platform and not relative to the 60S subunit (where uL5 is located) and these two observations cannot be compared, it might be considered that a highly-swiveled 40S head position in the TI-POST-2 state may facilitate release of 40S head-tRNA interactions as prerequisite for reverse-swivel and completion of translocation.

In TI-POST-3, we observe a 1° head tilt in TI-POST-3 compared to the classical POST state. A head tilt had been predicted to be important in translocation by MD simulations (Nguyen and Whitford, 2016) and head tilt has been directly observed in the context of tmRNA translocation in bacteria (Ramrath et al., 2012).

6. Discussion

Both details suggest that additional, not captured motions of the 40S head as exaggerated swivel and tilt could be part of translocation.

Conformational changes in the ribosome during translocation in mammalia compared to yeast

Recently, two independent studies have investigated the structural basis of viral type IV IRES translocation, which is an important step of the internal initiation pathway of this class of IRESs. Both studies have been performed in the yeast system. In one study, eEF2 was stalled by the non-hydrolyzable GTP analog GMPPCP (Murray et al., 2016), in the second one the antibiotic sordarin was used (Abeyrathne et al., 2016).

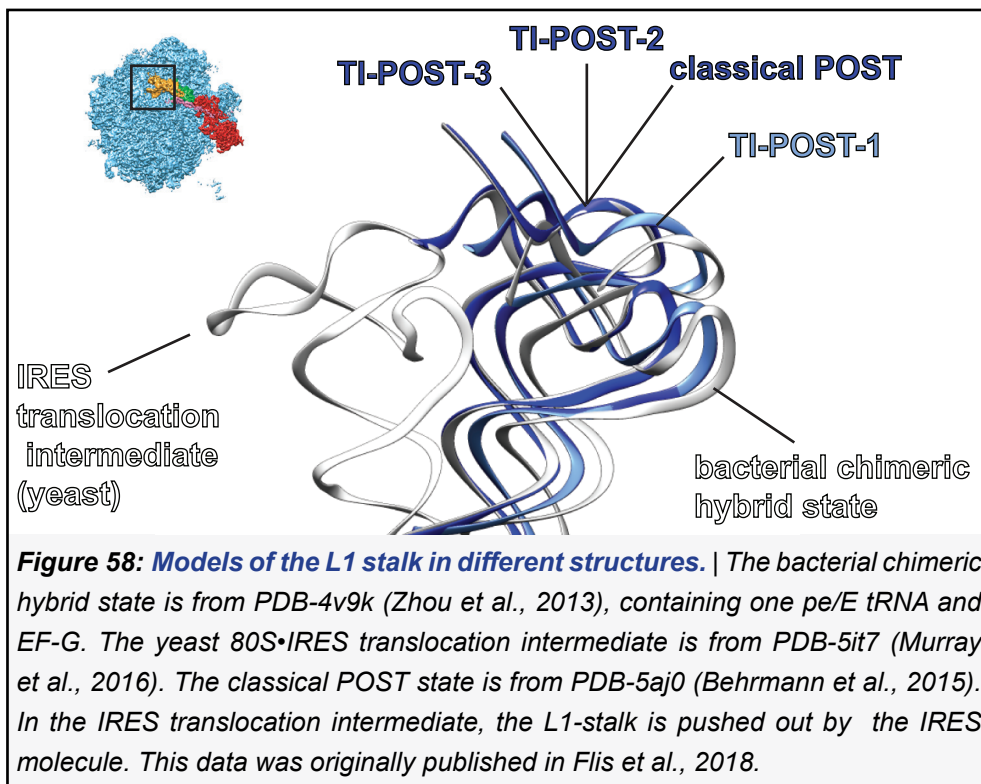
In principle, the yeast 80S•IRES•eEF2•GMPPCP complex represents a pre-hydrolysis state biochemically comparable to the here presented mammalian 80S•eEF2•GMPPNP•tRNA₂•mRNA complex. Surprisingly, however, stalling with non-cleavable GTP analogs apparently leads to different conformational states in both systems. Whereas in the IRES case a single early translocation intermediate related to a TI-PRE state was found (Murray et al., 2016), in the canonical system the non-hydrolysable GTP analog led to the stabilization of the three late translocation intermediates presented here.

The underlying differences in the conformational energy landscape of the respective complexes could, in principle, be caused by differences between yeast and rabbit 80S ribosomes or a functional difference between GMPPCP and GMPPNP. However, it is most likely that there are intrinsic differences in the translocation of type IV IRESs and a tRNA₂•mRNA module, because the tRNA-like element of the type IV IRES corresponds to an ASL of a single tRNA only and forms less interactions with the ribosome than the tRNA₂•mRNA module. The canonical interactions of an authentic tRNA₂•mRNA module formed by the tRNA body and the 3'-CCA-end as well as the complete second tRNA are missing. Hence, the ribosome is more restricted through the interactions with the tRNA₂•mRNA module than when containing an IRES and it may be a result of this restriction that the

6. Discussion

40S head domain stays attached to the tRNA₂•mRNA module during the transition from TI-POST-1 to TI-POST-2 and swivels back only after the 40S body/platform domain has reached a close-to-POST-state position. Also, when IRES is bound, the L1 stalk is observed in a very open conformation compared to the authentic intermediates (**Figure 58**).

Comparison with the five 80S•IRES•eEF2•Sordarin states (Abeyrathne et al., 2016) also shows the ribosome in different conformations than when translocating the tRNA₂•mRNA module (**Table 7**). Whereas the conformation of state II of the 80S•eEF2•Sordarin complex is somewhat in the same range as TI-POST-1, the next intermediate of IRES translocation neither exhibits back-rotation/back-rolling of the 40S body/platform domain nor a significant rise in the head swivel, both of which is characteristic for TI-POST-2. The tRNA₂•mRNA module is apparently also necessary for the complete opening of the P-gate, as the maximum width of the P-gate is 24 Å (state III of the 80S•eEF2•Sordarin complex) compared to ~28 Å in TI-POST-2 (**Table 7**).



6. Discussion

Table 7: Comparison of conformations of eEF2-bound ribosomes

Selected models of ribosome-eEF2/EF-G complexes compared to PDB-5aj0 and set into context with the presented TI-POST-intermediate state. References: 1. (Voorhees et al., 2014), 2. (Anger et al., 2013), 3. (Murray et al., 2016), 4. (Abeyrathne et al., 2016), 5. (Zhou et al., 2014), 6. (Gao et al., 2009), 7. (Ramrath et al., 2013) and 8. (Brilot et al., 2013). This data was originally published in Flis et al., 2018.

PDB-ID [class] (reference)	Organism	Stalling	Substrate	Body/platform rotation	Head rotation (swivel)	P-gate width (Å)
3j7p (1)	S. scrofa	-	-	8.5°	12.5°	22.5
4v6x (2)	H. sapiens	-	P/E tRNA	8°	14.7°	22.6
5it7 (3)	K. lactis	GMPPCP	IRES	7.4°	10.4°	20.6
5juo [I] (4)	S. cerevisiae	Sordarin	IRES	7.2°	11.6°	22
5jup [II] (4)	S. cerevisiae	Sordarin	IRES	2.6°	17.3°	22.6
5jus [III] (4)	S. cerevisiae	Sordarin	IRES	2.2°	17.3°	24
5jut ([IV] (4)	S. cerevisiae	Sordarin	IRES	1.3°	13.9°	20.9
5juu [V] (4)	S. cerevisiae	Sordarin	IRES	1.9°	3.2°	15.7
TI-POST-1	O. cuniculus	GMPPNP	tRNA ₂ •mRNA	4°	17.7°	27.4
TI-POST-2	O. cuniculus	GMPPNP	tRNA ₂ •mRNA	0.7°	19°	27.8
TI-POST-3	O. cuniculus	GMPPNP	tRNA ₂ •mRNA	0.1°	1.1°	17
4w29 (5)	T. thermophilus	FusA	tRNA ₂ •mRNA	7.4°	19.5°	27.5
4v5f (6)	T. thermophilus	FusA	tRNA ₂ •mRNA	3.8°	0.5°	17.2
4v7b (7)	E. coli	FusA	tRNA ₂ •mRNA	6.8°	17.1°	25.1
4v7d (8)	E. coli	FusA, viomycin	tRNA ₂ •mRNA	13.7°	3.4°	17.7

In summary, whereas translocation of type IV IRESs also involves rotation/back-rotation motions of the ribosomal subunits, the sequence of conformational changes or their distribution in the energy landscape appears to be different from the translocation of a canonical tRNA₂•mRNA module. **Table 7** also contains data on bacterial translocation stalled with fusidic acid.

6. Discussion

GTP hydrolysis limits late steps of translocation in the mammalian ribosome

The similarity between domain 1 (G-domain) of eEF2 and the decoding factor eFTu/eEF1A as well as domain 4 of eEF2 and the anticodon stem of a tRNA has provoked many theories about the origins of translocation. Translocation originally (in the RNA world) must have been induced by a tRNA alone. eFTu (eEF1A in mammalia) could have co-evolved with tRNA, leading to mimicry of the tRNA by the additional domain 4 that is characteristic of the translocase EF-G (Hartman and Smith, 2010).

In vitro experiments show that even at the present evolutionary level of the translational machinery, translocation is an intrinsic feature of the ribosome and EF-G/eEF2 is not necessary to carry it out. Translocation can occur spontaneously and independent of a translocase, yet at very low rates. Spontaneous or ‘non-enzymic’ translocation (Gavrilova and Spirin, 1971) is largely influenced by the concentration of Mg²⁺, and can be stimulated by thiol-specific reagents and loss of function of S12 and S13, because surprisingly, the ‘modern’ ribosome itself inhibits spontaneous translocation via these ribosomal proteins (Cukras et al., 2003; Gavrilova and Spirin, 1971; Gavrilova et al., 1976).

In vivo, eEF2’s contribution to efficiency, speed and accuracy of the translocation reaction is vital, but the exact mechanism of translocation and the contribution of EF-G/eEF2 is controversial. The classical view on GTPases consists in the notion that GTP hydrolysis is a mean for regulating affinity to the substrate, and such a role is also proposed for translational GTPases (Inoue-Yokosawa and Kaziro, 1974). From this perspective emerged the idea that the role of the translocase is to prevent back-slippage of the tRNA_A•mRNA module during thermodynamically driven back-rotation of the small subunit in order to bias tRNA_A•mRNA module movement into the new tRNA binding sites, reminiscent of a pawl in a Brownian ratchet (reviewed in (Spirin, 2009)).

6. Discussion

Some groups propose alternative models for the mechanism of eEF2, like eEF2 being a motor protein, an idea that was carried onward to the power stroke model (Rodnina et al., 1997). Those models suggest that the energy coming from GTP hydrolysis is used for an active motion of eEF2 that pushes the tRNAs in the direction of translocation. The key observation that led to this proposition was that in bacteria, GTP hydrolysis precedes tRNA movement (Rodnina et al., 1997), and that the conformation of free EF-G differs from the conformation of ribosome-bound EF-G (Czworkowski and Moore, 1997). smFRET and TIRF experiments supporting this idea followed (Chen et al., 2016), and the question on the exact role of GTP hydrolysis remain a controversial topic (Belardinelli et al., 2016; Chen et al., 2013; Liu et al., 2014; Wasserman et al., 2016).

However, an important piece is missing for understanding translocation: The available bacterial EF-G-bound structures stalled with GMPPNP or GMPPCP contain only one P/E or pe/E tRNA. A structure containing the full tRNA₂•mRNA module and elongation factor stalled with a non-hydrolysable nucleotide analog has not been visualized yet (discussed in (Gao et al., 2009; Penczek et al., 2006). All the more was it surprising that our three mammalian translocation intermediates with eEF2 stalled with GMPPNP did contain the complete tRNA₂•mRNA module.

To further investigate the mechanism of mammalian translocation, our collaborators Dr. Mikael Holm, Emily Rundlet and Prof. Dr. Scott Blanchard from Cornell University, New York, performed smFRET experiments on human ribosomes (**Figure 59 to Figure 61**). They used a Cy5-labeled Met-Phe-tRNA^{Phe} and P-site Cy3-labeled tRNA^{Met} prepared as described in (Ferguson et al., 2015). As mentioned in the results section above, the tRNA₂•mRNA module undergoes compaction during the transition from the rotated PRE-2 to the TI-POST-1 state, such that by monitoring the distance between the tRNAs, translocation can indirectly be followed. Accordingly, Mikael, Emily and Scott observed that upon addition of eEF2•GTP to the flow cell, in which the ribosomes are immobilized on a

6. Discussion

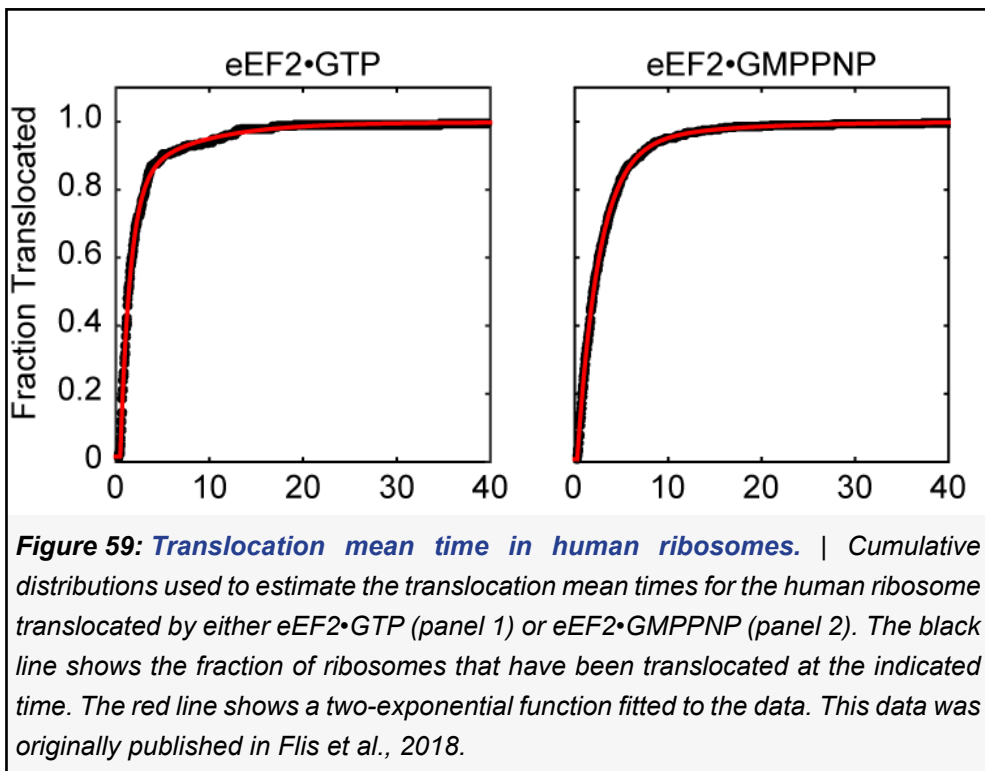
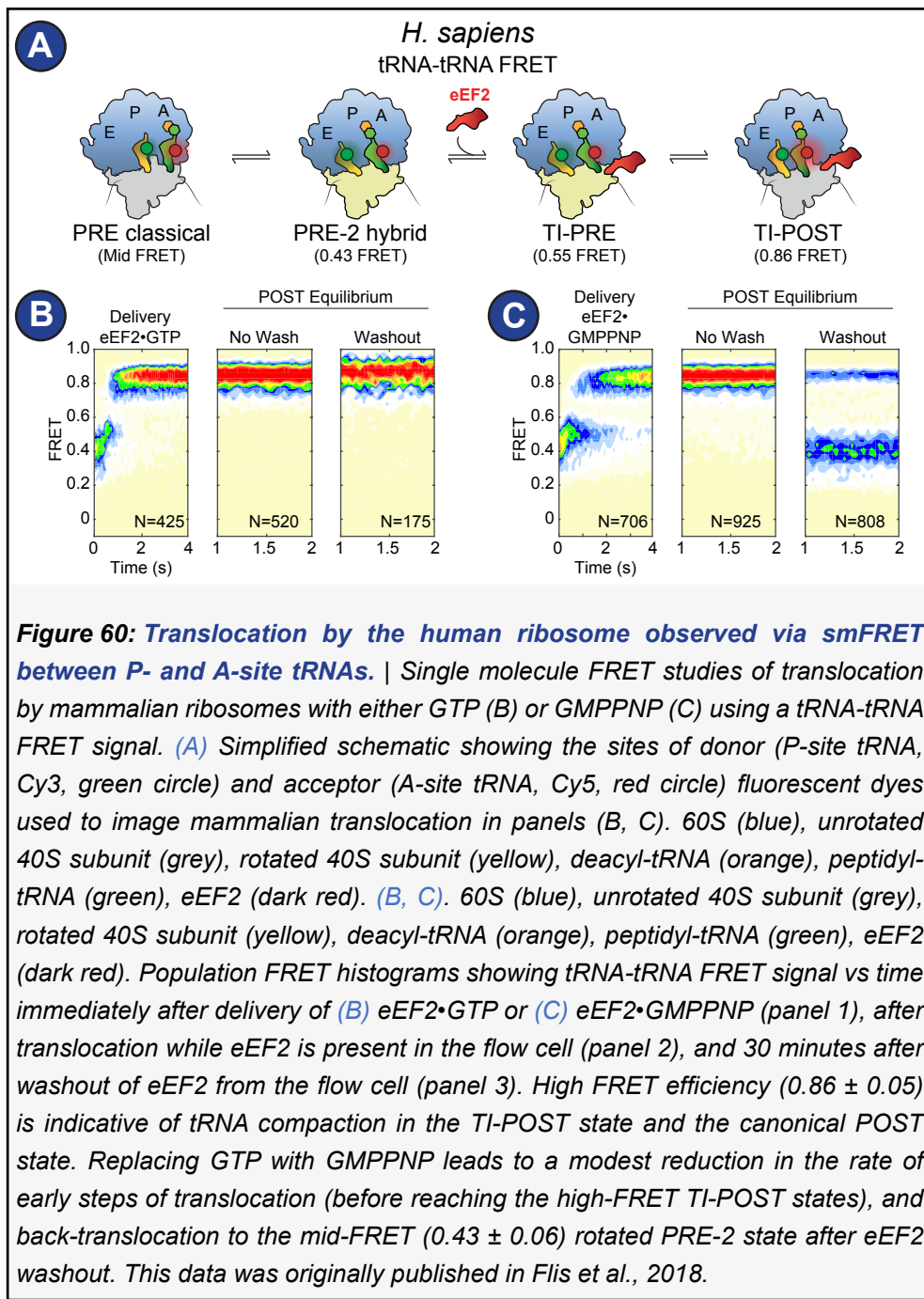


Figure 59: Translocation mean time in human ribosomes. | Cumulative distributions used to estimate the translocation mean times for the human ribosome translocated by either eEF2•GTP (panel 1) or eEF2•GMPPNP (panel 2). The black line shows the fraction of ribosomes that have been translocated at the indicated time. The red line shows a two-exponential function fitted to the data. This data was originally published in Flis et al., 2018.

surface, human rotated PRE-2 complexes, characterized by a FRET of 0.43 ± 0.06 (intermediate-FRET) (Ferguson et al., 2015), rapidly transitioned into a high-FRET (0.86 ± 0.05) and stayed in this state. The mean time of the transition to the POST-state with compacted tRNAs was hardly affected by whether GTP or GMPPNP was used: The time was estimated as 1.0 ± 0.15 s with GTP and 2.3 ± 0.3 s with GMPPNP (**Figure 59**). That measurement is consistent with efficient translocation and a thermodynamically stable POST state (Ferguson et al., 2015).

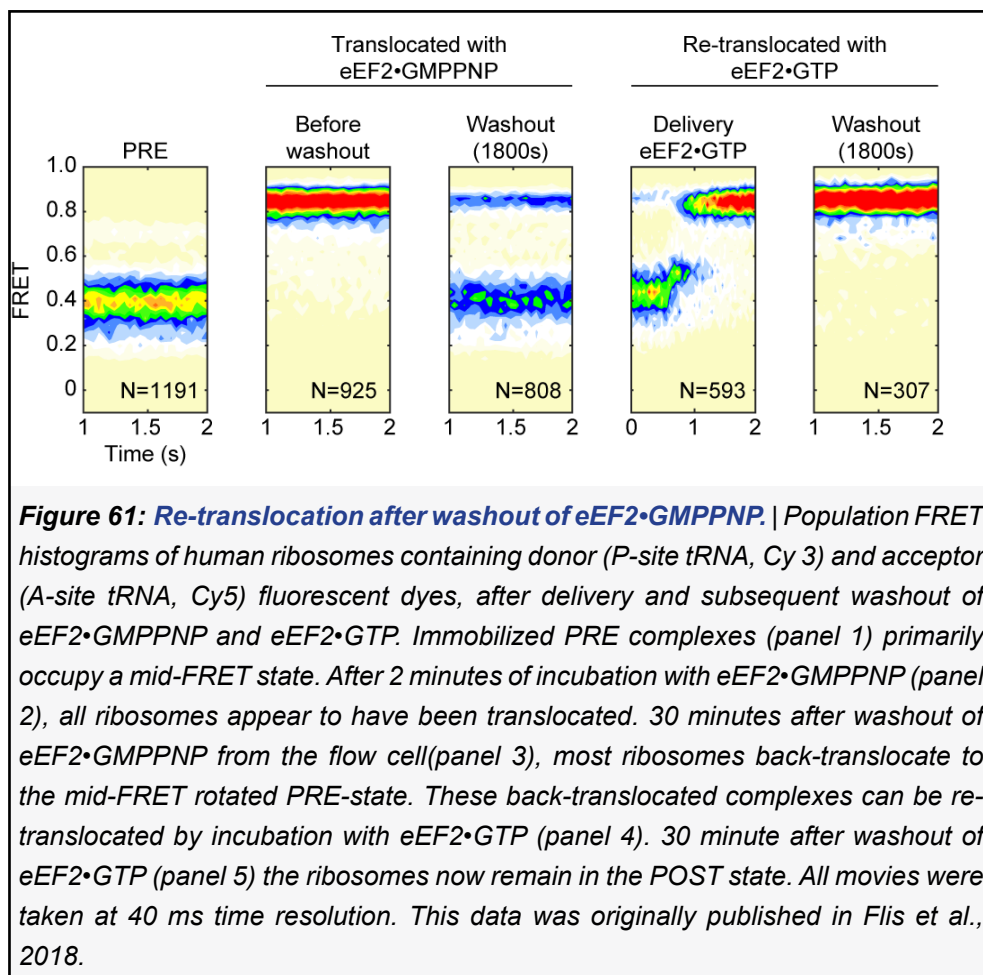
Surprisingly, while washing out eEF2•GTP from the flow cell had no effect on the presumed POST-complexes (**Figure 60B**), in the case of eEF2•GMPPNP, upon washout from the flow cell the high-FRET complex slowly transitioned into an intermediate FRET state (mean time 350 ± 75 s). This intermediate-FRET-state is consistent with a rotated, hybrid state PRE-2 complex (**Figure 60C and Figure 61**). Upon addition of eEF2•GTP, it transformed into the high-FRET (0.86 ± 0.05) again, and stayed in this state, consistent with irreversible POST complex formation (**Figure 61C**).

6. Discussion



Apparently in the mammalian system, translocation is not completed in the presence of GMPPNP and can be reversed by shifting the equilibrium (washout). Furthermore, the fact that re-addition of eEF2•GTP to the rotated, hybrid state PRE-2 leads to irreversible POST complex formation shows that eEF2•GMPPNP can dissociate from the rotated complex and be exchanged for eEF2•GTP (**Figure 61**). A recent study (Susorov et al., 2018) has also shown that both eEF2•GMPPNP and eEF2•GTP are able to catalyze reverse translocation when experimental conditions are such that the PRE

6. Discussion



state is favored relative to the POST state. Together with the here presented cryo-EM structures, these findings demonstrate that early steps of translocation, during which the inter-tRNA distances change, are largely unaffected by GMPPNP, while late steps of translocation, which structurally resemble TI-POST-1, -2 or -3 regarding tRNA positioning, are stalled.

Translocation by mammalian ribosomes compared to bacterial translocation reveals a key role of the E-site tRNA

The role of the E-site tRNA is controversial (Nierhaus, 1993; Semenkov et al., 1996; Wasserman et al., 2016). It is speculated to serve mRNA-stabilization, reading frame maintenance and processivity (Márquez et al., 2004; Myasnikov et al., 2014). Behrmann and colleagues

6. Discussion

observed that the E-site tRNA is always present in the mammalian ribosome in *ex vivo* derived polysomes, corroborated by smFRET studies (Behrmann et al., 2015; Ferguson et al., 2015).

It looks as if the propensity of the E-site tRNA to leave the ribosome depended on the domain of life. The experiments summarized in the following paragraphs further reveal that the difference in E site occupancy also has an impact on translocation.

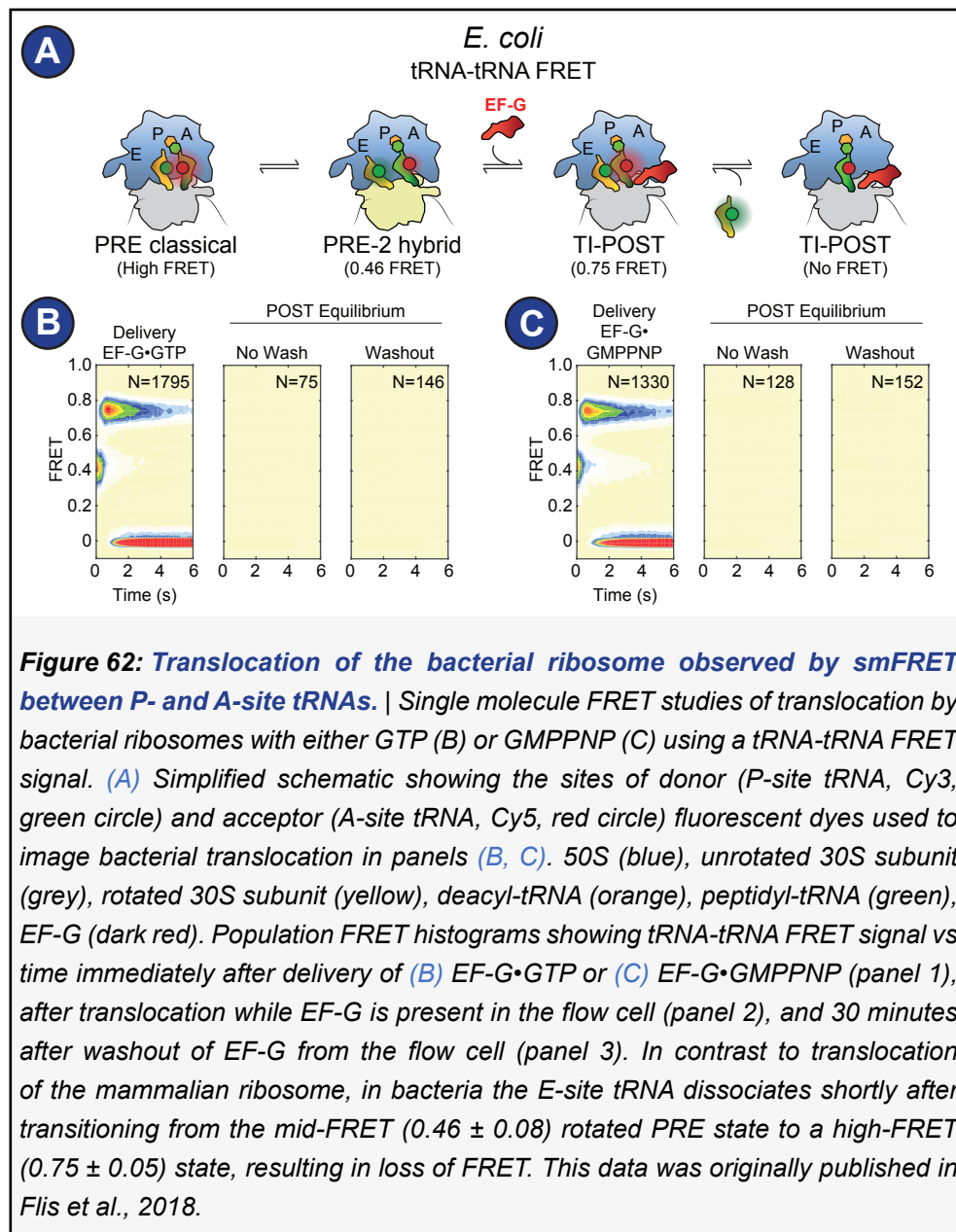
In bacteria, no ‘authentic’ translocation intermediate, that is a 70S complex bound to a complete tRNA₂•mRNA module and eEF2 with an active G-domain, could be visualized (discussed in (Gao et al., 2009; Penczek et al., 2006). The existing EF-G•GMPPNP•tRNA complexes (Connell et al., 2007; Pulk and Cate, 2013; Tourigny et al., 2013; Zhou et al., 2013) are characterized by a partly rotated 30S body/platform and a wide range of 30S head swivel.

The reason why eEF2•GMPPNP does not stall an ‘authentic’ translocation intermediate, while EF-G•GTP•FusA does, remained unclear. The assumed sequence of events is that GTP hydrolysis and P_i release must occur before fusidic acid can act and prevent dissociation of EF-G. smFRET *in vitro* studies suggest that in bacteria the E-site tRNA tends to dissociate quite quickly after full translocation (Wasserman et al., 2016), but the translocation intermediates stalled with fusidic acid contain chimeric hybrid tRNAs and so the pe/E site tRNA is still bound (‘authentic translocation intermediate’). GMPPNP or GMPPCP are expected to stall translocation intermediates at a much earlier, pre-GTP-hydrolysis state. Such a state should as well contain two tRNAs, presumably in hybrid positions. There is only one such structure, however, and it was not caught using a non-hydrolyzable GTP analog, but fusidic acid and Viomycin (Brilot et al., 2013). Here, whereas Fusidic acid prevented EF-G dissociation, viomycin presumably stabilized the rotated state via increasing the affinity of the A/P tRNA to the 30S A site.

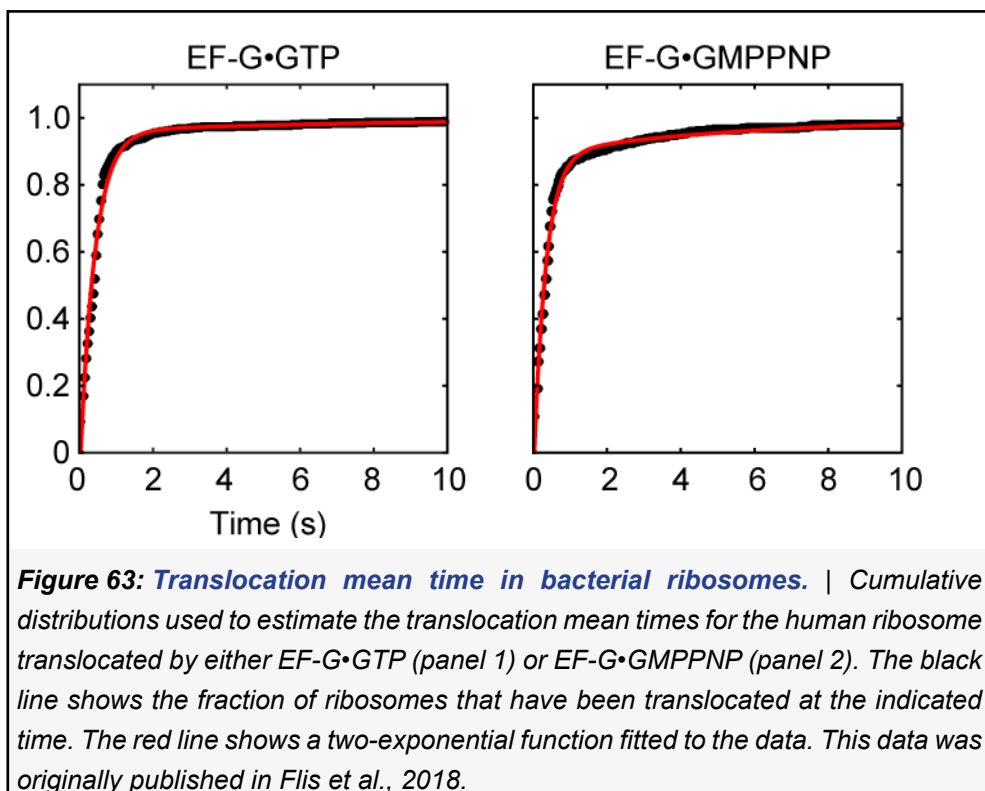
To compare translocation in human ribosomes with translocation in bacteria, our collaborators Mikael, Emily and Scott performed FRET experiments of bacterial (*E. coli*) ribosomes under the same conditions

6. Discussion

as in the experiments with human ribosomes. Upon addition of both EF-G•GTP and EF-G•GMPPNP, the initiated translocation led to a rapid transition from intermediate-FRET (0.46 ± 0.08) to high-FRET (0.75 ± 0.05) and then loss of the signal, consistent with short-lived tRNA compaction and subsequent dissociation of the E-site tRNA (**Figure 62**). The transition times did not differ significantly between EF-G•GTP and EF-G•GMPPNP, thus early steps of translocation seem not to be influenced by the nucleotide, as in the mammalian system (**Figure 63**).



6. Discussion

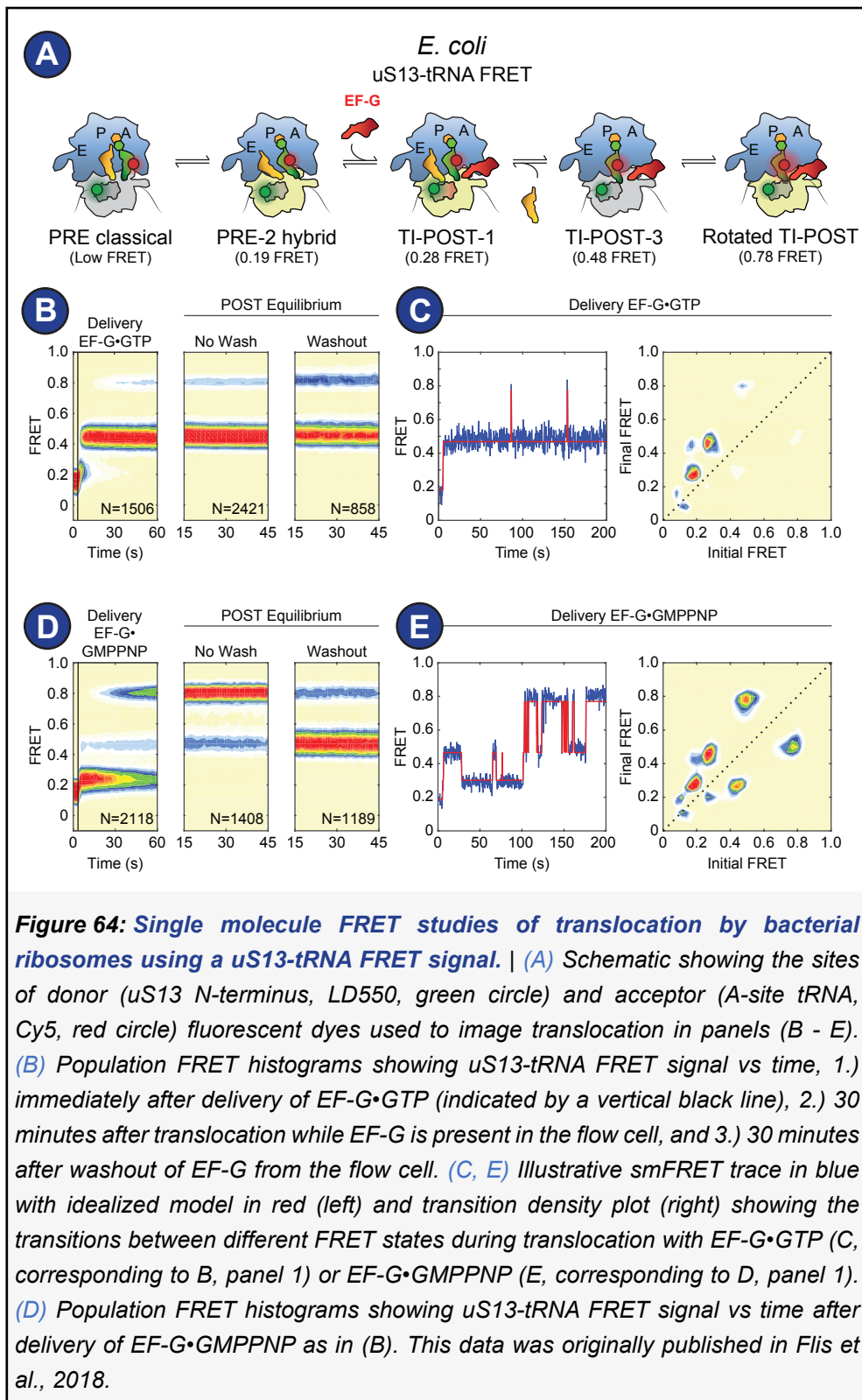


The early dissociation of the E-site tRNA in the bacterial case hampered further insights into late steps of translocation. Therefore, in a new setting, the elbow of the PRE-complex A-site tRNA and protein uS13 were labeled (Wasserman et al., 2016). Upon such labeling, the signal is expected to report distance changes between the P-site tRNA and the 30S head and thus register tRNA movement relative to the head as well as head swivel relative to a fixed tRNA.

In this new setting, the bacterial rotated PRE complex was represented by a low-FRET (0.19 ± 0.03) state, consistent with a large tRNA-30S head distance (Wasserman et al., 2016). Upon delivery of eEF2-GTP, this PRE complex rapidly transitioned into a short-lived (0.28 ± 0.03) higher FRET-state (TI-POST-1), followed by an intermediate-FRET state (0.48 ± 0.05) (classical POST) (**Figure 64A-C**). The resolution of TI-POST-1 and classical POST is attributed to the head swivel in which they differ.

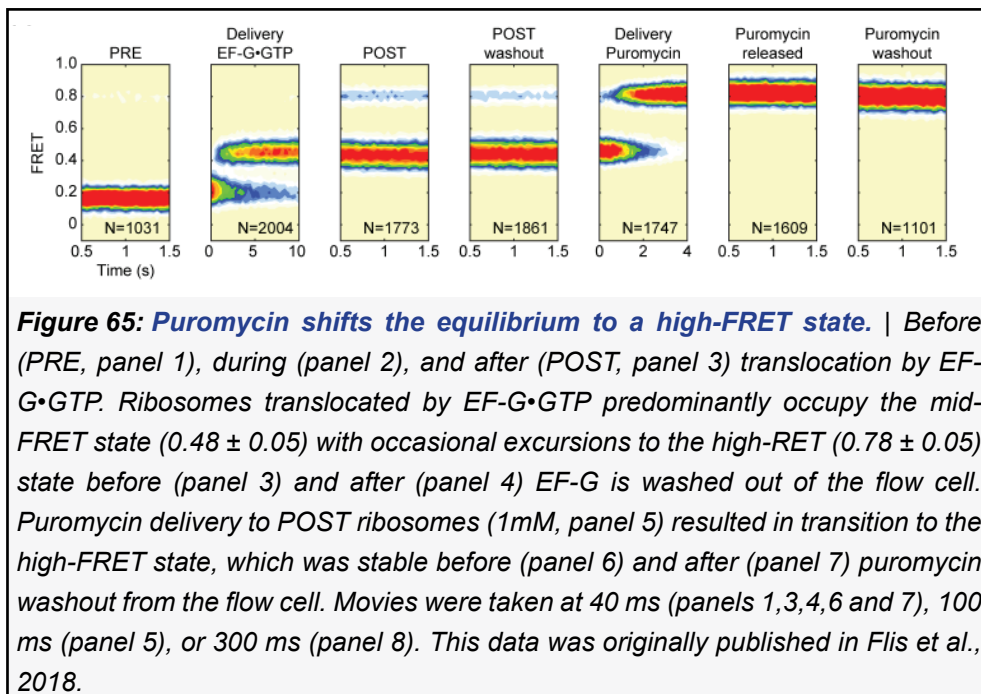
As previously described (Alejo and Blanchard, 2017; Wasserman et al., 2016), the POST-state ribosome achieved a stable equilibrium between intermediate- (0.48 ± 0.05) and high-FRET (0.78 ± 0.05) states (**Figure 64B**). The intermediate-FRET state reflects the

6. Discussion



expected conformation of the system after translocation: classically positioned P/P tRNA on the unrotated ribosome. The POST complex's transition to a high-FRET state conformation indicates a decrease in distance between the peptidyl tRNA elbow and *uS13*. Such a state

6. Discussion



is consistent with a P/E-like peptidyl-tRNA position, presumably accompanied by rotation of the small ribosomal subunit (Alejo and Blanchard, 2017). In line with this assignment, peptide release by puromycin dramatically shifted the equilibrium towards the high-FRET state (**Figure 65**). These observations support the notion that subunit rotation can occur within the POST-translocation ribosome when EF-G is bound.

When the bacterial ribosome was translocated in the presence of GMPPNP, our collaborators observed strikingly different behaviors (**Figure 64D, E**). Specifically, the overall lifetime of the TI-POST-1 state (0.28 ± 0.03 FRET) was extended more than 50-fold (**Figure 64D**). Strikingly, inspection of individual smFRET traces on path to complete translocation revealed that the GMPPNP-stalled transition from the TI-POST-1 state featured reversible transitions between TI-POST-1 and higher-FRET, POST-like configurations (**Figure 64E**). This unexpected finding suggests that non-productive translocation attempts can precede completion of translocation. Although the bacterial ribosome translocated by EF-G•GMPPNP ultimately reached the same FRET states as in the presence of GTP, the high-FRET ($0.78 \pm$

6. Discussion

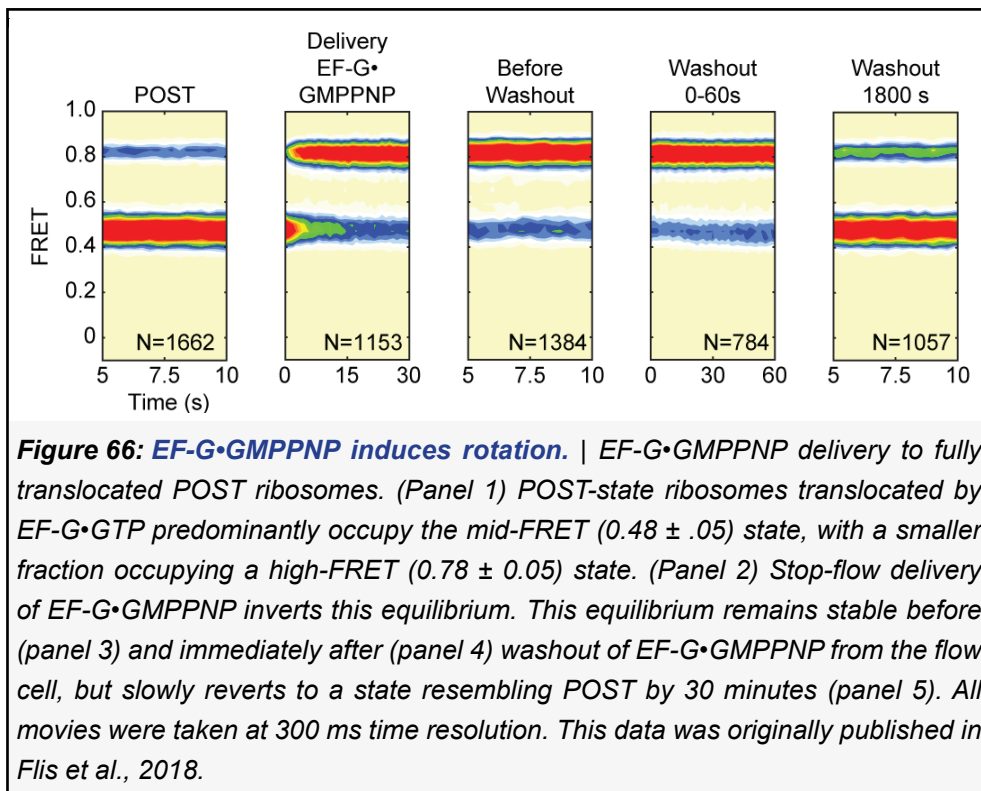


Figure 66: EF-G•GMPPNP induces rotation. | EF-G•GMPPNP delivery to fully translocated POST ribosomes. (Panel 1) POST-state ribosomes translocated by EF-G•GTP predominantly occupy the mid-FRET ($0.48 \pm .05$) state, with a smaller fraction occupying a high-FRET (0.78 ± 0.05) state. (Panel 2) Stop-flow delivery of EF-G•GMPPNP inverts this equilibrium. This equilibrium remains stable before (panel 3) and immediately after (panel 4) washout of EF-G•GMPPNP from the flow cell, but slowly reverts to a state resembling POST by 30 minutes (panel 5). All movies were taken at 300 ms time resolution. This data was originally published in Flis et al., 2018.

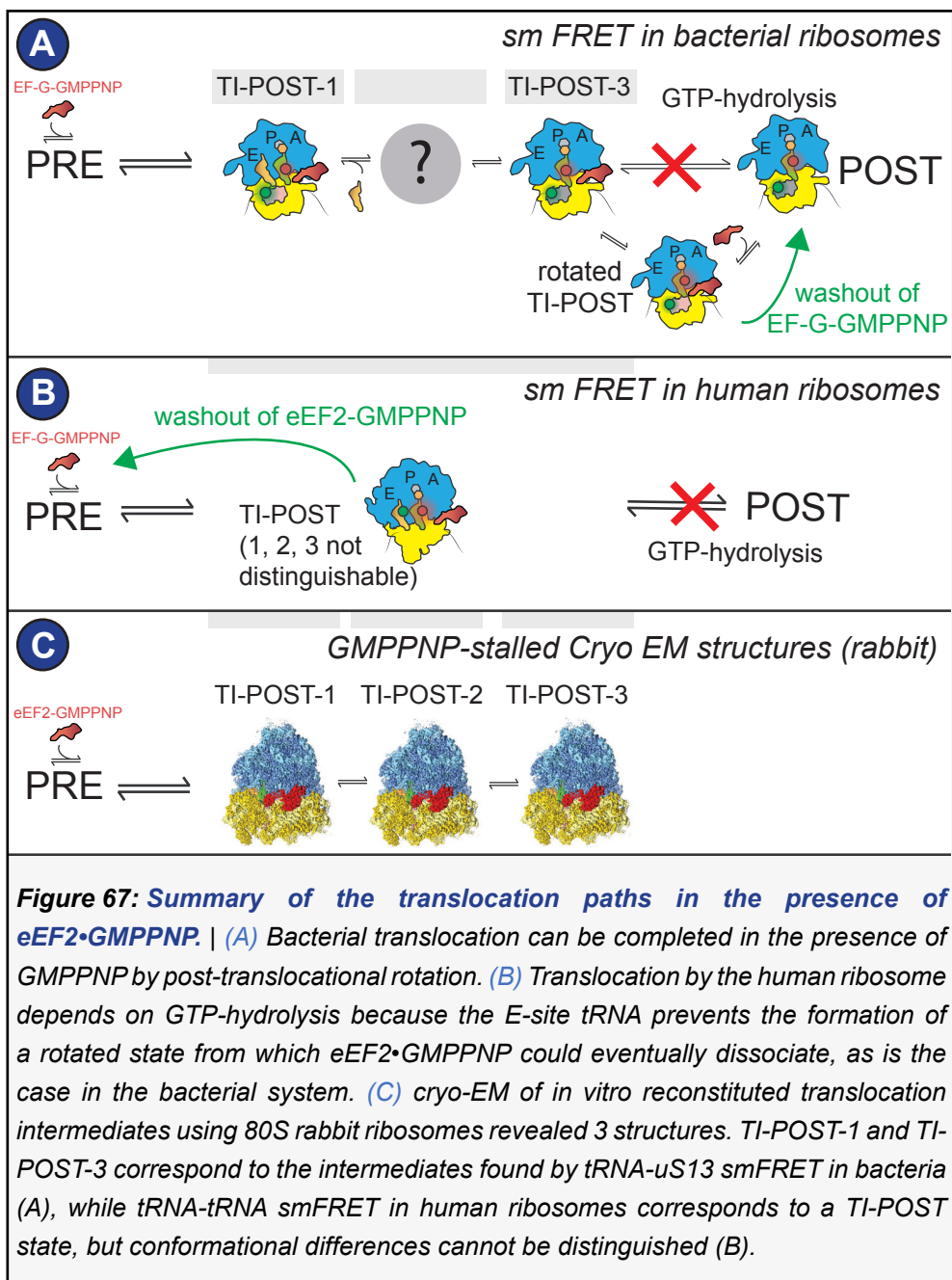
0.05) POST state conformation predominated at equilibrium (**Figure 64D**). This altered equilibrium persisted while EF-G•GMPPNP was present in the flow cell.

In contrast to the experiments on the mammalian ribosome (**Figure 60 and Figure 61**), EF-G•GMPPNP washout from the flow cell did not lead to reversion to the PRE state, but instead generated a ribosome complex that was indistinguishable from the canonical POST complex obtained with EF-G•GTP (**Figure 64D**). Addition of EF-G•GMPPNP to fully-translocated POST ribosomes rapidly returned the system to the high-FRET state (**Figure 66**), in line with the established kinetics of EF-G•GMPPNP binding (Munro et al., 2010).

In summary, the absence/presence of an E-site tRNA appears to be key for the outcome of translocation and an important feature that distinguishes mammalian from bacterial translocation mechanisms: E site tRNA dissociation in bacterial ribosomes allows for transient excursions to a rotated state in which the peptidyl-tRNA adopts a hybrid-like position.

Apparently, EF-G•GMPPNP binding is sufficient to overcome interactions of the 3'-CCA end of peptidyl-tRNA bearing short

6. Discussion



nascent peptides with the 50S P site to promote a P/E-like tRNA position. From this rotated state, EF-G could dissociate, such that the bacterial ribosome can complete translocation (however, in a prolonged time compared to physiological conditions) and reach a classical POST state. The so far obtained structures of EFG•GMPPNP- or EFG•GMPPCP-containing, rotated bacterial ribosomes (Connell et al., 2007; Pulk and Cate, 2013; Tourigny et al., 2013; Zhou et al., 2013) most likely represent this state after translocation (**Figure 67A**).

6. Discussion

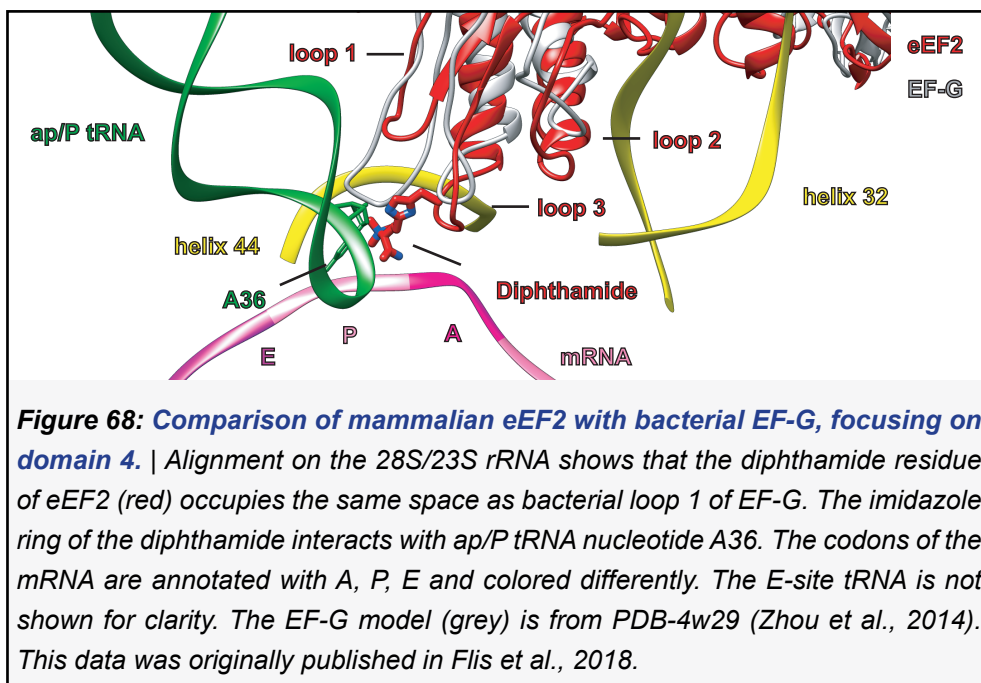
In mammalian ribosomes, although the bound eEF2•GMPPNP would favor a rotated state, this rotated state cannot be accomplished by pushing the peptidyl tRNA into the P/E state, because the deacyl tRNA in the E site is preventing such a conformational change. Instead, the ribosome has to choose back-translocation as a mean to get into a rotated conformation. This becomes apparent under washout (**Figure 67B**) and explains why we could capture ‘authentic’ translocation intermediates in the case of the mammalian ribosome (**Figure 67C**).

Concerning the role of GTP-hydrolysis, the transition from GTP to GDP via GDP+P_i doesn’t seem to be directly coupled (mechanically) to the conformational changes in the ribosome and the process of translocation. eEF2•GTP has a high affinity to bind both rotated (rotated PRE) and unrotated (classical PRE) ribosomes. Once bound, eEF2•GTP will drive the ribosome into a rotated conformation and stabilize the rotation (Ferguson et al., 2015). eEF2•GDP has a higher propensity to dissociate from the ribosome, and thus transition of eEF2•GTP to eEF2•GDP supports the thermodynamically driven 40S back-rotation and completion of translocation via eEF2•GDP dissociation.

The role of the diphthamide modification of eEF2

Comparison of eEF2 from our mammalian TI-POST structures with EF-G from a high-resolution bacterial TI-POST intermediate (Zhou et al., 2014) reveals that loop 1 in eEF2 is shorter than loop 1 in EF-G (**Supplemental figure 6**). In bacterial translocation intermediates, loop 1 forms a barrier on one side of the pe/E tRNA that in the mammalian case cannot be provided by loop 1. Interestingly, the diphthamide-residue protrudes from the neighboring loop 2 into the space created by the loop 1 deletion in the mammalian eEF2 (**Figure 68**). Thus, although we cannot see the complete density for the diphthamide modification, indicating its flexibility, it may be required to restrict the movement of the peptidyl-tRNA during translocation. Accordingly, the diphthamide residue may contribute to the pawl function of eEF2.

6. Discussion



Possible advantages of an ordered A-site codon

The mRNA position and conformation in TI-POST-1 to -3 is similar to that observed in the presence of an A-site tRNA undergoing codon-anticodon interaction (Selmer et al., 2006; Zhou et al., 2013). Although of distinct conformation, a structured mRNA quadruple is also decoded by eRF1 during translation termination. Clamping the upstream part of the mRNA and enforcing a stacked arrangement of mRNA nucleotides in the A site could ensure unimpeded elongation by maintaining the reading frame and priming the mRNA for the next round of tRNA selection.

6.2 The other eEF2-complexes

In vitro reconstituted 80S•tRNA₂•mRNA•eEF2•GDP complexes

Why is eEF2•GDP bound on the ribosome? In the previous section we stated that it is the non-hydrolysability of GMPPNP that makes it impossible for eEF2•GMPPNP to leave the 80S ribosome after translocation, and that it is the active state of the G-domain that

6. Discussion

induces rotation and reverse translocation. Surprisingly, we also see an 80S•tRNA₂•mRNA•eEF2-GDP complex when using GTP instead of GMPPNP.

The formation of the complex could have taken place via at least two possible paths: normal eEF2•GTP catalyzed translocation without dissociation of eEF2•GDP after GTP hydrolysis, or reverse translocation induced by either eEF2•GTP or eEF2•GDP. The latter possibility is more likely, as the puromycin reaction indicates nearly quantitative translocation. eEF2•GTP has a high affinity to bind both rotated (rotated PRE) and unrotated (classical PRE) ribosomes (Ferguson et al., 2015), and binding to the classical POST state will induce back-translocation, as proposed in this work and others (Nilsson and Nygård, 1992; Shoji et al., 2009; Susorov et al., 2018). As the tRNAs are bound in the chimeric hybrid state and the conformational similarity with TI-POST-2 is high, it seems that the TI-POST-2-like conformation is a local minimum in the energy landscape of such a reverse translocation.

Is back-translocation induced by eEF2•GDP or eEF2•GTP? Binding of eEF2•GDP could take place at very high concentrations; on the other hand, the affinity of eEF2•GTP to the ribosome is much higher. In the present experimental setting we have unimpeded translocation and thus accumulation of eEF2•GDP.

Finally, the presented structure could still be a mixture of several substates. The fragmentation of the 40S head in the final density map indicates that there are several 40S head conformations present. Because the 40S body/platform seems to be stable, this indicates that the final map might represent a mixture of TI-POST-2 and TI-POST-3-like conformations. Importantly, however, whereas in the above described GMPPNP case, TI-POST-3 is the largest population, here, the TI-POST-2-conformation predominates.

Ex vivo found monosomes binding eEF2

Interestingly, endogenous eEF2 has also been found to bind to monosomes that were purified *ex vivo* (Khatter et al., 2015; Voorhees

6. Discussion

et al., 2014). However, they do not represent actively translocating ribosomes. An actively translocating ribosome, captured as an intermediate, must be bound to an mRNA, and possess at least the Peptidyl tRNA, disclosed as such by evidence for a bound peptide chain at the CCA end. This is not the case in the observed structures; moreover, eEF2 in both cases is probably in a GDP conformation, suggested by the poorly resolved domain 3 and switch I.

Thus, although not contributing much to solving the mechanism of translocation, these structures could be helpful in understanding possible other roles of eEF2. The suggestion of such complexes being a storage form for subunits, that in case of elevated levels of translation could quickly be reintroduced to the active pool of ribosomes, seems probable, as storing subunits as 80S complexes would maintain the ratio of small and large subunits (Khatter et al., 2015; Voorhees et al., 2014).

6.3 The expansion of the polysomal energy landscape

What is the role of serum deprivation and serum restimulation and eS6 phosphorylation in the energy landscape of translation?

The energy landscape of translation elongation is quite similar in samples 'S' and 'D' and the distribution of states resembles the results from Behrmann et al., 2015. Thus, neither serum deprivation nor serum restimulation have any influence on the energy landscape of translation such as we can observe it via cryo-EM. Importantly, the polysomes that are isolated with the methods used in this work represent the cytosolic fraction only. The concentrations of digitonin used for cell lysis spare the other compartments in the cell, and thus for example the polysomes associated with the endoplasmatic reticulum are not part of the obtained sample (Jagannathan et al., 2011).

In the case of the sample from rabbit reticulocyte lysate ribosomes (80S reassembled from purified subunits), focused classification

6. Discussion

revealed a difference in ES6B (expansion segment 6B) definition, as if there could be different states distinguished by stability/flexibility. This observation led to the working hypothesis that it could be differences eS6 phosphorylation states within TI-POST-3 that led to splitting into two populations. Thus, comparison of 80S from the two polysome datasets that were treated to attenuate/enhance eS6 phosphorylation (via serum deprivation and restimulation) was expected to reveal marked differences. However, the RELION refinement focused on the 40S body/platform revealed no difference in the eS6 region of reconstructed 80S ribosomes from samples 'D' and 'S' except a slight difference in length of eS6 reminiscent of the one observed in the TI-POST-3 state. This small difference, however, could be as well attributed to a difference in quality or number of particle images.

Thus, with the employed methods, no clear evidence could be gathered for an effect of serum on either the energy landscape of translation nor the structure of eS6 and neighbouring 18S rRNA. As stated in section 5 (results), it cannot be excluded that further in-depth investigation of these structures, e.g. via focused classification, would reveal more heterogeneity, e.g. in the rRNA expansion segments, such as in the case of TI-POST-3 for samples 'D' and 'S'. However, the fact that no clear difference could be seen with the applied method already suggests that if there are differences, they are most likely small. Therefore, at present, we cannot find that eS6 phosphorylation has a major impact on the structure.

The phenotype of phosphorylation-incapable eS6 is striking. Phosphorylation of eS6 is associated with many physiological processes and has received much attention from a medical perspective. It appears to be required for the regulation of cell size, proliferation and hypertrophic responses under growth conditions and in some tissues, it might be involved in neoplastic transformation (Granot et al., 2009; Ruvinsky et al., 2005, 2009). In addition, there is evidence that eS6 phosphorylation is associated to adequate insulin secretion in glucose homeostasis and normal

6. Discussion

muscle function (Meyuhas et al., 2008 and references therein). Phosphorylation of eS6 by the S6K and RSK kinases is facilitated upon activation of the PI3K/mTOR/S6K and Ras/Raf/ERK/RSK kinase pathways, respectively. Dysregulated activity of these pathways causes malignant transformation and is involved in immunological responses and metabolic diseases (Bhat et al., 2015). Accordingly, eS6 phosphorylation is monitored as a biomarker for pathogenic signal transduction to guide therapeutic strategies, in particular the implementation of the mTORC1 inhibitors Sirolimus and Everolimus in malignancies and transplant rejection (Chaisuparat et al., 2013; Kim et al., 2013).

An explanation for the discrepancy between the fact that we couldn't find significant differences both concerning the impact on structure and on energy landscape, and on the other hand the observed phenotype, could lie in the different character of ribosomal particles due to their association with different organelles. Notably, there is a difference in conformation of ES6B observable in TI-POST-3, which was reconstituted using reticulocyte lysate ribosomes, whereas no significant difference was observed in the sample of cytosolic polysomes from HEK-cells. An important distinction between these two samples is the ribosome's association to cellular organelles: Ribosomal samples from reticulocytes consist of a cytosolic as well as an ER-associated fraction (Hallinan et al., 1962), whereas the method used to obtain polyribosomes from HEK-cells selectively isolates cytosolic polysomes (Jagannathan et al., 2011).

Thus, eS6 phosphorylation could play a role in the redistribution of ribosomes across other cell compartments and its effects may be observable only in specific fractions of ribosomes. An observation that supports the hypothesis that serum has an influence on the compartmentalization of ribosomes - whether this again could be mediated via eS6 phosphorylation, is an open question - is that consistently, the cell lysate from serum-stimulated HEK cells shows a lower OD (A260) (**Figure 42A**).

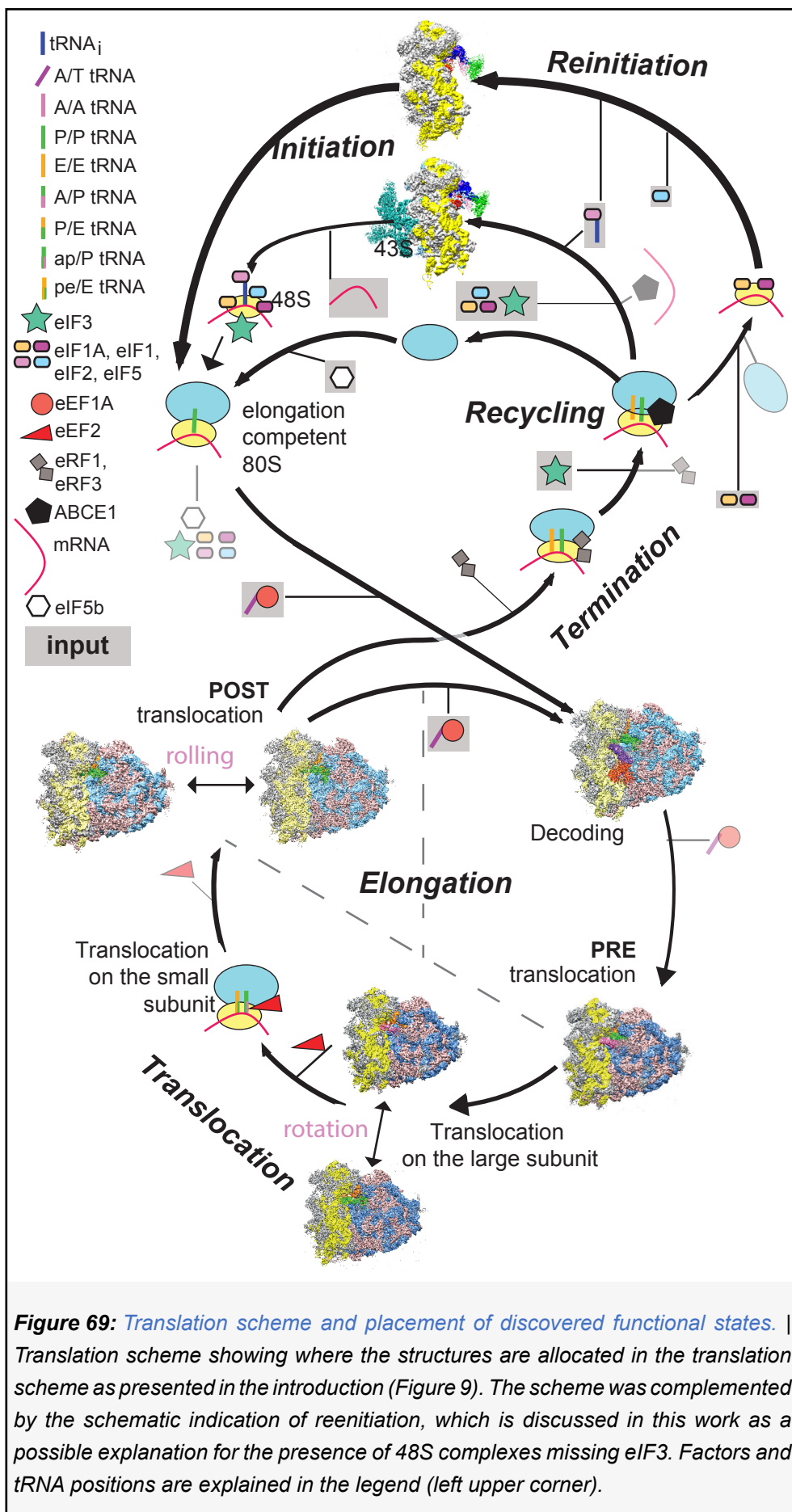
6. Discussion

Previously uncharacterized *ex vivo* states of translation

Different to the previously found sub states of the elongation cycle, the here presented results include differently rotated PRE states. Whereas previously, the rotated PRE state could be separated in two substates distinguished by tRNA positions (A/A, P/E and A/P, P/E), the here presented sorting adds another layer which is a difference in rotation within the rotated PRE states themselves (**Figure 51**). Very probably, the better data quality compared to previous datasets (Behrmann et al., 2015) is responsible for our ability to observe those states. Because of the hierarchical approach of sorting, differences in 40S subunit rotation override the fluctuations of the tRNAs. Further sorting of the states regarding the tRNA states revealed a dependence of the tRNA positions on the rotation state (**Figure 52**). In summary, these observations reveal that thermodynamically driven translocation on the 60S subunit includes local minima that can be observed via cryo-EM. Notably, it is always the A-site tRNA that varies, while the E site tRNA is stably bound in the same position on the 60S subunit in each of the rotated states.

Decoding is a slow, multistep process in translation. Heterogeneity within the ternary complex of decoding complexes has been observed before in the dataset from Behrmann et al., 2015 (data not published). The decoding complex found in the here presented samples has the potential to resolve post-GTP-hydrolysis steps of decoding. The two structures presented in the results section indicate that interdomain movements of eEF1A after GTP hydrolysis are important for the subsequent tRNA accommodation. The interdomain movement of eEF1A is associated with stalk base movement towards the tRNA (**Figure 54**), and it can be hypothesized that release of eEF1A-P-stalk contacts allow inward movement of the stalk base and initiate tRNA accommodation.

6. Discussion



6. Discussion

Notably, in theory this state could contain some particle images belonging the recycling complexes, which have been found in (Behrmann et al., 2015), but could not be revealed in our two datasets at DC6 level.

Finally, some few 2D classes showed particles resembling 40S subunits. An *ab initio* reconstruction in cryoSPARC using these classes resulted in a 48S complex. The presence of such a complex has not been described for previous polysomal datasets, however, their existence in yeast has been observed biochemically (Shirokikh et al., 2017). The work of Shirokikh and colleagues revealed that 48S complexes in polysomes accumulate on the start codon AUG or at the 3' end of the mRNA. The presence of a 48S complex without eIF3 could be explained by interpreting those complexes as reinitiation complexes, or 48S complexes, which are translating specific (e.g. highly unstructured) mRNAs (Kumar et al., 2016; Lee et al., 2016; Skabkin et al., 2013).

What is the limiting process that led to our observation of native initiation complexes? Apparently, the 48S complexes are ‘waiting’ for the next step to happen, which is ultimately the joining of the 60S subunit. It could be the availability of eIF5, eIF5B and/or 60S that is limiting. It is not clear if the presented states contain eIF2 bound to GDP or GTP, because the resolution is too low to say that. If it was GTP, this would be an indication for GTP-hydrolysis being a limiting factor, either because of limited availability of eIF5, or because of the speed of the reaction itself. If it was GDP, another possibility could be that some rearrangements in the ternary complex after GTP-hydrolysis must occur before subunit joining and that this is limiting. We could then draw a parallel to the apparently very slow rearrangements of eEF1A after GTP hydrolysis in decoding. GTP hydrolysis is only the first step and is followed by slow structural rearrangements of eEF1A and eIF2 that allow for their dissociation and the next steps of translation. This stickiness of some factors seems to be a peculiarity of the mammalian system, as in no other polysomal samples yet have any ribosomal structures been observed bound to factors (data

6. Discussion

from coworkers from Spahn group: Jan-Thorben Christiansen, Kaori Yamamoto and Julia Smirnova made reconstructions of bacterial, yeast and plant 80S polysomal energy landscapes, to be published).

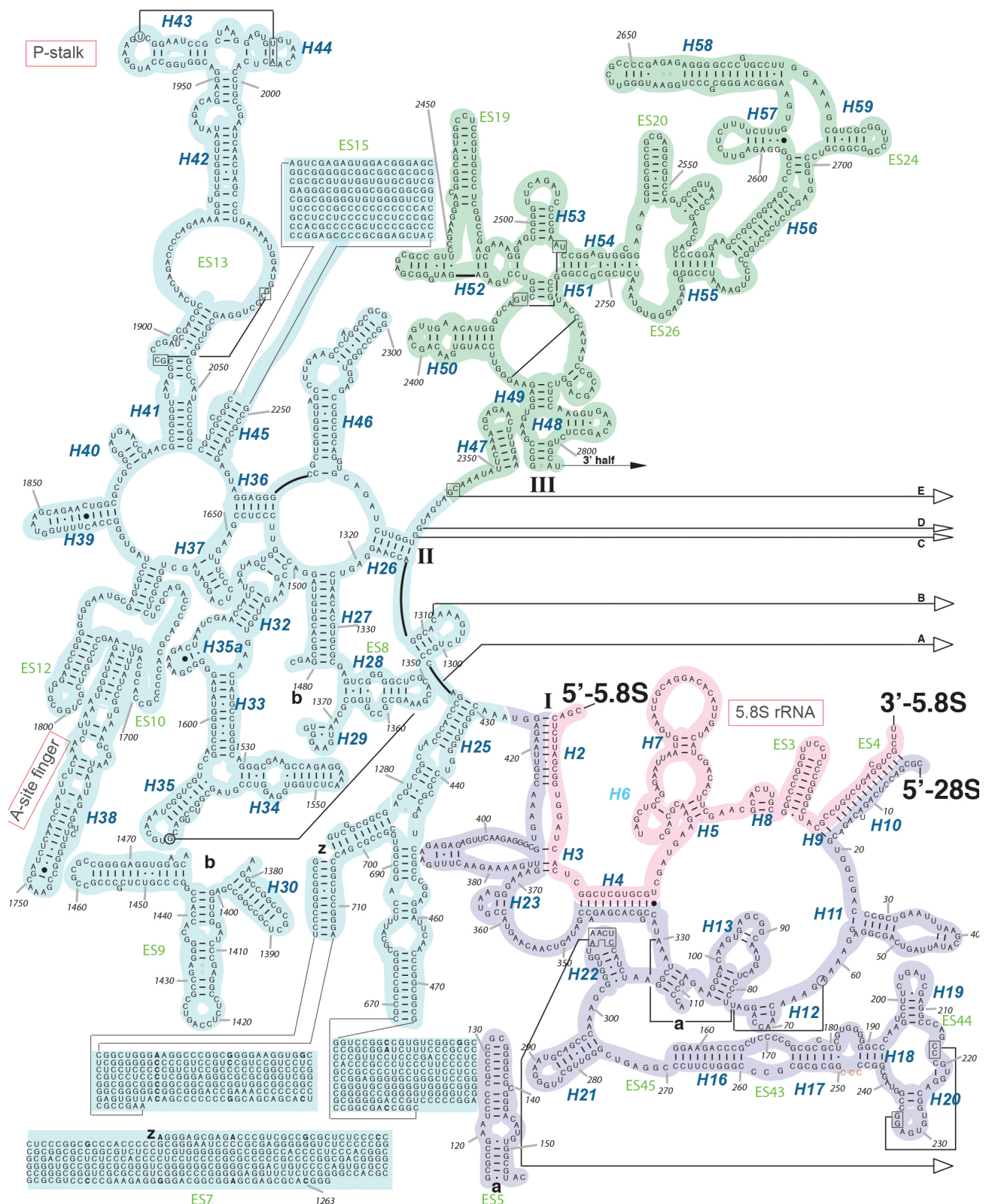
Figure 69 summarizes the expanded energy landscape and allocates the reconstructions from this work in a schematic representation of translation.

7. Conclusions

- GMPPNP stalls late steps of translocation in mammalian 80S ribosomes, leading to three late translocation intermediates captured via cryo-EM. Accordingly, GTP hydrolysis facilitates late steps of translocation in mammalian ribosomes, an observation corroborated by smFRET experiments.
- There are fundamental differences between bacterial and mammalian translocation that are due to E-site tRNA dissociation. Previous bacterial EF-G•GMPP(N/C)P bound structures can now be interpreted as late translocation intermediates after E-site tRNA dissociation, which are driven into a rotated state by EF-G•GMPP(N/C)P.
- The energy landscape of translating polysomes is not influenced by serum deprivation and serum restimulation, different from eS6-phosphorylation, which is enhanced in ribosomes from serum restimulated HEK-cells. Inspection of the eS6 region indicates that there is no major impact of eS6 phosphorylation on the structure of the ribosomal 40S subunit.
- The polysomal energy landscape can be subdivided into many more substate than are so far known, and the data which was collected in this work is of high quality that allows to reveal several substates of rotation in the PRE-states as well as movement in the factor of decoding states.
- Previously not observed snapshots of native initiation complexes from actively translating polysomes were captured in this work via cryo-EM and indicate that 48S initiation complex are present on the mRNA in two variants: with eIF3 and without.

8. Supplemental material

Secondary Structure: large subunit ribosomal RNA - 5' half *Homo sapiens*

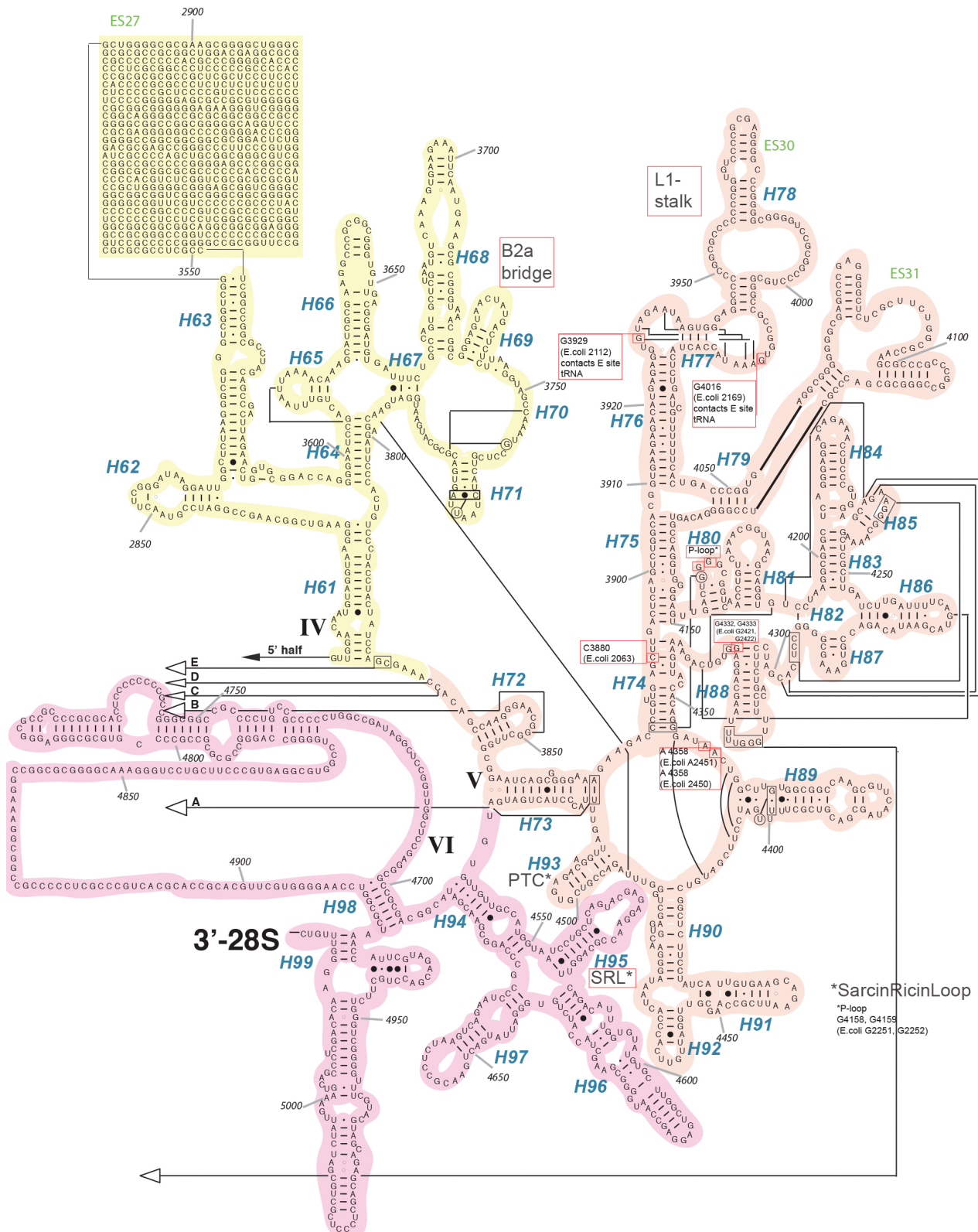


This map - version 2, October 2018 - is downloaded from <http://www.jufali.userpage.fu-berlin.de/rRNA-maps>.
This map is a numbered and annotated version of the entry 'Homo sapiens (J01866, M111167), 2.1 June 1997.
Citation and related information available at <http://www.rna.ccb.utexas.edu>.

Supplemental Figure 1: 28S rRNA secondary structure. 5' end.

8. Supplemental Material

Secondary Structure: large subunit ribosomal RNA - 3' half *Homo sapiens*

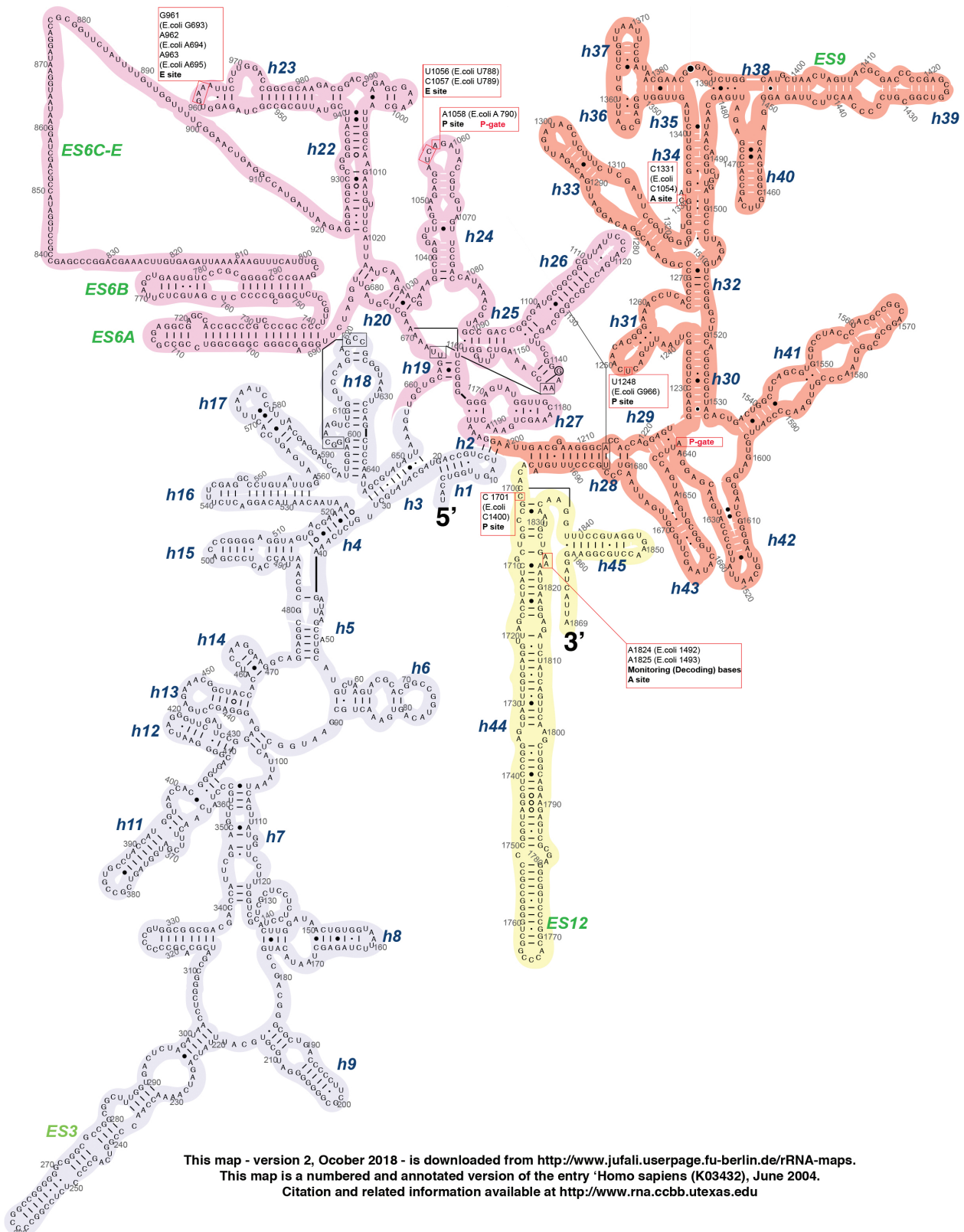


Supplemental Figure 2: 28S rRNA secondary structure, 3' end.

8. Supplemental Material

Secondary Structure: small subunit ribosomal RNA

Homo sapiens



8. Supplemental Material

Table 1

New name [#]	Taxonomic range [*]	Bacteria name	Yeast name	Human name
bS1	B	S1	–	–
eS1	A E	–	S1	S3A
uS2	B A E	S2	S0	SA
uS3	B A E	S3	S3	S3
uS4	B A E	S4	S9	S9
eS4	A E	–	S4	S4
uS5	B A E	S5	S2	S2
bS6	B	S6	–	–
eS6	A E	–	S6	S6
uS7	B A E	S7	S5	S5
eS7	E	–	S7	S7
uS8	B A E	S8	S22	S15A
eS8	A E	–	S8	S8
uS9	B A E	S9	S16	S16
uS10	B A E	S10	S20	S20
eS10	E	–	S10	S10
uS11	B A E	S11	S14	S14
uS12	B A E	S12	S23	S23
eS12	E	–	S12	S12
uS13	B A E	S13	S18	S18
uS14	B A E	S14	S29	S29
uS15	B A E	S15	S13	S13
bS16	B	S16	–	–
uS17	B A E	S17	S11	S11
eS17	A E	–	S17	S17
bS18	B	S18	–	–
uS19	B A E	S19	S15	S15
eS19	A E	–	S19	S19
bS20	B	S20	–	–
bS21	B	S21	–	–
bTHX	THX	–	–	–
eS21	E	–	S21	S21
eS24	A E	–	S24	S24
eS25	A E	–	S25	S25
eS26	E	–	S26	S26
eS27	A E	–	S27	S27
eS28	A E	–	S28	S28
eS30	A E	–	S30	S30
eS31	A E	–	S31	S27A
RACK1	E	–	Asc1	RACK1

[#] b: bacterial, e: eukaryotic, u: universal.

^{*} B: bacteria, A: archaea, E: eukaryotes.

Table 2

New name [#]	Taxonomic range [*]	Bacteria name	Yeast name	Human name
uL1	B A E	L1	L1	L10A
uL2	B A E	L2	L2	L8
uL3	B A E	L3	L3	L3
uL4	B A E	L4	L4	L4
uL5	B A E	L5	L11	L11
uL6	B A E	L6	L9	L9
eL6	E	–	L6	L6
eL8	A E	–	L8	L7A
bl9	B	L9	–	–
uL10	B A E	L10	P0	P0
uL11	B A E	L11	L12	L12
bl12	B	L7/L12	–	–
uL13	B A E	L13	L16	L13A
eL13	A E	–	L13	L13
uL14	B A E	L14	L23	L23
eL14	A E	–	L14	L14
uL15	B A E	L15	L28	L27A
eL15	A E	–	L15	L15
uL16	B A E	L16	L10	L10
bl17	B	L17	–	–
uL18	B A E	L18	L5	L5
eL18	A E	–	L18	L18
bl19	B	L19	–	–
eL19	A E	–	L19	L19
bl20	B	L20	–	–
eL20	E	–	L20	L18A
bl21	B	L21	–	–
eL21	A E	–	L21	L21
uL22	B A E	L22	L17	L17
eL22	E	–	L22	L22
uL23	B A E	L23	L25	L23A
uL24	B A E	L24	L26	L26
eL24	A E	–	L24	L24
bl25	B	L25	–	–
bl27	B	L27	–	–
eL27	E	–	L27	L27
bl28	B	L28	–	–
eL28	E	–	–	L28
uL29	B A E	L29	L35	L35
eL29	E	–	L29	L29
uL30	B A E	L30	L7	L7
eL30	A E	–	L30	L30
bl31	B	L31	–	–
eL31	A E	–	L31	L31
bl32	B	L32	–	–
eL32	A E	–	L32	L32
bl33	B	L33	–	–
eL33	A E	–	L33	L35A
bl34	B	L34	–	–
eL34	A E	–	L34	L34
bl35	B	L35	–	–
bl36	B	L36	–	–
eL36	E	–	L36	L36
eL37	A E	–	L37	L37
eL38	A E	–	L38	L38
eL39	A E	–	L39	L39
eL40	A E	–	L40	L40
eL41	A E	–	L41	L41
eL42	A E	–	L42	L36A
eL43	A E	–	L43	L37A
P1/P2	A E	–	P1/P2 (AB)	P1/P2 (ab)

[#] b: bacterial, e: eukaryotic, u: universal.

^{*} B: bacteria, A: archaea, E: eukaryotes.

Supplemental Figure 4: Ribosomal proteins of the small subunit (Ban et al., 2014)

8. Supplemental Material

		Domain 1 (G-domain) G1 P-loop	G2 switch 1	
H.sapiens	1	mvnftvdQIRAIMDKKANIRNMSVIAHVHDHGKSTLTDSDLVCKAGiiASARAGE---	TRFTDTRKDEQERCITIKSTAIS	76
S.cerev.	1	mvaftvdQMRSILMDKVTVNRNMSVIAHVHDHGKSTLTDSDLVQRAGiiSAAKAGE---	ARFTDTRKDEQERGITIKSTAIS	76
T.thermo	1	-----MAVKVEYDLKRLRNIGIAAHIDAGKTTERILYYTG--RIHKIGEVHEGAATMDFMEQERERGITITAAVTT		71
E.coli	1	-----MARTTP--IARYRNIGISAHI DAGTTTERILFYTG--VNHKIGEVHDAATMDWMEQE QERGITITSAATT		69
EF-G 2	1	-----MIRTVA-----LVGHAGSGKTLTEALLYKTG--AKERRGRVEEGTTTDTPEAKLHRTTVRTGVAP		61
		G3 switch 2	G4	
H.sapiens	77	LFYElsendlnfiKQS KDGAGFLINLIDSPGHVDFSSSEVTAALRVTDGALVVVDCVSGVCVQTE TVLRQ AIAERIKP VLM		156
S.cerev.	77	LYSEMsdedvkeiKQKTDGNSFLINLIDSPGHVDFSSSEVTAALRVTDGALVVVDTIEGVCVQTE TVLRQ ALGERIKP VVV		156
T.thermo	72	CFW-----KDHRINIIDTPGHVDFTIEVERSMRVLDGAIIVFDSSQGVEPQSETVWRQAEKYKVPRIAF		135
E.coli	70	AFWS-----GMAKQYEPRINIIDTPGHVDFTIEVERSMRVLDGAVMVYCAVGGVQPQSETVWRQANKYKVPRIAF		140
EF-G 2	62	LLFR-----G-----HRVFLLDAPGYGDFVGEIRGALEAADALVA SAEAGVQVGTERAWTVAERLGLPRMV		125
		G4 switch 3	G-domain insert	
H.sapiens	157	MNKMDRALLELQLEPEELYQT FqriveNVNVIISTYGEGESPMGNIMIDPV LGTVGF GSGLHWFA TLKQFAEMYVAKF		236
S.cerev.	157	INKVDRALLELQSKEDLYQT FarveSVN VIV STYADEV--LGDVQVYPARGTVAFGSGLHWFA TIRQFATRYAKF		233
T.thermo	136	ANKMDK TGA DLWL VIRT MQERL----GARPVVMQLPI GREDT FSGI IDV LRMK AYT YGN-DLG TDIREI PIPEEYLDQA		209
E.coli	141	VNKMDR MGANFLKVVNQIKTRL----GANPVPLQLAIGAEEHFTGVVDLVKMKAINWN DADQGVTF EYEDI PADM VELA		215
EF-G 2	126	VTKL DK-GGDYY ALLED LRSTL----GP-ILPIDLPL YEGGK WVG LI DV FH GKA RYEN---GEER EAEP PPEER ERV		194
H.sapiens	237	AAKGEQLGPAERAKK vEDMMKKLWG Dryfd pangk fsksatSPEGKKL PRTFCQLILDPIFkvfdaimnf kke etakli		316
S.cerev.	234	GV-----DKA K----MMDRLWGD sfffpk t k wtnk dt DAEGKPLERA FNMF ILDP I Frlft aimnf kk deip vll		300
T.thermo	210	REYHEKLVEVAADF DE-NIMLK YLEGE-----EPTEEELVAAIRKG TIDLKI-----		255
E.coli	216	NEWHQNLIESAAEASE-ELME KYLG -----ELTEAEIKGALRQ RVLNNEI-----		261
EF-G 2	195	QRFRQEVLEAIVETDE-G LLE KYLEGE-----EVTGEALEKAFHEAVRRG LL-----		240
H.sapiens	317	ekLDIKL DSED KDKEGKPLL KAVM Rrw l pagd all q mti HLPSPVTAQKYRC ELLyeg pPDDEAAMGIKSCDPKGPLMM		396
S.cerev.	301	ekLEIVLKGDEK DLEGK ALL KV VM Rkf lpa ad alle miv l HLPSPVTAQAYRAE Qlyeg pADDANCIAIKNC DPKA DML		380
T.thermo	256	--TPVFLGSALKNKVQ LLL DAVV D-----YLPSPLDIPPIK GTT----PEGE--V VEIHPDPNGPLAA		311
E.coli	262	--ILVTCGSAFKNKVQ AML DAVID-----YLPSPVDV PAINGIL----DDGKDTPAER HAS DDEPFSA		319
EF-G 2	241	--YPVALAS GEREI GVPL LILE-----ALPS PTE-----RFGDGPPLA		279
H.sapiens	397	YISKMVPTSDKGRF yAFGRVFSGLVSTGLKVRim gpNYTPGKKE dlylkPIQRTI LMMGRYVEPIEDVPCGNIVGLVGVD		476
S.cerev.	381	YVSKMVPTSDKGRF yAFGRV FAGTVKSGQKV Ri qgp NYVPGKK Ddl fikAIQRV LMMGRF VEPIDCPAGNIIGLVGID		460
T.thermo	312	LAFKIMADPYV GRL-TFIRVYSGT LSGSYVY---NTTKGRKE----RVARLLRMHANHREEVEELKAGDLGAVVGLK		381
E.coli	320	LAFKIA TDPFVG NL-TFFRVYSGV VNSGDTVL---NSVKA ARE----RFGRIVQMHANKREEIKEVRAGDIAAAIGLK		389
EF-G 2	280	KVFKVQVDPFMGQV-AYLRLYRGR LKPGDSLQ---S--EAGQV----RLPHLYVPMGKDLLEVEEAEAGFVLGVPKAE		347

8. Supplemental Material

477	QflVKTGTITTFEHAHNMRVMKFSV-----SPVVRVAVEAKNPADLPKLVEGLKRLAKSDPMVQCII-EESGEHIIAGA	549	H.sapiens
461	QflLKTGTLTTSEAHNMVKMFKFSV-----SPVVQVAVEVKNANDLPKLVEGLKRLSKSDPCVLTYM-SESGEHIVAGT	533	S.cerev.
382	E--TITGDTLVGEDAPRVLIESIEV-----PEPVIDVAIEPKTKADQEQLSALARLAEEDEPTFRVSTHPETGQTIIISGM	454	T.thermo
390	D--VTTGDTLCDPDAP-IIERMEF-----PEPVISIAVEPPTKADQEKMGLALGRLAKEDPSFRVWTDEESNQTIIAGM	461	E.coli
348	G--LHRGMVLWQGEKP---ESEEVpfarlPDPNVPVALHPKGRTDEARLGEALRKLLLEDPSLKLERQEETGELLWGH	421	EF-G 2
loop 1			
550	GELHLEICLKDLLEDHaCIPIKKSDPVVSYRETVSEES-----NVLC <u>LSKSPNKHNR</u> LYMKARPFPDGlaedidkgevs	624	H.sapiens
534	GELHLEICLQDLEHDHaGVPLKISPPVVAYRETVESES-----SQTA <u>LSKSPNKHNR</u> IYLKAEPIDEEvslaiengiinp	608	S.cerev.
455	GELHLEIIVDRLKREF-KVDANVGKPQVAYRETITKPV-DVEGKFIRQT <u>GGRGQYGHV</u> KIKVEPLPRG-----	520	T.thermo
462	GELHLDIIVDRMKREF-NVEANVGKPQVAYRETIRQKVtDVEGKHAKQS <u>GGRGQYGHV</u> VIDMYPLEPG-----	528	E.coli
422	GELHLATAKERLQ-DY-GVEVEFSVPKVPYRETICKVA-EGQGKYKKQ <u>GGH</u> QYGDVWLRLEPASE-----	485	EF-G 2
loop 2			
625	rqelkqrarylaekyewdvaearkiwcfgPDGTGPNILT <u>DITKGVqYLNEIKDSVVAGF</u> QWATKEGALCEENMRGVRFDV	704	H.sapiens
609	rddfkararimaddygwdvtdarkiwcfgPDGNNGPNLVID <u>QTKAVqYLHEIKDSVVAAF</u> QWATKEGPIFGEEMRSVRVNI	688	S.cerev.
521	-----S-GFEFNNA <u>IVGGV</u> -IPKEYIPAVQKGIEAMQSGPLIGFPVVDIKVT	567	T.thermo
529	-----SNPKGYEFIND <u>IKGGV</u> -IPGEYIPAVDKGIQEQLKAGPLAGYPVVDMGIRL	578	E.coli
486	-----YGFEWR <u>ITGGV</u> -IPSKYQEAIEEGIKEAAKKVLAGFPVMGFKAIV	530	EF-G 2
diphthamide			
loop 3			
705	HDVT <u>LHADAIHRGGQ</u> IIPTArrCLYASVLTAQPRLMPEPIYLVEIQCPEQVVGIIYGVLNKRGHVFEEQVAGtpMFVV	784	H.sapiens
689	LDVT <u>LHADAIHRGGQ</u> IIPTMrATYAGFLLADPKIQEPVFLVEIQCPEQAVGGIYSVNLNNKRQGVVSEEQRPGtpLFTV	768	S.cerev.
568	YDGS <u>YHEVDSSSEMAFKIAGSM</u> --AIKEAVQKGDPVILEPIMRVEVTPEEYMDVIGDLNARRGQILGMEPRGN--AQVI	643	T.thermo
579	HFGS <u>YHDVDSSELAFKLAASI</u> --AFKEGFKKAKPVILLEPIMKVEVETPEENTGDVIGDLSSRRGMLKGQESEVT--GVKI	654	E.coli
531	YNGS <u>YHEVDSSDIAFO</u> QIAASL--AFKKVMAEAHPVLLEPIYRLKVLAPQERVGDVLSDLQARRGRILGMEQEGA--LSVV	606	EF-G 2
785	KAYLPVNESFGFTAIDRSNTGGQAFPQCVFDHWQILPgdpfdnsSRPSQVVAETRKRKG1kegipaldnfldkl	858	H.sapiens
769	KAYLPVNESFGFTGELRQATGGQAFPQMVFDHWSTLGsdpldptSKAGEIVLAARKRHGmkeevpgwqeyydkl	842	S.cerev.
644	RAFVPLAEMFGYATDLRSKTQGRGSFVMFFDHYQEVP-----KQVQEKLII--KGQ-----	691	T.thermo
655	HAEVPLSEMFGYATQLRSLTGRASYTMEFLKYDEAP-----SNVAQAVIEARGK-----	704	E.coli
607	HAEVPLAEVLEYYKALPGLTGGAGAYTLEFSHYAEVP-----PHLAQRIVQERAQEG-----	658	EF-G 2

Supplemental Figure 6: Alignment of EF-G and eEF2 from different domains of life.(BLAST was used for alignment). The (rough) annotation of the switches, G-motifs and loops is based on the literature and PDB-6gz3 (Bourne et al., 1991; Czworkowski et al., 1994; Flis et al., 2018).

9. References

- Abeyrathne, P.D., Koh, C.S., Grant, T., Grigorieff, N., and Korostelev, A.A. (2016). Ensemble cryo-EM uncovers inchworm-like translocation of a viral IRES through the ribosome. *Elife* 5, 1–31.
- Adams, P.D., Afonine, P. V., Bunkóczki, G., Chen, V.B., Davis, I.W., Echols, N., Headd, J.J., Hung, L.-W., Kapral, G.J., Grosse-Kunstleve, R.W., et al. (2010). PHENIX : a comprehensive Python-based system for macromolecular structure solution. *Acta Crystallogr. Sect. D Biol. Crystallogr.* 66, 213–221.
- Afonina, Z.A., Myasnikov, A.G., Khabibullina, N.F., Belorusova, A.Y., Menetret, J.-F., Vasiliev, V.D., Klaholz, B.P., Shirokov, V.A., and Spirin, A.S. (2013). Topology of mRNA chain in isolated eukaryotic double-row polyribosomes. *Biochem.* 78, 445–454.
- Afonina, Z.A., Myasnikov, A.G., Shirokov, V.A., Klaholz, B.P., and Spirin, A.S. (2014). Formation of circular polyribosomes on eukaryotic mRNA without cap-structure and poly(A)-tail: a cryo electron tomography study. *Nucleic Acids Res.* 42, 9461–9469.
- Agirrezabala, X., Lei, J., Brunelle, J.L., Ortiz-Meoz, R.F., Green, R., and Frank, J. (2008). Visualization of the Hybrid State of tRNA Binding Promoted by Spontaneous Ratcheting of the Ribosome. *Mol. Cell* 32, 190–197.
- Alejo, J.L., and Blanchard, S.C. (2017). Miscoding-induced stalling of substrate translocation on the bacterial ribosome. *Proc. Natl. Acad. Sci.* 114, 201707539.
- Allen, G.S., Zavialov, A., Gursky, R., Ehrenberg, M., and Frank, J. (2005). The Cryo-EM Structure of a Translation Initiation Complex from *Escherichia coli*. *Cell* 121, 703–712.
- Amunts, A., Brown, A., Toots, J., Scheres, S.H.W., and Ramakrishnan, V. (2015). The structure of the human mitochondrial ribosome. *Science* (80-.). 348, 95–98.
- Andersen, C.B.F., Becker, T., Blau, M., Anand, M., Halic, M., Balar, B., Mielke, T., Boesen, T., Pedersen, J.S., Spahn, C.M.T., et al. (2006). Structure of eEF3 and the mechanism of transfer RNA release from the E-site. *Nature* 443, 663–668.
- Antoun, A., Pavlov, M.Y., Andersson, K., Tenson, T., and Ehrenberg, M. (2003).

9. References

- The roles of initiation factor 2 and guanosine triphosphate in initiation of protein synthesis.* EMBO J. 22, 5593–5601.
- Archer, S.K., Shirokikh, N.E., Beilharz, T.H., and Preiss, T. (2016). *Dynamics of ribosome scanning and recycling revealed by translation complex profiling.* Nature 535, 570–574.
- Bah, A., Vernon, R.M., Siddiqui, Z., Krzeminski, M., Muhandiram, R., Zhao, C., Sonenberg, N., Kay, L.E., and Forman-Kay, J.D. (2015). *Folding of an intrinsically disordered protein by phosphorylation as a regulatory switch.* Nature 519, 106–109.
- Ban, N., Beckmann, R., Cate, J.H.D., Dinman, J.D., Dragon, F., Ellis, S.R., Lafontaine, D.L.J., Lindahl, L., Liljas, A., Lipton, J.M., et al. (2014). *A new system for naming ribosomal proteins.* Curr. Opin. Struct. Biol. 24, 165–169.
- Bandi, H.R., Ferrari, S., Krieg, J., Meyer, H.E., and Thomas, G. (1993). *Identification of 40 S ribosomal protein S6 phosphorylation sites in Swiss mouse 3T3 fibroblasts stimulated with serum.* J. Biol. Chem. 268, 4530–4533.
- Bartesaghi, A., Aguerrebere, C., Falconieri, V., Banerjee, S., Earl, L.A., Zhu, X., Grigorieff, N., Milne, J.L.S., Sapiro, G., Wu, X., et al. (2018). *Atomic Resolution Cryo-EM Structure of β-Galactosidase.* Structure 26, 848–856.e3.
- Barth-Baus, D., Stratton, C.A., Parrott, L., Myerson, H., Meyuhas, O., Templeton, D.J., Landreth, G.E., and Hensold, J.O. (2002). *S6 phosphorylation-independent pathways regulate translation of 5'-terminal oligopyrimidine tract-containing mRNAs in differentiating hematopoietic cells.* Nucleic Acids Res. 30, 1919–1928.
- Becker, T., Armache, J.-P., Jarasch, A., Anger, A.M., Villa, E., Sieber, H., Motaal, B.A., Mielke, T., Berninghausen, O., and Beckmann, R. (2011). *Structure of the no-go mRNA decay complex Dom34–Hbs1 bound to a stalled 80S ribosome.* Nat. Struct. Mol. Biol. 18, 715–720.
- Behrmann, E., Loerke, J., Budkevich, T. V., Yamamoto, K., Schmidt, A., Penczek, P.A., Vos, M.R., Bürger, J., Mielke, T., Scheerer, P., et al. (2015). *Structural Snapshots of Actively Translating Human Ribosomes.* Cell 161, 845–857.
- Belandia, B., Brautigan, D., and Martín-Pérez, J. (1994). *Attenuation of ribosomal protein S6 phosphatase activity in chicken embryo fibroblasts transformed by Rous sarcoma virus.* Mol. Cell. Biol. 14, 200–206.
- Belardinelli, R., Sharma, H., Peske, F., Wintermeyer, W., and Rodnina, M. V. (2016). *Translocation as continuous movement through the ribosome.* RNA Biol. 13, 1–7.
- Ben-Shem, A., Jenner, L., Yusupova, G., and Yusupov, M. (2010). *Crystal Structure of the Eukaryotic Ribosome.* Science (80-.). 330, 1203–1209.

9. References

- Ben-Shem, A., Garreau de Loubresse, N., Melnikov, S., Jenner, L., Yusupova, G., and Yusupov, M. (2011). The structure of the eukaryotic ribosome at 3.0 Å resolution. *Science* (80-). 334, 1524–1529.
- Berman, H.M. (2000). The Protein Data Bank. *Nucleic Acids Res.* 28, 235–242.
- Bhat, M., Robichaud, N., Hulea, L., Sonenberg, N., Pelletier, J., and Topisirovic, I. (2015). Targeting the translation machinery in cancer. *Nat. Rev. Drug Discov.* 14, 261–278.
- Blanchard, S.C., Kim, H.D., Gonzalez, R.L., Puglisi, J.D., and Chu, S. (2004). tRNA dynamics on the ribosome during translation. *Proc. Natl. Acad. Sci.* 101, 12893–12898.
- Bommer, U., Burkhardt, N., Junemann, R., Spahn, C.M.T., Triana-Alonso, and F. Nierhaus, K.H. (1997). Ribosomes and polysomes. In *Subcellular Fractionation: A Practical Approach*, J. Graham and D. Rickwood, Eds., (Washington, DC: IRL Press), pp. 271–301.
- Bourne, H.R., Sanders, D.A., and McCormick, F. (1991). The GTPase superfamily: conserved structure and molecular mechanism. *Nature* 349, 117–127.
- Brandt, F., Carlson, L.-A.A., Hartl, F.U., Baumeister, W., and Grünewald, K. (2010). The Three-Dimensional Organization of Polyribosomes in Intact Human Cells. *Mol. Cell* 39, 560–569.
- Brilot, A.F., Korostelev, A.A., Ermolenko, D.N., and Grigorieff, N. (2013). Structure of the ribosome with elongation factor G trapped in the pretranslocation state. *Proc. Natl. Acad. Sci.* 110, 20994–20999.
- Budkevich, T., Giesebricht, J., Altman, R.B., Munro, J.B., Mielke, T., Nierhaus, K.H., Blanchard, S.C., and Spahn, C.M.T. (2011). Structure and Dynamics of the Mammalian Ribosomal Pretranslocation Complex. *Mol. Cell* 44, 214–224.
- Budkevich, T. V, El'skaya, A. V, and Nierhaus, K.H. (2008). Features of 80S mammalian ribosome and its subunits. *Nucleic Acids Res.* 36, 4736–4744.
- Budkevich, T. V, Giesebricht, J., Behrmann, E., Loerke, J., Ramrath, D.J.F., Mielke, T., Ismer, J., Hildebrand, P.W., Tung, C.S., Nierhaus, K.H., et al. (2014). Regulation of the mammalian elongation cycle by subunit rolling: A eukaryotic-specific ribosome rearrangement. *Cell* 158, 121–131.
- Carter, A.P., Clemons, W.M., Brodersen, D.E., Morgan-Warren, R.J., Hartsch, T., Wimberly, B.T., and Ramakrishnan, V. (2001). Crystal structure of an initiation factor bound to the 30S ribosomal subunit. *Science* 291, 498–501.
- Chaisuparat, R., Rojanawatsirivej, S., and Yodsanga, S. (2013). Ribosomal Protein

9. References

- S6 Phosphorylation is Associated with Epithelial Dysplasia and Squamous Cell Carcinoma of the Oral Cavity. *Pathol. Oncol. Res.* 19, 189–193.
- Chauvin, C., Koka, V., Nouschi, A., Mieulet, V., Hoareau-Aveilla, C., Dreazen, A., Cagnard, N., Carpentier, W., Kiss, T., Meyuhas, O., et al. (2014). Ribosomal protein S6 kinase activity controls the ribosome biogenesis transcriptional program. *Oncogene* 33, 474–483.
- Chen, J.Z., and Grigorieff, N. (2007). SIGNATURE: A single-particle selection system for molecular electron microscopy. *J. Struct. Biol.* 157, 168–173.
- Chen, C., Cui, X., Beausang, J.F., Zhang, H., Farrell, I., Cooperman, B.S., and Goldman, Y.E. (2016). Elongation factor G initiates translocation through a power stroke. *Proc. Natl. Acad. Sci.* 113, 7515–7520.
- Chen, J., Petrov, A., Tsai, A., O'Leary, S.E., and Puglisi, J.D. (2013). Coordinated conformational and compositional dynamics drive ribosome translocation. *Nat. Struct. Mol. Biol.* 20, 718–727.
- Chen, V.B., Arendall, W.B., Headd, J.J., Keedy, D.A., Immormino, R.M., Kapral, G.J., Murray, L.W., Richardson, J.S., and Richardson, D.C. (2010). MolProbity : all-atom structure validation for macromolecular crystallography. *Acta Crystallogr. Sect. D Biol. Crystallogr.* 66, 12–21.
- Cheng, Y., Grigorieff, N., Penczek, P.A., and Walz, T. (2015). A Primer to Single-Particle Cryo-Electron Microscopy. *Cell* 161, 438–449.
- Chou, F.-C., Sripakdeevong, P., Dibrov, S.M., Hermann, T., and Das, R. (2012). Correcting pervasive errors in RNA crystallography through enumerative structure prediction. *Nat. Methods* 10, 74–76.
- Connell, S.R., Takemoto, C., Wilson, D.N., Wang, H., Murayama, K., Terada, T., Shirouzu, M., Rost, M., Schüler, M., Giesebeck, J., et al. (2007). Structural Basis for Interaction of the Ribosome with the Switch Regions of GTP-Bound Elongation Factors. *Mol. Cell* 25, 751–764.
- Cornish, P. V., Ermolenko, D.N., Noller, H.F., and Ha, T. (2008). Spontaneous Intersubunit Rotation in Single Ribosomes. *Mol. Cell* 30, 578–588.
- Crick, F. (1970). Central Dogma of Molecular Biology. *Nature* 227, 561–563.
- Cukras, A.R., Southworth, D.R., Brunelle, J.L., Culver, G.M., and Green, R. (2003). Ribosomal proteins S12 and S13 function as control elements for translocation of the mRNA:tRNA complex. *Mol. Cell* 12, 321–328.
- Czworkowski, J., and Moore, P.B. (1997). The conformational properties of elongation factor G and the mechanism of translocation. *Biochemistry* 36, 10327–

9. References

10334.

Czworkowski, J., Wang, J., Steitz, T.A., and Moore, P.B. (1994). The crystal structure of elongation factor G complexed with GDP, at 2.7 Å resolution. *EMBO J.* 13, 3661–3668.

Danev, R., and Baumeister, W. (2017). Expanding the boundaries of cryo-EM with phase plates. *Curr. Opin. Struct. Biol.* 46, 87–94.

Dauden, M.I., Kosinski, J., Kolaj-Robin, O., Desfosses, A., Ori, A., Faux, C., Hoffmann, N.A., Onuma, O.F., Breunig, K.D., Beck, M., et al. (2017). Architecture of the yeast Elongator complex. *EMBO Rep.* 18, 264–279.

Davydova, E.K., and Ovchinnikov, L.P. (1990). ADP-ribosylated elongation factor 2 (ADP-ribosyl-EF-2) is unable to promote translocation within the ribosome. *FEBS Lett.* 261, 350–352.

Davydova, E.K., Malinin, N.L., and Ovchinnikov, L.P. (1993). Ribosomes terminated *in vitro* are in a tight association with non???phosphorylated elongation factor 2 (eEF???2) and GDP. *Eur. J. Biochem.* 215, 291–296.

Dubochet, J., Adrian, M., Chang, J.J., Homo, J.C., Lepault, J., McDowall, A.W., and Schultz, P. (1988). Cryo-electron microscopy of vitrified specimens. *Q. Rev. Biophys.* 21, 129–228.

Duncan, R., and McConkey, E.H. (1982). Preferential Utilization of Phosphorylated 40-S Ribosomal Subunits during Initiation Complex Formation. *Eur. J. Biochem.* 123, 535–538.

Dunkle, J.A., Wang, L., Feldman, M.B., Pulk, A., Chen, V.B., Kapral, G.J., Noeske, J., Richardson, J.S., Blanchard, S.C., and Cate, J.H.D. (2011). Structures of the Bacterial Ribosome in Classical and Hybrid States of tRNA Binding. *Science* (80-). 332, 981–984.

Egerton, R.F., Li, P., and Malac, M. (2004). Radiation damage in the TEM and SEM. *Micron* 35, 399–409.

Eliseev, B., Yeramala, L., Leitner, A., Karuppasamy, M., Raimondeau, E., Huard, K., Alkalaeva, E., Aebersold, R., and Schaffitzel, C. (2018). Structure of a human cap-dependent 48S translation pre-initiation complex. *Nucleic Acids Res.* 46, 2678–2689.

Emsley, P., and Cowtan, K. (2004). Coot: Model-building tools for molecular graphics. *Acta Crystallogr. Sect. D Biol. Crystallogr.* 60, 2126–2132.

Fasken, M.B., and Corbett, A.H. (2009). Mechanisms of nuclear mRNA quality

9. References

- control. *RNA Biol.* 6, 237–241.
- Ferguson, A., Wang, L., Altman, R.B., Terry, D.S., Juette, M.F., Burnett, B.J., Alejo, J.L., Dass, R.A., Parks, M.M., Vincent, C.T., et al. (2015). Functional Dynamics within the Human Ribosome Regulate the Rate of Active Protein Synthesis. *Mol. Cell* 60, 475–486.
- Flis, J., Holm, M., Rundlet, E.J., Loerke, J., Hilal, T., Dabrowski, M., Bürger, J., Mielke, T., Blanchard, S.C., Spahn, C.M.T., et al. (2018). tRNA Translocation by the Eukaryotic 80S Ribosome and the Impact of GTP Hydrolysis. *Cell Rep.* 25, 2676–2688.e7.
- Frank, J., and Agrawal, R.K. (2000). A ratchet-like inter-subunit reorganization of the ribosome during translocation. *Nature* 406, 318–322.
- Frank, J., Penczek, P., and Liu, W. (1992). Alignment, classification, and three-dimensional reconstruction of single particles embedded in ice. *Scanning Microsc. Suppl.* 6, 11-20; discussion 20-2.
- Frank, J., Radermacher, M., Penczek, P., Zhu, J., Li, Y., Ladjadj, M., and Leith, A. (1996). SPIDER and WEB: Processing and Visualization of Images in 3D Electron Microscopy and Related Fields. *J. Struct. Biol.* 116, 190–199.
- Frauenfelder, H., Sligar, S.G., and Wolynes, P.G. (1991). The energy landscapes and motions of proteins. *Science* 254, 1598–1603.
- Gao, H., Zhou, Z., Rawat, U., Huang, C., Bouakaz, L., Wang, C., Cheng, Z., Liu, Y., Zavialov, A., Gursky, R., et al. (2007). RF3 Induces Ribosomal Conformational Changes Responsible for Dissociation of Class I Release Factors. *Cell* 129, 929–941.
- Gao, Y.-G.Y., Selmer, M., Dunham, C.M., Weixlbaumer, A., Kelley, A.C., and Ramakrishnan, V. (2009). The Structure of the Ribosome with Elongation Factor G Trapped in the Posttranslocational State. *Science* (80-.). 326, 694–699.
- Gavrilova, L.P., and Spirin, A.S. (1971). Stimulation of "non-enzymic" translocation in ribosomes by p-chloromercuribenzoate. *FEBS Lett.* 17, 324–326.
- Gavrilova, L.P., Kostiashkina, O.E., Koteliansky, V.E., Rutkevitch, N.M., and Spirin, A.S. (1976). Factor-free ("non-enzymic") and factor-dependent systems of translation of polyuridylic acid by *Escherichia coli* ribosomes. *J. Mol. Biol.* 101, 537–552.
- Gesteland, R.F., Cech, T.R., A. (1999). *The RNA World* (Cold Spring Harbor, New York).
- Granot, Z., Swisa, A., Magenheim, J., Stolovich-Rain, M., Fujimoto, W., Manduchi,

9. References

- E., Miki, T., Lennerz, J.K., Stoeckert, C.J., Meyuhas, O., et al. (2009). LKB1 regulates pancreatic beta cell size, polarity, and function. *Cell Metab.* 10, 296–308.
- Greber, B.J., Bieri, P., Leibundgut, M., Leitner, A., Aebersold, R., Boehringer, D., and Ban, N. (2015). The complete structure of the 55S mammalian mitochondrial ribosome. *Science* (80-). 348, 303–308.
- Gressner, A.M., and Wool, I.G. (1974). The stimulation of the phosphorylation of ribosomal protein S6 by cycloheximide and puromycin. *Biochem. Biophys. Res. Commun.* 60, 1482–1490.
- Hallinan, T., Eden, E., and North, R. (1962). The Structure and Composition of Rat Reticulocytes. *Blood* 20.
- Hansen, J.L., Schmeing, T.M., Moore, P.B., and Steitz, T.A. (2002). Structural insights into peptide bond formation. *Proc. Natl. Acad. Sci. U. S. A.* 99, 11670–11675.
- Harauz, G. and van Heel, M. (1986). Exact Filters for General Geometry Three Dimensional Reconstruction. *Optik (Stuttg)*. 146–156.
- Hartman, H., and Smith, T.F. (2010). GTPases and the origin of the ribosome. *Biol. Direct* 5, 36.
- Hashem, Y., and Frank, J. (2018). The Jigsaw Puzzle of mRNA Translation Initiation in Eukaryotes: A Decade of Structures Unraveling the Mechanics of the Process. *Annu. Rev. Biophys.* 47, annurev-biophys-070816-034034.
- Hashem, Y., Des Georges, A., Dhote, V., Langlois, R., Liao, H.Y., Grassucci, R.A., Hellen, C.U.T., Pestova, T. V., and Frank, J. (2013). XStructure of the mammalian ribosomal 43S preinitiation complex bound to the scanning factor DHX29. *Cell* 153, 1108–1119.
- van Heel, M., and Schatz, M. (2005). Fourier shell correlation threshold criteria. *J. Struct. Biol.* 151, 250–262.
- van Heel, M., and Schatz, M. (2017). REASSESSING THE REVOLUTIONS RESOLUTIONS. *BioRxiv* 224402.
- Hilal, T., Yamamoto, H., Loerke, J., Bürger, J., Mielke, T., and Spahn, C.M.T. (2016). Structural insights into ribosomal rescue by Dom34 and Hbs1 at near-atomic resolution. *Nat. Commun.* 7, 13521.
- Hirashima, A., and Kaji, A. (1970). Factor dependent breakdown of polysomes. *Biochem. Biophys. Res. Commun.* 41, 877–883.

9. References

- Horan, L.H., and Noller, H.F. (2007). Intersubunit movement is required for ribosomal translocation. *Proc. Natl. Acad. Sci. U. S. A.* 104, 4881–4885.
- Hutchinson, J.A., Shanware, N.P., Chang, H., and Tibbetts, R.S. (2011). Regulation of ribosomal protein S6 phosphorylation by casein kinase 1 and protein phosphatase 1. *J. Biol. Chem.* 286, 8688–8696.
- Inoue-Yokosawa, N., and Kaziro, Y. (1974). The role of guanosine triphosphate in translocation reaction catalyzed by elongation factor G. *Biochemistry* 249, 4321–4323.
- Isken, O., and Maquat, L.E. (2007). Quality control of eukaryotic mRNA: Safeguarding cells from abnormal mRNA function. *Genes Dev.* 21, 1833–1856.
- Jackson, R.J., Hellen, C.U.T., and Pestova, T. V (2010). The mechanism of eukaryotic translation initiation and principles of its regulation. *Nat. Rev. Mol. Cell Biol.* 11, 113–127.
- Jackson, R.J., Hellen, C.U.T., and Pestova, T. V (2012). Termination and post-termination events in eukaryotic translation. *Adv. Protein Chem. Struct. Biol.* 86, 45–93.
- Jagannathan, S., Nwosu, C., and Nicchitta, C. V. (2011). Analyzing mRNA Localization to the Endoplasmic Reticulum via Cell Fractionation. (Humana Press, Totowa, NJ), pp. 301–321.
- de Jong, A.F., and Van Dyck, D. (1993). Ultimate resolution and information in electron microscopy II. The information limit of transmission electron microscopes. *Ultramicroscopy* 49, 66–80.
- Juhling, F., Mori, M., Hartmann, R.K., Sprinzl, M., Stadler, P.F., and Putz, J. (2009). tRNAdb 2009: compilation of tRNA sequences and tRNA genes. *Nucleic Acids Res.* 37, D159–D162.
- Kaczmarz, S. (1937). Przyblizone rozwiazywanie ukladow rownan liniowych. – Angenäherte Auflösung von Systemen linearer Gleichungen. *Bulletin International de l'Académie Polonaise des Sciences et des Lettres. Classe des Sciences Mathématiques et Naturelles. Série A, Sciences M. Cl. Des Sci. Mathématiques Nat. Série A*, S, 55–357.
- Karbstein, K. (2011). Inside the 40S ribosome assembly machinery. *Curr. Opin. Chem. Biol.* 15, 657–663.
- Khatter, H., Myasnikov, A.G., Natchiar, S.K., and Klaholz, B.P. (2015). Structure of the human 80S ribosome. *Nature* 520, 640–645.

9. References

- Kim, S.-H., Jang, Y.H., Chau, G.C., Pyo, S., and Um, S.H. (2013). Prognostic significance and function of phosphorylated ribosomal protein S6 in esophageal squamous cell carcinoma. *26*.
- Kolupaeva, V.G., Unbehaun, A., Lomakin, I.B., Hellen, C.U.T., and Pestova, T. V (2005). Binding of eukaryotic initiation factor 3 to ribosomal 40S subunits and its role in ribosomal dissociation and anti-association. *RNA* *11*, 470–486.
- Kozak, M. (1999). Initiation of translation in prokaryotes and eukaryotes. *Gene* *234*, 187–208.
- Krieg, J., Olivier, A.R., and Thomas, G. (1988). Analysis of 40S Ribosomal Protein S6 Phosphorylation During the Mitogenic Response. *Methods Enzym.* *164*, 575–581.
- Kucukelbir, A., Sigworth, F.J., and Tagare, H.D. (2013). Quantifying the local resolution of cryo-EM density maps. *Nat. Methods* *11*, 63–65.
- Kuhlbrandt, W. (2014). The Resolution Revolution. *Science* (80-). *343*, 1443–1444.
- Kumar, P., Hellen, C.U.T., and Pestova, T. V (2016). Toward the mechanism of eIF4F-mediated ribosomal attachment to mammalian capped mRNAs. *Genes Dev.* *30*, 1573–1588.
- Lee, A.S.Y., Kranzusch, P.J., Doudna, J.A., and Cate, J.H.D. (2016). eIF3d is an mRNA cap-binding protein that is required for specialized translation initiation. *Nature* *536*, 96–99.
- Li, X., Mooney, P., Zheng, S., Booth, C.R., Braunfeld, M.B., Gubbens, S., Agard, D.A., and Cheng, Y. (2013). Electron counting and beam-induced motion correction enable near-atomic-resolution single-particle cryo-EM. *Nat. Methods* *10*, 584–590.
- Li, Y., MITSUHASHI, S., IKEJO, M., MIURA, N., KAWAMURA, T., HAMAKUBO, T., and UBUKATA, M. (2012). Relationship between ATM and Ribosomal Protein S6 Revealed by the Chemical Inhibition of Ser/Thr Protein Phosphatase Type 1. *Biosci. Biotechnol. Biochem.* *76*, 486–494.
- Liao, H.Y., Hashem, Y., and Frank, J. (2015). Efficient Estimation of Three-Dimensional Covariance and its Application in the Analysis of Heterogeneous Samples in Cryo-Electron Microscopy. *Structure* *23*, 1129–1137.
- Liljas, A., Ehrenberg, M., and Åqvist, J. (2011). Comment on "The mechanism for activation of GTP hydrolysis on the ribosome". *Science* *333*, 37; author reply 37.

9. References

- Ling, C., and Ermolenko, D.N. (2016). Structural insights into ribosome translocation. *Wiley Interdiscip. Rev. RNA* 7, 620–636.
- Lipson, S.G. (Stephen G., Lipson, H. (Henry), and Tannhauser, D.S. (David S. (1995). *Optical physics* (Cambridge University Press).
- Liu, T., Kaplan, A., Alexander, L., Yan, S., Wen, J. Der, Lancaster, L., Wickersham, C.E., Fredrick, K., Fredrik, K., Noller, H., et al. (2014). Direct measurement of the mechanical work during translocation by the ribosome. *Elife* 3, e03406.
- Lodish, H.F. (1974). Model for the regulation of mRNA translation applied to haemoglobin synthesis. *Nature* 251, 365–448.
- Loerke, J., Giesebrecht, J., and Spahn, C.M.T. (2010). Multiparticle Cryo-EM of Ribosomes. *Methods Enzymol.* 483, 161–177.
- Lomakin, I.B., and Steitz, T.A. (2013). The initiation of mammalian protein synthesis and mRNA scanning mechanism. *Nature* 500, 307–311.
- Mao, Y., Wang, L., Gu, C., Herschhorn, A., Désormeaux, A., Finzi, A., Xiang, S.-H., and Sodroski, J.G. (2013). Molecular architecture of the uncleaved HIV-1 envelope glycoprotein trimer. *Proc. Natl. Acad. Sci. U. S. A.* 110, 12438–12443.
- Maracci, C., and Rodnina, M. V. (2016). Review: Translational GTPases. *Biopolymers* 105, 463–475.
- Marcotrigiano, J., Gingras, A.C., Sonenberg, N., and Burley, S.K. (1999). Cap-dependent translation initiation in eukaryotes is regulated by a molecular mimic of eIF4G. *Mol. Cell* 3, 707–716.
- Márquez, V., Wilson, D.N., Tate, W.P., Triana-Alonso, F., and Nierhaus, K.H. (2004). Maintaining the ribosomal reading frame: The influence of the E site during translational regulation of release factor 2. *Cell* 118, 45–55.
- Martin-Pérez, J., and Thomas, G. (1983). Ordered phosphorylation of 40S ribosomal protein S6 after serum stimulation of quiescent 3T3 cells. *Proc. Natl. Acad. Sci. U. S. A.* 80, 926–930.
- Mastronarde, D.N. (2005). Automated electron microscope tomography using robust prediction of specimen movements. *J. Struct. Biol.* 152, 36–51.
- Mazmanian, S.K., Liu, G., Ton-That, H., and Schneewind, O. (1999). *Staphylococcus aureus* sortase, an enzyme that anchors surface proteins to the cell wall. *Science* 285, 760–763.

9. References

- Meister, G. (2011). *RNA biology : an introduction* (Wiley-VCH).
- Melnikov, S., Ben-Shem, A., Garreau de Loubresse, N., Jenner, L., Yusupova, G., and Yusupov, M. (2012). One core, two shells: bacterial and eukaryotic ribosomes. *Nat. Struct. Mol. Biol.* 19, 560–567.
- Meyuhas, O. (2008). Chapter 1 Physiological Roles of Ribosomal Protein S6: One of Its Kind. *Int. Rev. Cell Mol. Biol.* 268, 1–37.
- Meyuhas, O. (2015). Ribosomal Protein S6 Phosphorylation: Four Decades of Research. In *International Review of Cell and Molecular Biology*, (Elsevier Ltd), pp. 41–73.
- Mieulet, V., Roceri, M., Espeillac, C., Sotiropoulos, A., Ohanna, M., Oorschot, V., Klumperman, J., Sandri, M., and Pende, M. (2007). S6 kinase inactivation impairs growth and translational target phosphorylation in muscle cells maintaining proper regulation of protein turnover. *Am. J. Physiol. Physiol.* 293, C712–C722.
- Milon, P., Konevega, A.L., Gualerzi, C.O., and Rodnina, M. V (2008). Kinetic checkpoint at a late step in translation initiation. *Mol. Cell* 30, 712–720.
- Mirande, M. (2010). Processivity of translation in the eukaryote cell: Role of aminoacyl-tRNA synthetases. *FEBS Lett.* 584, 443–447.
- Mitchell, S.F., and Parker, R. (2014). Principles and Properties of Eukaryotic mRNPs. *Mol. Cell* 54, 547–558.
- Moazed, D., and Noller, H.F. (1989). Intermediate states in the movement of transfer RNA in the ribosome. *Nature* 342, 142–148.
- Mohan, S., and Noller, H.F. (2017). Recurring RNA structural motifs underlie the mechanics of L1 stalk movement. *Nat. Commun.* 8, 14285.
- Munro, J.B., Altman, R.B., O'Connor, N., and Blanchard, S.C. (2007). Identification of Two Distinct Hybrid State Intermediates on the Ribosome. *Mol. Cell* 25, 505–517.
- Munro, J.B., Sanbonmatsu, K.Y., Spahn, C.M.T., and Blanchard, S.C. (2009). Navigating the ribosome's metastable energy landscape. *Trends Biochem. Sci.* 34, 390–400.
- Munro, J.B., Altman, R.B., Tung, C.-S., Sanbonmatsu, K.Y., and Blanchard, S.C. (2010). A fast dynamic mode of the EF-G-bound ribosome. *EMBO J.* 29, 770–781.
- Murray, J., Savva, C.G., Shin, B.S., Dever, T.E., Ramakrishnan, V., and Fernández, I.S. (2016). Structural characterization of ribosome recruitment and translocation

9. References

by type IV IRES. *Elife* 5.

Myasnikov, A.G., Afonina, Z.A., Ménétret, J.-F.F., Shirokov, V.A., Spirin, A.S., and Klaholz, B.P. (2014). The molecular structure of the left-handed supra-molecular helix of eukaryotic polyribosomes. *Nat. Commun.* 5, 5294.

Nguyen, K., and Whitford, P.C. (2016). Steric interactions lead to collective tilting motion in the ribosome during mRNA–tRNA translocation. *Nat. Commun.* 7, 10586.

Nielsen, P.J., Duncan, R., and McConkey, E.H. (1981). Phosphorylation of Ribosomal Protein S6 Relationship to Protein Synthesis in HeLa Cells. *Eur. J. Biochem* 120, 523–527.

Nierhaus, K.H. (1991). The assembly of prokaryotic ribosomes. *Biochimie* 73, 739–755.

Nierhaus, K.H. (1993). Solution of the ribosome riddle: how the ribosome selects the correct aminoacyl-tRNA out of 41 similar contestants. *Mol. Microbiol.* 9, 661–669.

Nilsson, L., and Nygård, O. (1992). Reduced puromycin sensitivity of translocated polysomes after the addition of elongation factor 2 and non-hydrolysable GTP analogues. *FEBS Lett.* 309, 89–91.

Nissen, P., Hansen, J., Ban, N., Moore, P.B., and Steitz, T.A. (2000). The structural basis of ribosome activity in peptide bond synthesis. *Science* 289, 920–930.

Ogle, J.M., Murphy IV, F. V., Tarry, M.J., and Ramakrishnan, V. (2002). Selection of tRNA by the ribosome requires a transition from an open to a closed form. *Cell* 111, 721–732.

Oppenheimer, N.J., and Bodley, J.W. (1981). Diphtheria toxin. Site and configuration of ADP-ribosylation of diphthamide in elongation factor 2. *J. Biol. Chem.* 256, 8579–8581.

Orlova, E. V., and Saibil, H.R. (2011). Structural Analysis of Macromolecular Assemblies by Electron Microscopy. *Chem. Rev.* 111, 7710–7748.

Panić, L., Tamarut, S., Sticker-Jantscheff, M., Barkić, M., Solter, D., Uzelac, M., Grabušić, K., and Volarević, S. (2006). Ribosomal protein S6 gene haploinsufficiency is associated with activation of a p53-dependent checkpoint during gastrulation. *Mol. Cell. Biol.* 26, 8880–8891.

Pelletier, J., and Sonenberg, N. (1988). Internal initiation of translation of eukaryotic mRNA directed by a sequence derived from poliovirus RNA. *Nature* 334, 320–325.

9. References

- Penczek, P.A., Frank, J., and Spahn, C.M.T. (2006). A method of focused classification, based on the bootstrap 3D variance analysis, and its application to EF-G-dependent translocation. *J. Struct. Biol.* 154, 184–194.
- Pende, M., Um, S.H., Mieulet, V., Sticker, M., Goss, V.L., Mestan, J., Mueller, M., Fumagalli, S., Kozma, S.C., and Thomas, G. (2004). S6K1(-/-)/S6K2(-/-) mice exhibit perinatal lethality and rapamycin-sensitive 5'-terminal oligopyrimidine mRNA translation and reveal a mitogen-activated protein kinase-dependent S6 kinase pathway. *Mol. Cell. Biol.* 24, 3112–3124.
- Pestova, T. V, and Hellen, C.U.T. (2003). Translation elongation after assembly of ribosomes on the Cricket paralysis virus internal ribosomal entry site without initiation factors or initiator tRNA. *Genes Dev.* 17, 181–186.
- Pettersen, E.F., Goddard, T.D., Huang, C.C., Couch, G.S., Greenblatt, D.M., Meng, E.C., and Ferrin, T.E. (2004). UCSF Chimera--a visualization system for exploratory research and analysis. *J. Comput. Chem.* 25, 1605–1612.
- Pisarev, A. V, Skabkin, M.A., Pisareva, V.P., Skabkina, O. V, Rakotondrafara, A.M., Hentze, M.W., Hellen, C.U.T., and Pestova, T. V (2010). The role of ABCE1 in eukaryotic posttermination ribosomal recycling. *Mol. Cell* 37, 196–210.
- Pulk, A., and Cate, J.H.D. (2013). Control of Ribosomal Subunit Rotation by Elongation Factor G. *Science* (80-.). 340, 1235970–1235970.
- Punjani, A., Rubinstein, J.L., Fleet, D.J., and Brubaker, M.A. (2017). cryoSPARC: algorithms for rapid unsupervised cryo-EM structure determination. *Nat. Methods* 14, 290–296.
- Radon, J. (1986). On the determination of functions from their integral values along certain manifolds. *IEEE Trans. Med. Imaging* 5, 170–176.
- Ramesh, M., and Woolford, J.L. (2016). Eukaryote-specific rRNA expansion segments function in ribosome biogenesis. *RNA* 22, 1153–1162.
- Ramrath, D.J.F., Yamamoto, H., Rother, K., Wittek, D., Pech, M., Mielke, T., Loerke, J., Scheerer, P., Ivanov, P., Teraoka, Y., et al. (2012). The complex of tmRNA-SmpB and EF-G on translocating ribosomes. *Nature* 485, 526–529.
- Ramrath, D.J.F., Lancaster, L., Sprink, T., Mielke, T., Loerke, J., Noller, H.F., and Spahn, C.M.T. (2013). Visualization of two transfer RNAs trapped in transit during elongation factor G-mediated translocation. *Proc. Natl. Acad. Sci.* 110, 20964–20969.
- Ramrath, D.J.F., Niemann, M., Leibundgut, M., Bieri, P., Prange, C., Horn, E.K., Leitner, A., Boehringer, D., Schneider, A., and Ban, N. (2018). Evolutionary shift

9. References

- toward protein-based architecture in trypanosomal mitochondrial ribosomes. *Science* (80-). 362, eaau7735.
- Ratje, A.H., Loerke, J., Mikolajka, A., Brünner, M., Hildebrand, P.W., Starosta, A.L., Dönhöfer, A., Connell, S.R., Fucini, P., Mielke, T., et al. (2010). Head swivel on the ribosome facilitates translocation by means of intra-subunit tRNA hybrid sites . *Nature* 468, 4–9.
- Reimer, L., and Kohl, H. (Helmut) (2008). *Transmission electron microscopy : physics of image formation* (Springer).
- Rodnina, M. V., Savelsbergh, A., Katunin, V.I., and Wintermeyer, W. (1997). Hydrolysis of GTP by elongation factor G drives tRNA movement on the ribosome. *Nature* 385, 37–41.
- Rogg, H., Wehrli, W., and Staehelin, M. (1969). Isolation of mammalian transfer RNA. *BBA Sect. Nucleic Acids Protein Synth.* 195, 13–15.
- Rohou, A., and Grigorieff, N. (2015). CTFFIND4: Fast and accurate defocus estimation from electron micrographs. *J. Struct. Biol.* 192, 216–221.
- Rosenthal, P.B., and Henderson, R. (2003). Optimal determination of particle orientation, absolute hand, and contrast loss in single-particle electron cryomicroscopy. *J. Mol. Biol.* 333, 721–745.
- Roux, P.P., Shahbazian, D., Vu, H., Holz, M.K., Cohen, M.S., Taunton, J., Sonenberg, N., and Blenis, J. (2007). RAS/ERK Signaling Promotes Site-specific Ribosomal Protein S6 Phosphorylation via RSK and Stimulates Cap-dependent Translation. *J. Biol. Chem.* 282, 14056–14064.
- Roy, A., Kucukural, A., and Zhang, Y. (2010). I-TASSER: a unified platform for automated protein structure and function prediction. *Nat. Protoc.* 5, 725–738.
- Rubinstein, J.L., and Brubaker, M.A. (2015). Alignment of cryo-EM movies of individual particles by optimization of image translations. *J. Struct. Biol.* 192, 188–195.
- Ruvinsky, I., Sharon, N., Lerer, T., Cohen, H., Stolovich-rain, M., Nir, T., Dor, Y., Zisman, P., and Meyuhas, O. (2005). Ribosomal protein S6 phosphorylation is a determinant of cell size and glucose homeostasis. *Genes Dev.* 2199–2211.
- Ruvinsky, I., Katz, M., Dreazen, A., Gielchinsky, Y., Saada, A., Freedman, N., Mishani, E., Zimmerman, G., Kasir, J., and Meyuhas, O. (2009). Mice Deficient in Ribosomal Protein S6 Phosphorylation Suffer from Muscle Weakness that Reflects a Growth Defect and Energy Deficit. *PLoS One* 4, e5618.
- Scheres, S.H.W. (2012). RELION: Implementation of a Bayesian approach to cryo-

9. References

- EM structure determination.* *J. Struct. Biol.* 180, 519–530.
- Schmeing, T.M., and Ramakrishnan, V. (2009). *What recent ribosome structures have revealed about the mechanism of translation.* *Nature* 461, 1234–1242.
- Schuette, J.-C., Murphy, F. V., Kelley, A.C., Weir, J.R., Giesebrecht, J., Connell, S.R., Loerke, J., Mielke, T., Zhang, W., Penczek, P.A., et al. (2009). *GTPase activation of elongation factor EF-Tu by the ribosome during decoding.* *EMBO J.* 28, 755–765.
- Schuwirth, B.S., Borovinskaya, M.A., Hau, C.W., Zhang, W., Vila-Sanjurjo, A., Holton, J.M., and Cate, J.H.D. (2005). *Structures of the Bacterial Ribosome at 3.5 Å Resolution.* *Science* (80-). 310, 827–834.
- Schweins, T., Geyer, M., Scheffzek, K., Warshel, A., Kalbitzer, H.R., and Wittinghofer, A. (1995). *Substrate-assisted catalysis as a mechanism for GTP hydrolysis of p21ras and other GTP-binding proteins.* *Nat. Struct. Biol.* 2, 36–44.
- Selmer, M., Dunham, C.M., Murphy, F. V., Weixlbaumer, A., Petry, S., Kelley, A.C., Weir, J.R., and Ramakrishnan, V. (2006). *Structure of the 70S ribosome complexed with mRNA and tRNA.* *Science* 313, 1935–1942.
- Semenkov, Y.P., Rodnina, M. V., and Wintermeyer, W. (1996). *The "allosteric three-site model" of elongation cannot be confirmed in a well-defined ribosome system from Escherichia coli.* *Proc. Natl. Acad. Sci. U. S. A.* 93, 12183–12188.
- Shine, J., and Dalgarno, L. (1974). *The 3'-Terminal Sequence of Escherichia coli 16S Ribosomal RNA: Complementarity to Nonsense Triplets and Ribosome Binding Sites.* *Proc. Natl. Acad. Sci.* 71, 1342–1346.
- Shirokikh, N.E., and Preiss, T. (2018). *Translation initiation by cap-dependent ribosome recruitment: Recent insights and open questions.* *Wiley Interdiscip. Rev. RNA* 9, e1473.
- Shirokikh, N.E., Archer, S.K., Beilharz, T.H., Powell, D., and Preiss, T. (2017). *Translation complex profile sequencing to study the in vivo dynamics of mRNA-ribosome interactions during translation initiation, elongation and termination.* *Nat. Protoc.* 12, 697–731.
- Shoemaker, C.J., Eyler, D.E., and Green, R. (2010). *Dom34:Hbs1 promotes subunit dissociation and peptidyl-tRNA drop-off to initiate no-go decay.* *Science* 330, 369–372.
- Shoji, S., Walker, S.E., and Fredrick, K. (2009). *Ribosomal Translocation: One Step Closer to the Molecular Mechanism.* *ACS Chem. Biol.* 4, 93–107.
- Simonetti, A., Marzi, S., Myasnikov, A.G., Fabbretti, A., Yusupov, M., Gualerzi,

9. References

- C.O., and Klaholz, B.P. (2008). Structure of the 30S translation initiation complex. *Nature* 455, 416–420.
- Skabkin, M.A., Skabkina, O. V, Hellen, C.U.T., and Pestova, T. V (2013). Reinitiation and other unconventional posttermination events during eukaryotic translation. *Mol. Cell* 51, 249–264.
- Spahn, C.M., Penczek, P.A., Leith, A., and Frank, J. (2000). A method for differentiating proteins from nucleic acids in intermediate-resolution density maps: cryo-electron microscopy defines the quaternary structure of the *Escherichia coli* 70S ribosome. *Structure* 8, 937–948.
- Spahn, C.M., Gomez-Lorenzo, M.G., Grassucci, R.A., Jørgensen, R., Andersen, G.R., Beckmann, R., Penczek, P.A., Ballesta, J.P., and Frank, J. (2004a). Domain movements of elongation factor eEF2 and the eukaryotic 80S ribosome facilitate tRNA translocation. *EMBO J.* 23, 1008–1019.
- Spahn, C.M.T., Jan, E., Mulder, A., Grassucci, R.A., Sarnow, P., and Frank, J. (2004b). Cryo-EM visualization of a viral internal ribosome entry site bound to human ribosomes: the IRES functions as an RNA-based translation factor. *Cell* 118, 465–475.
- Spirin, A.S. (2009). The Ribosome as a Conveying Thermal Ratchet Machine. *J. Biol. Chem.* 284, 21103–21119.
- Stapulionis, R., and Deutscher, M.P. (1995). A channeled tRNA cycle during mammalian protein synthesis. *Proc. Natl. Acad. Sci. U. S. A.* 92, 7158–7161.
- Sulić, S., Panić, L., Barkić, M., Merćep, M., Uzelac, M., and Volarević, S. (2005). Inactivation of S6 ribosomal protein gene in T lymphocytes activates a p53-dependent checkpoint response. *Genes Dev.* 19, 3070–3082.
- Suloway, C., Pulokas, J., Fellmann, D., Cheng, A., Guerra, F., Quispe, J., Stagg, S., Potter, C.S., and Carragher, B. (2005). Automated molecular microscopy: The new Leginon system. *J. Struct. Biol.* 151, 41–60.
- Susorov, D., Zakharov, N., Shuvalova, E., Ivanov, A., Egorova, T., Shuvalov, A., Shatsky, I.N., and Alkalaeva, E. (2018). Eukaryotic translation elongation factor 2 (eEF2) catalyzes reverse translocation of the eukaryotic ribosome. *J. Biol. Chem.* 293, 5220–5229.
- Tang, G., Peng, L., Baldwin, P.R., Mann, D.S., Jiang, W., Rees, I., and Ludtke, S.J. (2007). EMAN2: An extensible image processing suite for electron microscopy. *J. Struct. Biol.* 157, 38–46.
- Tourigny, D.S., Fernandez, I.S., Kelley, A.C., Ramakrishnan, V., Fernández, I.S., Kelley, A.C., and Ramakrishnan, V. (2013). Elongation factor G bound to the

9. References

- ribosome in an intermediate state of translocation. *Science* (80-). 340, 1235490–1235490.
- Triana, F., Nierhaus, K.H., and Chakraburty, K. (1994). Transfer RNA binding to 80S ribosomes from yeast: evidence for three sites. *Biochem Mol Biol Int* 33, 909–915.
- Tsuboi, T., Kuroha, K., Kudo, K., Makino, S., Inoue, E., Kashima, I., and Inada, T. (2012). Dom34:Hbs1 Plays a General Role in Quality-Control Systems by Dissociation of a Stalled Ribosome at the 3' End of Aberrant mRNA. *Mol. Cell* 46, 518–529.
- UniProt Consortium, T.U. (2008). The universal protein resource (UniProt). *Nucleic Acids Res.* 36, D190-5.
- Valle, M., Zavialov, A., Sengupta, J., Rawat, U., Ehrenberg, M., and Frank, J. (2003). Locking and unlocking of ribosomal motions. *Cell* 114, 123–134.
- Viero, G., Lunelli, L., Passerini, A., Bianchini, P., Gilbert, R.J., Bernabò, P., Tebaldi, T., Diaspro, A., Pederzolli, C., and Quattrone, A. (2015). Three distinct ribosome assemblies modulated by translation are the building blocks of polysomes. *J. Cell Biol.* 208, 581–596.
- Volarevic, S. (2000). Proliferation, But Not Growth, Blocked by Conditional Deletion of 40S Ribosomal Protein S6. *Science* (80-). 288, 2045–2047.
- Voorhees, R.M., Schmeing, T.M., Kelley, A.C., and Ramakrishnan, V. (2010). The Mechanism for Activation of GTP Hydrolysis on the Ribosome. *Science* (80-). 330, 835–838.
- Voorhees, R.M., Fernández, I.S., Scheres, S.H.W., and Hegde, R.S. (2014). Structure of the Mammalian Ribosome-Sec61 Complex to 3.4 Å Resolution. *Cell* 157, 1632–1643.
- Wasserman, M.R., Alejo, J.L., Altman, R.B., and Blanchard, S.C. (2016). Multiperspective smFRET reveals rate-determining late intermediates of ribosomal translocation. *Nat. Struct. Mol. Biol.* 23, 333–341.
- Wettenhall, R.E.H., and Morgan, F.J. (1984). Phosphorylation of hepatic ribosomal protein S6 and 80 and 40 S ribosomes. Primary structure of S6 in the region of the major phosphorylation sites for cAMP-dependent protein kinases. *J. Biol. Chem.* 259, 2084–2091.
- Wettenhall, R.E.H., Erikson, E., and Maller, J.L. (1992). Ordered multisite phosphorylation of Xenopus ribosomal protein S6 by S6 kinase II. *J. Biol. Chem.* 267, 9021–9027.
- Whitford, P.C., Ahmed, A., Yu, Y., Hennelly, S.P., Tama, F., Spahn, C.M.T., Onuchic,

9. References

- J.N., and Sanbonmatsu, K.Y. (2011). Excited states of ribosome translocation revealed through integrative molecular modeling. *Proc. Natl. Acad. Sci. U. S. A.* 108, 18943–18948.
- Wilson, D.N., and Nierhaus, K.H. (2007). The Weird and Wonderful World of Bacterial Ribosome Regulation. *Crit. Rev. Biochem. Mol. Biol.* 42, 187–219.
- Wittinghofer, A., and Vetter, I.R. (2011). Structure-Function Relationships of the G Domain, a Canonical Switch Motif. *Annu. Rev. Biochem.* 80, 943–971.
- Wool, I.G. (1979). The Structure and Function of Eukaryotic Ribosomes. *Annu. Rev. Biochem.*
- Xue, S., and Barna, M. (2012). Specialized ribosomes: a new frontier in gene regulation and organismal biology. *Nat. Rev. Mol. Cell Biol.* 13, 355–369.
- Yamamoto, H., Unbehaun, A., and Spahn, C.M.T. (2017). Ribosomal Chamber Music: Toward an Understanding of IRES Mechanisms. *Trends Biochem. Sci.* 42, 655–668.
- Yang, J., Yan, R., Roy, A., Xu, D., Poisson, J., and Zhang, Y. (2015). The I-TASSER Suite: protein structure and function prediction. *Nat. Methods* 12, 7–8.
- Yusupova, G., and Yusupov, M. (2017). Crystal structure of eukaryotic ribosome and its complexes with inhibitors. *Philos. Trans. R. Soc. B Biol. Sci.* 372, 20160184.
- Zernike, F. (1942). Phase contrast, a new method for the microscopic observation of transparent objects, Part I. *Physica* 9, 974–986.
- Zhang, K. (2016). Gctf: Real-time CTF determination and correction. *J. Struct. Biol.* 193, 1–12.
- Zheng, S.Q., Palovcak, E., Armache, J.-P., Verba, K.A., Cheng, Y., and Agard, D.A. (2017). MotionCor2: anisotropic correction of beam-induced motion for improved cryo-electron microscopy. *Nat. Methods* 14, 331–332.
- Zhou, J., Lancaster, L., Donohue, J.P., and Noller, H.F. (2013). Crystal Structures of EF-G – Ribosome States of Translocation. 340.
- Zhou, J., Lancaster, L., Donohue, J.P., and Noller, H.F. (2014). How the ribosome hands the A-site tRNA to the P site during EF-G-catalyzed translocation. *Science* (80-.). 345, 1188–1191.

10. Appendix

Publications

Flis et al., 'tRNA translocation by the eukaryotic 80S ribosome and the impact of GTP hydrolysis', *Cell reports*, 2018.

Flis, Giessmann and Schnettler Fernández, 'Auf den chemischen Spuren des Histon Codes', *Nachrichten in der Chemie*, 2015.

Acknowledgements

Christian M.T. Spahn supervised the thesis projects. Anett Un behaun supervised my work in the wet lab for the project on serum deprived restimulated polysomes, eS6-phosphorylation and *ex vivo* derived initiation complexes.

Birgit Schroer established 2D-Gel electrophoresis of ribosomal proteins. Tatyana Budkevich gave valuable tips on gel filtration for the preparation of the polysomes. Birgit Schroer as well as Helena Seibel, Brian Bauer and Christine Gotthold supported us in many experiments. Anja Koch provided us with HEK cells for serum treatment and harvesting and introduced me to the work with cell culture. Jörg Bürger helped with negative staining and freezing of the Cryo grids, occasions on which I always learnt a lot. Jörg Bürger also collected datasets of the polysomes for low-resolution screening on Spirit and coordinated storage and shipping of the grids to Heidelberg. Katharina Janek performed Mass Spectrometry of RNase digested polysome samples (48S fractions) and the eS6-spot from 2D-electrophoresis and supported us in the analysis of the data. iNEXT gave us beam time in Heidelberg, where Felix Weis imaged the samples. Part of the calculations were performed on the HLRN.

Tatyana Budkevich prepared the sample for the project on mammalian translocation intermediates, supported by Mary Dabrowski. Jörg Bürger

10. Appendix

froze the grids, and Jörg Bürger and Thorsten Mielke imaged the complex both on Spirit and Polara. Justus Loerke introduced me to SPIDER and helped me resolve many errors that occurred to me as a beginner. Justus Loerke and Enrico Mardus carried out part of the computational work for the translocation project: variability analysis and post-processing. Tarek Hilal and Thiemo Sprink showed me how to use Coot and Phenix. Thiemo Sprink discussed with me the mechanism of translocation and GTP hydrolysis and taught me a lot about it. Tarek Hilal contributed to some parts of the three models of the translocation intermediates. Emily Rundlet, Mikael Holm and Scott Blanchard performed the smFRET experiments that helped us understand the principles of mammalian translocation and contributed to the writing of the paper with helpful discussions, comments, and edits.

Annika Balke, Sophia Banchenko, Jan-Thorben Christiansen, Matthew Kraushar, Ferdinand Krupp, Rainer Nikolay, Julia Smirnova, Bo Qin, Hiroshi Yamamoto and Kaori Yamamoto were also always supportive, as well as all of the people already mentioned above, and basically all people from the Institute of Medical Physics and Biophysics.

My special thanks belongs to my family and friends.